



Max Planck **Graduate Center**  
mit der Johannes Gutenberg-Universität



# Inorganic Nanoparticles in Biological Inspired Catalysis and their Practical Applications

## **Dissertation**

zur Erlangung des akademischen Grades eines

„Doctor rerum naturalium“ (Dr. rer. nat.) der Fachbereiche:

08 - Physik, Mathematik und Informatik

09 - Chemie, Pharmazie und Geowissenschaften

10 - Biologie

Universitätsmedizin

vorgelegt von

**Karsten Korschelt**

geboren am 04.09.1990 in Worms

Mainz, August 2018



---

Die vorliegende Arbeit wurde im Zeitraum von November 2015 bis August 2018 am Institut für Anorganische Chemie und Analytische Chemie der Johannes Gutenberg-Universität Mainz in der Arbeitsgruppe von Prof. Dr. Wolfgang Tremel angefertigt und verfasst.



## **Declaration**

*I hereby declare that I wrote the dissertation submitted without any unauthorized external assistance and used only sources acknowledged in the work. All textual passages which are appropriated verbatim or paraphrased from published and unpublished texts as well as all information obtained from oral sources are duly indicated and listed in accordance with bibliographical rules. In carrying out this research, I complied with the rules of standard scientific practice as formulated in the statutes of Johannes Gutenberg-University Mainz to insure standard scientific practice.*

Mainz, August 2018

A handwritten signature in blue ink that reads "Karsten Koschelt". The signature is written in a cursive style with a large initial 'K'.









---

---

---

---

.

---

---

---

---

---

## List of Scientific Contributions

### First Author Contributions

- 1) **K. Korschelt**, R. Ragg, C. S. Metzger, M. Klünker, M. Oster, B. Barton, M. Panthöfer, D. Strand, U. Kolb, M. Mondeshki, S. Strand, J. Brieger M. N. Tahir, W. Tremel, Glycine-Functionalized Copper(II) Hydroxide Nanoparticles with High Intrinsic Superoxide Dismutase Activity, *Nanoscale*, **2017**, 9 (11), 3952-3960.
- 2) M. Hu,<sup>†</sup> **K. Korschelt**,<sup>†</sup> P. Daniel,<sup>†</sup> K. Landfester, W., M. B. Bannwarth, Fibrous Nanozyme Dressings with Catalase-like Activity for H<sub>2</sub>O<sub>2</sub> Reduction to Promote Wound Healing, *ACS Appl. Mater. Interfaces*, **2017**, 9 (43), 38024-38031.
- 3) **K. Korschelt**, M. N. Tahir, W. Tremel, A Step into the Future – Applications of Nanoparticle Enzyme Mimics, *Chem. Eur. J.*, **2018**, DOI: 10.1002/chem.201800384
- 4) **K. Korschelt**, R. Schwidetzky, F. Pfitzner, J. Strugatchi, K. Kirchhoff, M. Panthöfer, C. Schilling, M. von der Au, I. Lieberwirth, M. N. Tahir, C. Hess, B. Meermann, W. Tremel, CeO<sub>2-x</sub> Nanocrystals with Intrinsic Urease-Like Activity, *Nanoscale* **2018**, Accepted Manuscript, DOI: 10.1039/C8NR03556C.
- 5) M. Hu,<sup>†</sup> **K. Korschelt**,<sup>†</sup> M. Viel,<sup>†</sup> M. Kappl, K. Landfester, H. Thérien-Aubin, W. Tremel, Nanozymes in Fibrous Membranes with Haloperoxidase-Like Activity for combating biofouling, in preparation, **2018**.
- 6) D. Spetter,<sup>†</sup> **K. Korschelt**,<sup>†</sup> M. Oster, K. Kirchhoff, M. N. Tahir, W. Tremel, Selective Oxidation of Organic Sulfides with Single Metal Oxide and Mixed Metal Oxide Particles, in preparation **2018**.

<sup>†</sup> authors contributed equally

### Co-Author Contributions

- 1) M. Klueker, B. M. Connolly, D. M. Marolf, M. N. Tahir, **K. Korschelt**, P. Simon, U. Köhler, B. Barton, M. Panthöfer, U. Kolb, W. Tremel, Controlling the Morphology of Au-Pd Heterodimer Nanoparticles by Surface Ligands, submitted to *Inorganic Chemistry*, **2018**
- 2) M. N. Tahir, M. Klueker, F. Natalio, B. Barton, **K. Korschelt**, S. I. Shylin, M. Panthöfer, V. Ksenofontov, A. Möller, U. Kolb, W. Tremel, From Single Molecules to Nanostructured Materials: Formation of a Magnetic Foam Catalyzed by Pd@Fe<sub>x</sub>O Heterodimers, *ACS Appl. Nano Mater.*, **2018**, 1, 1050-1057.
- 3) M. Klueker, M. N. Tahir, R. Ragg, **K. Korschelt**, P. Simon, T. E. Gorelik, B. Barton, S. I. Shylin, M. Panthöfer, J. Herzberger, H. Frey, V. Ksenofontov, A. Möller, U. Kolb, Y. Grin, W. Tremel, Pd@Fe<sub>2</sub>O<sub>3</sub> Superparticles with Enhanced Peroxidase Activity by Solution Phase Epitaxial Growth, *Chem. Mater.* **2017**, 29, 1134 – 1146.
- 4) R. Ragg, A. M. Schilman, **K. Korschelt**, C. Wieseotte, M. Klueker, M. Viel, L. Völker, S. Preiß, J. Herzberger, H. Frey, K. Heinze, P. Blümner, M. N. Tahir, F. Natalio, W. Tremel, Intrinsic Superoxide Dismutase Activity of MnO Nanoparticles Enhances Magnetic Resonance Imaging Contrast, *J. Mater. Chem. B*, **2016**, 4, 7423 – 7428.

### Book Chapter Contributions

- 1) R. Ragg, **K. Korschelt**, K. Herget, F. Natalio, M. N. Tahir, W. Tremel, Inorganic Nanoparticles as Enzyme Mimics, *Biocatalysis & Nanotechnology*, Pan Stanford Publishing Pte. Ltd., **2017**.





## Summary

Native enzymes are maybe the most specialized catalysts, which were optimized by nature over thousands of years. They play a crucial role in uncountable biochemical processes and their dysfunctionality usually has serious impact for the superordinated organism. Nevertheless, native enzymes still have sharp limitations, especially in practical applications, beyond their natural occurrence. The practical use of the native or recombinant synthesized catalysts is limited to special pH- and temperature values and accompanied by high production costs.

Inspired by the central role of native enzymes in nature, a myriad of researchers is focussed on the exploration of functional and catalytically active enzyme replacements. Recently, various forms of enzyme-mimics, mainly supramolecules, metal complexes and metal oxide nanoparticles, have been reported in literature.

The catalytic properties of metal containing nanomaterials within the field of classical heterogeneous catalysis, are well known, but their potentials as enzyme replacements were overlooked for a long time. Such a development in past is quite surprising, because nature was everytime a great model for many researchers and there are many similarities between nanoparticles and native enzymes. Due to their size ranges native enzymes could in general be described as “nano” catalysts. Another important analogy of native enzymes and artificial nanozymes is, that enzyme-catalyzed reactions are formally similar to surface-catalyzed reactions. While the Michaelis Menten theory proposes that an enzyme (E) binds a substrate (S), forming an enzyme substrate complex (ES), which is subsequently transformed to a product (P) and the enzyme (E). The Eley-Rideal-mechanism describes catalytic process of a surface catalyzed reaction with the adsorption of a reactant ( $R_1$ ) onto the catalyst surface (C), while the second reactant ( $R_2$ ) directly interacts with the adsorbed species (from gas phase or from solution), followed by desorption of the product (P). This similarity is representing the basic idea behind the nanozyme research.

In the first years of exploring nanoparticles in the biocatalytic context, various enzyme mimics like peroxidases, catalases and superoxide dismutases were reported. Recently, especially the exploration of practical applications, mostly *in vitro* and *in vivo* studies, where the focal point of research.

The present thesis enables an insight into recent and current enzyme mimetic literature, focussing on possible practical applications. Studies conducted within the scope of this thesis will be described and discussed in context of the existing *status quo* in literature.

- 1) Glycine functionalized copper (II) hydroxide nanoparticles were synthesized on a simple and large-scale route, executed at room temperature in an aqueous solution. The nanoparticles were able to mimic the catalytic activity of native CuZn superoxide dismutase enzyme. In context of investigating the intrinsic superoxide dismutase-like activity, a novel calculation method for nanozymes was established, enabling the normalization of activities to one active surface site. Deeper studies of the reaction mechanism indicated properties of a catalytic process, rather than a simple oxidation of copper surface atoms. Glycine functionalized copper(II) hydroxide nanoparticles applied to commercial filter cigarettes were able to reduce reactive oxygen species in cigarette smoke.
- 2) A hematite containing polyvinyl alcohol fiber mesh was prepared *via* electrospinning and free alcohol groups of the mesh were crosslinked with glutaraldehyde. As-prepared meshes were not soluble in water, but swelling properties enabled a substrate diffusion into the fibers. Embedded hematite nanoparticles still exhibited a catalase-like activity, comparable to native catalase and not electrospun nanoparticles. The fibers were able to protect fibroblasts against cell death, triggered by elevated hydrogen peroxide concentrations.

- 3) Native enzymes like the vanadium haloperoxidases are important biocatalysts. The group haloperoxidases catalyse the reaction of  $X^-$  ( $X = \text{Br}, \text{Cl}, \text{I}$ ) and  $\text{H}_2\text{O}_2$  which forms hypohalous acids HOX. Formed HOX can halogenate organic compounds in different follow-up reactions. The formation of HOX can prevent the biofilm formation because of their biocidal activity. In this project a nanoceria containing polyvinyl alcohol fiber mesh was synthesized and the haloperoxidase-like activity was tested. It was found, that the prepared fibers still show a high activity in a haloperoxidase-like reaction. It was further demonstrated that the nanoparticle containing fibers show an improved stability, which was tested *via* atomic force microscopy. The catalytic activity and the mechanical stability enable that nanoceria containing fibers could practically be used to prevent the biofilm formation and to overcome the limitations of “free” nanoparticles like the reduction of active material with time due to leaching effects.
- 4) Native jack bean urease, an urea splitting enzyme, was the first native enzyme, which could be crystallized. Because of the reaction products ammonia and carbonate, generated in aqueous solution, a kinetic study of urease or possible urease mimics is time-consuming and not trivial. Hence, a time efficient lab assay was developed and nanoceria as the first nanozyme with urease-like activity was reported. In addition to the kinetic studies of cerium oxide nanoparticles, the influence of the surface ratio of cerium(III)/cerium(IV) was investigated, by synthesizing lanthanum doped ceriumoxide nanoparticles. It was found, that a lower ratio, which is synonymous with a higher cerium(IV) concentration at the nanoparticle surface, lead to a higher activity. In further analysis the influence of copper(II) ions, one of the strongest urease inhibitor, was investigated. We found, that copper(II) ions neither have influence on the catalytic activity of cerium oxide nanoparticles, nor on the lanthanum doped cerium oxide nanoparticles.

- 5) Various single metal oxide particles, like molybdenum, tungsten and vanadium oxide, were synthesized and their catalytic activity in an sulfide oxidation reaction, was investigated. To determine the catalytic activity of the different catalysts, kinetic studies were conducted using methyl phenyl sulfide as model substrate. The organic sulphide was oxidized with hydrogen peroxide as green and biocompatible oxidation agent in an aqueous media. We found, that the catalytic activity and the product formation could be enhanced with the use of molybdenum and tungsten mixed oxide particles. Mixed oxide particles with different Mo:W ratios were synthesized and their ability of facilitating the oxidation of methyl phenyl sulfide was investigated. We found, that all mixed oxide particles catalyzed the oxidation of methyl phenyl sulfide completely selective into the methyl phenyl sulfoxide or the methyl phenyl sulfone in presence of one or three equivalents of hydrogen peroxide. In addition to kinetic studies we investigated the influence of different functional groups of the organic sulfide and the effect of steric hindrance. In general, high turnovers could be achieved.

## Zusammenfassung

Natürlich vorkommende Enzyme sind wohl die am besten entwickelten und spezialisierten Katalysatoren der Welt, wurde ihre Funktionsweise doch über Jahrtausende von der Natur optimiert. Enzyme spielen in unzähligen biochemischen Prozessen eine zentrale Rolle und ihre Dysfunktion hat meist ernste Konsequenzen für den beheimatenden Organismus. Nichtsdestotrotz ist die praktische Anwendung natürlicher, oder rekombinant hergestellter Enzyme, außerhalb ihres natürlichen Auftretens stark limitiert. So ist ihre Funktionsweise und somit Verwendbarkeit auf definierte pH- und Temperaturbereiche limitiert und zudem stets von hohen Produktionskosten begleitet.

Inspiziert von der zentralen Rolle natürlicher Enzyme in der Natur beschäftigt sich eine Vielzahl an Wissenschaftlern mit der Erforschung von funktionellen und katalytisch aktiven Enzymersatzmaterialien. In den letzten Jahren wurden verschiedene Verbindungen beschrieben, die eine enzym-ähnliche Aktivität aufweisen. Dabei handelte es sich meistens um Supramoleküle, Metallkomplexe und Metalloxid-Nanopartikel.

Die katalytischen Eigenschaften von metallhaltigen Nanomaterialien in einer klassischen heterogenen Katalyse sind seit langer Zeit bekannt, doch wurde ihr Potential als Enzymersatz zunächst übersehen. Dabei besteht zwischen Reaktionen, katalysiert durch natürliche Enzyme, und nanopartikelkatalysierten Reaktionen eine interessante Analogie. Die Michaelis-Menten-Theorie beschreibt eine enzymkatalysierte Reaktion wie folgt: Das katalytisch aktive Zentrum eines Enzyms bindet ein Substrat, was zur Bildung eines Enzym-Substrat-Komplexes führt, welcher anschließend in das Produkt und das Enzym gespalten wird. In ähnlicher Art und Weise beschreibt der Eley-Rideal-Mechanismus eine klassisch heterogene Katalyse. In dieser wird der Reaktand an der Katalysatoroberfläche adsorbiert und kann so direkt mit einem zweiten Reaktanden (aus der Gas- oder Flüssigphase) in Wechselwirkung treten. Dies ist gefolgt von der Desorption des Reaktionsproduktes. Die Ähnlichkeit

der Michalis-Menten-Theorie und des Eley-Rideal-Mechanismus verdeutlicht die grundlegende Idee hinter der Erforschung von Nanopartikeln als Enzym-Mimetika.

In den ersten Jahren der Erforschung von Nanopartikeln im genannten biokatalytischen Kontext wurden verschiedene Enzym-Mimetika, wie zum Beispiel Peroxidasen, Katalasen und Superoxiddismutasen, beschrieben. In den letzten Jahren rückten jedoch hauptsächlich mögliche praktische Anwendungen, meist *in vitro* oder *in vivo* Studien, in den Fokus der Forschung.

Die vorliegende Dissertation gibt einen Einblick in die frühere und aktuelle Literatur im Bereich der Enzym-Mimetik und fokussiert sich dabei vornehmlich auf denkbare und praktische Anwendungen. Die im Rahmen der Arbeit durchgeführten praktischen Laboruntersuchungen werden beschrieben und im Kontext des *status quo* der Literatur diskutiert. Die vorliegende Arbeit ist aus den fünf nachfolgend beschriebenen Kapiteln aufgebaut.

- 1) Glycin-funktionalisierte Kupfer(II)-hydroxid Nanopartikel wurden mittels einer einfachen und in großem Maßstab durchgeführten Synthese, bei Raumtemperatur dargestellt. Die Nanopartikel zeigten eine intrinsische Superoxiddismutase-Aktivität ähnlich der des natürlichen CuZn Superoxiddismutase-Enzyms. Im Kontext der Untersuchungen dieser Aktivität wurde weiterhin eine neue Berechnungsmethode für katalytische Aktivitäten von Nanopartikeln, welche eine Normierung auf ein Oberflächenatom ermöglicht, beschrieben. Genauere Studien des Reaktionsverlaufes zeigten zudem, dass die Reaktion Eigenschaften eines katalytischen Zyklus aufweist. Das Integrieren der Nanopartikel in kommerziell erhältliche Filterzigaretten führte zu einer Reduktion von reaktiven Sauerstoffverbindungen im Zigarettenrauch.

- 2) Hämatit-Nanopartikel wurden in Polymerfasern, bestehend aus Polyvinylalkohol, durch Elektrospinnerei eingebettet. Das dabei erhaltene Polymerfasernetzwerk wurde im Anschluss durch Reaktion der freien Alkoholgruppen mit 1,5-Pentandial (Glutaraldehyd) quervernetzt, was dazu führte, dass das erhaltene Netz in Wasser unlöslich war. Jedoch zeigte das gesamte Netzwerk ein Quellverhalten, wodurch Wasser und somit wasserlösliche Substrate in die Fasern diffundieren konnten. Die eingesponnenen Hämatit-Nanopartikel zeigten eine Katalase-Aktivität, ähnlich derer nativer Katalase und nicht eingesponnener Partikel in wässriger Lösung. Die dargestellten Polymerfasern waren zudem in der Lage Fibroblasten vor dem Zelltod, ausgelöst durch erhöhte Wasserstoffperoxid-Konzentration, zu schützen.
  
- 3) Natürliche Enzyme, wie z.B. die Vanadium Haloperoxidase, sind wichtige Biokatalysatoren. Die Gruppe der Haloperoxidasen katalysiert die Reaktion von Halogeniden  $X^-$  mit  $H_2O_2$ , woraus sich Hypohalogenige Säuren HOX bilden. Das gebildete HOX besitzt eine biozide Wirkung und kann die Biofilmbildung verhindern bzw. hemmen. In diesem Projekt wurden Ceroxid Nanopartikel in Polymerfasern aus Polyvinylalkohol eingesponnen und auf ihre Haloperoxidase Aktivität untersucht. Trotz des Einbringens der Nanopartikel in die Polymermatrix zeigten diese noch immer eine hohe Haloperoxidase-Aktivität. Weiterhin wurde mit Hilfe von AFM Messungen gezeigt, dass die Nanopartikel beinhaltenden Polymerfasern eine erhöhte Stabilität aufweisen. Die katalytische Aktivität gepaart mit der mechanischen Stabilität ist die Grundlage für eine mögliche praktische Anwendung im Bereich Antifouling. Dabei ermöglicht die Fixierung der Partikel in der Faser zudem das Überschreiten der Anwendungsgrenzen von freien Partikeln in Lösung, welche sehr leicht ausgewaschen werden.

- 4) Die native Urease, ein Harnstoff spaltendes Enzym, war das erste natürliche Enzym, welches erfolgreich kristallisiert werden konnte. Aufgrund der Reaktionsprodukte in wässriger Lösung (Ammonium- und Carbonationen) ist eine kinetische Analyse der Urease sowie potentieller Urease-Mimetika meist extrem zeitaufwendig und nicht gerade trivial. In diesem Kontext wurde eine praktikable und effiziente Labormethode entwickelt und mit Ceroxid der erste auf Nanopartikeln basierende Ersatz für natürliche Urease beschrieben. Weiterhin wurde der Einfluss der Nanopartikeloberfläche auf die katalytische Aktivität untersucht. Hierzu wurden lanthandotierte Nanopartikel synthetisiert und somit das Oberflächenverhältnis von Cer(III)/Cer(IV) verändert. Hierbei wurde gezeigt, dass ein geringeres Oberflächenverhältnis, also eine erhöhte Konzentration an Cer(IV) auf der Partikeloberfläche, zu einer erhöhten Aktivität führt. In weiteren Untersuchungen wurde der Einfluss von Cu(II)-Ionen, einer der stärksten Ureaseinhibitoren untersucht. Diese hatten weder auf die Ceroxid Nanopartikel, noch auf die lanthandotierten Nanopartikel, einen Einfluss.



- 5) Verschiedene Metalloxid-Partikel, wie zum Beispiel Molybdän-, Wolfram und Vanadiumpentoxid, wurden synthetisiert und ihre katalytische Aktivität in einer Oxidationsreaktion von Sulfiden untersucht. Zur Untersuchung der katalytischen Aktivitäten der verschiedenen Metalloxid Partikel, Thioanisol wurde als Modell Substrat für organische Sulfide verwendet. Das organische Sulfid wurde in Anwesenheit von Wasserstoffperoxid, welches als „grünes“ und biokompatibles Oxidationsmittel gilt, in wässriger Lösung oxidiert. Die katalytische Aktivität und die Bildung des Produktes konnten durch die Synthese und Verwendung von Molybdän-Wolfram Mischoxid-Partikeln gesteigert werden. Mischoxid-Partikel mit verschiedenen Mo:W-Verhältnissen wurden synthetisiert und ihre Aktivität als Katalysator in der Oxidation von Thioanisol untersucht. Alle hergestellten und verwendeten Partikel katalysierten die Oxidation von Thioanisol selektiv entweder zu Methylphenylsulfoxid oder zu Methylphenylsulfon in Anwesenheit von einem bzw. drei Äquivalenten Wassertoffperoxid. Hierbei zeigte sich, dass Molybdän-Wolfram-Mischoxide mit einem Mo:W-Verhältnis von 1.6:1 die höchste Aktivität aufwiesen. Zur weiteren Charakterisierung der katalytischen Aktivitäten und zur Untersuchung des Einflusse verschiedener funktioneller sowie sterisch mehr oder weniger anspruchsvoller Gruppen, wurde eine weiter Bandbreite organischer Sulfide verwendet und deren Oxidationen untersucht. Insgesamt konnten hohe Umsatzzahlen erreicht werden.



---

## List of Abbreviations

$^{13}\text{C}$ -Gly	$^{13}\text{C}$ Marked Glycine
<b>AA</b>	Ascorbic Acid
<b>AAS</b>	Atomic Absorption Spectroscopy
<b>Acac</b>	Acetyl Acetate
<b>AD</b>	Alzheimer's Disease
<b>AFM</b>	Atomic Force Microscopy
<b>Assym.</b>	Asymmetric
<b>BBB</b>	Blood Brain Barrier
<b>BET</b>	Brunauer Emmett Teller
<b>Br<sub>4</sub>PR</b>	Bromophenol Blue
<i>C. officinalis</i>	<i>Corallina officinalis</i>
<b>CAT</b>	Catalase
<b>CCD</b>	Charge Coupled Device
<b>CSE</b>	Cigarette Smoke Extract
<b>CuZn SOD</b>	Copper Zinc Superoxide Dismutase
<b>d</b>	Doublet
<b>dd</b>	Doublet of a Doublet
<b>D<sub>2</sub>O</b>	Deuterated Water
<b>DANN</b>	Deoxyribonucleic Acid
<b>DSPE-PEG-TPP</b>	1,2-distearoyl-sn-glycero-3-phosphoethanolamine- <i>N</i> - [carboxy (polyethylene glycol) triphenylphosphonium

---

<i>E. coli</i>	<i>Escherichia Coli</i>
<b>EC SOD</b>	Extracellular Superoxide Dismutase
<b>EDX Spectroscopy</b>	Energy-Dispersive X-Ray Spectroscopy
<b>EM</b>	Electron Microscopy
<b>EPR Effect</b>	Enhanced Permeability and Retention Effect
<b>ETD</b>	Everhart-Thornley Detector
<b>EuTc</b>	Europium Tetracycline complex
<b>EuTc-HP</b>	Europium Tetracycline Hydrogen Peroxide Complex
<b>F-HG</b>	Flavin-Dependent Halogenases
<b>Fig</b>	Figure
<b>FTIR Spectroscopy</b>	Fourier-Transform Infrared Spectroscopy
<b>FWHM</b>	Full Width at Half Maximum
<b>GA</b>	Glutaraldehyde
<b>Gly</b>	Glycine
<b>Gly-Cu(OH)<sub>2</sub> NPs</b>	Glycine Functionalized Copper(II) Hydroxide Nanoparticles
<b>Gly-Ni(OH)<sub>2</sub> NPs</b>	Glycine Functionalized Nickel(II) Hydroxide Nanoparticles
<b>GPx</b>	Glutathione Peroxidase
<b>GSH</b>	Reduced Glutathione
<b>GSSG</b>	Oxidized Glutathione
<b>HF<sub>n</sub></b>	Human Heavy-Chain Ferritin
<b>HOX</b>	Hypohalous Acids

---

---

<b>HP</b>	Hydrogen Peroxide
<b>HPOs</b>	Haloperoxidases
<b>HR-TEM</b>	High Resolution Transmission Electron Microscopy
<b>IC<sub>50</sub></b>	Required Concentration of Catalyst to Achieve a 50% Inhibition
<b>ICP</b>	Inductively Coupled Plasma
<b>INT</b>	Iodonitrotetrazolium Chloride
<b>IR</b>	Infrared
<b>Lys</b>	Lysine
<b>M</b>	Molar Mass
<b>m</b>	Multiplet
<b>MAS</b>	Magic Angle Spinning
<b><i>m</i>-CPBA</b>	<i>Meta</i> -chloroperoxybenzoic Acid
<b>MilliQ Water</b>	Ultrapure Water of Type 1
<b>Mn SOD</b>	Manganese Superoxide Dismutase
<b>MNPs</b>	Magnetite Nanoparticles
<b>MOPS</b>	3-( <i>N</i> -morpholino)propanesulfonic acid
<b>MPs</b>	Microparticles
<b>MPS</b>	Methyl Phenyl Sulfide
<b>MPSO</b>	Methyl Phenyl Sulfoxide
<b>MS</b>	Mass Spectrometry
<b>NADPH</b>	Nicotinamide Adenine Dinucleotide Phosphate
<b>Nanoceria</b>	Cerium oxide nanoparticles

---

## List of Abbreviation

---

<b>Nd:YAG</b>	Neodymium-Doped Yttrium Aluminium Garnet
<b>NI-HG</b>	Non-Heme Iron(II) Dependent Halogenases
<b>NIR</b>	Near Infrared
<b>NMR Spectroscopy</b>	Nuclear Magnetic Resonance Spectroscopy
<b>NOS</b>	Nitric Oxide Synthase
<b>NO<sub>x</sub></b>	Nitrogen Oxides
<b>NP</b>	Nanoparticle
<b>NR</b>	Nanorod
<b>PBS</b>	Phosphate Buffered Saline
<b>PEG</b>	Polyethylene Glycol
<b>PLGA</b>	Poly(lactic-co-glycolic acid)
<b>PR</b>	Phenol Red
<b>PVA</b>	Poly Vinyl Alcohol
<b>P-XRD</b>	Powder X-ray Diffraction
<b>q</b>	Quartet
<b>QS</b>	Quorum Sensing
<b>Ref</b>	Reference
<b>RNS</b>	Reactive Nitrogen Species
<b>ROS</b>	Reactive Oxygen Species
<b>Rpm</b>	Rounds per Minute
<b>Rps</b>	Rounds per Second
<b>RT</b>	Room Temperature
<b>s</b>	Singulet

---

<b>SA</b>	Surface Area
<b>SAED</b>	Selected Area Electron Diffraction
<b>SEM</b>	Scanning Electron Microscopy
<b>SI</b>	Supporting Information
<b>SOD</b>	Superoxide Dismutase
<b>SuOx</b>	Sulfite Oxidase
<b>t</b>	Triplet
<b>Tab</b>	Table
<b>TAMRA</b>	5-carboxytetramethylrhodamine
<b>TEM</b>	Transmission Electron Microscopy
<b>TfR 1</b>	Transferrin Receptor 1
<b>TGA</b>	Thermogravimetry
<b>TMSP</b>	3-(Trimethylsilyl)propionic-2,2,3,3 d <sub>4</sub> sodium salt
<b>TON</b>	Turnover Number
<b>TPP</b>	Triphenylphosphonium
<b>Urea-SCR</b>	Urea in Selective Catalytic Reduction
<b>UV</b>	Ultra Violet
<b>V</b>	Volume
<b>vCD Detector</b>	Low-Voltage High-Contrast Detector
<b>V-HPOs</b>	Vanadium Haloperoxidases
<b>Vis</b>	Visible
<b>VT</b>	Variable Temperature
<b>XO</b>	Xanthine Oxidase

---

## List of Abbreviation

---

<b>XPS</b>	X-Ray Photoelectron Spectroscopy
------------	----------------------------------

<b>XRD</b>	X-ray Diffraction
------------	-------------------

<b><math>\Delta</math>Abs</b>	Change of Absorption
-------------------------------	----------------------

<b><math>\lambda_{em}</math></b>	Emission Wavelength
----------------------------------	---------------------

<b><math>\lambda_{max}</math></b>	Maximum Absorption Wavelength
-----------------------------------	-------------------------------



# Table of Content

<b>1. Introduction</b>	<b>1</b>
<b>2. Theoretical Background</b>	<b>3</b>
2.1 Inorganic Nanoparticles as Enzyme Mimics	3
2.1.1 References	14
2.2 A Step into the Future – Applications of Nanoparticle Enzyme Mimics	20
2.2.1 Abstract	21
2.2.2 Introduction	21
2.2.3 Nanozymes as ROS Scavengers for Biomedical Applications	24
2.2.4 Nanozymes for Tumor and Cancer Therapy	31
2.2.5 Nanozymes for Enzyme Replacement Therapy	35
2.2.6 Nanozymes for Environmental Applications	37
2.2.7 Comparing Particle and Enzyme Activities	42

2.2.8 Conclusion and Outlook	44
2.2.9 References	46
<b>3. Results and Discussion</b>	<b>55</b>
3.1 Glycine-Functionalized Copper(II) Hydroxide Nanoparticles with High Intrinsic Superoxide Dismutase Activity	56
3.1.1 Abstract	57
3.1.2 Introduction	57
3.1.3 Experimental	60
3.1.4 Results and Discussion	66
3.1.5 Conclusions	74
3.1.6 References	76
3.1.7 Supporting Information	82
3.2 Fibrous Nanozyme Dressings with Catalase-like Activity for H <sub>2</sub> O <sub>2</sub> Reduction to Promote Wound Healing	96
3.2.1 Abstract	97

3.2.2 Introduction	97
3.2.3 Experimental	101
3.2.4 Results and Discussion	105
3.2.5 Conclusions	115
3.2.6 References	116
3.2.7 Supporting Information	121
<b>3.3 Nanozymes in Fibrous Membranes with Haloperoxidase-Like Activity</b>	<b>126</b>
3.3.1 Abstract	127
3.3.2 Introduction	127
3.3.3 Experimental	131
3.3.4 Results and Discussion	136
3.3.5 Conclusions	142
3.3.6 References	143
3.3.7 Supporting Information	149

3.4 CeO <sub>2-x</sub> Nanorods with Intrinsic Urease-Like Activity	152
3.4.1 Abstract	153
3.4.2 Introduction	154
3.4.3 Experimental	157
3.4.4 Results and Discussion	164
3.4.5 Conclusions	175
3.4.6 References	176
3.4.7 Supporting Information	181
3.5 Mixed Oxide Particles with Enhanced Catalytic Activity	203
3.5.1 Abstract	204
3.5.2 Introduction	204
3.5.3 Experimental	209
3.5.4 Results and Discussion	213
3.5.5 Conclusions	222
3.5.6 References	223

---

3.5.7 Supporting Information	227
<b>4. Conclusion and Outlook</b>	<b>245</b>
<b>5. Appendix</b>	<b>I</b>
5.1 List of Figures	I
5.2 List of Tables	X
5.3 Author Contributions	XIII
5.3.1 Manuscript: "A Step into the Future – Applications of Nanoparticle Enzyme Mimics"	XIII
5.3.2 Manuscript: "Glycine-Functionalized Copper(II) Hydroxide Nanoparticles with High Intrinsic Superoxide Dismutase Activity"	XIV
5.3.3 Manuscript: "Fibrous Nanozyme Dressings with Catalase-like Activity for H <sub>2</sub> O <sub>2</sub> Reduction to Promote Wound Healing"	XVI
5.3.4 Manuscript: "Nanozymes in Fibrous Membranes with Haloperoxidase-Like Activity for combating biofouling"	XVII
5.3.5 Manuscript: "CeO <sub>2-x</sub> Nanorods with Intrinsic Urease-Like Activity"	XVIII

5.3.6 Manuscript: “Selective Oxidation of Organic Sulfides with Single Metal Oxide and Mixed Metal Oxide Particles”	XX
--	----

# 1. Introduction

In every decade of natural science research, scientists were inspired by nature or natural processes. The reasons for using native inspirations are easily to understand by observing the complexity of physical, biological and biochemical processes and the problem-solving mechanisms provided by nature. Of course, these processes were optimized over thousands of years and they are under a continuous development process, but “perfect” model systems for many ecological and environmental problems can be found in natural surroundings. Research based on native sources has different approaches like for example the exploration and description of natural processes by reproducing them in lab scale and monitoring the characteristics. Another approach is to use natural models as inspiration, try to mimic their characteristics and to overcome their disadvantages or improve the efficiency with artificial materials. This approach enables the development of novel applications. There are many examples that can illustrate the relevance of native models for modern inventions. In the following, two impressive examples are shortly named and described.

The pictures and videos of lotus flowers in the rain, from which the water droplets easily drip off, are familiar to nearly everyone. The so-called lotus-effect describes the surface area reducing behaviour of water droplets on top of the lotus flowers. Inspired by this phenomenon, scientists explored nanomaterial containing car paints with similar characteristics. Nowadays, these paints offer a protection against impurities with an improved drying process without water residuals. Next to such obvious relationships between modern developments and their native models, a great success in industry was achieved inspired by small details in nature. For example, the developments of novel swimminug suits for competitive athletes, a foil for passenger aircrafts and a paint for ship hulls in the year 2009 had the same native model - the shark. The movement of a shark looks very smart and needs to be very efficient. Considering the physical build of these animals, their high acceleration, speed and endurance are surprising. Investigations of their skin with

a scanning electron microscope demonstrated the secret of their high efficiency. The shark skin has a high number of riblets with which a low drag can be achieved and they offer an efficient way of draining water at the interface of solid skin and the liquid. Similar principles improve the aerodynamic of planes, water resistance of swimming suites and ship hulls.

A widely occurring principle, which is omnipresent in nature and in modern industry, is the use of catalysts to facilitate or enable chemical or biochemical processes. While nature solves the problem of low reaction rates with enzymes or other catalytic species, industry uses artificial compounds like noble metals, metal complexes or nanomaterials to enable or prefer a specific reaction. Native enzymes were developed, optimized and adjusted by nature over a long time and we can describe them nowadays as highly active catalysts with a high selectivity towards the presence of different substrates. They play a crucial role in different biochemical processes and a dysfunction forms the basis of serious complications for the superordinated organism. Many scientists over the past thirteen years, and still nowadays, are driven by the important role of native enzymes and they are focussed on the exploration of functional and active enzyme replacements.

The target of the present thesis was to synthesize and characterize inorganic nanoparticles that can mimic the catalytic activity of native enzymes. Further studies about practical applications were focussed on overcoming limitations, given by the implementation of extracted or recombinant synthesized enzymes.



## 2. Theoretical Background

The following part of the thesis shortly describes the basic ideas of enzyme mimic research with focus on nanoparticulate enzyme replacements.

### 2.1. Inorganic Nanoparticles as Enzyme Mimics

The research about artificial compounds that can mimic native enzymes, so called enzyme mimics, is a still upcoming and interesting part of biomimetic chemistry. Ronald Breslow, for the first time, named compounds with an enzyme-like activity as “artificial enzymes”.<sup>1</sup> The basic idea behind using enzyme mimics and hence the main target of the scientists, is to overcome the disadvantages of native enzymes, like high production costs, inhibition effects by different substrates like metal ions, the low stability and the aspect that a practical use is limited by specific pH and temperature values.<sup>2-4</sup> In recent years a wide variety of possible enzyme replacements like metal containing model complexes,<sup>5-7</sup> polymers,<sup>8</sup> supramolecules,<sup>9</sup> and nanomaterials<sup>10-13</sup> have been reported with great success. The high response in modern literature is reflected by the still increasing number of publications in scientific journals. The number of publications in the year 2017 with the keyword “enzyme mimic” was approximately 1.7 times higher than the number ten years before and even three times higher than twenty years before.<sup>14</sup> All of the above-mentioned strategies of mimicking native enzymes have their justification, connected to special advantages and disadvantages.

The current work is focussed on alternatives for native enzymes based on metal containing nanomaterials. Hence, a comparison of the so called “nanozymes”<sup>2,15</sup> with their native counterparts is given in the following. While the use of inorganic nanoparticles as heterogeneous catalysts is widely known, their excellent properties as enzyme replacements were overlooked for a long time. However, a practical application in this field is promising because nanoparticles are size comparable to native enzymes<sup>2,3</sup> and especially enzymes that uses metal ions in their catalytic active

## 2. Theoretical Background

---

site (metalloenzymes) are great inspirations.<sup>16,17</sup> It is an auspicious and strategic approach to previously explore nanozymes based on metal ions that are present in the active site of native enzymes and to improve the system with chemical and biological know-how in a second step. In contrast to the synthesis or extraction processes of native enzymes, the preparation of nanoparticles is cost efficient and can be executed in a multi gram scale.<sup>18,19</sup> Because of their large surface area and therefore high number of active surface sites, nanozymes exhibit efficiencies that may increase the one of their native model.<sup>20</sup> Also, the limitations of enzymes to a physiological environment can be circumvented, as nanozymes are stable over wide pH and temperature ranges<sup>2,3</sup> and they are further tunable by surface functionalization or changing the chemical composition.<sup>21</sup> In contrast to the similarity of native enzymes and nanozymes and the possibility of overcoming the described limitations, there are some challenges and problems which currently need to be solved. One of the main tasks is the low specificity of nanozymes which goes hand in hand with a mostly low biocompatibility (Figure 1).<sup>3</sup>

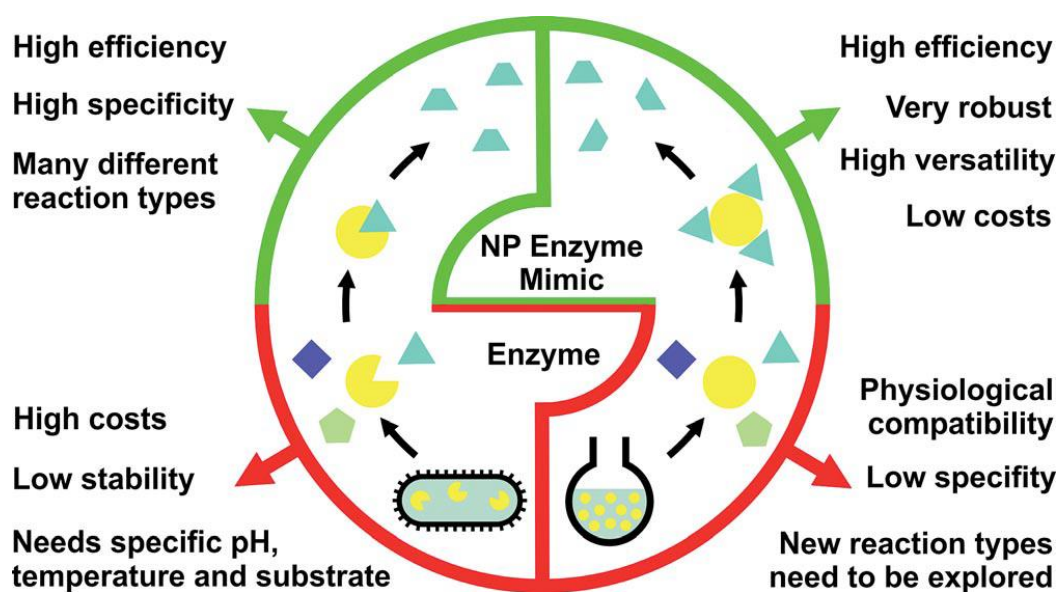


Figure 1. Schematic representation of advantages and disadvantages of native enzymes compared to nanoparticle enzyme mimics, the so called “nanozymes”. Reprinted with permission from Ref<sup>3</sup>. Copyright John Wiley and Sons.

In recent years a wide variety of different nanomaterials, in most cases metal oxide species, has been reported in literature.<sup>2,3,22</sup> Monitoring the wide variety of nanoparticles with enzyme-like activity also illustrates that almost exclusively native oxido reductases served as native model systems (Table 1).<sup>22</sup>

**Table 1.** Inorganic Nanoparticles with enzyme like activities and practical applications<sup>22</sup>

<b>Nanomaterial</b>	<b>Enzyme-like activity</b>	<b>Application</b>	<b>Ref.</b>
Fe <sub>3</sub> O <sub>4</sub> NPs	Peroxidase	Tumor targeting and visualization	23
		Immunoassays	10
		H <sub>2</sub> O <sub>2</sub> and glucose detection	24
$\gamma$ -Fe <sub>2</sub> O <sub>3</sub> NPs	Peroxidase		25
$\gamma$ -FeOOH graphene	Peroxidase	Phenole degradation	26
FePO <sub>4</sub> microflowers	Peroxidase	H <sub>2</sub> O <sub>2</sub> biosensor	27
FeS nanosheets	Peroxidase	H <sub>2</sub> O <sub>2</sub> detection	28
FeTe nanorods	Peroxidase	Glucose detection	29
FePt NPs	Peroxidase		30
CuO nanostructures	Peroxidase	Pollutant removal in wastewater	31

## 2. Theoretical Background

---

<b>Nanomaterial</b>	<b>Enzyme-like activity</b>	<b>Application</b>	<b>Ref.</b>
CuS polyhedral structures	Peroxidase		33
Cu <sub>3</sub> (PO <sub>4</sub> ) <sub>2</sub> NC	Peroxidase	Pollutant removal	32
CuS polyhedral structures	Peroxidase		33
Cu nanoclusters	Peroxidase	H <sub>2</sub> O <sub>2</sub> and glucose detection	34
CuInS <sub>2</sub> NC	Peroxidase	H <sub>2</sub> O <sub>2</sub> detection	35
Co <sub>3</sub> O <sub>4</sub> NPs	Peroxidase	H <sub>2</sub> O <sub>2</sub> detection	36
CoFe LDHs	Peroxidase	H <sub>2</sub> O <sub>2</sub> and glucose detection	37
CoFe <sub>2</sub> O <sub>4</sub> /cyclodex.	Peroxidase	H <sub>2</sub> O <sub>2</sub> detection	38
CeO <sub>2</sub> NPs	Peroxidase	H <sub>2</sub> O <sub>2</sub> and glucose detection	39
CePO <sub>4</sub> :Tb,Gd NPs	Peroxidase	Magnetic-fluorescent imaging	40

---

## 2. Theoretical Background

---

<b>Nanomaterial</b>	<b>Enzyme-like activity</b>	<b>Application</b>	<b>Ref.</b>
MnO <sub>2</sub> NPs	Peroxidase	Immunoassays	41
MnSe NPs	Peroxidase	H <sub>2</sub> O <sub>2</sub> and glucose detection	42
ZnO NPs	Peroxidase	Carvedilol determination	43
ZnFe <sub>2</sub> O <sub>4</sub> /ZnO NC	Peroxidase	Glucose detection	44
BiFeO <sub>3</sub> NPs	Peroxidase	H <sub>2</sub> O <sub>2</sub> and glucose detection	45
MoS <sub>2</sub> nanosheets	Peroxidase	Glucose detection in blood	46
WC nanorods	Peroxidase	Catalysis in organic solvents	47
VO <sub>2</sub> nanoplates	Peroxidase		48
V <sub>2</sub> O <sub>3</sub> NC	Peroxidase	Glucose detection	49

## 2. Theoretical Background

---

<b>Nanomaterial</b>	<b>Enzyme-like activity</b>	<b>Application</b>	<b>Ref.</b>
Ir NPs	Peroxidase	Cell protect. against H <sub>2</sub> O <sub>2</sub>	50
Pd-Ir core shell nanocubes	Peroxidase	Imunoassays	51
Au NPs	Peroxidase	H <sub>2</sub> O <sub>2</sub> and glucose detection	52
Pt nanocrystals	Peroxidase		53
Au/CuS NC	Peroxidase	Pollutant removal in wastewater	54
Bi/Au NPs	Peroxidase	Thrombin determination	55
Ag/Pt, Ag/Pd, Ag/Au NC	Peroxidase		56
Ag/Pt NC	Peroxidase	Thrombin determination	57
Au/Pt NC	Peroxidase	Imunoassays	58
Au/Pd NC	Peroxidase	Imunoassays	59

## 2. Theoretical Background

<b>Nanomaterial</b>	<b>Enzyme-like activity</b>	<b>Application</b>	<b>Ref.</b>
Si-dots	Peroxidase	Glucose detection	60
V <sub>2</sub> O <sub>5</sub> nanowires	Peroxidase	Catalysis in organic solvents	61
V <sub>2</sub> O <sub>5</sub> nanowires	Haloperoxidase	Antifouling agent	62
V <sub>2</sub> O <sub>5</sub> nanowires	Glutathione Peroxidase	ROS reduction	63
Fe <sub>3</sub> O <sub>4</sub> NPs	Catalase		25
γ-Fe <sub>2</sub> O <sub>3</sub> NPs	Catalase		25
FePt NPs	Catalase		30
Ir NPs	Catalase	Cell protect. against H <sub>2</sub> O <sub>2</sub>	50
Co <sub>3</sub> O <sub>4</sub> NPs	Catalase	Calcium detection in milk	36, 64
Au/Pt NC	Catalase		56



## 2. Theoretical Background

---

<b>Nanomaterial</b>	<b>Enzyme-like activity</b>	<b>Application</b>	<b>Ref.</b>
CeO <sub>2</sub> NPs	Catalase		65
LaNiO <sub>3</sub> nanofibers	Catalase	H <sub>2</sub> O <sub>2</sub> and glucose detection	66
CeO <sub>2</sub> NPs	SOD	Stroke treatment	
		Cell protect. in radiation therapy	20, 67
		Antioxidant properties	68
		Anti-inflammation	69, 70
		Neuroprotection	71
FePO <sub>4</sub> microflowers	SOD		27
Pt NPs	SOD	ROS reduction	72
CeO <sub>2</sub> NPs	Oxidase	Immunoassay for tumor detection	73
CoFe <sub>2</sub> O <sub>4</sub> NPs	Oxidase	Luminol oxidation	74

## 2. Theoretical Background

---

<b>Nanomaterial</b>	<b>Enzyme-like activity</b>	<b>Application</b>	<b>Ref.</b>
MnFe <sub>2</sub> O <sub>4</sub> NC	Oxidase		75
LaNiO <sub>3</sub> nanofibers	Oxidase	H <sub>2</sub> O <sub>2</sub> and glucose detection	76
MnO <sub>2</sub> NPs/nanowires	Oxidase	Immunoassays	41
Mn <sub>3</sub> O <sub>4</sub> octahedrons	Oxidase	Sensor for phenols and tannic acid	77
Au NPs	Oxidase	Glucose oxidation and detection	78
Pt NPs	Oxidase		79
Au/Pt NC	Oxidase	Immunoassays	56
MoO <sub>3</sub> NPs	Sulfite Oxidase	SuOx deficiency treatment	80

---

NP, nanoparticle; NC, nanocomposite; LDH, layered-double-hydroxide.

While in the first years of enzyme mimetic research the enzyme-like activity itself was estimated as application for the nanoparticles, recently applications based on their catalytic activity attracted a lot of attention. Two different approaches for practical applications are reported in literature. First the substitution of the native enzyme in their natural surrounding and second the use of the catalytic activity to solve environmental problems, in most cases *ex vitro*. Both approaches will be discussed in the following chapter based on representative examples from current literature.

### 2.1.1 References

1. R. Breslow, L. E. Overman, *J. Am. Chem. Soc.* **1970**, *92*, 1075-1077.
2. H. Wei, E. Wang, *Chem. Soc. Rev.* **2013**, *42*, 6060-6093.
3. R. Ragg, M. N. Tahir, W. Tremel, *Eur. J. Inorg. Chem.* **2016**, 1906-1915
4. K. Korschelt, R. Schwidetzky, F. Pfitzner, J. Strugatchi, K. Kirchhoff, M. Panthöfer, C. Schilling, M. von der Au, I. Lieberwirth, M. N. Tahir, C. Hess, B. Meermann, W. Tremel, *Nanoscale*, 2018, Accepted Manuscript, DOI: 10.1039/C8NR03556C.
5. L. Que Jr., W. B. Tolman, *Nature* **2008**, *455*, 333-340.
6. D. Rokhsana, D. M. Dooley, *J. Biol. Inorg. Chem.* **2008**, *13*, 371-383.
7. A. J. Kirby, F. Hollfelder, in: *From Enzyme Models to Model Enzymes*, The Royal Society of Chemistry, **2009**, p. 61–194.
8. K. Kirkorian, A. Ellis, L. J. Twyman, *Chem. Soc. Rev.* **2012**, *41*, 6138-6159.
9. J. Meeuwissen, J. N. H. Reek, *Nat. Publ. Gr.* **2010**, *2*, 615-621.
10. L. Gao, J. Zhuang, L. Nie, J. Zhang, Y. Zhang, N. Gu, T. Wang, J. Feng, D. Yang, S. Perrett, X. Yan, *Nat. Nanotechnol.* **2007**, *2*, 577-583.
11. K. Herget, P. Hubach, S. Pusch, P. Deglmann, H. Götz, T. E. Gorelik, I. A. Gural'skiy, F. Pfitzner, T. Link, S. Schenk, M. Panthöfer, V. Ksenofontov, U. Kolb, T. Opatz, R. André, W. Tremel, *Adv. Mater.* **2017**, *29*, 1603823.
12. Z. Li, X. Yang, Y. Yang, Y. Tan, Y. He, M. Liu, X. Liu, Q. Yuan, *Chem. Eur. J.* **2018**, *24*, 409-415.
13. X. Wang, Y. Hu, H. Wie, *Inorg. Chem. Front.* **2016**, *3*, 41-60.

14. WEB Of Science,  
*http://apps.webofknowledge.com/RAMore.do?product=WOS&search\_mode=GeneralSearch&SID=E4hGz3OaukTx4BVL1J7&qid=1&ra\_mode=more&ra\_name=PublicationYear&colName=WOS&viewType=raMore*, access **30.06.2018**.
15. F. Manea, F. B. Houillon, L. Pasquato and P. Scrimin, *Angew. Chem., Int. Ed.* **2004**, *43*, 6165–6169.
16. R. H. Holm, P. Kennepohl, E. I. Solomon, *Chem. Rev.* **1996**, *7*, 2239-2314.
17. A. Latorre-Sánchez, J. A. Pomposo, *Polym. Int.* **2016**, *65*, 855-860.
18. H. Hiramatsu, F. E. Osterloh, *Chem. Mater.* **2004**, *16*, 2509-2511.
19. J. Yao, Y. Cheng, M. Zhou, S. Zhao, S. Lin, X. Wang, J. Wu, S. Li, H. Wie, *Chem. Sci.* **2018**, *9*, 2927-2933.
20. C. Korsvik, S. Patil, S. Seal, W. T. Self, *Chem. Commun.* **2007**, 1056-1058.
21. M. Kluecker, M. Mondeshki, M. N. Tahir, W. Termel, *Langmuir* **2018**, *34*, 1700-1710.
22. Grunwald, P. *Biocatalysis and Nanotechnology*; Pan Stanford Publishing Pte. Ltd, 2017.
23. K. Fan, C. Cao, Y. Pan, D. Lu, D. Yang, J. Feng, L. Song, M. Liang, X. Yan, *Nat. Nanotechnol.* **2012**, *7*, 459-464
24. H. Wei, E. Wang, *Anal. Chem.* **2008**, *80*, 2250-2254.
25. Z. Chen, J.-J. Yin, Y.-T. Zhou, Y. Zhang, L. Song, M. Song, S. Hu, N. Gu, *ACS Nano* **2012**, *6*, 4001-4012.
26. C. Peng, B. Jiang, Q. Liu, Z. Guo, Z. Xu, Q. Huang, H. Xu, R. Tai, C. Fan, *Energy Environ. Sci.* **2011**, *4*, 2035-2040.

27. W. Wang, X. Jiang, K. Chen, *Chem. Commun.* **2012**, 48, 7289-7291.
28. Z. Dai, S. Liu, J. Bao, H. Ju, *Chem. Eur. J.* **2009**, 15, 4321-4326.
29. P. Roy, Z.-H. Lin, C.-T. Liang, H.-T. Chang, *Chem. Commun.* **2012**, 48, 4079-4081.
30. J. Fan, J.-J. Yin, B. Ning, X. Wu, Y. Hu, M. Ferrari, G. J. Anderson, J. Wei, Y. Zhao, G. Nie, *Biomaterials* **2011**, 32, 1611-1618.
31. Y. Liu, G. Zhu, C. Bao, A. Yuan, X. Shen, *Chin. J. Chem.* **2014**, 32, 151-156.
32. Y. Huang, X. Ran, Y. Lin, J. Ren, X. Qu, *Chem. Commun.* **2015**, 51, 4386-4389.
33. W. He, H. Jia, X. Li, Y. Lei, J. Li, H. Zhao, L. Mi, L. Zhang, Z. Zheng, *Nanoscale* **2012**, 4, 3501-3506.
34. L. Hu, Y. Yuan, L. Zhang, J. Zhao, S. Majeed, G. Xu, *Anal. Chim. Acta* **2013**, 762, 83-86.
35. H. Liu, C. Gu, W. Xiong, M. Zhang, *Sensors Actuators B: Chem.* **2015**, 209, 670-676.
36. J. Mu, Y. Wang, M. Zhao, L. Zhang, *Chem. Commun.* **2012**, 48, 2540-2542.
37. Y. Zhang, J. Tian, S. Liu, L. Wang, X. Qin, W. Lu, G. Chang, Y. Luo, A. M. Asiri, A. O. Al-Youbi, X. Sun, *Analyst* **2012**, 137, 1325-1328.
38. S. He, W. Shi, X. Zhang, J. Li, Y. Huang, *Talanta* **2010**, 82, 377-383.
39. X. Jiao, H. Song, H. Zhao, W. Bai, L. Zhang, Y. Lv, *Anal. Methods* **2012**, 4, 3261-3267.
40. W. Wang, X. Jiang, K. Chen, *Chem. Commun.* **2012**, 48, 6839-6841.

41. X. Liu, Q. Wang, H. Zhao, L. Zhang, Y. Su, Y. Lv, *Analyst* **2012**, *137*, 4552-4558.
42. F. Qiao, L. Chen, X. Li, L. Li, S. Ai, *Sensors Actuators B: Chem.* **2014**, *193*, 255-262.
43. P. Biparva, S. M. Abedirad, S. Y. Kazemi, *Talanta* **2014**, *130*, 116-121.
44. M. Zhao, J. Huang, Y. Zhou, X. Pan, H. He, Z. Ye, X. Pan, *Chem. Commun.* **2013**, *49*, 7656-7658.
45. W. Luo, Y.-S. Li, J. Yuan, L. Zhu, Z. Liu, H. Tang, S. Liu, *Talanta* **2010**, *81*, 901-907.
46. T. Lin, L. Zhong, L. Guo, F. Fu, G. Chen, *Nanoscale* **2014**, *6*, 11856-11862.
47. N. Li, Y. Yan, B.-Y. Xia, J.-Y. Wang, X. Wang, *Biosens. Bioelectron.* **2014**, *54*, 521-527.
48. L. Zhang, F. Xia, Z. Song, N. A. S. Webster, H. Luo, Y. Gao, *RSC Adv.* **2015**, *5*, 61371-61379.
49. L. Han, L. Zeng, M. Wei, C. M. Li, A. Liu, *Nanoscale* **2015**, *7*, 11678-11685.
50. H. Su, D.-D. Liu, M. Zhao, W.-L. Hu, S.-S. Xue, Q. Cao, X.-Y. Le, L.-N. Ji, Z.-W. Mao, *ACS Appl. Mater. Interfaces* **2015**, *7*, 8233-8242.
51. X. Xia, J. Zhang, N. Lu, M. J. Kim, K. Ghale, Y. Xu, E. McKenzie, J. Liu, H. Ye, *ACS Nano* **2015**, *9*, 9994-10004.
52. Y. Jv, B. Li, R. Cao, *Chem. Commun.* **2010**, *46*, 8017-8019.
53. M. Ma, Y. Zhang, N. Gu, *Colloids Surf. Physicochem. Eng. Aspects* **2011**, *373*, 6-10.
54. Q. Cai, S. Lu, F. Liao, Y. Li, S. Ma, M. Shao, *Nanoscale* **2014**, *6*, 8117-8123.

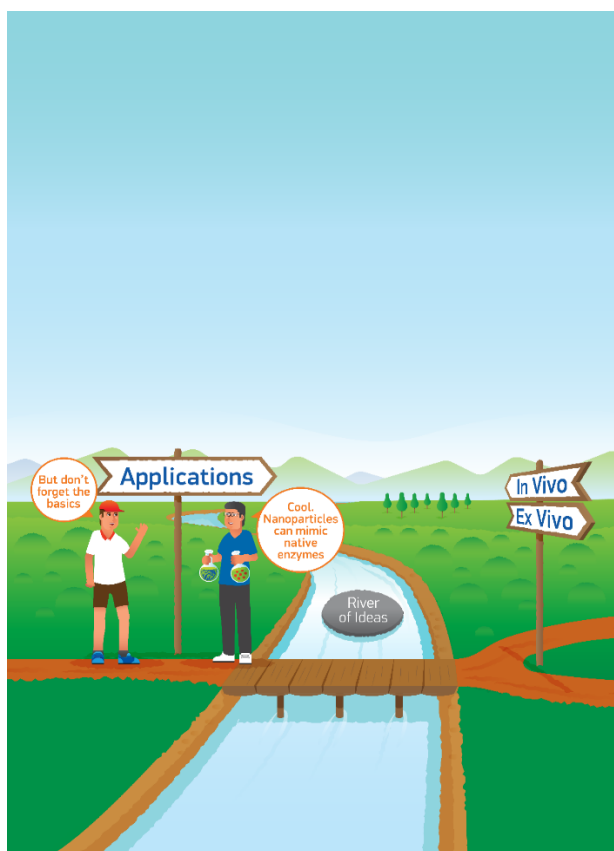
55. C.-W. Lien, C.-C. Huang, H.-T. Chang, *Chem. Commun.* **2012**, 48, 7952-7954.
56. W. He, X. Wu, J. Liu, X. Hu, K. Zhang, S. Hou, W. Zhou, S. Xie, *Chem. Mater.* **2010**, 22, 2988-2994.
57. C. Zheng, A. Zheng, B. Liu, X.-L. Zhang, Y. He, J. Li, H. Yang, G. Chen, *Chem. Commun.* **2014**, 50, 13103.
58. W. He, Y. Liu, J. Yuan, J.-J. Yin, X. Wu, X. Hu, K. Zhang, J. Liu, C. Chen, Y. Ji, Y. Guo, *Biomaterials* **2011**, 32, 1139-1147.
59. Y. Nangia, B. Kumar, J. Kaushal, C. Raman Suri, *Anal. Chim. Acta* **2012**, 751, 140-145.
60. Q. Chen, M. Liu, J. Zhao, X. Peng, X. Chen, N. Mi, B. Yin, H. Li, Y. Zhang, S. Yao, *Chem. Commun.* **2014**, 50, 6771-6774.
61. R. André, F. Natálio, M. Humanes, J. Leppin, K. Heinze, R. Wever, H. C. Schröder, W. E. G. Müller, W. Tremel, *Adv. Funct. Mater.* **2011**, 21, 501-509;
62. F. Natalio, R. Andre, A. F. Hartog, B. Stoll, K. P. Jochum, R. Wever, W. Tremel, *Nat. Nanotechnol.* **2012**, 7, 530-535
63. A. A. Vernekar, D. Sinha, S. Srivastava, P. U. Paramasivam, P. D'Silva, G. Mugesh, *Nat. Commun* **2014**, 5, 5301.
64. J. Mu, L. Zhang, M. Zhao, Y. Wang, *ACS Appl. Mater. Interfaces* **2014**, 6, 7090-7098.
65. T. Pirmohamed, J. M. Dowding, S. Singh, B. Wasserman, E. Heckert, A. S. Karakoti, J. E. S. King, S. Seal, W. T. Self, *Chem. Commun.* **2010**, 46, 2736-2738
66. A. G. J. Ligtenbarg, R. Hage, B. L. Feringa, *Coord. Chem. Rev.* **2003**, 237, 89-101.



67. C. K. Kim, T. Kim, I.-Y. Choi, M. Soh, D. Kim, Y.-J. Kim, H. Jang, H.-S. Yang, J. Y. Kim, H.-K. Park, S. P. Park, S. Park, T. Yu, B.-W. Yoon, S.-H. Lee, T. Hyeon, *Angew. Chem. Int. Ed.* **2012**, *51*, 11039-11043;
68. L. Zhang, L. Laug, W. Münchgesang, E. Pippel, U. Gösele, M. Brandsch, M. Knez, *Nano Lett.* **2009**, *10*, 219-223.
69. S. M. Hirst, A. S. Karakoti, R. D. Tyler, N. Sriranganathan, S. Seal, C. M. Reilly, *Small* **2009**, *5*, 2848-2856.
70. J. Chen, S. Patil, S. Seal, J. F. McGinnis, *Nat. Nanotechnol.* **2006**, *1*, 142-150.
71. A. Asati, S. Santra, C. Kaittanis, S. Nath, J. M. Perez, *Angew. Chem. Int. Ed.* **2009**, *48*, 2308-2312.
72. a) I. Celardo, M. De Nicola, C. Mandoli, J. Z. Pedersen, E. Traversa, L. Ghibelli, *ACS Nano* **2011**, *5*, 4537-4549;
73. G. P. Bolwell, P. Wojtaszek, *Physiol. Mol. Plant Pathol.* **1997**, *51*, 347-366.
74. A. A. Vernekar, T. Das, S. Ghosh, G. Mugesh, *Chem. Asian J.* **2016**, *11*, 72-76.
75. M. Comotti, C. Della Pina, R. Matarrese, M. Rossi, *Angew. Chem. Int. Ed.* **2004**, *43*, 5812-5815.
76. B. Wang, S. Gu, Y. Ding, Y. Chu, Z. Zhang, X. Ba, Q. Zhang, X. Li, *Analyst* **2013**, *138*, 362-367.
77. X. Zhang, S. He, Z. Chen, Y. Huang, *J. Agric. Food. Chem.* **2013**, *61*, 840-847.
78. C.-J. Yu, T.-H. Chen, J.-Y. Jiang, W.-L. Tseng, *Nanoscale* **2014**, *6*, 9618-9624.
79. R. Grasselli, *Top. Catal.* **2002**, *21*, 79-88
80. R. Ragg, F. Natalio, M. N. Tahir, H. Janssen, A. Kashyap, D. Strand, S. Strand, W. Tremel, *ACS Nano* **2014**, *8*, 5182-5189.

## 2.2. A Step into the Future – Applications of Nanoparticle Enzyme Mimics

The manuscript “A Step into the Future – Applications of Nanoparticle Enzyme Mimics” was written and published as Concept Article for *Chemistry A European Journal*.



This chapter describes fundamental concepts and new developments of the field of nanoparticle enzyme mimics with a focus on practical *in vivo* and *ex vivo* applications.

The article is an adapted reproduction of the manuscript published in the scientific journal *Chemistry – A European Journal* (*Chem. Eur. J* 2018, DOI: 10.1002/chem.201800384), which is reproduced with permission of the Royal Society of Chemistry. Detailed authorship contributions are attached in the Appendix (chapter 5.3.2).

### 2.2.1 Abstract

We describe elementary concepts, up-to-date developments, and perspectives of the emerging field of nanoparticle enzyme mimics (so-called “nanozymes”) at the interface of chemistry, biology, materials, and nanotechnology. The design and synthesis of functional enzyme mimics is a long-standing goal of biomimetic chemistry. Metal complexes, polymers and engineered biomolecules capturing the structure of natural enzymes or their active centers have been made to achieve high rates and enhanced selectivities. Still, the design of new “artificial enzymes” that are not related to proteins but with capacity of production and stability at industrial level, remains a goal. Inorganic nanoparticles bear this potential. Although it seems counterintuitive to compare nanoparticles and natural enzymes because they appear very different they share many common features: nano-size, irregular shape, and rich surface chemistry. These features enable nanomaterials to mimic reactions of natural enzymes. Representative examples with biomedical and environmental applications are given.

### 2.2.2 Introduction

Living organisms are the most ingenious chemists. A vast number of reactions is catalyzed by a plethora of enzymes in every cell. Enzymes have a number of advantages over conventional catalysts: they work in water, at ambient conditions and neutral pH. This makes them suitable for low energy, non-toxic and eco-friendly chemical processes. The quest to use Nature’s enzymatic repertoire of chemical transformations, e.g. microbial enzymes, has sparked interest in industry and medicine. Enzymes are used in agriculture, for the production of food, chemicals, and pharmaceuticals.<sup>[1]</sup> It is possible to modify natural enzymes, chemically or by protein engineering, in such a way that their specificity is tuned, even up to the point where an engineered enzyme catalyzes a new reaction.<sup>[2,3]</sup> However, many synthetically useful reactions still remains a challenge and cannot be carried out with natural or engineered enzymes because of their limited stability, catalytic activity under harsh condition, ease of production and costs.

Therefore, enzyme mimics have been high-profile targets for chemists.<sup>[4]</sup> Enzymes are more than highly developed catalysts: They can recognize molecules different from their specific substrate (and product) as part of the controlled mechanisms of the cell. As other macromolecules are dynamic with interconverting conformations on time scales ranging from femtoseconds to minutes. “True” enzyme mimics seek to reproduce the three-dimensional arrangement of the functional groups at the active site in a synthetic framework to speed-up reactions.<sup>[4]</sup> This strategy is related to enzyme engineering. A minimum requirement for a “true” enzyme mimic is to achieve an interaction between two substrates before to the actual catalytic reaction.

An emerging strategy uses protein scaffolds with natural<sup>[5]</sup> and non-natural<sup>[6]</sup> metals to probe new applications of metalloproteins. This has been partially successful and added to our understanding of protein folding, optimization and design.<sup>[7]</sup> The insertion of multi-metal (instead of single metal) sites<sup>[8,9]</sup> for metal-based electron- or proton-delivery may aid in the *de novo* development of enzymes<sup>[9]</sup> or in the discovery of new reactivity patterns.<sup>[10]</sup>

Much effort has been invested in the synthesis of (supra)molecular models that are more stable and cost efficient than their natural counterparts.<sup>[11]</sup> Many supramolecular compounds contain a receptor or cavitand that is connected to an active site, with the aim to mimic reactions carried out by enzymes. This approach has led to elegant examples of catalytically active model compounds that display enhanced selectivity or activity. Still, catalytically active model compounds in the presence of other competing reactions inside living cells or even organisms, remain a challenge.<sup>[12]</sup>

Different from most enzymes, nanoparticle enzyme mimics (so-called “nanozymes”) can operate in aqueous as well as in non-aqueous systems, and they are available cost-efficiently at an industrial-scale. Metal and metal oxide nanoparticles are highly reactive, as demonstrated by their use in catalysis.<sup>[13]</sup> In solution they are stabilized typically with surfactants and or polymers. Their

reactivity may be higher than that of enzymes, because any surface site can be catalytically active, whereas enzymes have only a single binding site, although with exceptional specificity and selectivity. Especially the use of NPs as enzyme mimics is advantageous in applications where the steric information of native enzymes plays minor importance e.g. the catalytic reactions involving small molecules such as different oxygen radicals and hydrogen peroxide ( $\text{H}_2\text{O}_2$ ) as substrates. Moreover, the stability and production costs make nanozymes interesting candidates for a variety of medical and environmental applications.

This has been shown in a landmark paper by Yan and coworkers on the peroxidase mimicking activity of iron oxide nanoparticles at different pH and temperature values and by a comparison with native horseradish peroxidase.<sup>[14]</sup> The smallest  $\text{Fe}_3\text{O}_4$  NPs showed the highest catalytic activity, i.e. the high surface area of  $\text{Fe}_3\text{O}_4$  NPs are responsible for their “quasi-enzymatic” activity.

Meanwhile a broad variety of nanozymes has been reported.<sup>[15-17]</sup> The most prominent examples are peroxidases,<sup>[18]</sup> catalases,<sup>[19]</sup> superoxide dismutases (SODs).<sup>[20]</sup> The oldest and simplest SOD mimic is the  $\text{Mn}^{2+}$  ion. It has been shown long ago that  $\text{Mn}^{3+}$  provides protection against oxy-radical-mediated damage<sup>[21]</sup> by forming transient  $\text{MnO}_2^+$  species which disproportionate to  $\text{Mn}^{2+}$ ,  $\text{O}_2$ , and  $\text{H}_2\text{O}_2$ .<sup>[22]</sup> Similarly, manganous phosphate can remove superoxide under physiological conditions.<sup>[23]</sup> As a general rule, oxygen-affine metals (e.g. Mn, Fe, Ce, Cu) that can switch their oxidation states by one unit, can exhibit mimic for SOD activity.<sup>[24]</sup> Other redox (oxidoreductases,<sup>[25]</sup> oxidases,<sup>[26-28]</sup> sulfite oxidase,<sup>[29]</sup> haloperoxidases<sup>[30,31,32]</sup>) or acid base systems<sup>[33,34]</sup> with promising applications have been described. Their solubility and environmental or physiological compatibility may require post-synthetic modifications (e.g. surface functionalization). This concept article highlights and comments on future prospects for some biomedical and environmental applications of nanoparticle (NP) enzyme mimics.

### 2.2.3 Nanozymes as ROS Scavengers for Biomedical Applications

Reactive oxygen species (ROS) are reactive molecules and free radicals derived from molecular oxygen that are formed by all aerobic species.<sup>[35]</sup> They are produced as byproducts during the mitochondrial electron transport of aerobic respiration, by oxidoreductases and metal catalyzed oxidation, and they can lead to a variety of deleterious reactions. The sequential reduction of oxygen leads to the formation superoxide radicals ( $\cdot\text{O}_2^-$ ), hydrogen peroxide ( $\text{H}_2\text{O}_2$ ), hydroxyl radicals ( $\cdot\text{OH}$ ) and nitric oxide ( $\cdot\text{NO}$ ). Elevated concentrations of reactive oxygen species (ROS) play a central role in the formation of oxidative cell damages.<sup>[35]</sup> Enzymatic sources of reactive oxygen species (ROS) are components of the mitochondrial electron transport chain, xanthine oxidase, the cytochrome P450 monooxygenases, lipoxygenase, nitric oxide synthase, or NADPH oxidase.<sup>[35]</sup> Superoxide radicals ( $\cdot\text{O}_2^-$ ) must be removed by dismutation to  $\text{H}_2\text{O}_2$  with SODs, to allow a survival of the cell in the presence of oxygen.  $\text{H}_2\text{O}_2$  is still an oxidant, but can diffuse out of the cell and is thus not as harmful as the superoxide anion.  $\text{H}_2\text{O}_2$  is eliminated subsequently with the aid of catalases, peroxiredoxins, or glutathione peroxidases.<sup>[35,36,37]</sup>

Vanadium forms a variety of peroxide systems.<sup>[38]</sup> Similarly,  $\text{V}_2\text{O}_5$  nanoparticles possess intrinsic peroxidase mimicking activity,<sup>[39]</sup> where the catalytic activity is strongly related to defects located at the particle surface. Thus, it did not come as a surprise that defective  $\text{V}_2\text{O}_5$  nanoparticles can act as glutathione peroxidase (GPx) mimic as well.<sup>[40,41]</sup> The GPx/glutathione system is thought to be a major defense in low-level oxidative stress. Glutathione peroxidase is a selenium-containing antioxidant enzyme that reduces  $\text{H}_2\text{O}_2$  and lipid peroxides to water and lipid alcohols, while glutathione is oxidized in turn to glutathione disulfide. Reduced glutathione is essential for regulating the intracellular redox state of vascular cells in biochemical pathways.<sup>[42,43]</sup> Without GPx activity or adequate glutathione levels,  $\text{H}_2\text{O}_2$  and lipid peroxides are not detoxified and may be converted to OH-radicals and lipid peroxy radicals by transition metals (e.g.  $\text{Fe}^{2+}$ ). Native glutathione peroxidase, and the  $\text{V}_2\text{O}_5$  mimic oxidize GSH (reduced

glutathione) to GSSG (oxidized glutathione) at the expense of H<sub>2</sub>O<sub>2</sub>, thereby reducing the intracellular H<sub>2</sub>O<sub>2</sub> concentration and protecting the organism from oxidative damage. Control experiments with other metal oxides with peroxidase-like activity showed that only V<sub>2</sub>O<sub>5</sub> can mediate GSH oxidation under physiological conditions because of the stability of the V-peroxo species.

The reduction of superoxide radicals and H<sub>2</sub>O<sub>2</sub> concentrations through the superoxide dismutase and catalase-like activities of nanoceria (CeO<sub>2</sub> nanoparticles) were reported in two seminal papers by Seal, Self and coworkers,<sup>[19,20]</sup> together with the cell-protective effect of nanoceria against radiation induced cell damage.<sup>[44,45]</sup> The Ce<sup>3+</sup>/Ce<sup>4+</sup> ratio at the NP surface is important for the enzymatic activity. Higher Ce<sup>3+</sup>/Ce<sup>4+</sup> ratios led to an enhanced SOD-activity,<sup>[20]</sup> whereas catalase-like behavior was observed for lower Ce<sup>3+</sup>/Ce<sup>4+</sup> ratios,<sup>[19]</sup> FePO<sub>4</sub> microflowers<sup>[46]</sup> and metal (e.g. Pt) nanoparticles<sup>[47]</sup> have been reported to show SOD-like activities as well. The use of nanoceria particles as a therapy for a variety of diseases provides a unique platform technology.

**Neurodegenerative disorders.** Elevated superoxide concentrations are responsible mechanisms for ischemic injuries and stroke diseases.<sup>[48]</sup> Using the ROS scavenging effect of nanoceria Kim *et al.* investigated the *in vivo* application by treating ischemic stroke diseases.<sup>[44]</sup> They analyzed the neuroprotective effects of nanoceria by inducing stroke in lab rats, followed by intravenous injection of nanoceria in concentrations of 0.1-1.5 mg/kg. The analysis of the stroke-damaged brain areas revealed that intermediate concentrations (0.5 and 0.7 mg/kg) had positive effects, whereas low (0.1 and 0.3 mg/kg) and high (1.0 and 1.5 mg/kg) concentrations of nanoceria did not reduce the infarct volume significantly. This treatment reduced the stroke infarct volume by 50% (compared to controls) (Figure 1). An analysis of the nanoceria concentration showed elevated levels in liver, kidney and heart. The nanoceria concentration in non-damaged brain areas was very low, but very high in stroke affected cells. Since the blood-brain barrier (BBB) is damaged by ischemic stroke diseases and allows the passage of nanoceria

## 2. Theoretical Background

whereas an integral barrier in the healthy brain region prevents membrane penetration.<sup>[44]</sup>

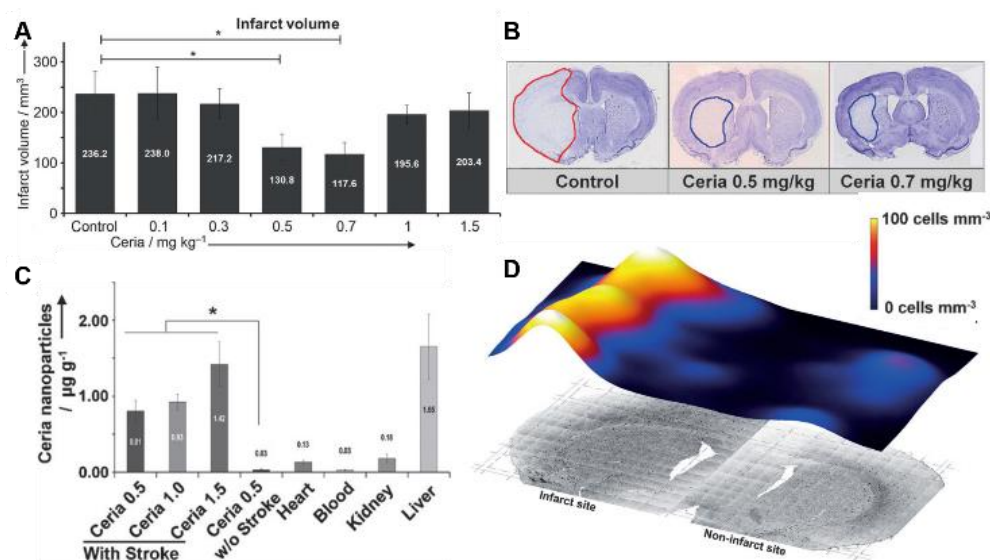


**Figure 1. Nanoceria combat ischemic stroke diseases.** (A) Reduction of stroke damaged brain areas up to 50 % for mediate concentrations of 0.5-0.7 mg/kg. (B) Microscopy images of stroke damaged rat brains illustrating the positive effect of nanoceria. (C) Enhanced nanoceria concentrations where mainly found in the liver and the stroke damaged brain area, whereas healthy brain tissue did not show significantly elevated concentrations. (D) Fluorescence signals of rhodamine B functionalized nanoceria prove their concentration in stroke damaged brain tissues (left).<sup>[44]</sup> Reprinted with permission from ref<sup>[44]</sup>

It was further shown that a combination of the GPx activity of V<sub>2</sub>O<sub>5</sub> and the SOD and catalase activity of MnO<sub>2</sub> can efficiently reduce ROS and protect cells against oxidative cell stress.<sup>[49]</sup> It is worth mentioning that an medical use of V<sub>2</sub>O<sub>5</sub> is not permitted worldwide.

In recent years evidence has accrued that the brain in Alzheimer's disease (AD), a common form of neurodegenerative disorder with dementia, is under increased oxidative stress.<sup>[50,51]</sup> Oxidative stress due to chronic hypoperfusion leads to mitochondrial damage. Mitochondria play a crucial role in cellular bioenergetics and cell-survival. The mitochondrial function degrades with aging, and their damage leads to increased intracellular formation of oxidants and pro-oxidants.<sup>[52]</sup> The prolonged oxidative stress and the resultant hypoperfusion in the brain tissues



stimulate the expression of nitric oxide synthase (NOS) enzymes, which further drives the formation of ROS and reactive nitrogen species (RNS).<sup>[53]</sup> The ROS and RNS collectively contributes to the dysfunction of the BBB and damage of the brain parenchymal cells. Cellular changes show that oxidative stress precedes the appearance of the key histopathologies of the disease, neurofibrillary tangles, senile plaques and neuronal death.<sup>[54-56]</sup>

The development of drugs for the treatment of AD for breaking the vicious cycles of oxidative stress and neurodegeneration offer new opportunities. These approaches include inhibitors of advanced glycation end products, as well as antioxidants and anti-inflammatory substances, which prevent free radical production or reduce free radical concentrations.<sup>[56,57]</sup> To protect the affected cells, ceria NPs were coated with 1,2-distearoyl-sn-glycero-3-phosphoethanolamine-*N*-[carboxy (polyethylene glycol) triphenylphosphonium (DSPE-PEG-TPP), a substituted polyethylene glycol carrying a triphenylphosphonium (TPP) cation at the PEG terminal. This lipophilic cation targets mitochondria because of their negative mitochondrial membrane potential. For low CeO<sub>2</sub> NP concentrations (< 0.125 mM) no toxic effects on human neuroblastoma cells (SH-SY5Y cells) were observed. Although CeO<sub>2</sub> NPs did not eliminate subicular A $\beta$  deposition significantly, they reduced oxidative stress in mitochondria *in vitro* and *in vivo* and suppress neuronal death in a 5XFAD transgenic Alzheimer's disease mouse model. The triphenylphosphonium-conjugated ceria NPs mitigate reactive gliosis and morphological mitochondrial damage (Figure 2).<sup>[58,59]</sup>

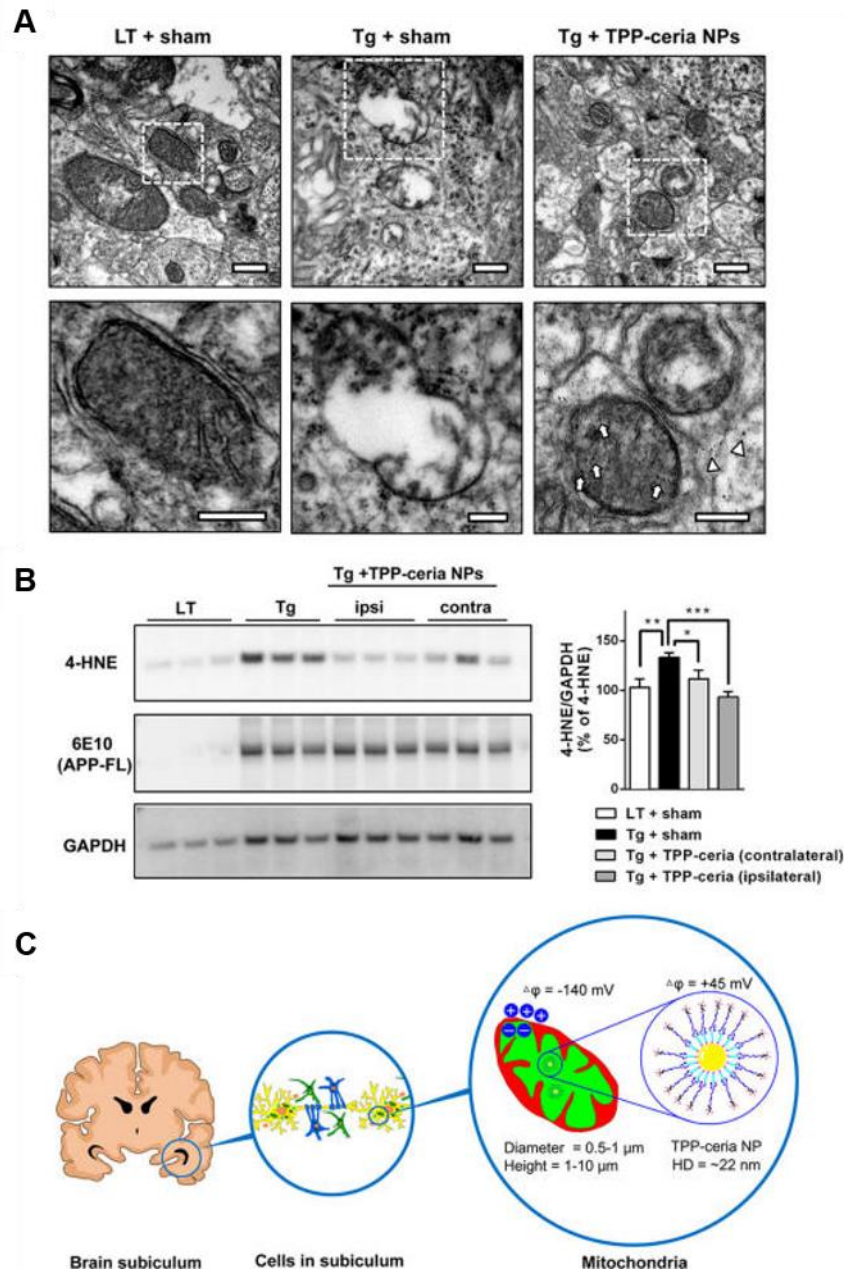


**Figure 2. Retrieval of mitochondrial structure by reducing oxidative stress with TPP-ceria NPs. (A)** TEM pictures and enlarged sections of the mitochondria of a transgenic mouse model + saline (Tg + sham), a wild type mouse model + saline and a transgenic mouse model + TPP coated ceria NPs (scale bar 500 nm for overview images and 250 nm for the increased). **(B)** Western blot evaluation of oxidative stress markers of the NP attended 5XFAD mice. **(C)** Illustration of the mitochondria targeting of TPP coated ceria NPs. Reprinted with permission from ref<sup>[58]</sup>

**Tissue engineering.** The concentrations of ROS and oxygen ( $O_2$ ) can promote or decelerate the progression and duration of the wound healing process.<sup>[60]</sup> Based on the antioxidant activity of nanoceria, the therapeutic effect of the NPs on the wound healing process was explored. Nanoceria promotes cell proliferation and has been used for tissue engineering.<sup>[61–65]</sup> Hybrid materials containing  $CeO_2$  NPs embedded in poly(lactic-co-glycolic acid) (PLGA) scaffolds promoted murine cardiac and mesenchymal stem cells growth. The positive effects were attributed initially to the antioxidant properties.<sup>[66]</sup> Subsequent studies with surface engineered particles revealed that  $Ce^{4+}$  dominant regions favored and  $Ce^{3+}$  dominant regions inhibited cell proliferation by restricting cell spreading and weakening cell–material interactions.<sup>[62]</sup> This was in harmony with the finding that surface  $Ce^{3+}$  may show biotoxic effects.<sup>[66]</sup>

Nanoceria accelerates cutaneous wound healing in mice by promoting the growth of keratinocytes, fibroblasts, and vascular endothelial cells. The therapeutic efficacy was owing to the enhanced proliferation and migration of these cells (Figure 3).<sup>[63]</sup>

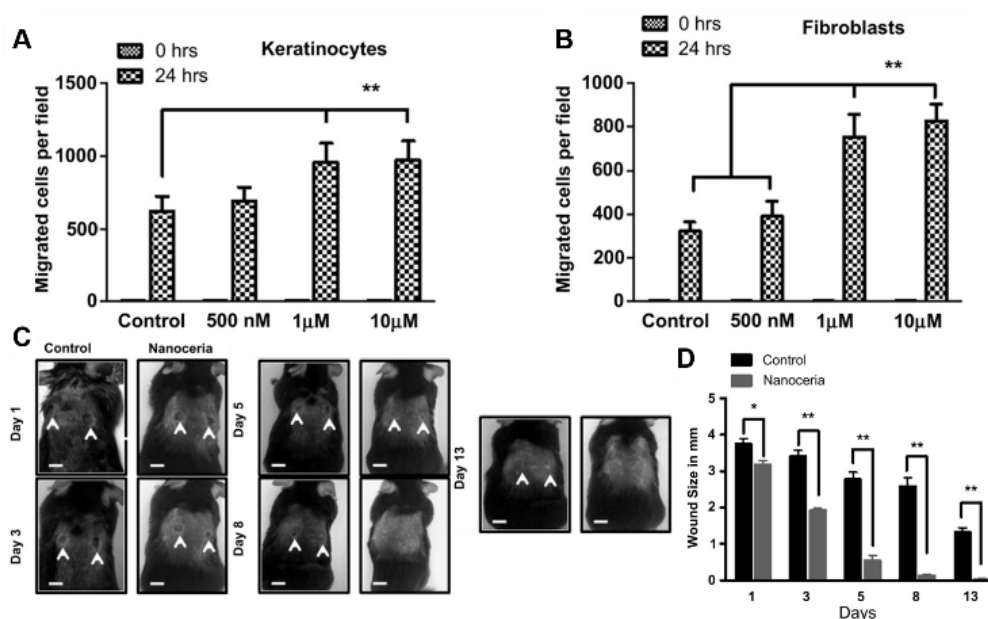


**Figure 3. Cerium oxide NPs can promote the wound healing process.** Cell migration of keratinocytes (A) and fibroblasts (B) could be enhanced in presence of 1  $\mu\text{M}$  and 10  $\mu\text{M}$  nanoceria. (C) The NPs affect the wound healing, which was investigated with mice experiments. Skin incisions on the back of mice were periodically treated with nanoceria solutions, while controls were covered with deionized water. (D) NP treated wounds recovered faster than the controls and the wound size was clearly reduced.<sup>[63]</sup> Reprinted with permission from ref<sup>[63]</sup>

While high ROS concentrations prohibit healing, a good inflow of  $\text{O}_2$  to the wound is desired. Electrospun cross-linked poly(vinyl alcohol) (PVA) membranes containing integrated hematite NPs contemptuously reduce  $\text{H}_2\text{O}_2$  and increase  $\text{O}_2$  levels.<sup>[67]</sup> The high water permeability of the porous PVA membrane and the catalase-like activity of embedded hematite nanoparticles can efficiently convert  $\text{H}_2\text{O}_2$  into  $\text{O}_2$  as shown by a catalase assay. The proliferation of fibroblasts at a critically high  $\text{H}_2\text{O}_2$  concentration was demonstrated by incubating the cells in the presence of the catalytic membrane. The catalytic membranes provide an improved environment for cell proliferation in wounds and can be applied in wound healing dressing.

**Cardioprotection.** Nanoceria was shown to protect cardiac progenitor cells from oxidative stress.<sup>[68]</sup> Treatment with nanoceria inhibited the progressive left ventricular dysfunction and dilatation in an *in vivo* mouse model with ischemic cardiomyopathy. A decrease of pro-inflammatory cytokines (tumor necrosis factor- $\alpha$  and interleukin-1 $\beta$ ) and downregulation of endoplasmic reticulum stress-associated genes) revealed the therapeutic effect to be related to the inhibition of myocardial oxidative stress, ER stress and inflammatory processes.<sup>[69]</sup> Heart hypertrophy following pulmonary arterial hypertension could be reduced by nanoceria treatment as well.<sup>[70]</sup>

### 2.2.4 Nanozymes for Tumor and Cancer Therapy

Normal cells generate energy oxidative phosphorylation in the mitochondria. In contrast, cancer cells use aerobic glycolysis for generating ATP and to cover their energy supply. This so-called Warburg effect<sup>[71]</sup> is one of the fundamental metabolic changes associated with malignant transformations. The Warburg effect leads to changes of the mitochondrial redox potential, ultimately changing ROS generation.<sup>[72]</sup> This provides a direct link between changes of the glucose metabolism and tumorigenesis due to signal transduction *via* ROS generation. Excessive ROS damages cell membranes and nucleic acids, while insufficient ROS disturbs signaling processes that are beneficial for cell proliferation. The anticancer activities of nanoceria intervene at the ROS equilibrium and were evaluated using mice with xenografted melanoma. Treatment with nanoceria reduced tumor volume and weight, which showed the translational promise of the nanoceria.<sup>[73]</sup> Similarly, nanoceria could inhibit ovarian tumor growth *via* an anti-angiogenic mechanism.<sup>[74]</sup>

The intrinsic peroxidase activity of iron oxide and ceria NPs were the first examples of nanoparticle enzyme mimics.<sup>[14,20]</sup> Natural peroxidases with vanadium or iron active sites catalyze the decomposition of peroxide to water and molecular oxygen. Based on the intrinsic peroxidase-like activity of iron oxide NPs Yan and coworkers explored a strategy for targeting and imaging tumors simultaneously.<sup>[75]</sup>

By encapsulating iron oxide NPs in human heavy-chain ferritin (HF<sub>n</sub>) the functionalization with complex targeting ligands could be circumvented. The targeting is based on the selective binding of HF<sub>n</sub> to the transferrin receptor 1 (TfR 1), which is overexpressed in tumor cells. The imaging relies on the peroxidase activity of iron oxide NP, which leads to a color reaction using peroxidase substrates in the presence of H<sub>2</sub>O<sub>2</sub>. The engineered magnetoferritin-NP complex binds to tumor cells with a higher sensitivity (98 %) and specificity (of 95 %) than comparable antibody-based methods. The magnetoferritin-NP complex is a promising candidate for cancer and tumor treatment.<sup>[75]</sup>

Based on the Fenton or Haber-Weiss reaction iron oxide NPs with a peroxidase activity form oxygen radicals in the presence of H<sub>2</sub>O<sub>2</sub> under physiological conditions.<sup>[76,77]</sup> The increased ROS level induces oxidative stress which combats bacteria and cancer cells. *In vitro* studies with bacteria and *in vivo* investigations of ROS formation showed the peroxidase-like activity of magnetite NPs.<sup>[77]</sup> The antibacterial effects and *in vitro* tumor cell studies were reported using an *Escherichia coli* (*E. coli*) and a HeLa cell model. The results of both studies are in harmony with the adopted mechanism and increasing ROS levels. While H<sub>2</sub>O<sub>2</sub> and magnetite NPs alone did not show high cytotoxic effects in the bacteria study nor in cell analysis, the combination of substrate and catalyst showed promoted cell death. Further experiments showed the tumor imaging and treatment, whereas the cell uptake of MNPs is based on the EPR effect. A T<sub>2</sub>-weighted MR imaging enables the visualization of tumor tissues and an apoptosis based on intracellular ROS formation (Figure 4).<sup>[77]</sup>

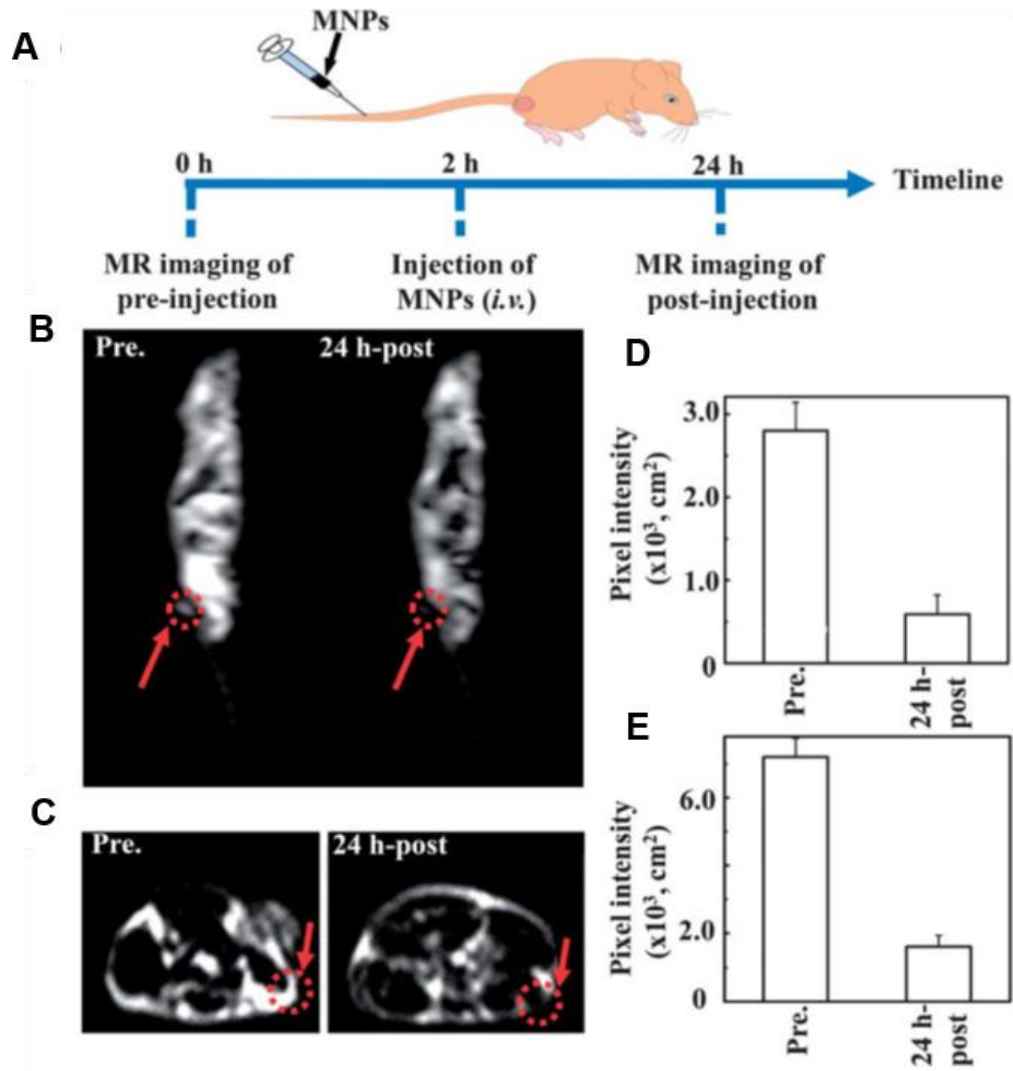


**Figure 4.** *In vivo* tumor imaging with MNPs. (A) Implementation of the MR imaging *in vivo* studies. T<sub>2</sub> weighted MR images of the (B) Sagittal and (C) frontal layer before and 24 h after the injection of MNPs. Associated relative pixel intensities of the (D) sagittal and (E) frontal layer at the same term.<sup>[77]</sup> Reprinted with permission from ref<sup>[77]</sup>

## 2. Theoretical Background

An intravenously injection of MNPs and the injection of  $H_2O_2$  into the affected tissues every four days demonstrated the tumor inhibition efficiency *in vivo*. The results show that the tumor volume did not increase by treating mice with MNPs and  $H_2O_2$ , whereas MNPs and  $H_2O_2$  alone just showed a small positive effect, compared to control animals (Figure 5).<sup>[77]</sup>

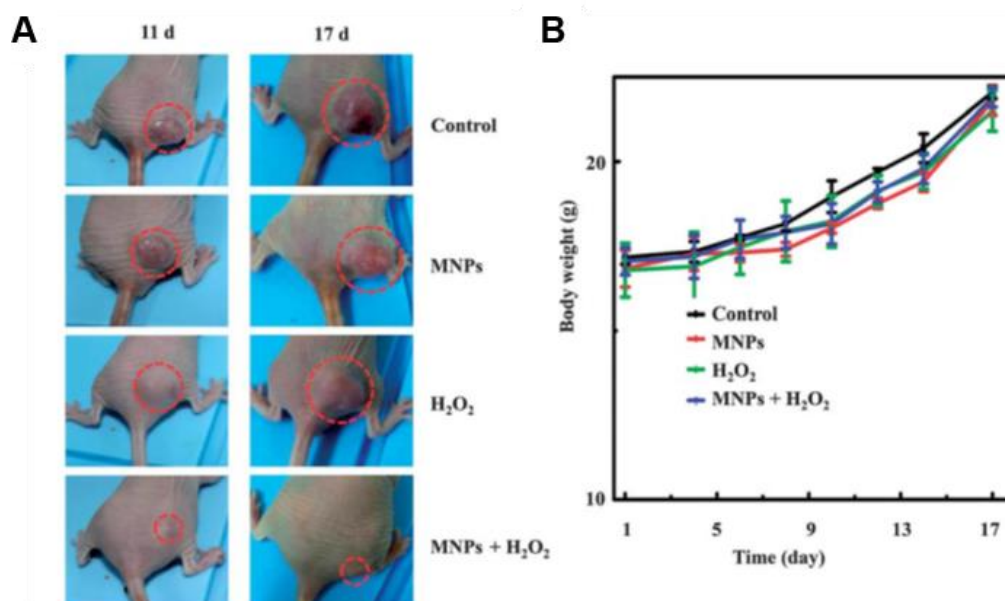


**Figure 5. Tumor treatment with MNPs and  $H_2O_2$ , forming ROS.** (A) Images of the temporal tumor development in presence of MNPs,  $H_2O_2$ , MNPs and  $H_2O_2$  and without MNPs and  $H_2O_2$ . (B) Body weight of the test mice demonstrated no significant reduction of the body mass.<sup>[77]</sup> Reprinted with permission from ref<sup>[77]</sup>



### 2.2.5 Nanozymes for Enzyme Replacement Therapy

In nature molybdenum is an essential part of the molybdenum cofactor of several enzymes, where it aids in the catalysis of redox and oxygen transfer reactions.<sup>[78]</sup> In mammals, the molybdenum cofactor is incorporated in sulfite oxidase (SuOx), an enzyme located in the mitochondrial intermembrane space of liver and kidney cells.<sup>[79]</sup> SuOx is a unique oxidase catalyzing the oxidation of sulfite to sulfate as the final step in the metabolism of sulfur containing amino acids, therefore playing a major role in cellular detoxification of sulfur. Genetic deficiency in SuOx leads to severe neurological damage resulting in early childhood death.<sup>[80]</sup>

The chemistry behind the SuOx activity has been comprehensively studied using model complexes, but none of those biomimetic compounds showed activity under physiological conditions.<sup>[81,82]</sup> MoO<sub>3</sub> nanoparticles ( $\varnothing \approx 2$  nm) mimic the enzymatic activity of SuOx *in vitro*.<sup>[29]</sup> MoO<sub>3</sub> nanoparticles were functionalized with a customized TPP-ligand, which promotes accumulation at the mitochondrial membrane, where SuOx is located.

The SuOx activity of the MoO<sub>3</sub>-TPP NPs was analyzed monitoring the reduction of ferricyanide (Figure 6 B, blue diamonds). Different from most enzymatic experiments with nanomaterials, where Michaelis-Menten behavior prevails, a sigmoidal behavior towards sulfite, indicating cooperative binding of substrates (with a Hill coefficient  $n = 2.35 \pm 0.15$ ) to the catalytic site (of enzymes) was observed. The MoO<sub>3</sub>-TPP nanoparticles catalyze the sulfite oxidation with a turnover frequency that is comparable to that of human SuOx mutants.<sup>[80,83]</sup> Selective mitochondria targeting of the functionalized MoO<sub>3</sub>-TPP nanoparticles (Figure 6 C, merge) was demonstrated by co-localization of the MoO<sub>3</sub>-TAMRA-TPP NPs (Figure 6 C, red channel), which were additionally labeled with the fluorescent marker 5-carboxytetramethylrhodamine (TAMRA), with the commercially available mitochondria targeting dye MitoTracker Green (Figure 6 C, green channel). *In vitro* studies in cells with reduced levels of functional sulfite oxidase showed that the SuOx activity of the deficient cells could be fully

## 2. Theoretical Background

recovered when treated with functionalized MoO<sub>3</sub>-TPP NPs showing the potential of the MoO<sub>3</sub> nanoparticles as SuOx mimic *in vitro*.<sup>[29]</sup> So far, no efficient treatment for the severe disease sulfite oxidase deficiency (genetic deficiency of SuOx) has been reported.<sup>[84]</sup> Therefore MoO<sub>3</sub> NPs might be used as SuO<sub>x</sub> enzyme replacement in a therapeutic treatment of this disease.

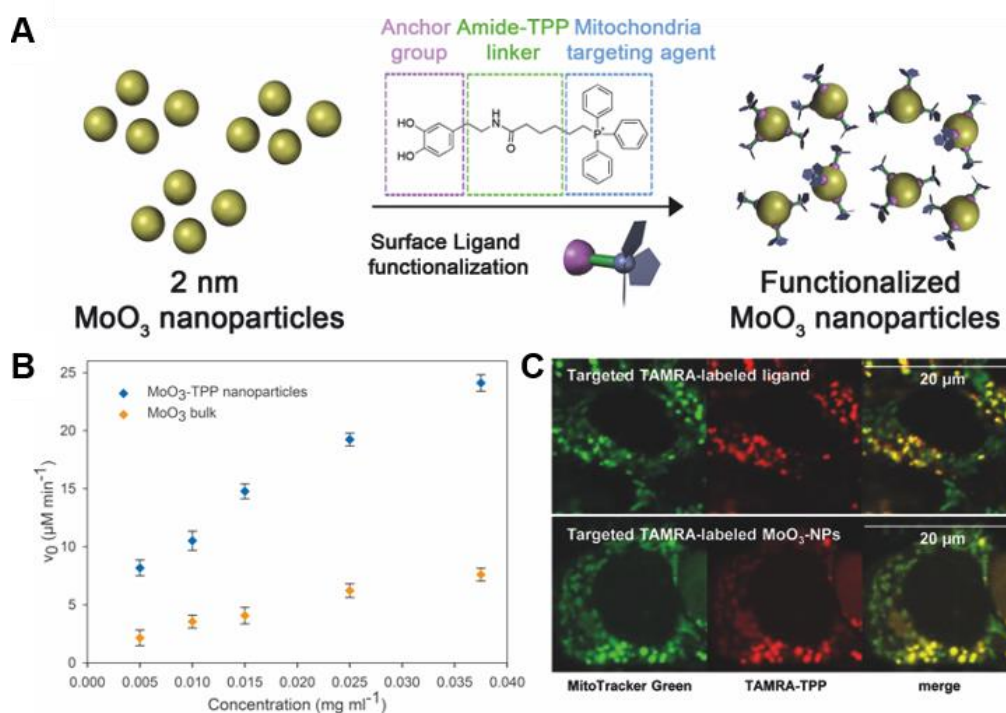


**Figure 6. MoO<sub>3</sub>-TPP NPs with intrinsic sulfite oxidase activity.** (A) Schematic representation of the functionalization of MoO<sub>3</sub> NPs with TPP-ligand. (B) SuOx activity of TPP functionalized NPs (blue) and bulk MoO<sub>3</sub> (orange) was analyzed by monitoring the ferricyanide reduction at 420 nm. (C) The selective mitochondria targeting of MoO<sub>3</sub>-TPP NPs was analyzed using an HEPG2 cell line. A modification of the ligand with TAMRA enables the spectroscopic localization. Colocalization experiments with MitoTracker green showed the selective mitochondria location.<sup>[29]</sup> Reprinted with permission from ref.<sup>[29]</sup>

### 2.2.6 Nanozymes for Environmental Applications

**Antimicrobial activity of haloperoxidase mimics.** Marine algae produce a cocktail of halogenated compounds. Their biosynthesis relies on halogenating enzymes, among them heme iron(II)- or vanadium dependent haloperoxidases (HI-HPO, V-HPO) or (ii) flavin- and non-heme iron(II) dependent halogenases (F-HG, NI-HG). Vanadium-dependent haloperoxidase (V-HPO) catalyzes the oxidation of halides ( $\text{Cl}^-$ ,  $\text{Br}^-$ ,  $\text{I}^-$ ) in presence of hydrogen peroxide ( $\text{H}_2\text{O}_2$ ) to hypohalous acids (HOX) according to:  $\text{Br}^- + \text{H}_2\text{O}_2 \rightarrow \text{HOBr} + \text{H}_2\text{O}$ .<sup>[85]</sup> HOX can react in follow-up reactions to halogenated organic compounds.<sup>[86]</sup> While haloperoxidases (HPOs) use hydrogen peroxide, halogenases (HGs) utilize dioxygen molecules as oxidant. Halogenating enzymes are important biocatalysts for the formation of natural products,<sup>[87]</sup> metabolic reactions,<sup>[88]</sup> in oxidative stress response and signal transduction.<sup>[89,90]</sup> They also catalyze the formation of halogenated compounds in the atmosphere<sup>[91,92]</sup> and in specific host defense and antimicrobial systems.<sup>[93]</sup> Hypohalous acids combat biofilm formation through their biocidal activity or the formation of signaling molecules involved in intracellular communication.<sup>[94]</sup> Bacterial adhesion and colonization is controlled by quorum sensing (QS), i.e. cell-to-cell communication.<sup>[94]</sup> When cell-to-cell communication is blocked by halogenated (and therefore inactive) compounds, bacteria cannot form organized community structures such as biofilms.<sup>[95]</sup>

An industrial application of naturally occurring V-HPOs in marine coatings is possible, but limited due to high production costs and the long-term stability of the native enzyme.<sup>[96]</sup> Similar as V-HPOs,  $\text{V}_2\text{O}_5$  nanowires exhibited a strong haloperoxidase activity by mediating the formation of hypobromous acid (HOBr) not only from  $\text{H}_2\text{O}_2$  and  $\text{Br}^-$  in laboratory scale, but even under seawater conditions, where  $\text{H}_2\text{O}_2$  was generated in  $\mu\text{M}$  amounts by sunlight.<sup>[97]</sup>  $\text{V}_2\text{O}_5$  nanowires embedded in commercial paints, applied onto stainless steel plates and incubated for 60 days in the Atlantic Ocean showed strong antifouling activity in open sea tests.<sup>[30]</sup> Biofouling was observed only on untreated controls, whereas the  $\text{V}_2\text{O}_5$  impregnated test plates did not show any signs of biofouling. As  $\text{V}_2\text{O}_5$  is a widely

used catalyst,<sup>[30]</sup> V<sub>2</sub>O<sub>5</sub> nanowires could be a useful alternative to common antifouling agents, but the toxic, cancerogenic and mutagenic properties of vanadium compounds will prevent commercial use.

Like already mentioned above nanoceria exhibit a mixed valence state Ce<sup>3+</sup>/Ce<sup>4+</sup> at the particle surface, which directly affects the catalytic activity.<sup>[98]</sup> Ce<sup>3+</sup> ions are known to catalyze the halogenation of malonic acid. Thus, the antibacterial activity of nanoceria<sup>[99]</sup> are presumably not a result of its SOD activity, but of its halogenating properties. Nanoceria showed, in fact, a strong brominating activity, as demonstrated with phenol red in the presence of Br<sup>-</sup> and H<sub>2</sub>O<sub>2</sub> (Figure 7). Bromination reactions in the presence of nanoceria and the marine alga *Corallina officinalis* showed similar results, illustrating the oxidative halogenation properties of nanoceria. Laboratory and field tests with paint formulations containing 2 wt% of CeO<sub>2-x</sub> nanorods showed a reduction in biofouling comparable to Cu<sub>2</sub>O, the most typical biocidal pigment (Figure 7).<sup>[31]</sup> Nanoceria has the potential to be a non-toxic and sustainable substitute for conventional inorganic/organic biocides.

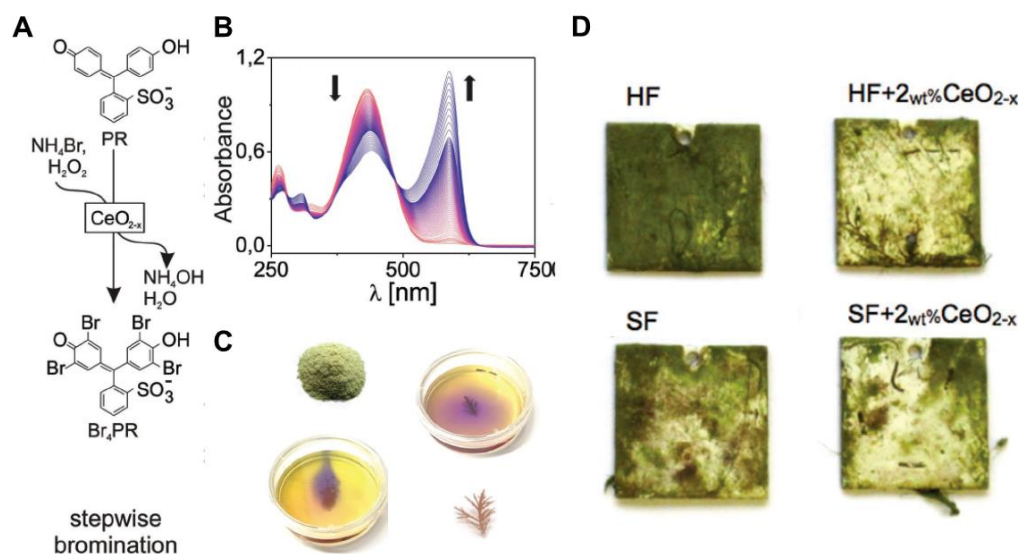


**Figure 7. Antifouling properties of nanoceria.** (A) Reaction process of the bromination reaction of phenol red (PR) to bromophenol blue ( $\text{Br}_4\text{PR}$ ) in presence of  $\text{H}_2\text{O}_2$  and  $\text{Br}^-$ , catalyzed by nanoceria. (B) Kinetic absorption scans demonstrating the reaction process over time. (C) An illustration of the bromination of PR in presence  $\text{H}_2\text{O}_2$  and  $\text{Br}^-$  catalyzed by nanoceria (2.1 mg, left) and the algae *C. officinalis* (7.1 mg, right) showed similar behavior. (D) Pictures of stainless steel plates coated with soft (S) and hard (F) formulations. SF and HF were mixed with 2 wt% of nanoceria to investigate their anti-fouling activity under sweater conditions, whereas negative samples were prepared only with the formulation paint. After more than seven weeks the stainless steel plates without nanoceria showed strong algae formation, while the NP containing formulations inhibited the accumulation significantly.<sup>[31]</sup> Reprinted with permission from ref<sup>[31]</sup>

**ROS reduction in cigarette smoke.** In aerobic organisms there is a balance between the native ROS formation and the degradation, which is mainly catalyzed by native enzymes like SOD or catalases.<sup>[100]</sup> ROS are produced in living organisms not only as a result of normal cellular metabolism, but also through environmental factors, such as air pollutants or cigarette smoke.<sup>[101-103]</sup> “Oxidative stress” is the shift in the balance between oxidants and antioxidants in favor of oxidants. SOD is one of the enzymatic antioxidants that are effective in blocking harmful effects of ROS. However, in pathological conditions, the antioxidant systems can be overwhelmed. The superoxide radical is the predominant radical species in cigarette smoke.<sup>[104]</sup> Glycine functionalized copper(II) hydroxide NPs (Gly-Cu(OH)<sub>2</sub>) show a strong intrinsic SOD-like activity, even higher than the natural CuZn SOD (Figure 8 A). Gly-Cu(OH)<sub>2</sub> NPs were shown to reduce superoxide levels in cigarette smoke extracts (CSE) (Figure 8 B). Control measurements with native CuZn SOD showed low efficiencies which may be attributed to a possible decomposition of the enzyme. Further experiments demonstrated that Gly-Cu(OH)<sub>2</sub> NPs reduce ROS levels after embedding in commercial cigarette filters (Figure 8 C). While investigations of the cytotoxicity of CSEs prepared with NP containing filter cigarettes did not show cytotoxic effects on lung cancer cell lines, control measurements conducted with commercial filter cigarettes showed increased cell death (Figure 8 D).<sup>[105]</sup>

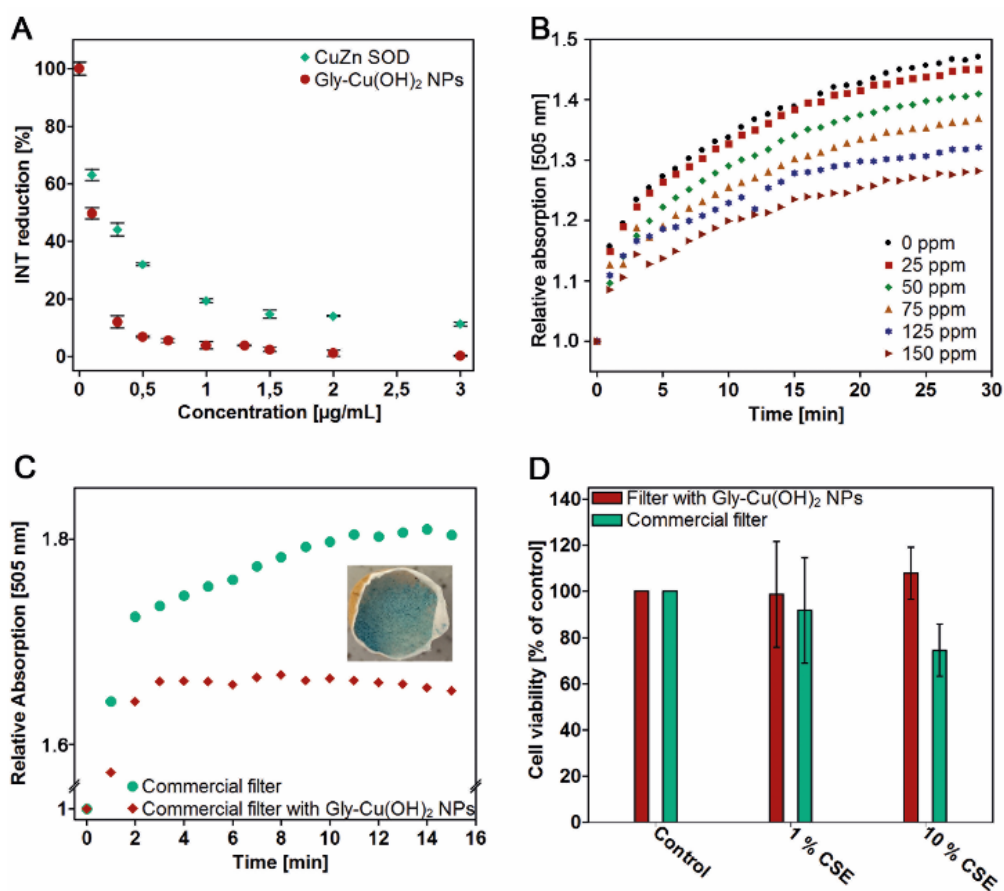


**Figure 8. Reduction of superoxide radicals in cigarette smoke using the intrinsic superoxide dismutase-like activity of Gly-Cu(OH)<sub>2</sub> NPs.** (A) The reduction of superoxide radicals in PBS buffered system, catalyzed by Gly-Cu(OH)<sub>2</sub> NPs (red) and native CuZn SOD (green), was monitored based on the inhibition of INT reduction ( $\lambda_{\text{max}} = 505 \text{ nm}$ ). The artificial NPs demonstrated a higher activity than their natural counterpart. (B) Reduction of superoxide radicals in an aqueous cigarette smoke extract in presence of various concentrations of Gly-Cu(OH)<sub>2</sub> NPs determined with the relative absorption at 505 nm. (C) A comparison of commercial filter cigarettes (green) with filter cigarettes, equipped with Gly-Cu(OH)<sub>2</sub> NPs (red), demonstrated the superoxide reduction in cigarette smoke, monitored with the relative absorption of reduced INT species. (D) A comparison of the cytotoxic effects of CSEs, generated with commercial filter cigarettes and NP containing cigarettes, demonstrated the positive effect of the NPs.<sup>[105]</sup> Reprinted with permission from ref<sup>[105]</sup>

### 2.2.7 Comparing Particle and Enzyme Activities

Although biochemical processes are accelerated by enzymes, biocatalysis and heterogeneous catalysis are mechanistically related.<sup>[106,107]</sup> Assuming a surface reaction to involve the steps  $A + S \rightleftharpoons AS \rightarrow \text{Products}$ , where A is the reactant, S are an enzyme or surface site, AS the substrate complex and  $k_1$ ,  $k_{-1}$  and  $k_2$  are the rate constants for adsorption, desorption and reaction to the final product. The global reaction rate  $r$  is given by  $k_2\theta C_S$ , (with  $C_S$  is the total number of – occupied and unoccupied – sites, provided that  $k_2$ , the rate constant of the enzyme/substrate complex is  $\gg k_1/k_{-1}$  ( $= K_m$ , the Michaelis constant). Although functions of enzymes are governed by the enzyme dynamics,<sup>[107]</sup> an enzyme is typically much larger than its substrate and the reaction environment it exposes is so different from the surrounding solvent that it may be considered a solid catalyst.<sup>[108]</sup> The radii of enzymes and nanoparticles are comparable to nanometer-sized cellular features, and the interactions of enzymes and nanoparticles with soluble molecules have comparable strength,<sup>[109]</sup> specificity and complexity. Therefore, enzyme mimetic catalysis with nanoparticles has been successful, where small molecular species (peroxides, superoxides or sulfites) are involved and steric demands play only a minor role for the specificity of the reaction.

NPs are highly reactive, as demonstrated by their use of in heterogeneous catalysis.<sup>[110]</sup> Typically, they are stabilized with capping ligands. Their activity and selectivity are determined by their size and the atomic structure of the exposed surface planes. The most active particles in catalysis have diameters of only a few nanometers, i.e. they contain between a few hundred and a few thousand atoms. Their catalytic activity ( $k_{cat}$ ) may even be higher than that of enzymes, because *any* surface site can be catalytically active. This raises the question, how reaction rates of nanoparticles and enzymes can be compared.



$k_{cat}$  is the maximum reaction rate ( $v_{max}$ ) for a given enzyme concentration ( $[E]$ ) and corresponds to the turnover *per* time.<sup>[111]</sup> Most natural enzymes have one active site, the protein backbone is responsible for selectivity. Catalysis by inorganic NPs proceeds at surface sites without steric selection.<sup>[110]</sup> Some of the surface sites may be blocked by surfactants, whose surface coverage is difficult to determine. The evaluation of nanoparticle reactivity is not straightforward, and different *modi operandi* are currently being used: (i) surface area,<sup>[31]</sup> (ii) assuming that each nanoparticle contains one active site,<sup>[14,20,112]</sup> (iii) molar ion concentrations<sup>[30,31]</sup> and (iv) number of active surface sites.<sup>[103,113]</sup> Each method has its advantages and disadvantages.

**Surface area.** Normalizing catalytic activity to the Brunauer Emmett Teller (BET) surface area is a standard tool in heterogeneous catalysis. It was used for determining the halogenation activity of CeO<sub>2-x</sub> NPs.<sup>[31]</sup> A direct comparison with a native enzyme is difficult, because the active site of an enzyme is not represented by the surface area.

**A single active site for each NP** was assumed when the peroxidase-like activity of iron oxide NPs and the superoxide dismutase activity of nanoceria were given.<sup>[14,20]</sup> The thought behind this definition is a comparison of the enzyme with a well-defined NP entity. The drawback is that a nanoparticle certainly contains more than one (typically  $\sim 10^7$ ) active site, depending on the surface/volume ratio of the NP,<sup>[105]</sup> but allows estimating an average activity per NP.<sup>[14,20,112]</sup> This method was used many times in enzyme mimetic literature and is widely accepted.

**Molar ion concentrations.** To avoid this problem, a normalization to molar ion concentrations was used.<sup>[30,31]</sup> Converting catalyst mass to ion concentration yields activities *per* metal ion. This approach assumes that a NP consists of a large number of metal (and counter) ions but ignores that only surface atoms are involved in catalysis, i.e. a spherical Cu(OH)<sub>2</sub> NP with a diameter of 150 nm contains  $\sim 10^{10}$  ions,  $\sim 0.1\%$  of them being surface ions.<sup>[105]</sup>

**Catalytic activity normalized to the number of active surface sites** can overcome all these problems.<sup>[105,113]</sup> Using particle volume and surface area (obtained from BET surface area and transmission electron microscopy (TEM)) the total number of metal atoms *per* NP and the number of surface atoms can be derived from the dimensions of the nanoparticle and the number of unit cells contained within. A prerequisite for deriving these numbers are (i) monodisperse particles and (ii) a well-defined particle morphology.

### 2.2.8 Conclusion and Outlook

This article describes concepts, up-to-date developments, and perspectives of the emerging field of nanoparticle enzyme mimics (so-called “nanozymes”). As one of the most exciting fields, the research on “nanozymes” lies at the interface of chemistry, biology, medicine, materials, and nanotechnology. Although it is counterintuitive to compare nanomaterials and enzymes because they seem quite different, a careful comparison reveals them to have many features in common like size, irregular shape, surface chemistry, etc. These similarities allow using nanomaterials as functional enzyme mimics where a practical use of native or recombinant enzymes is hampered by their stability, immunogenicity, short half-life, and production costs. Representative examples highlight nanomaterials with enzyme mimicking activities, their catalytic mechanisms, and their applications in areas ranging from therapeutics for neurodegenerative disorders, enzyme replacement, cancer diagnostics and tissue engineering to antifouling.

Finally, nanoparticle enzyme mimics have been suggested to play an important role as catalysts in the evolution of life. Since their discovery, deep-sea vents these vents have been suggested as the cradle of life. These vents, whose color depends on the compounds dispersed in the water, contain minerals with high levels of iron, manganese, copper, and zinc (black smokers) or barium, calcium, and silicon (white smokers).<sup>[114,115]</sup> Several of these minerals have a high surface area-to-volume ratio and provide potential sites for enzyme-like heterogeneous catalysis.<sup>[116]</sup> Primitive cells may have contained only a few “enzymes”, catalyzing

reactions with broad substrate specificity. These “enzymes” then may have been recruited for metabolic pathways while more specific and efficient catalysts could have developed later. Therefore, “proto-enzymes” may have been multifunctional in the early stages. Nanoparticle enzyme mimics are prototype examples of multifunctional catalysts.  $\text{CeO}_{2-x}$  nanoparticles have been reported to have peroxidase, SOD, catalase, phosphatase and esterase properties. Mineral surface adsorption or catalysis may have been important and this multifunctionality may have been relevant for plausible synthetic pathways toward the molecules of life.<sup>[117]</sup>

### 2.2.9 References

1. S. Heux, I. Meynial-Salles, M. J. O'Donohue, C. Dumon, *Biotechnol. Adv.* **2015**, *33*, 1653-1670.
2. Artificial Enzymes (ed. R. Breslow), Wiley-VCH, Weinheim, **2005**.
3. T. K. Hyster, T. R. Ward, *Angew. Chem. Int. Ed.* **2016**, *55*, 7344 – 7357.
4. D. Güçlü, A. Szekrenyi, X. Garrabou, M. Kickstein, S. Junker, P. Clapes, W.-D. Fessner, *ACS Catal.* **2016**, *6*, 1848–1852.
5. F. Yu, V. M. Cangelosi, M.L. Zastrow, M. Tegoni, J. S. Plegaria, A. G. Tebo, C. S. Mocny, L. Ruckthong, H. Qayyum, V. L. Pecoraro, *Chem. Rev.* **2014**, *114*, 3495–3578.
6. C. E. Valdez, Q. A. Smith, M. R. Nechay, A. N. Alexandrova, *Acc. Chem. Res.* **2014**, *47*, 3110–3117.
7. I. D. Petrik, J. Liu, Y. Lu, *Curr. Opin. Chem. Biol.* **2014**, *19*, 67–75.
8. K. N. Ferreira, T. M. Iverson, K. Maghlaoui, J. Barber, S. Iwata, *Science* **2004**, *303*, 1831–1838.
9. G. Kiss, N. Celebi-Ölcüm, R. Moretti, D. Baker, K. N. Houk, *Angew. Chem. Int. Ed.* **2013**, *52*, 5700 –5725.
10. H. Renata, Z. J. Wang, F. H. Arnold, *Angew. Chem. Int. Ed.* **2015**, *54*, 3351 – 3367.
11. M. J. Wiester, P. A. Ulmann, C. A. Mirkin, *Angew. Chem. Int. Ed.* **2011**, *50*, 114-137.
12. G. Y. Tonga, Y. Jeong, B. Duncan, T. Mizuhara, R. Mout, R. Das, S. T. Kim, Y.-C. Yeh, B. Yan, S. Hou, V. M. Rotello, *Nature Chem.* **2015**, *7*, 597–603.
13. R. Ye, T. J. Hurlburt, K. Sabyrov, S. Alayoglu, G. A. Somorjaia, *Proc. Natl. Acad. Sci. U.S.A.* **2016**, *113*, 5159–5166.

14. L. Gao, J. Zhuang, L. Nie, J. Zhang, Y. Zhang, N. Gu, T. Wang, J. Feng, D. Yang, S. Perrett, X. Yan, *Nature Nanotech.* **2007**, *2*, 577-853.
15. H. Wei, E. Wang, *Chem. Soc. Rev.* **2013**, *42*, 6060-6093.
16. R. Ragg, M. N. Tahir, W. Tremel, *Eur. J. Inorg. Chem.* **2016**, 1906-1915.
17. X. Wang, Y. Hua, H. Wei, *Inorg. Chem. Front.* **2016**, *3*, 41-60.
18. Z. Li, X. Yang, Y. Yang, Y. Tan, Y. He, M. Liu, X. Liu, Q. Yuan, *Chem. Eur. J.* **2017**, *23*, 1-8.
19. T. Pirmohamed, J. M. Dowding, S. Singh, B. Wassermann, E. Heckert, A. S. Karakoti, J. E. S. King, S. Seal, W. T. Self, *Chem. Commun.* **2010**, *46*, 2736-2738.
20. C. Korsvik, S. Patil, S. Seal, W. T. Self, *Chem. Commun.* **2007**, 1056-1058.
21. F. S. Archibald, I. Fridovich, *Arch. Biochem. Biophys.* **1982**, *214*, 452-463.
22. D. E. Cabelli, B. H. J. Bielski, *J. Phys. Chem.* **1984**, *88*, 3111-3115.
23. K. Barnese, E. B. Gralla, D. E. Cabelli, J. S. Valentine, *J. Am. Chem. Soc.*, **2008**, *130*, 4604-4606.
24. Y. Sheng, I. A. Abreu, D. E. Cabelli, M. J. Maroney, A.-F. Miller, M. Teixeira, J. S. Valentine, *Chem. Rev.* **2014**, *114*, 3854-3918.
25. J. M. Slocik, A. O. Govorov, R. R. Naik, *Angew. Chem. Int. Ed.* **2008**, *47*, 5335 – 5339.
26. A. A. Vernekar, T. Das, S. Ghosh, G. Mugesh, *Chem. Asian J.* **2016**, *11*, 72 – 76.
27. M. Comotti, C. Della Pina, R. Matarrese, M. Rossi, *Angew. Chem. Int. Ed.* **2004**, *43*, 5812-5815.
28. A. Asati, S. Santra, C. Kaittanis, S. Nath, J. M. Perez, *Angew. Chem. Int. Ed.* **2009**, *48*, 2308-2312.

29. R. Ragg, F. Natalio, M. N. Tahir, H. Janssen, A. Kashyap, D. Strand, S. Strand, W. Tremel, *ACS Nano* **2014**, *8*, 5182-5189.
30. F. Natalio, R. André, A. F. Hartog, B. Stoll, K. P. Jochum, R. Wever, W. Tremel, *Nature Nanotech.* **2012**, *7*, 530-535.
31. K. Herget, P. Hubach, S. Pusch, P. Deglmann, H. Götz, T. E. Gorelik, I. A. Guralskiy, F. Pfitzner, T. Link, S. Schenk, M. Panthöfer, V. Ksenofontov, U. Kolb, T. Opatz, R. André, W. Tremel, *Adv. Mater.* **2017**, *29*, 1603823.
32. F. Natalio, R. André, S. A. Pihan, M. Humanes, R. Wever, W. Tremel, *J. Mater. Chem.* **2011**, *21*, 11923-11929.
33. M. H. Kuchma, C. B. Komanski, J. Colon, A. Teblum, A. E. Masunov, B. Alvarado, S. Babu, S. Seal, J. Summy, C.H. Baker, *Nanomed. Nanotechnol., Biol. Med.* **2010**, *6*, 738-744.
34. A. A. Vernekar, T. Das, G. Mugesh, *Angew Chem. Int. Ed.* **2016**, *55*, 1412-1416.
35. J. F. Turrens, *J. Physiol.* **2003**, *552*, 335-344.
36. P. D. Ray, B.-W. Huang, Y. Tsuji, *Cell. Signal.* **2012**, *24*, 981-990.
37. L. A. Sena N. S. Chandel, *Mol. Cell.* **2012**, *48*, 158-167.
38. A. Butler, M. J. Clague, G. E. Meister, *Chem. Rev.*, **1994**, *94*, 625-638.
39. R. André, F. Natálio, M. Humanes, J. Leppin, K. Heinze, R. Wever, H. C. Schröder, W. E. G. Müller, W. Tremel, *Adv. Funct. Mater.* **2011**, *21*, 501-509.
40. G. Zampella, L. Bertini, L. De Gioia, *Chem. Commun.* **2014**, *50*, 304-307.
41. A. A. Vernekar, D. Sinha, S. Srivastava, P. U. Paramasivam, P. D'Silva, G. Mugesh, *Nat. Commun.* **2014**, *5*, 5301.
42. Y.-M. Go, D. P. Jones, *Biochim Biophys Acta* **2008**, *1780*, 1273-1290.

43. H. Molavian, A. M. Tonekaboni, M. Kohandel, S. Sivaloganathan, *Sci. Rep.* **2016**, *6*, 27439.
44. C. K. Kim, T. Kim, I.-Y. Choi, M. Soh, D. Kim, Y.-J. Kim, H. Jang, H.-S. Yang, J. Y. Kim, H.-K. Park, S. P. Park, S. Park, T. Yu, B.-W. Yoon, S.-H. Lee, T. Hyeon, *Angew. Chem. Int. Ed.* **2012**, *51*, 11039-11043.
45. R. W. Tarnuzzer, J. Colon, S. Patil, S. Seal, *Nano Lett.* **2005**, *5*, 2573-2577.
46. W. Wang, X. Jiang, K. Chen, *Chem. Commun.* **2012**, *48*, 7289-7291.
47. L. Zhang, L. Laug, W. Münchgesang, E. Pippel, U. Gösele, M. Brandsch, M. Knez, *Nano Lett.* **2010**, *10*, 219-223.
48. C. L. Allen, U. Bayraktutan, *Int. J. Stroke* **2009**, *4*, 461-470.
49. Y. Huang, Z. Liu, C. Liu, E. Ju, Y. Zhang, J. Ren, X. Qu, *Angew. Chem. Int. Ed.* **2016**, *55*, 6646-6650.
50. R. Jakob-Roetne, H. Jacobsen, *Angew. Chem. Int. Ed.* **2009**, *48*, 3030-3059.
51. H. W. Querfurth, F. M. LaFerla, *N. Engl. J. Med.* **2010**, *362*, 329-344.
52. M. T. Lin, M. F. Beal, *Nature* **2006**, *443*, 787-795.
53. B. Westermann, *Sci. Signaling* **2009**, *2*, 29, 1-7.
54. J. W. Lustbader, M. Cirilli, C. Lin, H. W. Xu, K. Takuma, N. Wang, C. Caspersen, X. Chen, S. Pollak, M. Chaney, *Science* **2004**, *304*, 448-452.
55. H. Du, L. Guo, F. Fang, D. Chen, A. A. Sosunov, G. M. McKhann, Y. Yan, C. Wang, H. Zhang, J. D. Molkenin, F. J. Gunn-Moore, J. P. Vonsattel, O. Arancio, J. X. Chen, S. D. Yan, *Nat. Med.* **2008**, *14*, 1097-1105.
56. Y. Huang, L. Mucke, *Cell* **2012**, *148*, 1204-1222.
57. M. J. McManus, M. P. Murphy, J. L. Franklin, *J. Neurosci.* **2011**, *31*, 15703-15715.

58. H. J. Kwon, M.-Y. Cha, D. Kim, D. K. Kim, M. Soh, K. Shin, T. Hyeon, I. Mook-Jung, *ACS Nano* **2016**, *10*, 2860–2870.
59. M. Li, P. Shi, C. Xu, J. Rena, X. Qu, *Chem. Sci.* **2013**, *4*, 2536-2542.
60. J. Kanta, *Acta Medica (Hradec Kralove)* **2011**, *54*, 97-101.
61. C. Mandoli, F. Pagliari, S. Pagliari, G. Forte, P. Di Nardo, S. Licoccia, E. Traversa, *Adv. Funct. Mater.* **2010**, *20*, 1617–1624.
62. T. Naganuma, E. Traversa, *Biomaterials* **2014**, *35*, 4441–4453.
63. S. Chigurupati, M. R. Mughal, E. Okun, S. Das, A. Kumar, M. McCaffery, S. Seal, M. P. Mattson, *Biomaterials* **2013**, *34*, 2194–2201.
64. A. S. Karakoti, O. Tsigkou, S. Yue, P. D. Lee, M. M. Stevens, J. R. Jones, S. Seal, *J. Mater. Chem.* **2010**, *20*, 8912–8919.
65. S. Ponnuram, G. D. O’Connell, I. V. Chernyshova, K. Wood, C. T-H. Hung, P. Somasundaran, *Tissue Engineering Part A* **2014**, *20*, 2908–2919.
66. G. Pulido-Reyes, I. Rodea-Palomares, S. Das, T. S. Sakthivel, F. Leganes, R. Rosal, S. Seal, F. Fernandez-Punas, *Sci. Rep.* **2015**, *5*, 15613.
67. M. Hu, K. Korschelt, P. Daniel, K. Landfester, W. Tremel, M. B. Bannwarth, *ACS Appl. Mater. Interfaces* **2017**, *9*, 38024–38031.
68. F. Pagliari, C. Mandoli, G. Forte, E. Magnani, S. Pagliari, G. Nardone, S. Licoccia, M. Minieri, P. DiNardo, E. Traversa, *ACS Nano* **2012**, *6*, 3767–3775.
69. J. L. Niu, A. Azfer, L. M. Rogers, X. H. Wang, P. E. Kolattukudy, *Cardiovascular Res.* **2007**, *73*, 549–559.
70. M. B. Kolli, N. D. P. K. Manne, R. Para, S. K. Nalabotu, G. Nandyala, T. Shokuhfar, K. He, A. Hamlekhan, J. Y. Ma, P. S. Werhner, L. Dornon, R. Arvapalli, K. M. Rice, E. R. Blough, *Biomaterials* **2014**, *35*, 9951–9962.
71. H. Pelicano, D. S. Martin, R.-H. Xu, P. Huang, *Oncogene* **2006**, *25*, 4633–4646.



72. P. Li, D. Zhang, L. Shen, K. Dong, M. Wu, Z. Ou, D. Shi, *Sci. Rep.* **2016**, *6*, 22831
73. L. Alili, M. Sack, C. von Montfort, S. Giri, S. Das, K. S. Carroll, K. Zanger, S. Seal, P. Brenneisen, *Antiox. Redox Signal.* **2013**, *19*, 765–778.
74. S. Giri, A. Karakoti, R. P. Graham, J. L. Maguire, C. M. Reilly, S. Seal, R. Rattan, V. Shridhar, *PLoS ONE* **2013**, *8*, e54578.
75. K. Fan, C. Cao, Y. Pan, D. Lu, D. Yang, J. Feng, L. Song, M. Liang, X. Yan, *Nature Nanotech.* **2012**, *7*, 459-464.
76. C. C. Winterbourn, *Tox. Let.* **1995**, *82-83*, 969-974.
77. D. Zhang, Y.-X. Zhao, Y.-J. Gao, F. P. Gao, Y.-S. Fan, X.-J. Li, Z.-Y. Duan, H. Wang, *J. Mater. Chem. B* **2013**, *1*, 5100-5107.
78. R. Hille, *Dalton Trans.* **2013**, *42*, 3029-3042.
79. G. Schwarz, R. R. Mendel, M. W. Ribbe, *Nature* **2009**, *460*, 839-847.
80. R. M. Garrett, J. L. Johnson, T. N. Graf, A. Feigenbaum, K. V. Rajagopalan, *Proc. Natl. Acad. Sci. USA* **1998**, *95*, 6394-6398.
81. S. Groysman, R. H. Holm, *Biochem.* **2009**, *48*, 2310-2320;
82. Z. Xiao, C. G. Young, J. H. Enemark, A. G. Wedd, *J. Am. Chem. Soc.* **1992**, *114*, 9194-9195.
83. E. Karakas, H. L. Wilson, T. N. Graf, S. Xiang, S. Jaramillo-Busquets, K. V. Rajagopalan, C. Kisker, *J. Biol. Chem.* **2005**, *280*, 33506-33515.
84. A. Veldman, J. A. Santamaria-Araujo, S. Sollazzo, J. Pitt, R. Gianello, J. Yaplitto-Lee, F. Wong, C. A. Ramsden, J. Reiss, I. Cook, J. Fairweather, G. Schwarz, *Pediatrics* **2010**, *125*, e1249-e1254.
85. R. Wever, W. Hemrika, *Handbook of Metalloproteins* (eds A. Messerschmidt, R. Huber, T. Poulos, K. Wieghardt), John Wiley & Sons, Chichester, **2001**, 1417-1428.

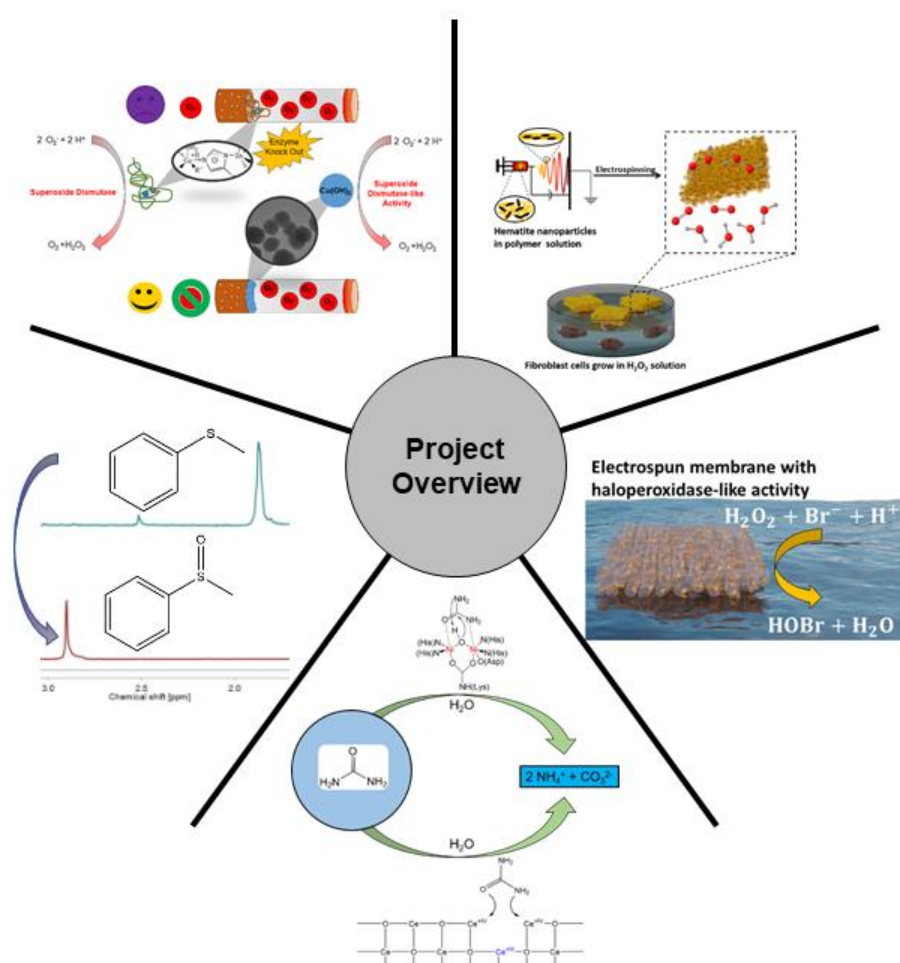
86. R. Wever, W. Hemrika, *Vanadium Haloperoxidases in Handbook of Metalloproteins*, John Wiley & Sons, Ltd, Hoboken, **2006**.
87. C. S. Neumann, D. G. Fujimori, C. T. Walsh, *Chem. Biol.* **2008**, *15*, 99-109.
88. A. Butler, J. N. Carter-Franklin, *Nat. Prod. Rep.* **2004**, *21*, 180-188.
89. C. C. Winterbourn, *Toxicology* **2002**, *181-182*, 223-227.
90. M. P. Lesser, *Annu. Rev. Physiol.* **2006**, *68*, 253-278.
91. C. Paul, G. Pohnert, *Nat. Prod. Rep.* **2011**, *28*, 186-195.
92. R. Wever, M. A. van der Horst, *Dalton Trans.* **2013**, *42*, 11778-11786.
93. P. G. Furtmüller, M. Zederbauer, W. Jantschko, J. Helm, M. Bogner, C. Jakopitsch, C. Obinger, *Arch. Biochem. Biophys.* **2006**, *445*, 199-213.
94. A. Butler, M. Sandy, *Nature* **2009**, *460*, 848-854.
95. M. R. Detty, R. Ciriminna, F. V. Bright, M. Pagliaro, *Acc. Chem. Res.* **2014**, *47*, 678-687.
96. M. Sandy, J. N. Carter-Franklin, J. D. Martin, A. Butler, *Chem. Commun.* **2011**, *47*, 12086-12088.
97. W. M. Draper, D. G. Crosby, *Arch. Environ. Contain. Toxicol.* **1983**, *12*, 121-126.
98. Y. Lin, J. Ren, X. Qu, *Acc. Chem. Res.* **2014**, *47*, 1097-1105.
99. R. J. Field, E. Körös, R. N. Noyes, *J. Am. Chem. Soc.* **1972**, *94*, 8649-8664.
100. T. Finkel, N. J. Holbrook, *Nature* **2000**, *408*, 239-247.
101. W. Domej, K. Oettl, W. Renner, *Int. J. COPD* **2014**, *9(1)*, 1207-1224.
102. W. A. Pryor, K. Stone *Ann. N. Y. Acad. Sci.* **1993**, *686*, 12-27.
103. W. A. Pryor, *Environ. Health Perspect.* **1997**, *105*, 875-882.

104. M. Tsuchiya, D. F. T. Thompson, Y. J. Suzukui, C. E. Cross, L. Packer, *Arch. Biochem. Biophys.* **1992**, 299, 30-37.
105. K. Korschelt, R. Ragg, C. S. Metzger, M. Kluncker, M. Oster, B. Barton, M. Panthöfer, D. Strand, U. Kolb, M. Mondeshki, S. Strand, J. Brieger, M. N. Tahir, W. Tremel, *Nanoscale* **2017**, 9, 3952-3960.
106. R. A. van Santen, M. Neurock, *Molecular Heterogeneous Catalysis*, Wiley-VCH, Weinheim, Germany, 2006
107. A. Kohen, Role of Dynamics in Enzyme Catalysis: Substantial versus Semantic Controversies. *Acc. Chem. Res.*, **2015**, 48 (2), pp 466–473
108. B. A. Grzybowski, W. T. S. Huck, *Nat. Nanotechnol.* **2016**, 11, 585-592.
109. C. G. Bezzu, M. Helliwell, J. E. Warren., D. R. Allen, N. B. McKeown, *Science* **2010**, 327, 1627-1630.
110. G. Rothenberg, *Catalysis - Concepts and Green Applications*. Wiley-VCH, Weinheim, 2008.
111. M. Harada, K. Fukasawa, B. Y. Hiraoka, M. Mogi, A. Barth, K. Neubert, *Biochim. Biophys. Acta* **1985**, 830, 341-344.
112. R. Ragg, A. M. Schilmann, K. Korschelt, C. Wieseotte, M. Kluncker, M. Viel, L. Völker, S. Preiß, J. Herzberger, H. Frey, K. Heinze, P. Blümmler, M. N. Tahir, F. Natalio, W. Tremel, *J. Mater. Chem. B*. **2016**, 4, 7423-7428.
113. M. Kluncker, M. N. Tahir, R. Ragg, K. Korschelt, P. Simon, T. E. Gorelik, B. Barton, S. I. Shylin, M. Panthöfer, J. Herzberger, H. Frey, V. Ksenofontov, A. Möller, U. Kolb, J. Grin, W. Tremel, *Chem. Mater.* **2017**, 29, 1134-1146.
114. M. Colín-García, A. Heredia, G. Cordero, A. Camprubí, A. Negrón-Mendoza, F. Ortega-Gutiérrez, H. Beraldi, S. Ramos-Bernal, *Boletín de la Sociedad Geológica Mexicana* **2016**, 68, 599–620.

115. A. Y. Mulkidjanian, M. Y. Galperin, *Biol Direct* **2009**, *4*, 27.
116. H. J. Cleaves, A. M. Scott, F. C. Hill, J. Leszczynski, N. Sahai, R. Hazen. *Chem. Soc. Rev.* **2012**, *41*, 5502–5525.
117. W. Martin, J. Baross, D. Kelley, M. J. Russell, *Nature Rev. Microbiol.* **2008**, *6*, 805-814.

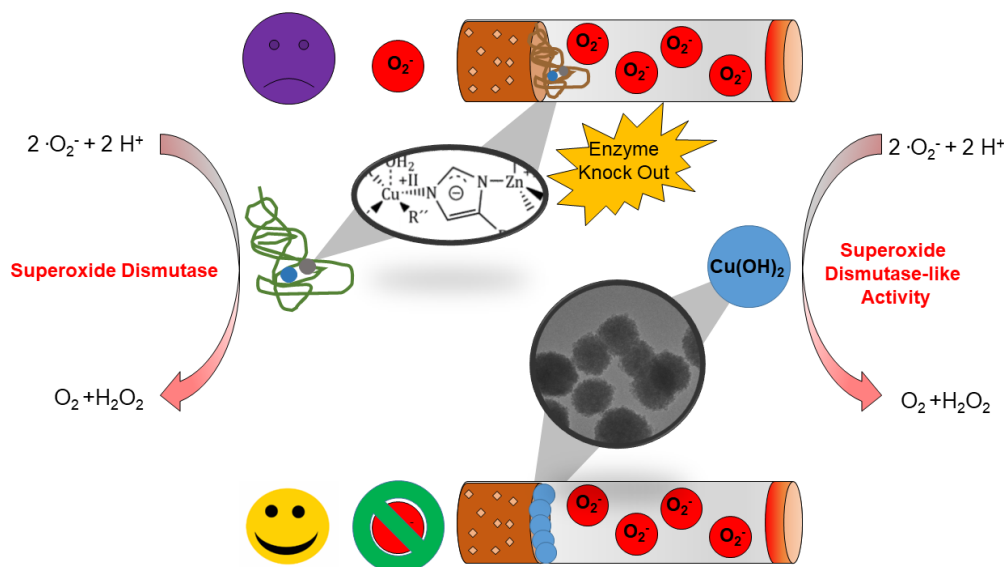
### 3. Results and Discussion

In the following chapter the results of the practical laboratory work are presented and discussed, considering current and recent literature. The subsections are all published, submitted or prepared for submission to journals with a peer review process. Thus, every part has its own references, supporting information, citation style, table and figure numbers, having regard to the requirements of the corresponding journal.



This part describes various enzyme mimics like e.g. superoxide dismutases, urease, haloperoxidase and catalase as well as their possible practical applications in cigarette filter systems, for water purification, for promoting the wound healing process and possible antibacterial properties. An additional study reports on the catalytic properties of various catalysts in a green-route for sulfide oxidations.

### 3.1. Glycine-Functionalized Copper(II) Hydroxide Nanoparticles with High Intrinsic Superoxide Dismutase Activity



The current project describes the exploration of ROS reducing NPs, containing copper ions that are present in the active site of native CuZn SOD enzymes. Inspired by the great influence of external sources, like tobacco consumption, on intracellular ROS levels, the possibility of reducing oxygen radicals in cigarette smoke with Cu(OH)<sub>2</sub> NPs was explored, overcoming the stability problems of their natural counterpart.

This chapter is an adapted reproduction of the manuscript published in *Nanoscale* **2017**, 9, 3952–3960, which is reproduced with permission of the Royal Society of Chemistry. Detailed authorship contributions are attached in the Appendix (chapter 5.3.2).

Special thank goes to B. Klasen and M. Wuttke for preliminary experiments of the nanoparticles synthesis as well as to R. Schwidetzky for his great assistance during the first cigarette experiments. I am also grateful for the support in P-XRD measurements by R. Jung-Pothman and for the possibility of using the oxygen sensitive electrode of Dr. S. Hobe, B. Niethard and Prof. Dr. H. Paulsen.

### 3.1.1 Abstract

Superoxide dismutases (SOD) are a group of enzymes that catalyze the dismutation of superoxide ( $O_2^-$ ) radicals into molecular oxygen ( $O_2$ ) and  $H_2O_2$  as a first line of defense against oxidative stress. Here, we show that glycine-functionalized copper(II) hydroxide nanoparticles (Gly-Cu(OH)<sub>2</sub> NPs) are functional SOD mimics, whereas bulk Cu(OH)<sub>2</sub> is insoluble in water and catalytically inactive. In contrast, Gly-Cu(OH)<sub>2</sub> NPs form water-dispersible mesocrystals with a SOD-like activity that is larger than that of natural CuZn enzyme counterpart. Based on this finding, we devised an application where Gly-Cu(OH)<sub>2</sub> NPs were incorporated in cigarette filters. Cigarette smoke contains high concentrations of toxic reactive oxygen species (ROS,  $>10^{16}$  molecules/puff) including superoxide and reactive nitrogen species which lead to the development of chronic and degenerative diseases *via* oxidative damage and subsequent cell death. Embedded in cigarette filters Gly-Cu(OH)<sub>2</sub> NPs efficiently removed ROS from smoke, thereby protecting lung cancer cell lines from cytotoxic effects. Their stability, ease of production and versatility make them a powerful tool for a wide range of applications in environmental chemistry, biotechnology and medicine.

### 3.1.2 Introduction

Although human cells rely on molecular oxygen ( $O_2$ ) as the final acceptor of electrons in respiration, reactive oxygen species (ROS)<sup>1,2</sup> like short-lived hydroxyl radicals ( $\cdot OH$ ), singlet oxygen ( $^1O_2$ ) and superoxide radicals ( $\cdot O_2^-$ ) or long-lived hydrogen peroxide ( $H_2O_2$ )<sup>3</sup> leak from the respiratory enzymes and wreak havoc on cells by causing mutations in DNA or attacking essential enzymes.<sup>1</sup> ROS were initially recognized only as toxic byproducts of the aerobic metabolism, but later found to play important roles as secondary messengers in key physiological phenomena as well.<sup>1,3,4</sup> Whether ROS serve as signaling molecules or cause oxidative damage to tissues depends on the balance between the ROS formation and scavenging. Environmental stress induced by UV irradiation, heat, or cigarette smoke leads to elevated ROS concentrations.<sup>2,5,6</sup>

To combat potential danger by ROS, nature has developed an antioxidant machinery with enzymatic components like superoxide dismutase (SOD) or catalase (CAT), combined with non-enzymatic antioxidants like ascorbic acid (AA) or reduced glutathione (GSH).<sup>2,7</sup> SOD plays a critical role in reducing oxidative stress implicated in atherosclerosis and other life-threatening diseases like ischemic stroke and septic shock, Alzheimer's, Parkinson's, and coronary artery diseases, or tumor growth.<sup>8-13</sup>

Human SODs occur in three different forms: Cytosolic copper/zinc SOD (CuZn SOD), mitochondrial manganese SOD (Mn SOD), and extracellular SOD (EC SOD).<sup>14-17</sup> Natural SODs containing copper, manganese, nickel, or iron control the concentration of superoxide radicals.<sup>18</sup> The best studied example is CuZn SOD, in which a copper center shuttling between the Cu(II)/Cu(I) redox states catalyzes the disproportionation of superoxide into dioxygen and hydrogen peroxide (eq. 1-3).<sup>18,19</sup>



By scavenging free oxygen radicals, SOD can interrupt inflammatory cascades, thereby limiting further disease progression.<sup>7</sup> Many studies reported liposomal-encapsulated SOD injection to be effective not only for the treatment of systemic inflammatory diseases but also of skin ulcer lesions due to burn and wounds.<sup>20</sup> Although recombinant CuZn SODs have been made, their applications are limited because of high production costs, low stability, and short biological half-life.<sup>21</sup> Therefore, synthetic analogues capable of mimicking natural enzymes are of particular interest.<sup>22-24</sup>

Some SOD mimics, mainly supramolecules<sup>25</sup> and metal complexes,<sup>26-28</sup> have been reported. However, enzyme mimics based on nanomaterials are - different from natural enzymes and supramolecules - more cost-efficient and stable over a wide pH and temperature range. Due to their large surface area nanomaterials have a high density of catalytically active sites and, hence, high catalytic activities.<sup>21,29</sup> After first reports



on the catalytic antioxidant activity of vanadium oxide,<sup>30</sup> supported gold,<sup>31-33</sup> cerium oxide (CeO<sub>2</sub>, nanoceria),<sup>10,34,35</sup> and manganese phosphate NPs,<sup>36,37</sup> the catalytic<sup>38,39</sup> and therapeutic<sup>10,40-42</sup> effects of nanoceria have been tested in cell culture and animal models of diseases. Considering the importance of SODs there is a need for functional SOD mimics with sufficient reactivity and stability.

Our approach was to explore the SOD activity of nanomaterials containing metal ions that are present as essential constituents in the active sites of natural SODs<sup>43</sup> and assuming that the peripheral enzyme loops are less relevant for small molecule substrates (like  $\cdot\text{O}_2^-$ ). Here we show that glycine functionalized copper(II) hydroxide nanoparticles (Gly-Cu(OH)<sub>2</sub> NPs) exhibit a high intrinsic SOD-like activity that is even higher than that of natural CuZn SOD. The Cu(II) sites in Gly-Cu(OH)<sub>2</sub> NPs fulfill the central requirement for an efficient SOD mimic by being susceptible to a one-electron reduction, while the intermediate Cu(I) state is temporarily stabilized through ligand binding.<sup>44</sup>

An application of the intrinsic SOD-like activity of Gly-Cu(OH)<sub>2</sub> NPs is demonstrated by incorporating them into cigarette filters. Cigarette smoke contains high concentrations of toxic radicals ( $>10^{16}$  molecules/puff) including ROS and reactive nitrogen species.<sup>45,46</sup> Oxidative damage resulting from exposure to these free radicals is a likely mechanism by which smoking can lead to cancer, or cardiovascular and chronic pulmonary diseases.<sup>47-49</sup> Hence, antioxidants like glutathione, vitamin A, C, and E, tea polyphenols or SOD formulations have been included in cigarette and other tobacco products to reduce the free radical damage in oropharynx and respiratory tract, but their temperature stability sets narrow limits on their use.<sup>50</sup> Gly-Cu(OH)<sub>2</sub> NPs embedded in cigarette filters greatly reduced ROS concentrations in cigarette smoke while showing no toxic side effects in cell tests.

### 3.1.3 Experimental

**Chemicals.** Copper(II) acetate ( $\geq 99\%$ , Sigma-Aldrich), glycine (Gly) (Sigma-Aldrich),  $^{13}\text{C}$ -glycine 99 atom%  $^{13}\text{C}$  (Sigma-Aldrich), sodium hydroxide (Sigma-Aldrich), xanthine (purity  $\geq 99\%$ , Sigma), xanthine oxidase (XO) from bovine milk (0.1-0.4 u/mg proteine; 18 mg protein/mL, Sigma), CuZn superoxide dismutase (SOD) from bovine (3232 U/mg, Sigma), iodinitrotetrazolium chloride (INT, Sigma Aldrich), PBS buffer (Sigma Aldrich), deuterated water ( $^{18}\text{O}$ ; 97 atom%, Aldrich), copper(I) iodide (Aldrich), copper(II) chloride (Acros), sodium dithionite (Merck), ethanol (Sigma-Aldrich), AlamarBlue<sup>®</sup> (Biozol) were used without further purification. Further on Magnum filter cigarettes (Joh. Wilh. von Eicken GmbH) were used. All reactions were carried out with milliQ water.

**Synthesis of copper(II) amino acid complexes.** *Cis*-Cu(Gly)<sub>2</sub> monohydrate/ $^{13}\text{C}$  enriched Cu(Gly)<sub>2</sub> ( $^{13}\text{C}$ -Cu(Gly)<sub>2</sub>) was prepared as described elsewhere.<sup>51</sup> Briefly copper(II) acetate monohydrate (0.1 mol/2.62·10<sup>-3</sup> mol) and glycine/ $^{13}\text{C}$  glycine (0.2 mol/1.31·10<sup>-3</sup> mol) were each dissolved in 250 mL/16.7 mL of water, heated up to 343 K, and the solutions were combined. The mixture was quenched with 250 mL/16.7 mL of ethanol, cooled to 273 K, and the reaction product was isolated by vacuum filtration. Subsequently, the precipitate was washed several times with ethanol, dried under high-vacuum, and characterized by IR spectroscopy (Fig. S2) and elemental analysis: Yield: 78% of blue crystals; IR  $\tilde{\nu}$ : 3331, 3254, 3157, 2975, 2920, 1675, 1603, 1572, 1438, 1419, 1386, 1320, 1195, 1183, 1170, 1117, 1059, 1038, 958, 917, 740, 668 cm<sup>-1</sup>. Elemental analysis calculated for CuC<sub>4</sub>H<sub>10</sub>N<sub>2</sub>O<sub>5</sub> (229.68 g·mol<sup>-1</sup>): 20.92% C, 4.39% H, 12.20% N; found: 20.96% C, 4.95% H, 12.21% N.

**Synthesis of Gly-Cu(OH)<sub>2</sub> NPs.** Gly-Cu(OH)<sub>2</sub> NPs/<sup>13</sup>C-Gly-Cu(OH)<sub>2</sub> NPs were synthesized by dissolving 0.041 mol/0.029 mol of *cis*-Cu(Gly)<sub>2</sub>/<sup>13</sup>C-Cu(Gly)<sub>2</sub> under constant stirring at room temperature in 130 mL/99 mL water. After 15 min, 6 mL/4.6 mL of a 1.2 M sodium hydroxide solution were added quickly in one portion with a 12 mL syringe. After additional stirring for 15 min, the blue precipitate was isolated by centrifugation (9000 rpm, 10 min) and washed with water and ethanol. The reaction products were dried under high vacuum, characterized by transmission electron microscopy (TEM), high resolution TEM (HR-TEM), IR-, <sup>1</sup>H- and <sup>13</sup>C-NMR spectroscopy and powder X-ray diffraction (P-XRD).

**Superoxide dismutase assay.** For the analysis the following solutions were used: Xanthine solution (the required amount of xanthine was dissolved in 1 mL of water and 10 μL of 10 M sodium hydroxide solution and filled up afterwards to the final concentration: 0.76 mg·mL<sup>-1</sup>), PBS buffer (50 mM, pH = 7.4), INT solution (1.26 mg·mL<sup>-1</sup> in 50 mM PBS buffer), XO (1:40).

The SOD activities of Gly-Cu(OH)<sub>2</sub> NPs, bulk Cu(OH)<sub>2</sub> and CuZn SOD were investigated using an UV-Vis assay with INT as dye. For the analysis, the degree of INT reduction based on superoxide radicals was observed at 505 nm.<sup>52,53</sup> Superoxide radicals in aqueous solution were generated *in situ* with xanthine oxidase (XO) and xanthine as substrates.<sup>54</sup> At the beginning, the maximum slope (100% control) was set to (0.0250 ± 0.0010) ΔAbs/min by adapting the amount of XO. In addition to the set amount of XO, the solution contained 100 μL of xanthine and 200 μL of INT. The cuvette was filled up to a volume of 1 mL with PBS-buffer. Finally the SOD activity was investigated by varying the concentration of Gly-Cu(OH)<sub>2</sub> NPs, bulk Cu(OH)<sub>2</sub> and CuZn SOD. The change in absorbance was monitored over a period of one minute.

**Oxygen formation.** The formation of elemental oxygen during the SOD reaction was observed with an oxygen sensitive electrode in a thermostated measuring cell (298 K). The cell was calibrated with a saturated sodium dithionite solution. For the analysis of the oxygen formation, a solution as described for the UV-Vis assay (but without INT) was used. The slope without XO was observed for one minute, in order to model the background. In the second step, XO was added to start the reaction. The slope, which represents the formation of oxygen, was monitored over a period of four minutes.

**SOD reaction mechanism.** The SOD reaction with Gly-Cu(OH)<sub>2</sub> NPs was investigated with a modified Evan's Method.<sup>55</sup> For the analysis, the NMR shift was logged on the signal of deuterated water between every measurement. The shift of the water NMR signal with respect to the logged signal was analyzed for the following solutions: 1) 1 mg·mL<sup>-1</sup> of Gly-Cu(OH)<sub>2</sub> NPs in water; 2) 1 mg·mL<sup>-1</sup> of CuCl<sub>2</sub> in water; 3) 1 mg·mL<sup>-1</sup> of CuI in water; 4) 870 μL of PBS buffer, 100 μL of xanthine, 20 μL of XO and 10 μL of Gly-Cu(OH)<sub>2</sub> NP solution (1 mg·mL<sup>-1</sup>).

**Cigarette smoke measurements.** Cigarette smoke experiments were conducted by preparing a cigarette smoke extract (CSE) using 1 M PBS buffer and commercial cigarettes. Cigarette smoke was channeled through the buffer solution with a flow of 0.3-0.5 L·min<sup>-1</sup>. The as-prepared CSE was transferred to a 96 well plate. Each well contained 80 μL of CSE and 20 μL of INT. For the first measurements, the effect of Gly-Cu(OH)<sub>2</sub> NPs in aqueous solution was investigated. Here, each well contained different NP concentrations. In subsequent measurements, Gly-Cu(OH)<sub>2</sub> NPs were applied to the filter. The evolution of the INT reduction as a function of time was monitored at 505 nm with a microplate fluorometer.

**AlamarBlue® assay.**<sup>56</sup> A549 cells were plated onto a 96 well-plate (15 000 cells/150 µl). Subsequently, the cells were annealed to attach at 37°C (5% CO<sub>2</sub>). After 24 h, the cell medium was removed and the cells were washed three times with 1 M PBS buffer. A negative control was carried out by incubating the cells with 70% ethanol for 10 min. Afterwards, 10% AlamarBlue® was added and the cells were incubated in fresh cell media for 3 h (37°C, 5% CO<sub>2</sub>) before the fluorescence was recorded on a fluorescence microplate reader at 540 nm (emission 600 nm). The resulting counts were normalized to the number of living cells, which were identified with crystal violet dye by washing three times with PBS, adding a 0.2% crystal purple solution (50 µl/well), and incubating the cells for 10 min at 37°C. After incubation, the cells were washed again and treated with 40 µl of 10% acetic acid for lysis and measured on a plate reader at 540 nm.

#### **Characterization Details.**

**NMR measurements.** All NMR experiments were performed on a Bruker ARX 400 spectrometer with a  $^1\text{H}$  frequency of 399.83 MHz. Samples were dissolved in  $\text{D}_2\text{O}$  and the spectra were analyzed with Mnova NMR software.

**Solid state NMR measurements.**  $^{13}\text{C}$ -NMR-spectra were recorded on a Bruker Advance DSX 400 spectrometer using a commercial Bruker 2.5 mm 2 channel probe head allowing fast spinning. The VT (variable temperature) experiments were conducted at 20 kHz MAS (magic angle spinning) using a 90 degree excitation pulse and averaging 20 k scans using a recycle delay of 0.2 sec. At such high spinning speeds, the frictional heating is significant, which results in approx. 5 K higher effective sample temperatures (depending mostly on the bearing gas pressure, however, also on the rotor used).

**IR-spectroscopy.** The IR-spectra were measured on a Nicolet iS10 FT-IR spectrometer from Thermo Scientific in the range of 4000 - 650  $\text{cm}^{-1}$ .

**X-ray diffraction.** Diffraction data were collected with a Siemens D5000 diffractometer equipped with a Ge (220) monochromator using  $\text{Cu K}\alpha$ -radiation. The data analysis were analyzed using the EVA software package. Rietveld refinements (for details see Supporting Information) were done with the *Topas Academic* Software.<sup>57</sup>

**UV-Vis-spectroscopy.** Spectral data were collected with a Cary Varian 5G UV-Vis-NIR spectrometer using a 1 mL micro-cuvette with a size of 12.5 x 12.5 x 45 mm from Brand.

**Elemental analysis.** For the elemental analysis, a vario EL cube from the company Elementar was used.

**Transmission electron microscopy.** TEM images were acquired on a Zeiss LEO 906E transmission electron microscope using an acceleration voltage of 120 kV (Carl Zeiss, Oberkochen, Germany). High resolution TEM was performed using an FEI Tecnai F30 S-TWIN with field emission gun, operating at 300 kV (FEI Company, Hillsboro, OR, USA), and a 4k x 4k pixel slow scan CCD camera (Gatan, Pleasanton, CA, USA). In-line holograms were obtained by focal series reconstruction, using 20 images recorded at 790 000 x primary magnification with 6 nm focal increment and a Gerchberg-Saxton algorithm implemented in Python. Samples were prepared by drop-casting a NP suspension onto a thin, holey amorphous carbon film suspended on a 300 mesh copper TEM grid (3 mm).

**Oxygen electrode.** To investigate the evolution of elemental oxygen, a Hansatech oxygen electrode S1 connected to a manual writer was used. The electrode was equipped with an atmosphere isolated measurement cell including a pressure equalisation with a capillary. As electrodes, a Pt cathode and Ag anode were used. The temperature was held at 25°C by a thermostat.

**Atomic absorption spectroscopy (AAS).** The Cu(OH)<sub>2</sub>/glycine ratio of the NPs was determined by AAS. The AAS experiments were conducted using a Perkin-Elmer 5100 ZL atom absorption spectrometer with a Zeeman furnace module and a Cu hollow-cathode lamp at 324.8 nm.

**Plate reader.** For the measurements conducted with 96 well-plates, a Fluoroskan Ascent microplate reader from Thermo Fisher Scientific and the Software Ascent 2.6 from Thermo Electron Corporation was used.

### 3.1.4 Results and Discussion

**Glycine-functionalized Cu(OH)<sub>2</sub> nanoparticles (Gly-Cu(OH)<sub>2</sub> NPs).** Gly-Cu(OH)<sub>2</sub> NPs were prepared in two steps (Fig. 1). In the first step, the precursor complex *cis*-bis(glycinato) copper(II) monohydrate (Cu(Gly)<sub>2</sub>) was prepared by mixing aqueous solutions of copper(II) acetate and glycine at 343 K.<sup>51</sup> The complex was isolated by vacuum filtration and washed several times with ethanol. Gly-Cu(OH)<sub>2</sub> NPs were synthesized on a multi-gram scale by adding an aqueous solution of NaOH to an aqueous solution of Cu(Gly)<sub>2</sub> (Fig. 1).<sup>51</sup> The precipitate was isolated by centrifugation and the product was washed with water and ethanol.



**Fig. 1.** Synthesis, enzymatic activity, and application of Gly-Cu(OH)<sub>2</sub> NPs. Cu(Gly)<sub>2</sub> was prepared by mixing aqueous solutions of copper(II) acetate and glycine. Addition of NaOH to a solution of Cu(Gly)<sub>2</sub> in water at room temperature (RT) led to the formation of Gly-Cu(OH)<sub>2</sub> NPs with high intrinsic SOD activity. As-synthesized NPs as part of cigarette filters reduce the concentration of superoxide radicals, produced by commercial cigarettes.



The phase identity and morphology of the as-prepared NPs were controlled by powder X-ray diffraction (P-XRD), transmission electron microscopy (TEM), and high-resolution TEM (HR-TEM) (Fig. 2 and Fig. 3A). TEM showed the presence of spherical Gly-Cu(OH)<sub>2</sub> NPs with diameters of ≈150 nm. The HR-TEM analysis revealed these NPs to be aggregates of smaller subcrystals with similar morphology and domain sizes of approx. 13 x 5 x 7 nm, as determined by Rietveld refinement to the X-ray powder data (Fig. 3A, Tab. S1, Supporting Information).

Glycine coordination of copper is a prerequisite for the formation of Gly-Cu(OH)<sub>2</sub> NPs, as attempts to synthesize them by adding NaOH to a solution of copper(II) acetate in presence of glycine (without isolating the precursor complex) lead only to the precipitation of Cu(OH)<sub>2</sub> without surface functionalization (Fig. S1, Supporting Information) due to the low solubility product of Cu(OH)<sub>2</sub>. The glycine functionalization of the Gly-Cu(OH)<sub>2</sub> NPs was demonstrated by IR-spectroscopy (Fig. 3B), <sup>13</sup>C solid state nuclear magnetic resonance (NMR) spectroscopy (Fig. 3C), and atom absorption spectroscopy (AAS), which revealed a glycine content of ≈16%. Fig. 3B shows a comparison of the IR spectra of Gly-Cu(OH)<sub>2</sub> NPs (red) and commercially available bulk Cu(OH)<sub>2</sub> (blue). The characteristic IR bands of Gly-Cu(OH)<sub>2</sub> NPs are broadened (compared to the bulk), because of the smaller crystallite size.<sup>58</sup> The bands at 3570, 3301 cm<sup>-1</sup> and 913, 701 cm<sup>-1</sup> (Fig. 3B), corresponding to OH stretching and deformation modes, are characteristic for Cu(OH)<sub>2</sub>.<sup>59</sup> A comparison with the spectra of glycine and Cu(Gly)<sub>2</sub> (Fig. S2, SI) indicates that the additional bands at 1603, 1379, and 1325 cm<sup>-1</sup> can be assigned to the asymmetric and symmetric carboxylate and CH<sub>2</sub> stretching vibrations of the amino acid.<sup>60</sup>

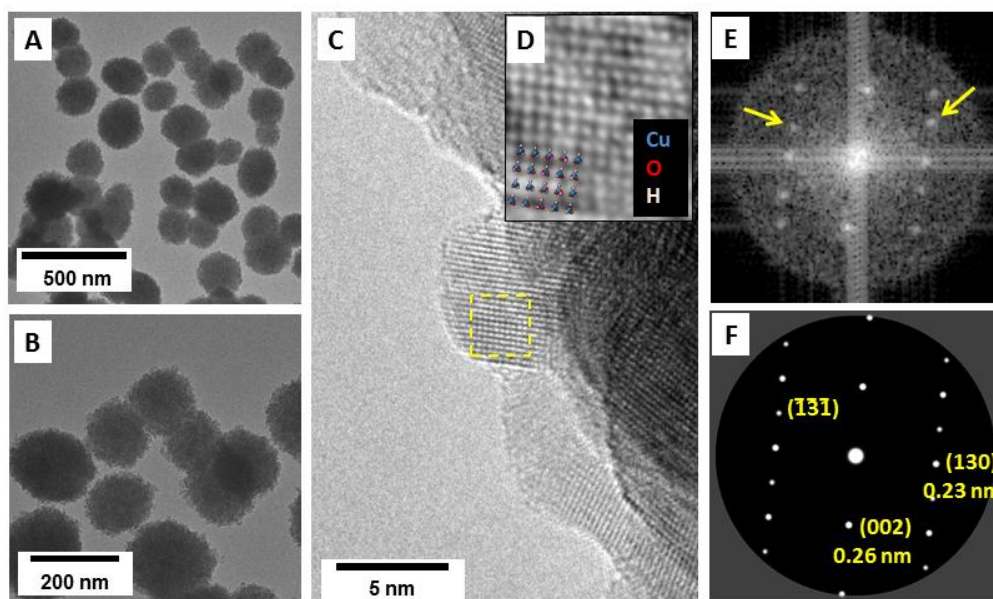


**Fig. 2.** TEM imaging of Gly-Cu(OH)<sub>2</sub> NPs. **(A, B)** TEM images of Gly-Cu(OH)<sub>2</sub> NPs synthesized from Cu(Gly)<sub>2</sub>. **(C)** At the edge of a cluster, individual NPs (crystallites) are observed by HR-TEM. **(D)** The phase of the in-line hologram (boxed area in **(C)**) shows the atomic lattice, while the contrast is dominated by Cu (blue spheres in overlaid model of Cu(OH)<sub>2</sub>, viewed in 310 direction). **(E, F)** Comparison of the power spectrum calculated from the phase image and the simulated single-crystal diffraction pattern of Cu(OH)<sub>2</sub> 310 show good agreement. However, the shift of ( $\pm 1 -3 \pm 1$ ) reflections points towards local disorder (arrowheads in **(E)**).

The <sup>13</sup>C solid state NMR experiments further confirmed the functionalization of the Gly-Cu(OH)<sub>2</sub> NPs. Fig. 3C illustrates the <sup>13</sup>C spectra of the Cu(Gly)<sub>2</sub> complex, a <sup>13</sup>C enriched Cu(Gly)<sub>2</sub> (<sup>13</sup>C-Cu(Gly)<sub>2</sub>) complex and the <sup>13</sup>C-Gly-Cu(OH)<sub>2</sub> NPs recorded at 20 kHz MAS at ambient and high temperature. <sup>13</sup>C enrichment at the CH<sub>2</sub> position of glycine was necessary due to the low signal intensity of the <sup>13</sup>C solid state NMR spectra of the NPs as the amount of surface-bound amino acid is by default significantly lower compared to the molecular precursor complex. We assign the resonances at -308 ppm to the CH<sub>2</sub> group and the resonance at -205 ppm to the CO group of glycine in the precursor complex.<sup>61</sup> The <sup>13</sup>C spectrum of the <sup>13</sup>C-Gly-Cu(OH)<sub>2</sub> NPs reveals a signal at -265 ppm with a full width at half maximum (fwhm) of about 7800 Hz related to the <sup>13</sup>C enriched CH<sub>2</sub> group of the <sup>13</sup>C-Gly-Cu(OH)<sub>2</sub> NPs. The significant inhomogeneous broadening is attributed to the disordered glycine ligands on the NP surface. The resonance of the CO group is too low to be detected at these conditions. All <sup>13</sup>C NMR

spectra recorded at higher temperature exhibit a low field temperature-dependent shift of approx. 50 ppm of the carbon resonances for all functional groups in both complexes and a shift of about 35 ppm for the CH<sub>2</sub> group in the NP spectra, which is attributed to a stronger deshielding of all <sup>13</sup>C resonances related with the weaker hydrogen bonding at higher temperatures. At the same time the fwhm is hardly affected by higher temperature. IR and NMR spectroscopic results consistently show the glycine surface functionalization of the NPs. In essence, Gly-Cu(OH)<sub>2</sub> NPs are mesocrystals,<sup>62-64</sup> which are stabilized by glycine surface ligands occluded between the individual nanoparticle domains. In the absence of the glycine surface ligand oriented attachment of crystallographically aligned Cu(OH)<sub>2</sub> nanoparticles occurs. As a result, the nanocrystals crystallographically fuse to crystallites with low surface area and virtually no catalytic activity.

### 3. Results and Discussion

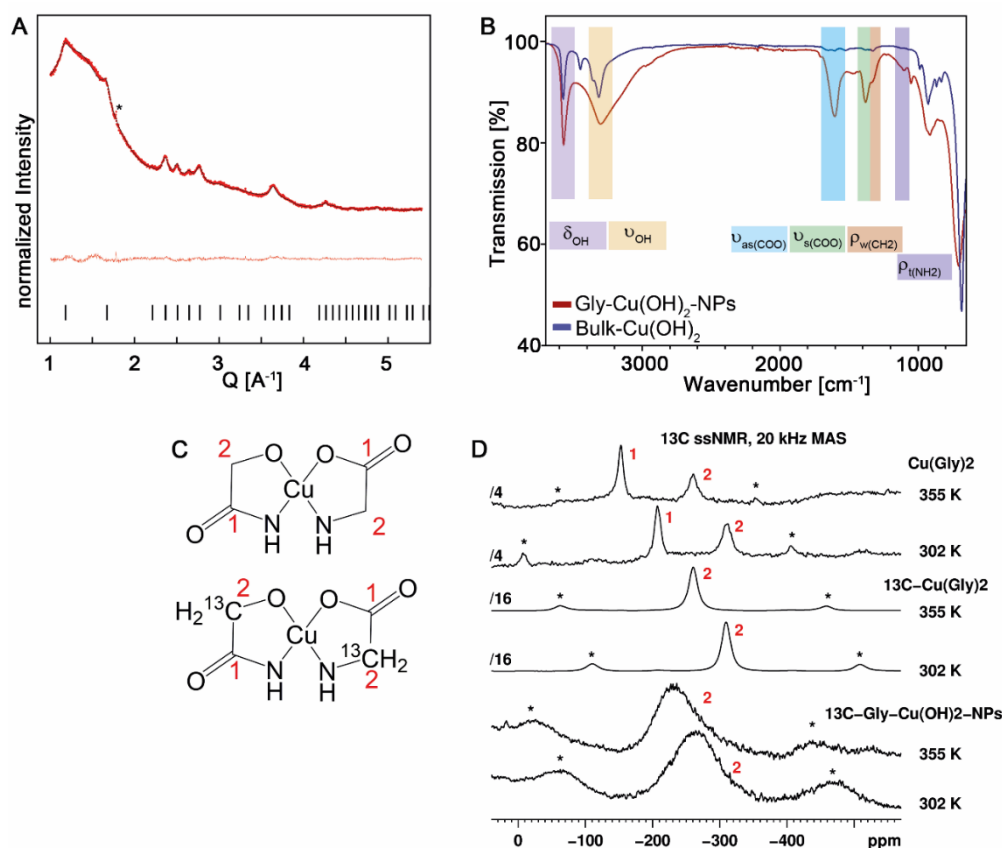


**Fig. 3.** Phase characterization and functionalization of Gly-Cu(OH)<sub>2</sub> NPs. (A) P-XRD pattern of Gly-Cu(OH)<sub>2</sub> NPs. The red dots represent the measured data, the black line the calculated pattern, and the red line is the residual of the measured pattern and the calculated 13.4 by 5.4 by 6.6 nm anisotropic Gly-Cu(OH)<sub>2</sub> NPs. The black ticks mark the pattern of the base-centered orthorhombic Cu(OH)<sub>2</sub> cell. A reflection from a minor impurity is marked with \* and can be attributed to azurite (Cu<sub>3</sub>(CO<sub>3</sub>)<sub>2</sub>(OH)<sub>2</sub>). (B) IR spectra of bulk Cu(OH)<sub>2</sub> and Gly-Cu(OH)<sub>2</sub> NPs. Bands at 3570, 3301 cm<sup>-1</sup> (NPs) and 3572, 3313 cm<sup>-1</sup> (bulk) are associated to the OH deformation, and the OH stretch at 913, 701 cm<sup>-1</sup> (NPs) and 924, 683 cm<sup>-1</sup> (bulk) are characteristic for Cu(OH)<sub>2</sub>.<sup>59</sup> The band broadening for the NPs (compared to the bulk) is due to the smaller crystallite size.<sup>58</sup> Bands at 1603, 1379, and 1325 cm<sup>-1</sup> in the spectra of the NPs originating from the asymmetric and symmetric CO<sub>2</sub> and the CH<sub>2</sub> stretch of glycine<sup>60</sup> show that the amino acid is surface bound to the NPs. (C) Structures of the Cu(Gly)<sub>2</sub> and the <sup>13</sup>C enriched Cu(Gly)<sub>2</sub> complex. (D) <sup>13</sup>C single pulse excitation solid state NMR spectra of the complexes Cu(Gly)<sub>2</sub>, <sup>13</sup>C-Cu(Gly)<sub>2</sub>, and <sup>13</sup>C-Gly-Cu(OH)<sub>2</sub> NPs recorded at 20 kHz MAS, 0.5 s recycle delay, and effective sample temperatures of resp. 302 and 355 K. A shift of about 50 ppm for both complexes and of about 35 ppm is observed at higher temperatures. With 1 and 2 are denoted the carbonyl group and resp. the CH<sub>2</sub> group of glycine. The asterisks denote spinning sidebands.

**SOD-like activity of Gly-Cu(OH)<sub>2</sub> NPs.** The decomposition of superoxide radicals by Gly-Cu(OH)<sub>2</sub> NPs in an SOD-like reaction was demonstrated with a colorimetric UV-vis assay using iodinitrotetrazolium chloride (INT) as superoxide sensitive dye.<sup>52</sup> Superoxide radicals in aqueous solution were generated *in situ* with xanthine/xanthine oxidase (XO) in a phosphate buffered (PBS, pH = 7.4) system.<sup>54</sup> In absence of SOD (or SOD-active NPs), superoxide radicals reduce INT, which is associated with a color change from colorless to red ( $\lambda_{\max} = 505$  nm). The inhibition of the INT reduction as a function of the CuZn SOD or Gly-Cu(OH)<sub>2</sub> NP concentrations demonstrate the SOD activity. Gly-Cu(OH)<sub>2</sub> NPs showed a high intrinsic SOD-like activity.(Fig. 4A).

The decay plots in Fig. 4A were used to determine the concentrations of the catalyst with SOD activity required to achieve a 50% inhibition of the INT reduction (defined as IC<sub>50</sub>) and the rate constants  $k$  for the reaction with superoxide (Table S2).<sup>65</sup> The rate constant of the reaction was determined from the  $k_{\text{INT}} = 3.94 \cdot 10^4 \text{ M}^{-1}\text{s}^{-1}$  (see SI) for the reduction of INT by superoxide. In a first step, the SOD activities were determined for molar nanoparticle concentrations ( $k = 8.72 \cdot 10^{14} \text{ M}^{-1}\text{s}^{-1}$ , SI).<sup>35,66</sup> However, different from SOD enzymes that typically have only a single active site, nanoparticles have many independent catalytic surface sites.<sup>18,21</sup> As turnover numbers (TON) and catalytic rate constants are given *per* active subunit (as in classical enzymology),<sup>67</sup> we determined the activity of the nanoparticles normalized to one active site. The number of catalytically active Cu(II) sites *per* NP was estimated based on the Cu(OH)<sub>2</sub> structure (lepidocrocite type)<sup>68</sup> and the particle size determined by TEM. Gly-Cu(OH)<sub>2</sub> NPs were approximated as ideal spheres terminated by their (310) surfaces (Fig. 2). Accordingly, two Cu(II) sites were assumed on the (310) surface of a Cu(OH)<sub>2</sub> unit cell. The total (310) surface area of a single NP contains approx.  $2.62 \cdot 10^7$  Cu(II) sites. In the next step, the ratio between the crystal volume and the volume of the Cu(OH)<sub>2</sub> unit cell was calculated and multiplied by the number of Cu(II) sites in a single Cu(OH)<sub>2</sub> unit cell (4 Cu<sup>2+</sup>/cell), which corresponds to a total of  $4.53 \cdot 10^{10}$  Cu atoms within a single Cu(OH)<sub>2</sub> NP. The ratio of  $2.62 \cdot 10^7$  surface Cu sites/ $4.53 \cdot 10^{10}$  total Cu sites *per* NP was used as a calibration factor ( $5.78 \cdot 10^{-4}$ ) to convert the total Cu(OH)<sub>2</sub> concentration determined by atomic absorption spectroscopy (AAS) to the number of

active Cu(II) surface sites. Thus, a copper concentration of  $5.02 \cdot 10^{-10}$   $\mu\text{M}$  ( $\text{IC}_{50}$  per active site) was estimated for evaluating  $k_{\text{cat}} = 3.91 \cdot 10^{10} \text{ M}^{-1}\text{s}^{-1}$  (calculation SI). The calculated SOD activities were compared with the SOD activities for molar Gly-Cu(OH)<sub>2</sub> concentrations and the activity of the CuZn SOD. The experimental  $\text{IC}_{50}$  values and rate constants indicate that the SOD activity of Gly-Cu(OH)<sub>2</sub> NPs is larger than that of (i) their natural counterpart, CuZn SOD, (ii) commercially available bulk Cu(OH)<sub>2</sub> (Table S2, SI), (iii) nanoceria ( $k_{\text{cat}} = 3.6 \cdot 10^9 \text{ M}^{-1}\text{s}^{-1}$ ),<sup>35</sup> and (iv) of a SOD mimetic Cu(II) bistriazole complex ( $\text{IC}_{50} = 0.18 \mu\text{M}$ ).<sup>27</sup> While the lower activity of CuZn SOD (molar nanoparticle concentrations) compared to the Gly-Cu(OH)<sub>2</sub> NPs may be attributed to the surface area, the higher activity per active site is surprising. It could be attributed to the fact that the NP surface is more stable towards physiological conditions than natural enzyme where the presence of organic framework around the active center also plays a prominent role in defining the enzymatic activity.

**Reaction mechanism.** In order to establish the postulated reaction mechanism (equation (3)) and the characteristics of the Gly-Cu(OH)<sub>2</sub> catalyzed SOD reaction, the formation of elemental oxygen, one decomposition product of the SOD reaction, was monitored using an oxygen sensitive electrode (Fig. S3). In addition, the catalytic cycle of the SOD reaction with Gly-Cu(OH)<sub>2</sub> NPs was investigated with a modified Evan's method.<sup>55</sup> During the reaction, the catalytically active Cu(II) site was reduced in the first and reoxidized in the second step (eq. (3)). This requires Cu to shuttle between the oxidation states +II and +I. Cu(I) is diamagnetic and, therefore, does not induce a paramagnetic shift of the NMR signals, whereas the interaction of the nuclear spin of the H<sub>2</sub>O protons with the magnetic field of paramagnetic Cu(II) shifts the resonance signal to lower fields. The paramagnetic shift of the H<sub>2</sub>O NMR signal during the Gly-Cu(OH)<sub>2</sub> catalyzed dismutation of the superoxide radicals remained unchanged (Fig. S5), whereas an oxidation/reduction would lead to an upfield shift due to the formation of diamagnetic Cu(I). Thus, the SOD reaction shows the characteristics of a catalytic cycle (rather than that of a mere oxidation of Cu surface atoms). As additional control, the inhibiting effect of Gly-Cu(OH)<sub>2</sub> NPs on the formation of superoxide was measured, because blocking of the formation of superoxide should lead to a higher

apparent SOD activity. The formation of uric acid, one of the products of the xanthine/XO system, was quantified by measuring the absorbance at 290 nm (A<sub>290</sub>, an absorption maximum of uric acid, Table S3), and showed that Gly-Cu(OH)<sub>2</sub> NPs did not inhibit the superoxide formation.

**Reducing the ROS level in cigarette smoke with Gly-Cu(OH)<sub>2</sub> NPs.** Because of high SOD activity, Gly-Cu(OH)<sub>2</sub> NPs can remove ROS species from cigarette smoke to prevent oxidative damage. This may be especially important as epidemiological evidence established that smoking is one of the most important extrinsic factors of premature morbidity and mortality. The particular advantages of using Gly-Cu(OH)<sub>2</sub> NPs rather than nanoceria are (i) that Gly-Cu(OH)<sub>2</sub> NPs show a higher SOD activity<sup>35</sup> and (ii) their good water dispersibility due to the glycine surface functionalization (nanoceria is difficult to disperse). The ROS reduction was probed with cigarette smoke extract (CSE) prepared from commercial filter cigarettes (Magnum), by channeling the cigarette smoke through a 1 M PBS buffer solution. The required maelstrom was regulated with a vacuum pump, and the gas flow (0.3 - 0.5 L·min<sup>-1</sup>) was controlled with a flowmeter. The superoxide concentration (i.e. the ability of Gly-Cu(OH)<sub>2</sub> NPs to reduce the radical concentration) was monitored using INT as superoxide sensitive dye. INT reduction triggered by ROS in cigarette smoke extract was observed spectrophotometrically at 505 nm using a 96-well plate reader with NP dispersions (concentrations of which were varied systematically) and INT solutions in the wells (i.e. 96 samples were exposed simultaneously to cigarette smoke to establish optimum reaction conditions, Fig. S6). To achieve reliable results and to minimize the effect that every cigarette is slightly different in composition, every experiment was done ten times. The spectrophotometric results were compatible with an increase of the ROS reduction for an aqueous cigarette smoke extract containing dispersed Gly-Cu(OH)<sub>2</sub> NPs (Fig. 4B). An 11% inhibition of the INT reduction was achieved for NP concentrations of 150 ppm, while controls with recombinant CuZn SOD (optimized concentrations) showed only a 2% inhibition of INT reduction (Fig. S7). The results are in harmony with the SOD activity measurements as a function of the Gly-Cu(OH)<sub>2</sub> NP concentrations.

### 3. Results and Discussion

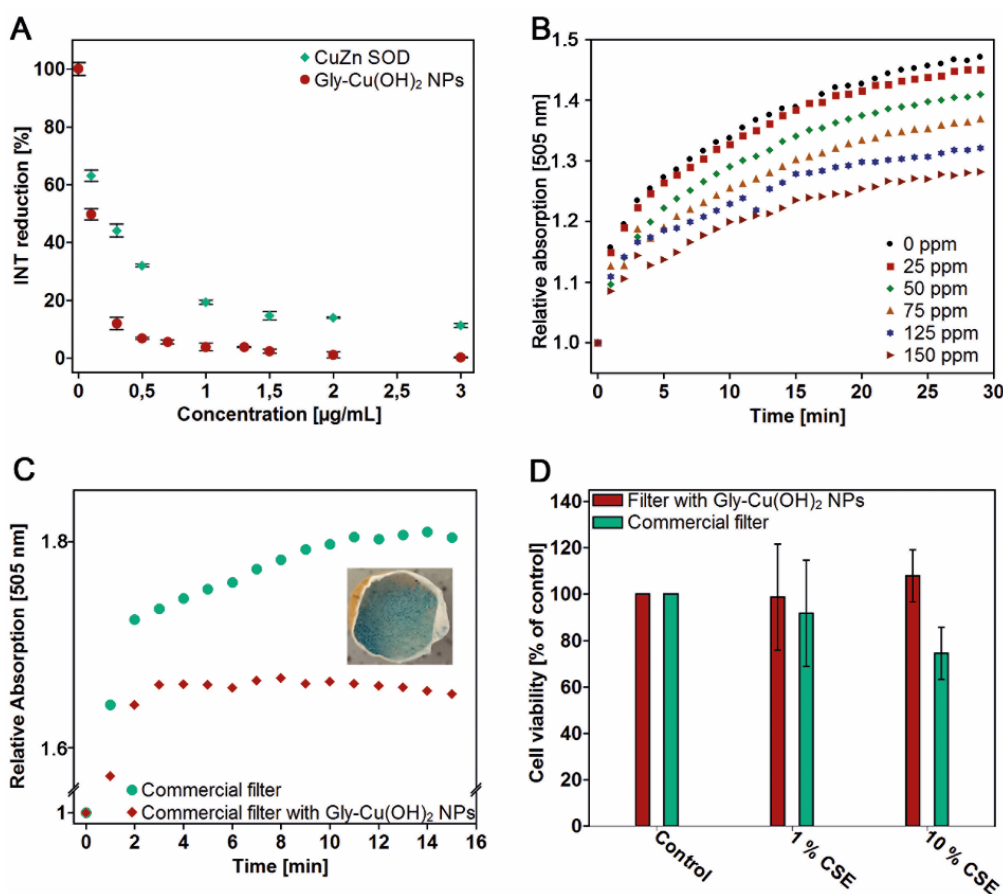


**Fig. 4.** Catalytic efficiency of Gly-Cu(OH)<sub>2</sub> NPs and reduction of superoxide concentration in cigarette smoke. **(A)** SOD-like activity of Gly-Cu(OH)<sub>2</sub> NPs (red) and natural CuZn SOD (green), determined from the inhibition of the INT reduction ( $\lambda_{\max} = 505 \text{ nm}$ ) in a PBS buffered xanthine/XO system. Gly-Cu(OH)<sub>2</sub> NPs show enhanced activity compared to natural SOD. **(B)** Relative absorption of reduced INT due to reduction by superoxide radicals in the absence (and presence, concentration-dependent) of Gly-Cu(OH)<sub>2</sub> NPs in solution. CSE was treated with Gly-Cu(OH)<sub>2</sub> NPs and the INT reduction was monitored for 30 minutes. **(C)** Relative absorption of the reduced INT species at 505 nm for CSE prepared with a commercial filter (green) and a filter containing solid NPs (red). An inhibition of the INT reduction was observed based on the decomposition of superoxide by Gly-Cu(OH)<sub>2</sub> NPs. **(D)** Cytotoxicity of CSE produced with commercial cigarette filters (green) and with filter systems containing Gly-Cu(OH)<sub>2</sub> NPs (red).



An immediate application of the ROS degradation is to integrate the Gly-Cu(OH)<sub>2</sub> NPs in cigarette filters to reduce ROS in cigarette smoke. Commercial cigarettes were used to determine the ROS reduction effect by comparing the INT reduction in cigarette smoke after passing a commercial filter and a commercial filter containing solid embedded Gly-Cu(OH)<sub>2</sub> NPs. In the presence of Gly-Cu(OH)<sub>2</sub> NPs, the INT reduction was inhibited due to ROS degradation in a solid/gas reaction by approx. 10% (Fig. 4C) compared to an untreated commercial filter. A comparison of the cytotoxicity of cigarette smoke extracts generated by (i) commercial Magnum cigarettes, (ii) cigarette smoke extract pretreated with Gly-Cu(OH)<sub>2</sub> NPs (Fig. S8), and (iii) cigarette smoke extract generated by cigarettes equipped with Gly-Cu(OH)<sub>2</sub> NPs using an AlamarBlue<sup>®</sup> assay with A549 cells<sup>69</sup> revealed a pronounced cytotoxicity of commercial cigarettes. Controls performed with cigarette smoke extracts generated with a filter systems containing solid embedded Gly-Cu(OH)<sub>2</sub> NPs showed no toxic behavior (Fig. 4D) which also indicates the thermal stability of Gly-Cu(OH)<sub>2</sub> NPs under smoking conditions.<sup>70</sup>

#### 3.1.5 Conclusions

We have demonstrated the intrinsic SOD-like activity of Gly-Cu(OH)<sub>2</sub> NPs. Although bulk Cu(OH)<sub>2</sub> is highly insoluble in water ( $K_L = 5.6 \cdot 10^{-20} \text{ mol}^3 \cdot \text{L}^{-3}$ ) and therefore catalytically inactive,<sup>71</sup> as-synthesized Gly-Cu(OH)<sub>2</sub> NPs were readily dispersible in aqueous media and catalyzed the decomposition of superoxide much more efficiently than CuZn SOD, their natural counterpart. During the SOD-like reaction, Cu shuttles between the oxidation states +II and +I, demonstrated by the paramagnetic shift of the <sup>1</sup>H-NMR signal of water during the dismutation of the superoxide radicals. Due to their extraordinarily high SOD activity, Gly-Cu(OH)<sub>2</sub> NPs incorporated in cigarette filters efficiently removed toxic ROS radicals from cigarette smoke. Gly-Cu(OH)<sub>2</sub> NPs may find use as SOD replacement in cosmetic creams, because SOD reduces free radical damage, prevents aging, reducing facial wrinkles, and hyperpigmentation or depigmentation, or protects against UV rays. The SOD-like activity of Gly-Cu(OH)<sub>2</sub> NPs can reduce mutagenicity effects of other SOD substitutes compounds like quercetin.<sup>72</sup>

### 3.1.6 References

- 1 K. Apel and H. Hirt, *Annu. Rev. Plant Biol.* 2004, **55**, 373–399.
- 2 T. Finkel and N. J. Holbrook, *Nature* 2000, **408**, 239–247.
- 3 J. S. Valentine, L. D. Wertz, T. J. Lyons, and L.-L. Liou, *Curr. Opin. Chem. Biol.* 1998, **2**, 253–262.
- 4 K. T. Kishida and E. Klann, *Antioxid. Redox Singal.* 2007, **9**, 233–244.
- 5 E. Cadenas, A. Boveris, C. I. Ragan, and A. O. M. Stoppani, *Arch. Biochem. Biophys.* 1977, **180**, 248–257.
- 6 A. Schulze and A. L. Harris, *Nature* 2012, **491**, 364–73.
- 7 B. Halliwell and J. M. Gutteridge, *Methods Enzymol.* 1990, **186**, 1–85.
- 8 A. Bravard, L. Sabatier, F. Hoffschir, M. Ricoul, C. Luccioni, and B. Dutrillaux, *Int. J. Cancer* 1992, **51**, 476–480.
- 9 P. Jenner and C. W. Olanow, *Neurology* 1996, **47**, 161–170.
- 10 C. K. Kim, T. Kim, I.-Y. Choi, M. Soh, D. Kim, Y.-J. Kim, H. Jang, H.-S. Yang, J. Y. Kim, H.-K. Park, S. P. Park, S. Park, T. Yu, B.-W. Yoon, S.-H. Lee, and T. Hyeon, *Angew. Chem. Int. Ed. Engl.* 2012, **51**, 11039–11043.
- 11 U. Landmesser, R. Merten, S. Spiekermann, K. Bu, H. Drexler, and B. Hornig, *Circulation* 2000, **101**, 2264–2270.
- 12 S. E. Safford, T. D. Oberley, M. Urano, and D. K. St. Clair, *Cancer Res.* 1994, **54**, 4261–4265.
- 13 E. Panieri and M. M. Santoro, *Cell Death* 2016, *Dis.* **7**, e2253.
- 14 W. Kaim, B. Schwederski, and A. Klein, *Bioinorganic Chemistry - Inorganic Elements in the Chemistry of Life: An Introduction and Guide.* (Wiley, 2013).

- 15 A. F. Miller, *FEBS Lett.* 2012, **586**, 585–595.
- 16 G. Tabbi, W. L. Driessen, J. Reedijk, R. P. Bonomo, N. Veldman, and A. L. Spek, *Inorg. Chem.* 1997, **36**, 1168–1175.
- 17 S. Miriyala, I. Spasojevic, A. Tovmasyan, D. Salvemini, Z. Vujaskovic, D. St. Clair, and I. Batinic-Haberle, *Biochim. Biophys. Acta: Mol. Basis Dis.* 2012, **1822**, 794–814.
- 18 I. A. Abreu and D. E. Cabelli, *Biochim. Biophys. Acta: Proteins Proteomics* 2010, **1804**, 263–274.
- 19 F. Yu, V. M. Cangelosi, M. L. Zastrow, M. Tegoni, J. S. Plegaria, A. G. Tebo, C. S. Mocny, L. Ruckthong, H. Qayyum, and V. L. Pecoraro, *Chem. Rev.* 2014, **114**, 3495–3578.
- 20 Y. Niwa, *Dermatologica* 1989, **179**, 101–106.
- 21 H. Wei and E. Wang, *Chem. Soc. Rev.* 2013, **42**, 6060–6093.
- 22 L. Gao, J. Zhuang, L. Nie, T. Zhang, J. Feng, D. Yang, and S. Perrett, and X. Yan, *Nat. Nanotechnol.* 2007, **2**, 577–583.
- 23 K. Fan, C. Cao, Y. Pan, D. Lu, D. Yang, J. Feng, L. Song, M. Liang, and X. Yan, *Nat. Nanotechnol.* 2012, **7**, 459–464.
- 24 L. Gao, and X. Yan, *Sci. China* 2016, **59**, 400–402.
- 25 Z. Dong, Y. Wang, Y. Yin, and J. Liu, *Curr. Opin. Colloid Interface Sci.* 2011, **16**, 451–458.
- 26 M. Kose, P. Goring, P. Lucas, and V. Mckee, *Inorg. Chim. Acta* 2015, **435**, 232–238.
- 27 Y.-H. Zhou, W.-Q. Wan, D.-L. Sun, J. Tao, L. Zhang, X.-W. Wei, and Z. Anorg. Allg. Chem. 2014, **640**, 249–253.

- 28 D. Pursche, M. U. Triller, C. Slinn, N. Reddig, A. Rompel, and B. Krebs, *Inorg. Chim. Acta* 2004, **357**, 1695–1702.
- 29 R. Ragg, M. N. Tahir, and W. Tremel, *Eur. J. Inorg. Chem.* 2015, 1906–1915.
- 30 A. A. Vernekar, D. Sinha, S. Srivastava, P. U. Paramasivam, P. D'Silva, and G. Mugesh, *Nat. Commun.* 2014, **5**, 5301.
- 31 Y. Tao, Y. Lin, Z. Huang, J. Ren, and X. Qu, *Adv. Mater.* 2013, **25**, 2594-2599.
- 32 J. Li, W. Liu, X. Wu, and X. Gao, *Biomaterials* 2015, **48**, 37-44.
- 33 Y. Tao, E. Ju, J. Ren, and X. Qu, *Adv. Mater.* 2015, **27**, 1097-1104.
- 34 J. Chen, S. Patil, S. Seal, and J. F. McGinnis, *Nat. Nanotechnol.* 2006, **1**, 142–150.
- 35 C. Korsvik, S. Patil, S. Seal, W. T. Self, *Chem. Commun.* 2007, 1056–1058.
- 36 K. Barnese, E. B. Gralla, D. E. Cabelli, J. S. Valentine, *J. Am. Chem. Soc.* 2008, **130**, 4604–4606.
- 37 X. Shen, Q. Wang, Y. Liu, W. Xue, L. Ma, S. Feng, M. Wan, F. Wang, C. Mao, *Sci. Rep.* 2016, **6**, 28989.
- 38 Y. Li, X. He, J. J. Yin, Y. Ma, P. Zhang, J. Li, Y. Ding, J. Zhang, Y. Zhao, Z. Chai, *Angew. Chem. Int. Ed.* 2015, **54**, 1832–1835.
- 39 K. Herget, P. Hubach, S. Pusch, P. Deglmann, H. Götz, T. E. Gorelik, I. A. Gural'skiy, F. Pfitzner, T. Link, S. Schenk, M. Panthöfer, V. Ksenofontov, U. Kolb, T. Opatz, R. André, W. Tremel, *Adv. Mater.* **2017**, *29*, 1603823.
- 40 C. Walkey, S. Das, S. Seal, J. Erlichman, K. Heckman, L. Ghibelli, E. Traversa, and J. F. McGinnis, *Environ. Sci. Nano* 2015, **2**, 33–53.
- 41 W. Lin, Y.-W. Huang, X.-D. Zhou, Y. Ma, *Int. J. Toxicol.* 2006, **25**, 451–457.

- 42 R. Ragg, A. M. Schilman, K. Korschelt, C. Wieseotte, M. Klueker, M. Viel, L. Völker, S. Preiß, J. Herzberger, H. Frey, K. Heinze, P. Blümner, M. N. Tahir, F. Natalio, and W. Tremel, *J. Mater. Chem. B* 2016, **4**, 7423-7428.
- 43 F. Wiesemann, S. Teipel, B. Krebs, and U. Hoeweler, *Inorg. Chem.* 1994, **33**, 1891–1898.
- 44 P. Kamau and R. B. Jordan, *Inorg. Chem.* 2001, **40**, 3879–3883.
- 45 W. A. Pryor and K. Stone, *Ann. N. Y. Acad. Sci.* 1993, **686**, 12–27.
- 46 B. Dellinger, L. Khachatryan, S. Masko, and S. Lomnicki, *Mini. Rev. Org. Chem.* 2011, **8**, 427–433.
- 47 W. A. Pryor, *Environ. Health Perspect.* 1997, **105**, 875–882.
- 48 B. Messner and D. Bernhard, *Arterioscler. Thromb. Vasc. Biol.* 2014, **34**, 509–515.
- 49 W. Domej, K. Oettl, and W. Renner, *Int. J. COPD* 2014, **9**, 1207–1224.
- 50 T. Hersh and R. Hersh, Antioxidants to neutralize tobacco free radicals. WO2002091866 A1, 2002.
- 51 P. O'Brien, *J. Chem. Educ.* 1982, **59**, 1052–1053.
- 52 A. Z. Haghighi and R. Wei, *Anal. Lett.* 1998, **31**, 981–990.
- 53 J. M. McCord, *Curr. Protoc. Toxicol.* 2001, Chapter 7, Unit 7.3.
- 54 I. Fridovich, *J. Biol. Chem.* 1970, **245**, 4053–4057.
- 55 D. F. Evans, *J. Chem. Soc.* 1959, 2003–2005.
- 56 J. Strozynski, J. Heim, S. Bunbanjerdasuk, N. Wiesmann, J. Zografidou, S. K. Becker, A. M. Meierl, H. Gouveris, H. Lüddens, F. Grus, and J. Brieger, *J. Proteomics* 2015, **113**, 154–161.

- 57 R.W. Cheary and A. Coelho, *J. Appl Crystallogra.* 1992, **25**, 109–121.
- 58 M. F. Zhang, J. -M. Liu, and Z. G. Liu, *Appl. Phys. A* 2004, **79**, 1753–1756.
- 59 E. A. Secco and G. G. Worth, *Can. J. Chem.* 1987, **65**, 2504–2508.
- 60 J. R. Kincaid and K. Nakamoto, *Spectrochim. Acta Part A Mol. Spectrosc.* 1976, **32**, 277–283.
- 61 G. Szalontai, R. Csonka, G. Speier, J. Kaizer, and J. Sabolovic, *Inorg. Chem.* 2015, **54**, 4663–4677.
- 62 E. V. Sturm and H. Cölfen, *Chem. Soc. Rev.* 2016, **45**, 5821–5833.
- 63 L. Bahrig, S. G. Hickey, and A. Eychmuller, *CrystEngComm* 2014, **16**, 9408–942.
- 64 T. Tachikawa and T. Majima, *NPG Asia Mater.* 2014, **6**, e100
- 65 Y. Cheng and W. H. Prusoff, *Biochem. Pharmacol.* 1973, **22**, 3099–3108.
- 66 R. Ragg, F. Natalio, M. N.Tahir, H. Janssen, A. Kashyap, D. Strand, S. Strand, and W. Tremel, *ACS Nano* 2014, **8**, 5182–5189.
- 67 I. H. Segel, *Enzyme Kinetics: Behavior and Analysis of Rapid Equilibrium and Steady-State Enzyme Systems*; Wiley-Interscience, 1993; Vol. **2**.
- 68 H. R. Oswald, A. Reller, H. W. Schmalle, and E. Dubler, *Acta Crystallogr. Sect. C Cryst. Struct. Commun.* 1990, **46**, 2279–2284.
- 69 J. Strozynski, J. Heim, S. Bunbanjerdasuk, N. Wiesmann, J. Zografidou, S. K. Becker, A. M. Meierl, H. Gouveris, H. Lüddens, F. Grus, and J. Brieger, *J. Proteomics* 2015, **113**, 154–161.
- 70 Y. Cudennec and A. Lecerf, *Solid State Sciences*, 2003, **5**, 1471–1474.
- 71 F. K. Küster and A. Thiel, *Rechentafeln für die Chemische Analyse*, de Gruyter, 2002.

72 P. S. Makena, S. C. Pierce, K.-T. Chung, and S. E. Sinclair, *Environ. Mol. Mutagen.* 2009, **50**, 451–459.

### 3.1.7 Supporting Information

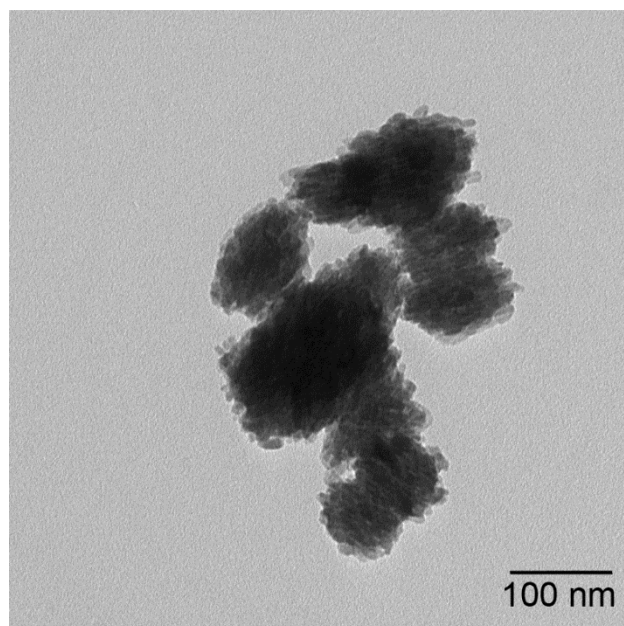


**Fig. S1.** TEM image of  $\text{Cu(OH)}_2$  precipitated from an aqueous solution of copper(II) sulfate, glycine and of sodium hydroxide solution. The synthesis of Gly- $\text{Cu(OH)}_2$  NPs was not successful directly from the components without isolating the *cis*-bis(glycinato) copper(II) monohydrate ( $\text{Cu(Gly)}_2$ ) intermediate. Only an insoluble  $\text{Cu(OH)}_2$  precipitate was formed instead.



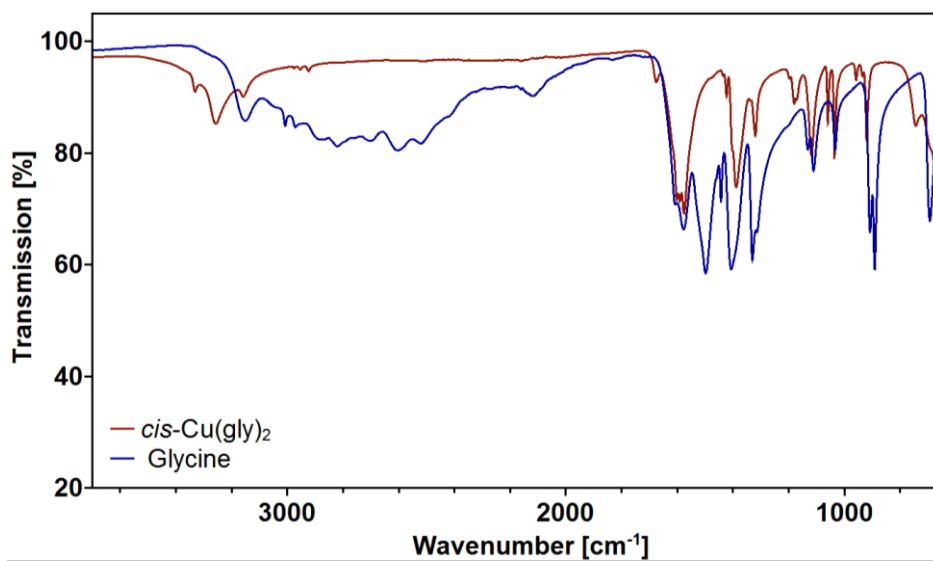


**Fig. S2. IR spectra of *cis*-bis(glycinato) copper(II) monohydrate (red line) and glycine (blue line).** Characteristic bands: NH<sub>2</sub> vibration<sup>1,2</sup> at 3331, 3254 and 3157 cm<sup>-1</sup>; asym. COO stretch at 1603 cm<sup>-1</sup>; sym. COO stretch at 1386 cm<sup>-1,1,2</sup>

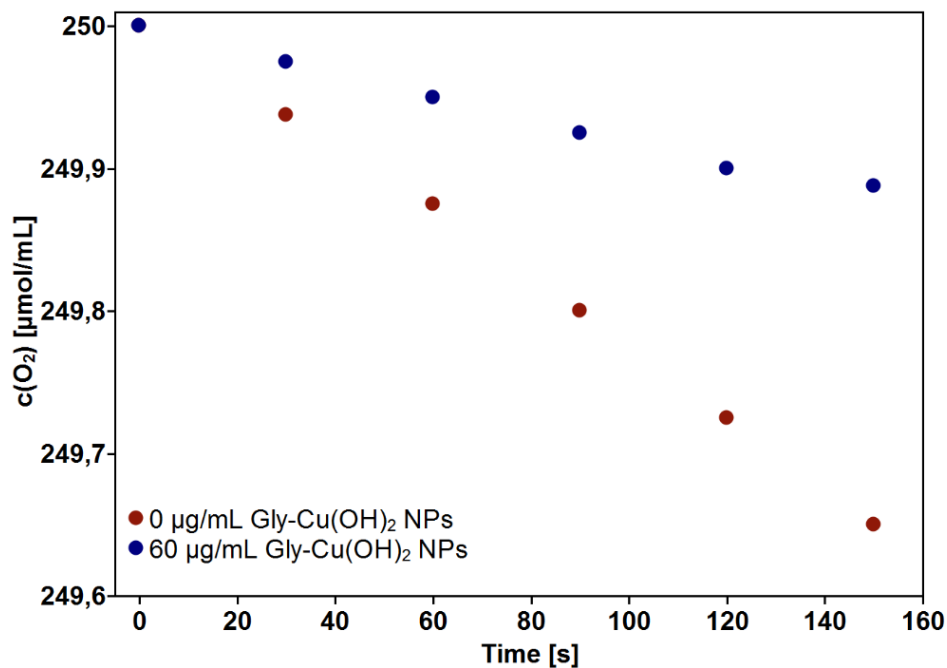


**Fig. S3. Oxygen evolution of Gly-Cu(OH)<sub>2</sub> NPs when exposed to superoxide radicals generated by xanthine/xanthine oxidase (XO).** Molecular oxygen (O<sub>2</sub>) is depleted by the enzymatic activity of XO (red) forming superoxide radicals. In general superoxide dismutation by SOD-active materials leads to the formation of hydrogen peroxide and oxygen (50% each). Gly-Cu(OH)<sub>2</sub> NPs reduce the oxygen depletion to approx. 50% (blue), which is equivalent to the formation of an equivalent amount of O<sub>2</sub>.

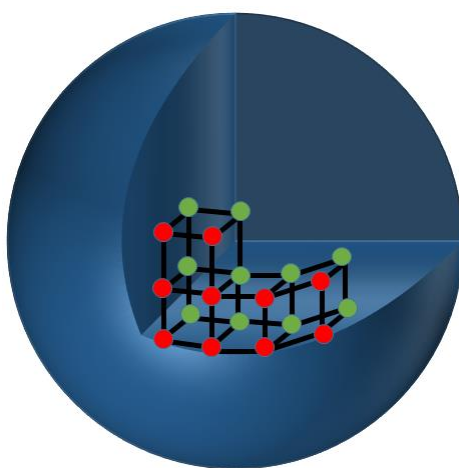


**Fig. S4. Schematic representation of a spherical Cu(OH)<sub>2</sub> NP showing the catalytically active Cu atoms at the NP surface (red) and inactive atoms inside the NP volume (green).** To simplify the representation a simple cubic unit cell instead of the orthorhombic lepidocrocite structure of Cu(OH)<sub>2</sub> is shown.

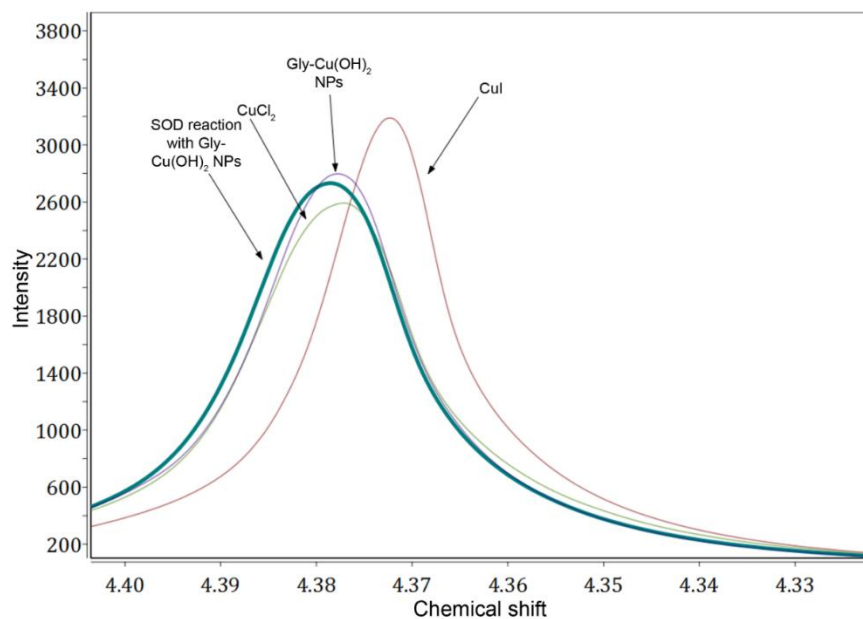


**Fig. S5.** NMR spectra of the SOD-like reaction catalyzed by Gly-Cu(OH)<sub>2</sub> NPs recorded with the Evans method.<sup>3</sup> The <sup>1</sup>H-NMR signal of an aqueous solution of paramagnetic copper(II) compounds (Gly-Cu(OH)<sub>2</sub> NPs and CuCl<sub>2</sub>) shows a broadened and downfield shifted H<sub>2</sub>O resonance with respect to a solution containing diamagnetic CuI. For the water signal after the SOD-like reaction a paramagnetic shift was observed, which can be explained with the shuttling of copper between the oxidation states +II and +I during the reaction and the recovery of the catalyst.

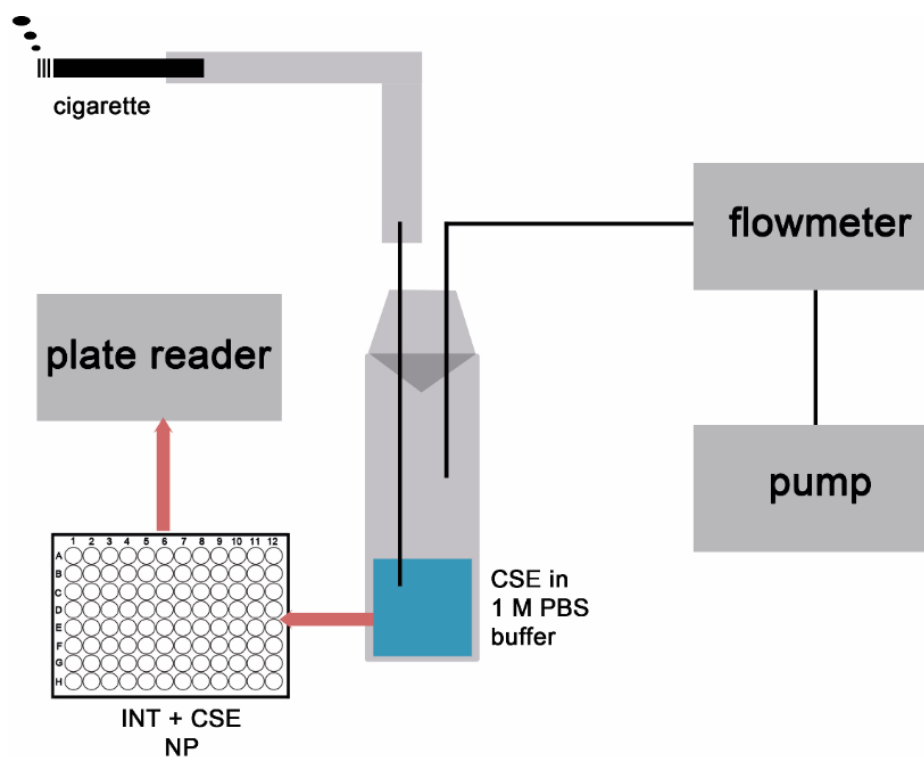


**Fig. S6. Setup for cigarette smoke experiments.** A cigarette smoke extract (CSE) was produced using a commercial Magnum cigarette. A constant maelstrom ( $0.3-0.5 \text{ L}\cdot\text{min}^{-1}$ ) was ensured with a vacuum pump and a flowmeter. The CSE extract was analyzed with INT as superoxide sensitive dye and different amounts of Gly-Cu(OH)<sub>2</sub> NPs on a 96-well-plate reader.

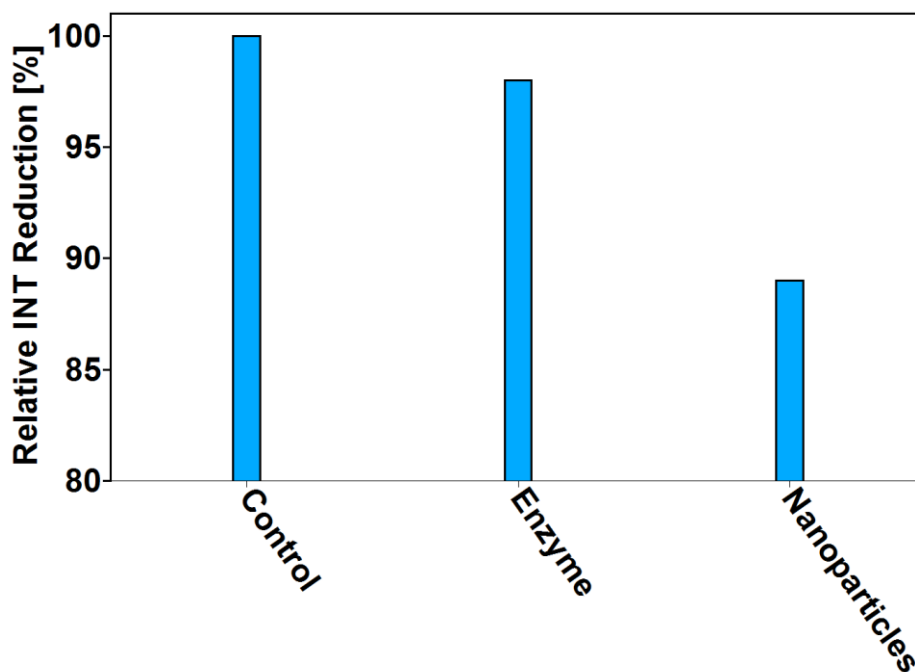


Fig. S7. Inhibition of INT reduction by Gly-Cu(OH)<sub>2</sub> NPs and CuZn SOD shows a higher efficiency of reducing superoxide level of the Gly-Cu(OH)<sub>2</sub> NPs.

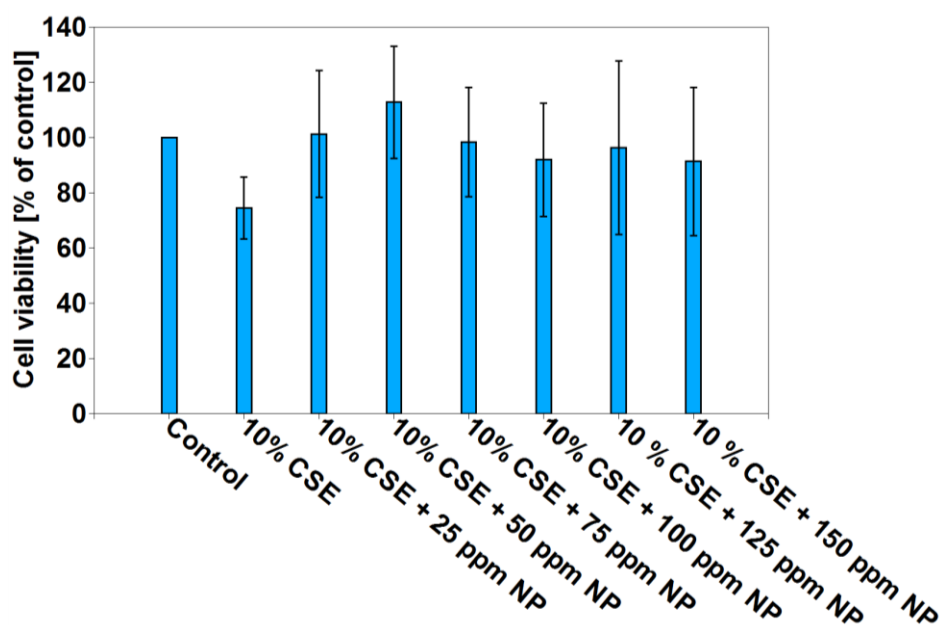


Fig. S8. Cytotoxicity of cigarette smoke extract (CSE) for A549 cells. The cytotoxicity was determined with an AlamarBlue<sup>®</sup> assay after reacting the cells with CSE that were treated before with different amounts of Gly-Cu(OH)<sub>2</sub> NPs.<sup>4</sup> A 10% CSE showed toxic behavior. Treating the CSE with Gly-Cu(OH)<sub>2</sub> NPs reduced the cytotoxicity.

**Tab. S1. Details of the X-ray powder diffraction measurement and the refinement of the x-ray diffraction data.**

	<b>Gly-Cu(OH)<sub>2</sub> NPs</b>
Diffractometer	Siemens D5000
Sample preparation	Powder between two Scotch ® Magic tape stripe
Measuring mode	Transmission
Wavelength	CuK $\alpha_1$ , 1.540596 Å
Measuring range	$10 \leq 2\Theta /^\circ \leq 90$ , $\Delta 2\Theta /^\circ = 0.0078$ ; $0.72 \leq Q/\text{Å}^{-1} \leq 5.76$  2s /step, sum of 2 individual scans
Temperature / K	298
Profile fit	Rietveld refinement according to reported crystal structure models
Background / Parameters	Chebyshev / 16
Profile function	Fundamental Parameters Approach / correction for anisotropic crystallite size
Program	TOPAS Academic V5.0
No. of variables	25
R <sub>exp</sub>	1.70
R <sub>wp</sub>	1.31
GoF	1.45

### 3. Results and Discussion

---

	<b>Gly-Cu(OH)<sub>2</sub> NPs</b>
Durban-Watson statistic	0.96
Cu(OH) <sub>2</sub>	
Space group	<i>Cmc2<sub>1</sub></i>
Cell parameters /Å	$a = 2.9474(7)$ $b = 10.630(5)$ $c = 5.305(2)$
Crystallite size /nm	13.4(4) by 5.4(1) by 6.6(1)
Fraction /% wt	100
B <sub>iso</sub>	1.0(1)

### 3. Results and Discussion

**Tab. S2. Catalytic activities of Gly-Cu(OH)<sub>2</sub> NPs, bulk Cu(OH)<sub>2</sub> and natural CuZn SOD with respect to molar concentration and *per* active site.**

Sample	Concentration to receive a 50% inhibition of the INT reduction [μg·mL <sup>-1</sup> ]	IC <sub>50</sub> for molar NP concentrations [μM]	IC <sub>50</sub> <i>per</i> active site [μM]	k for molar NP concentrations [M <sup>-1</sup> s <sup>-1</sup> ]	k <i>per</i> active site [M <sup>-1</sup> s <sup>-1</sup> ]
Gly-Cu(OH) <sub>2</sub> NPs	0.101 ± 2.0·10 <sup>-3</sup>	2.25·10 <sup>-14</sup>	5.02·10 <sup>-10</sup>	8.72·10 <sup>14</sup>	3.91·10 <sup>10</sup>
CuZn SOD	0.231 ± 2.1·10 <sup>-2</sup>	9.82·10 <sup>-3</sup>	9.82·10 <sup>-3</sup>	1.98·10 <sup>9</sup>	1.98·10 <sup>9</sup>
bulk Cu(OH) <sub>2</sub>	0.384 ± 2.6·10 <sup>-2</sup>	----	----	----	----

**Tab. S3. Change of absorbance at 290 nm** due to the formation of uric acid in presence (three different concentrations) and in absence (control) of Gly-Cu(OH)<sub>2</sub> NPs. Gly-Cu(OH)<sub>2</sub> NPs do not inhibit radical formation in the xanthine/XO system. The effect of Gly-Cu(OH)<sub>2</sub> NPs on superoxide generation with a xanthine/xanthine oxidase (XO)-system was investigated by observing the change of absorbance at 290 nm, based on the formation of uric acid as one of the reaction products. The change of absorbance was detected over a period of one minute.

V(NP) [μL] of a 0.1 mg·mL <sup>-1</sup> stock solution	Change of absorbance at 290 nm [ΔAbs/s]	Error [Δ(ΔAbs/s)]
0	2.19·10 <sup>-3</sup>	4.49·10 <sup>-5</sup>
1	2.09·10 <sup>-3</sup>	1.11·10 <sup>-4</sup>
5	1.96·10 <sup>-3</sup>	1.78·10 <sup>-5</sup>
10	2.08·10 <sup>-3</sup>	7.12·10 <sup>-5</sup>



#### Rate constant of the INT reduction by superoxide

The rate constant for the reduction of INT by superoxide radicals was calculated as outlined below. The decomposition rate (R) of superoxide due to the reaction with SOD or INT can be described as a function of the rate constant (k) and the concentrations of superoxide and INT/SOD.<sup>5</sup>

$$R_{\text{INT}} = k_{\text{INT}} \cdot [\cdot \text{O}_2^-] \cdot [\text{INT}] \quad (1.1)$$

$$R_{\text{SOD}} = k_{\text{SOD}} \cdot [\cdot \text{O}_2^-] \cdot [\text{SOD}] \quad (1.2)$$

If the reduction of INT is inhibited for 50% both rates of the superoxide dismutation are equal.

$$k_{\text{SOD}} \cdot [\cdot \text{O}_2^-] \cdot [\text{SOD}] = k_{\text{INT}} \cdot [\cdot \text{O}_2^-] \cdot [\text{INT}] \quad (1.3)$$

(1.3) leads to

$$k_{\text{INT}} = k_{\text{SOD}} \cdot \frac{[\text{SOD}]}{[\text{INT}]} \quad (1.4)$$

with  $k_{\text{SOD}} = 2 \cdot 10^9 \text{ M}^{-1}\text{s}^{-1}$ .<sup>5</sup> The resulting rate constant of the INT reduction by superoxide is:

$$k_{\text{INT}} = 3.94 \cdot 10^4 \text{ M}^{-1}\text{s}^{-1} \quad (1.5)$$

#### Calculation of SOD activities

The calculation of catalytic activities of nanoparticle samples were done in two different ways. While it is widespread to calculate catalytic activities of NPs normalized to a single nanoparticle, we eventually determined the activity *per* active site.

#### Calculation of IC<sub>50</sub> value for molar nanoparticle concentrations

IC<sub>50</sub> values for molar NP concentrations were obtained as outlined below. The number of NPs *per* liter was confirmed using average particle dimensions deduced from TEM and the density of Cu(OH)<sub>2</sub>. A normalization with the Avogadro constant leads to molar NP concentrations. We approximated the NP morphologies as ideal spheres.

The concentration to achieve a 50% inhibition of the INT reduction was  $8.48 \cdot 10^{-5} \text{ g} \cdot \text{L}^{-1}$ .

The dimensions of the NPs were obtained from TEM ( $d = 152.6 \text{ nm}$ ) and the density of copper(II) hydroxide was used ( $\rho_{\text{Cu(OH)}_2} = 3.368 \text{ g} \cdot \text{cm}^{-3}$ ).

Volume *per* particle ( $V_{\text{NP}}$ ):

$$V_{\text{NP}} = 1.86 \cdot 10^{-15} \text{ cm}^3 \quad (1.6)$$

Mass *per* nanoparticle ( $m_{\text{NP}}$ ):

$$m_{\text{NP}} = \rho_{\text{Cu(OH)}_2} \cdot V_{\text{NP}} = 6.27 \cdot 10^{-15} \text{ g} = 6.27 \cdot 10^{-9} \mu\text{g} \quad (1.7)$$

With the measured amount of Gly-Cu(OH)<sub>2</sub>-NPs to achieve a 50% inhibition of the INT reduction and the amount of copper hydroxide (84%) determined by AAS, an IC<sub>50</sub> concentration of  $\text{IC}_{50} = 8.48 \cdot 10^{-5} \text{ g} \cdot \text{L}^{-1}$  was calculated. The molar nanoparticle concentration was determined with Avogadro's constant.

$$(\text{NPs} \cdot \text{L}^{-1}) = \text{IC}_{50} \cdot m_{\text{NP}}^{-1} = 1.35 \cdot 10^{10} \text{ L}^{-1} \quad (1.8)$$

$$c_{\text{NP}} = (\text{NP} \cdot \text{L}^{-1}) \cdot N_{\text{A}}^{-1} = 2.25 \cdot 10^{-14} \mu\text{M} \quad (1.9)$$

#### Calculation of SOD activity per active site

The catalytic activity of Gly-Cu(OH)<sub>2</sub>-NPs was calculated normalized to an active surface site. For nanomaterials, as only surface atoms (Figure S4, red) are involved in catalytic reactions, while Cu atoms in the bulk (Figure S4, green) are not accessible to surface reactions and therefore inactive.

Figure S4 illustrates the approach to estimate the number of catalytically active surface atoms with respect to the number of bulk atoms per nanoparticle from the particle volume and the bulk analytical composition.

With the average NP diameter ( $d = 152.6$  nm) the average surface area ( $SA_{NP}$ ) and the average volume ( $V_{NP}$ ) of a single NP were determined. For simplicity, the NPs were approximated as ideal spheres.

$$\text{Surface area: } SA_{NP} = \pi d^2 = 7.32 \cdot 10^4 \text{ nm}^2 \quad (1.10)$$

$$\text{Volume: } V_{NP} = (1/6) \pi d^3 = 1.86 \cdot 10^6 \text{ nm}^3 \quad (1.11)$$

The number of active sites *per* NP was estimated based on the Cu(OH)<sub>2</sub> crystal structure (lepidocrocite type) assuming that the particles are terminated by the [310] surface. The unit cell parameters are  $a = 0.0294741$  nm;  $b = 0.10593$  nm;  $c = 0.052564$  nm (determined by P-XRD, Table S1).

The surface area of the terminating [310] layer was determined from the unit cell parameters.

Surface area of terminating surface:

$$SA_{[310]} = 5.59 \cdot 10^{-3} \text{ nm}^2 \quad (1.12)$$

$$\text{Volume unit cell: } V_{UC} = a \cdot b \cdot c = 1.64 \cdot 10^{-4} \text{ nm}^3 \quad (1.13)$$

The unit cell contains four Cu atoms in total, two Cu atoms are situated at the [310] surface layer. The number of [310] layers at the NP surface is given as quotient of the surface area (SA) of a NP and the surface area of the terminating layer:

$$N_{[310]} = SA_{NP} / SA_{[310]} = 1.31 \cdot 10^7 \quad (1.14)$$

The number of catalytic active Cu atoms per unit cell is equal to the number of Cu atoms on the [310] layer:

$$N_{\text{catalytic active Cu atoms}} = N_{\text{Atoms at [310]}} \cdot N_{[310]} = 2.62 \cdot 10^7 \quad (1.15)$$

In an analogue way the amount of unit cells *per* nanoparticle ( $N_{UC/NP}$ ) was determined as quotient of the nanoparticle volume and the unit cell volume:

$$N_{UC/NP} = V_{NP} \cdot V_{UC}^{-1} = 1.13 \cdot 10^{10} \quad (1.16)$$

The number of Cu atoms *per* nanoparticle ( $N_{Cu/NP}$ ) is obtained by multiplication with the number of Cu atoms *per* unit cell (4):

$$N_{Cu/NP} = N_{Cu/UC} \cdot N_{UC} = 4.53 \cdot 10^{10} \quad (1.17)$$

The ratio of (catalytically active) Cu surface and (inactive) bulk atoms were used to calculate the total concentration of active Cu(II) sites from the total Cu concentration (determined by AAS).

$$P = (N_{\text{catalytic active Cu atoms}}) \cdot (N_{Cu/NP})^{-1} = 5.78 \cdot 10^{-4} \quad (1.18)$$

#### **Rate constants of the SOD reaction catalyzed by Gly-Cu(OH)<sub>2</sub> NPs**

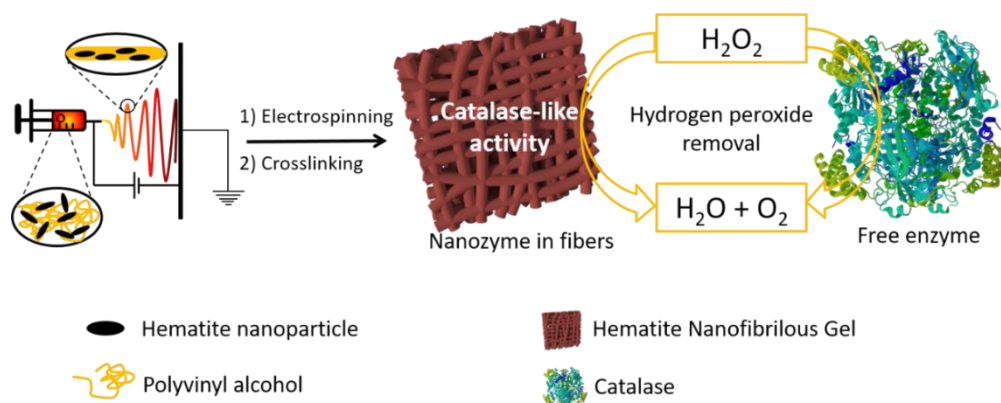
Rate constants were determined using equation (1.19) and  $k_{INT} = 3.94 \cdot 10^4 \text{ M}^{-1}\text{s}^{-1}$  (1.5).

$$k_{Cu(OH)_2} = k_{INT} \cdot \frac{[INT]}{[Cu(OH)_2]} \quad (1.19)$$

#### References

1. Sen, D. N.; Mizushima, S.-I.; Curran, C.; Quagliano, J. V. *J. Am. Chem. Soc.* 1955, **77**, 211–212.
2. O'Brien, P. *J. Chem. Educ.* 1982, **59**, 1052–1053.
3. Evans, D. F. *J. Chem. Soc.* 1959, 2003–2005.
4. J. Strozynski, J. Heim, S. Bunbanjerdsuk, N. Wiesmann, J. Zografidou, S. K. Becker, A. M. Meierl, H. Gouveris, H. Lüddens, F. Grus, J. Brieger, *J. Proteomics* 2015, **113**, 154–161.
5. McCord, J. M. *Curr. Protoc. Toxicol.* 2001, Chapter 7, Unit 7.3.

## 3.2 Fibrous Nanozyme Dressings with Catalase-like Activity for H<sub>2</sub>O<sub>2</sub> Reduction to Promote Wound Healing



The following chapter describes the production of a hematin NP containing polyvinyl alcohol (PVA) fiber mesh, which could reduce H<sub>2</sub>O<sub>2</sub>, similar to the native catalase enzyme. This effect was further investigated in an *in vitro* study, where fibroblasts were protected against cell death triggered by elevated H<sub>2</sub>O<sub>2</sub> levels. The cover picture was designed during the project in cooperation with all authors.

The chapter is an adapted reproduction of the manuscript published in *ACS Appl. Mater. Interfaces* **2017**, 9, 38024–38031, which is reproduced with permission of the American Chemical Society. Detailed authorship contributions are attached in the Appendix (chapter 5.3.3).

A great thank goes to Dr. S. Hobe, B. Niethard and Prof. Dr. H. Paulsen for providing an oxygen sensitive electrode, Dr. V. Mailänder, Dr. C. Campanhac and J. Pereira for the support with cell experiments and data analysis, Dr. M. Panhöfer and R. Jung-Pothmann for XRD analysis, Dr. S. Wooh and Y. Yao for the water contact angle measurements, E. Muth for FTIR, G. Glasser for SEM imaging and S. Schuhmacher for support by illustrations.

### 3.2.1 Abstract

The concentrations of the redox-pair hydrogen peroxide ( $\text{H}_2\text{O}_2$ ) and oxygen ( $\text{O}_2$ ) can promote or decelerate the progression and duration of the wound healing process. While  $\text{H}_2\text{O}_2$  can reach critically high concentrations and prohibit healing, a sufficient  $\text{O}_2$  inflow to the wound is commonly desired. Herein, we describe the fabrication and use of a membrane that can contemptuously decrease  $\text{H}_2\text{O}_2$  and increase  $\text{O}_2$  levels. Therefore, hematite nanozyme particles were integrated into electrospun and cross-linked poly(vinyl alcohol) membranes. Within the dual-compound membrane, the polymeric mesh provides a porous scaffold with high water permeability and the nanozymes acts as a catalyst with catalase-like activity that can efficiently convert  $\text{H}_2\text{O}_2$  into  $\text{O}_2$  as shown by a catalase assay. When comparing the growth of fibroblasts at an  $\text{H}_2\text{O}_2$  concentration of 50  $\mu\text{M}$ , the growth was largely enhanced when applying the nanozyme dressing. Thus, application of the nanozyme dressing can significantly reduce the harmful effect of higher  $\text{H}_2\text{O}_2$  concentrations. The described catalytic membranes could be used in the future to provide an improved environment for cell proliferation in wounds and thus applied as advanced wound healing dressings.

### 3.2.2 Introduction

Wound dressings can accelerate and improve the wound healing process.<sup>1</sup> They provide an environment that allows oxygen permeation, maintains moisture for materials diffusion, prevents infection, and promotes tissue formation.<sup>2</sup> Two important key metabolites involved in the healing process are the redox-pair hydrogen peroxide ( $\text{H}_2\text{O}_2$ ) and oxygen ( $\text{O}_2$ ). While a high concentration of  $\text{H}_2\text{O}_2$  causes a delayed healing *via* preventing the connective tissue formation,<sup>3</sup>  $\text{O}_2$  can help to improve the healing efficiency.<sup>4</sup> Therefore, the wound healing process can be promoted by down-regulating  $\text{H}_2\text{O}_2$  levels and increasing  $\text{O}_2$  levels.<sup>5</sup> A contemptuous adjustment of  $\text{H}_2\text{O}_2$  and  $\text{O}_2$  concentrations can be achieved by catalytic conversion of  $\text{H}_2\text{O}_2$  into  $\text{H}_2\text{O}$  and  $\text{O}_2$  through enzymatic catalysis with catalase, a naturally occurring enzyme.

The production of catalase can be achieved by direct synthesis or extraction from natural systems.<sup>6</sup> Such a production process is however accompanied with high production costs and the natural enzyme is highly sensitive to changes in environmental conditions and possesses a short biological half-life.<sup>7</sup> Hence, recent research has focused on the replacement of natural enzymes by synthesizing artificial compounds, so called enzyme mimics, which can imitate the catalytic behavior of natural enzymes.<sup>8,9</sup> To the present day various enzyme-mimics have been reported such as metal complexes,<sup>10,11</sup> supramolecular chemistry<sup>12</sup> and inorganic nanoparticles (NPs).<sup>13,14</sup> The use of inorganic NPs as enzyme mimics comprises the advantages of cost efficiency and much higher stability than their natural counterparts while possessing comparable sizes.<sup>6,7,15</sup> In addition, the so called nanozymes exhibit a high number of catalytically active surface atoms, enabling high activities. It is thus not surprising that they can react more efficient than natural enzymes, which commonly feature only one active center.<sup>6,16,17</sup>

Recently, different classes of nanozymes have been reported to reduce the concentration of H<sub>2</sub>O<sub>2</sub>.<sup>18</sup> Among them, hematite NPs show a catalase-like activity and have been used to convert H<sub>2</sub>O<sub>2</sub> to H<sub>2</sub>O.<sup>19,20</sup> Hematite ( $\alpha$ -Fe<sub>2</sub>O<sub>3</sub>) is a weakly magnetic and highly stable iron (III) oxide, which is stable with respect to corrosion, non-toxic, and many simple low cost synthetic procedures have been described. Template assisted synthesis<sup>21</sup>, forced hydrolysis<sup>22</sup>, sol-gel methods<sup>23</sup> and hydrothermal routes<sup>24</sup> in aqueous solution even without organic surfactants and in large quantities are viable routes. This makes hematite an excellent material for applications in wound treatment to mimic catalase and reduce H<sub>2</sub>O<sub>2</sub> concentrations.

Integration of iron oxide nanoparticles in nanofibrous membranes can be achieved by either directly assembling the magnetic particles under an external magnetic field<sup>25,26</sup> or electrospinning the particles together with a templating polymer.<sup>27-29</sup> Electrospinning<sup>30-32</sup> or pressurized gyration process<sup>33</sup> can be used to fabricate nanofiber mats for wound dressings. Recently, portable electrospinning devices<sup>34,35</sup> have been used for *in situ* production of wound dressing materials. The high surface-to-volume ratio and porosity of the electrospun membranes exhibit a promising water



absorption ability to meet the requirement of strong oxygen permeation.<sup>36</sup> Additionally, the high surface area membranes are ideal as heterogeneous catalysts.<sup>37,38</sup> However, a catalytically active membrane that can regulate H<sub>2</sub>O<sub>2</sub> and O<sub>2</sub> levels to improve the wound environment could not be achieved to date.

Here, we report an electrospun hybrid nanofibrous material as dressing for wound healing, with a high porosity, wettability and the ability to simultaneously decrease the H<sub>2</sub>O<sub>2</sub> and increase the O<sub>2</sub> concentration. As shown in **Figure 1**, a polyvinyl alcohol (PVA) solution and a suspension of hematite nanoparticles were mixed to electrospin the nanozyme containing nanofibers. PVA was used as the scaffold material and the hematite nanoparticles were implemented as catalytic moieties. After electrospinning and crosslinking, the water-permeable PVA gel possesses a high porosity and good wettability. The encapsulated hematite shows catalase-like activity by reducing the amount of H<sub>2</sub>O<sub>2</sub> and producing O<sub>2</sub>. When incubating fibroblasts at 50 μM H<sub>2</sub>O<sub>2</sub> concentration, the catalytically active membrane efficiently reduces the H<sub>2</sub>O<sub>2</sub> concentration and enables good cell proliferation. Thanks to this catalase-like activity, the hybrid nanofibrous gel can be used for improving the wound healing process.

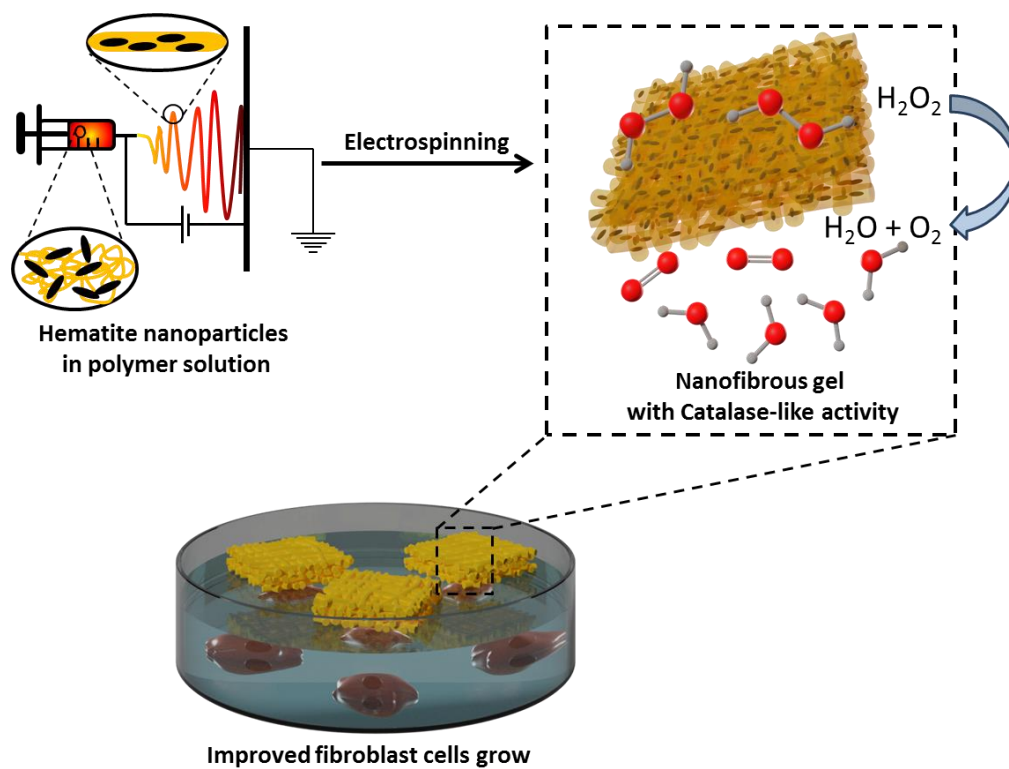


**Figure 1.** Schematic illustration of the fabrication procedure of hematite nanofibrous gels *via* electrospinning and their use as catalase mimics to convert hydrogen peroxide into water and oxygen to yield an improved fibroblast growth.

### 3.2.3 Experimental

#### Chemicals

FeCl<sub>3</sub>·6H<sub>2</sub>O and tetrahydrofuran (THF) were purchased from Acros Organics (Fisher Scientific), KH<sub>2</sub>PO<sub>4</sub> was purchased from Sigma Aldrich (Germany). Polyvinyl alcohol (PVA, Polysciences Inc.,  $M_w = 125000 \text{ g}\cdot\text{mol}^{-1}$ ), glutaraldehyde (GA, Merck KGaA, 50% aqueous solution), and hydrochloric acid (HCl, Sigma-Aldrich, 37 wt.%, AR grade) were used for electrospinning and crosslinking.

**Nanoparticle synthesis.** 20 mmol FeCl<sub>3</sub> and 0.4 mmol KH<sub>2</sub>PO<sub>4</sub> were added to 1 L of water (MilliQ) to form a clear yellowish solution that was magnetically stirred and heated under reflux for 72 h. The resulting brown, turbid dispersion was then filtered through a 3.1 μm syringe filter (CME, Roth Germany). Portions of 20 mL were precipitated using THF (volume ratio 1:2) and collected by centrifugation. The brown powder was dried at 70 °C in air.

Solutions for electrospinning experiments of 5 wt.%, 15 wt.% and 25 wt.% were prepared by dispersing hematite nanopowder in water (MilliQ) by sonicated for 20 min.

**Electrospinning and cross-linking.** The different concentrations of hematite nanoparticle dispersions (5 wt.%, 15 wt.% and 25 wt.%) were combined with the 15 wt.% PVA solution at a ratio of 1:2 for a total polymer concentration of 10 wt.% and mixed by mechanical stirring through vortex until a homogenous dispersion was obtained. The resulting dispersion was filled into a 1 mL syringe and electrospun at 20-25% relative humidity and room temperature onto an aluminum foil support (20 cm distance, 0.3 mL·h<sup>-1</sup> feed rate, 0.8 mm tip diameter, +18 and 0 kV). During the electrospinning, a TEM grid was used to collect samples for TEM measurement. Afterward, the electrospun mats were reacted with 1 mL of 50 wt.% glutaraldehyde (GA) and 20 μL of 37 wt.% HCl in a vacuum oven. The acetal bridges can be formed between aldehyde groups of GA and the hydroxyl groups of PVA. HCl was the catalyst for this crosslinking reaction. Afterwards, the crosslinked nanofibrous mats were put in the fume hood for 24 h to evaporate the unreacted GA and HCl.

**Wettability and water stability of cross-linked electrospun mats.** The wettability of the PVA mats was measured on a static contact angle measuring system equipped with a side camera (IDS uEye camera) and a goniometer. To test the water stability of the PVA mats, the mats were immersed into water for 1 h and transferred into the fume hood to evaporate excess water overnight. The morphology of the PVA mats before and after water immersion were observed by scanning electron microscopy (SEM; Hitachi SU8000, Japan).

**Tests for catalytic activity.** To measure catalytic activities europium(III) chloride hexahydrate and 3-(*N*-morpholino)propanesulfonic acid (MOPS) sodium salt (98%) from Alfa Aesar, tetracycline hydrochloride, catalase enzyme (3000-5000 U·mg<sup>-1</sup>) and hydrogen peroxide (H<sub>2</sub>O<sub>2</sub>) from Sigma-Aldrich were used. All chemicals were used without further purification and reactions were conducted with MilliQ water. The catalase-like activity of the tested materials were investigated similar to the fluorescence assay reported by Wu *et al.*<sup>39</sup> The procedure is briefly described as followed: in a first step, the PVA fibers were washed several times with MilliQ water to remove free NPs that were possibly not completely cocooned in the polymer matrix. The fibers were added into the wells of a 96 well plate, which was placed in a temperature controlled (303 K) 96 well plate reader. In free wells the fluorescently active EuTc-HP complex was generated by mixing 65 μL EuTc solution, 20 μL H<sub>2</sub>O<sub>2</sub> solution (5 mmol·L<sup>-1</sup>) and 165 μL MOPS buffer solution (10 mmol·L<sup>-1</sup>) (details see SI). The mixture was incubated at 303 K for 10 min. To start the reaction, the EuTc-HP solution was added to the fiber containing wells. The reaction process was observed for 10 min based on the decrease of fluorescence intensity. Control measurements were conducted by varying the concentration of native catalase (Detailed description and concentrations of stock solutions see SI).

**Cell-viability experiments.** 50 mg of PVA membranes without hematite nanoparticles and PVA membranes with high loading of hematite nanoparticles were incubated separately with H<sub>2</sub>O<sub>2</sub> at 50 μM for 10 min in the shaking bed. Then, the membranes and H<sub>2</sub>O<sub>2</sub> solutions were mixed with the fibroblast cell line NIH-3T3 for overnight incubation. After 16 h incubation, the cells were washed with phosphate-buffered saline solution and detached from the culture vessel with 2.5% trypsin (Gibco, Germany). Before measuring on the CyFlow ML cytometer (Partec, Germany), the cells were stained with 650 μL of propidium iodide solution (diluted in phosphate-buffered saline solution to a final concentration of 2.0 μg·mL<sup>-1</sup>) to assess the cell viability. To compare the significant difference between different samples, an unpaired student's t-test assuming equal variances was performed. Calculated p values were considered to be significant for \*p < 0.05, \*\*p < 0.01, \*\*\*p < 0.001.

**Characterization. Plate reader.** Plate reader measurements were conducted using an Infinite 200 Pro Plate reader from TECAN. Additionally flat bottom 96 well plates black from Greiner bio-one were used for the catalase assay. The excitation filter was set to 405 nm and the emission filter to 620 nm.

*Electron microscopy (EM).* The morphology of the PVA meshes were observed by transmission electron microscopy (TEM; JEOL JEM1400, Japan) and scanning electron microscopy (SEM; Hitachi SU8000, Japan). The PVA meshes were electrospun on a 400-mesh copper grid and silicon wafer for the TEM and SEM measurement, respectively.

TEM images of the pure NP were taken with a Tecnai G2 Spirit from FEI (Hillsboro, USA) with LaB6 cathode crystal, twin objective and a US 1000 CCD camera from Gatan (Pleasanton, USA). For sample preparation the particles were dispersed in water or ethanol and one drop of the dispersion was dried on a carbon coated copper grit from Science Services. The size of nanofibers was obtained by analyzing SEM images of electrospun samples with IMAGE J software. Each sample was measured 100 times to calculate the average number and standard deviation.

*Fourier-transform infrared spectroscopy (FTIR).* The functional groups of crosslinked PVA meshes were measured by Fourier-transform infrared spectroscopy (FTIR) in the 400 - 4000  $\text{cm}^{-1}$  range. 20 mg of the individual samples were mixed with KBr powder to make a pellet.

*Powder X-ray diffraction (XRD).* The crystal structure and the crystallinity were analyzed on a D8 Advance diffractometer equipped with a Sol-X energy dispersive detector using molybdenum  $K\alpha$ -radiation ( $\lambda = 0.72 \text{ \AA}$ ). The nanoparticle powder was dispersed on a scotch<sup>TM</sup> tape (which causes a broad reflection at low Bragg angles).

*Thermogravimetry (TGA).* Thermogravimetric measurements of the nanoparticles were performed on a Pyris TGA 6 with nitrogen atmosphere in a corundum crucible at a heating rate of 5  $^{\circ}\text{C}\cdot\text{min}^{-1}$  for functionalized particles from 50 to 700  $^{\circ}\text{C}$  after 20 min at 50  $^{\circ}\text{C}$ . At 700  $^{\circ}\text{C}$  the temperature was held for 1 min.

### 3.2.4 Results and discussion

Spindle-shaped nanoparticles were prepared by forced hydrolysis of ferric chloride in water.<sup>22</sup> The solution was refluxed for three days in the presence of catalytic amounts of  $\text{KH}_2\text{PO}_4$ . The resulting particles were not coated with a surfactant layer, and are self-stabilized in water, allowing a direct and unhindered accessibility for substrate molecules to the catalytically active particle surface. High solid contents of the particles in aqueous PVA solution were achieved by centrifugation.

Analysis of the shape and morphology of the iron oxide nanoparticles was performed by transmission electron microscopy (TEM, **Figure 2**). The nanoparticles have an anisotropic shape (**Figure 2 a - b**), and their aspect ratio was determined from the TEM images to be approximately 5:1 (**Figure 2c**). The particles are highly crystalline as seen from the electron diffraction pattern (**Figure 2 d**). Powder XRD analysis revealed the phase of the particles to be pure  $\alpha\text{-Fe}_2\text{O}_3$  (hematite).

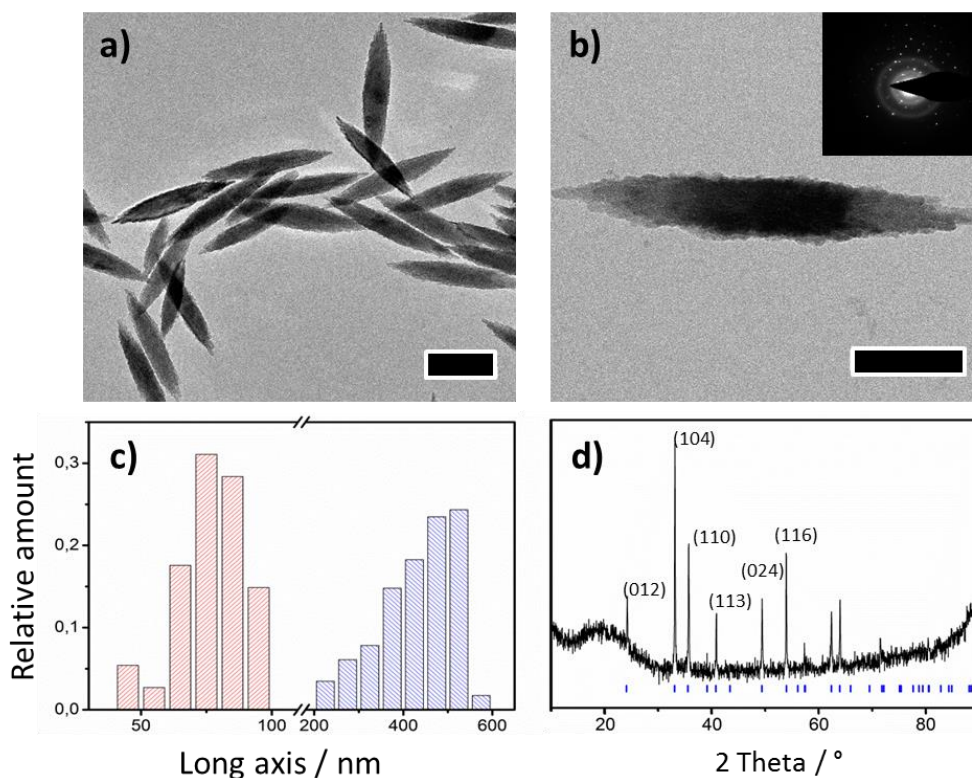


**Figure 2.** TEM pictures of  $\alpha$ - $\text{Fe}_2\text{O}_3$  spindle-shaped particles (scale bar is 200 nm and 100 nm in a) and b), respectively. Size distribution of long and short axis of the particles as determined from TEM images (c). All reflections of the powder XRD pattern can be assigned to hematite (d).

To integrate the hematite nanoparticles in non-woven fabric mats, they were electrospun together with poly(vinyl alcohol) (PVA). Simple mixing of a PVA solution and a hematite suspension and subsequent electrospinning allowed a homogeneous integration of different amounts of hematite in the resulting fibers (**Figure 3a-d**). The hematite nanoparticles were oriented in the fiber axis-direction after the electrospinning process. Without loading the nanoparticles, the size of the fiber is  $299 \pm 34$  nm. When the loading percentage of hematite nanoparticles was increased, the viscosity of the electrospun solution increased as well, which resulted in thicker fibers (the average size of nanofibers is  $305 \pm 33$  nm,  $351 \pm 41$  nm, and  $412 \pm 64$  nm, respectively). After washing away loosely bound nanoparticles and cross-linking, the concentrations of the PVA mats were determined by TGA (**Figure 3e**). With increasing amounts of hematite nanoparticles, the color of the electrospun mats turned from light to darker brown (inset photos in **Figure 3**). To



determine the particle loading inside the cross-linked PVA fibers, the mass loss in TGA heating curves up to 700 °C was used from each sample and normalized between 0 and 100 % for pure PVA and pure nanoparticles, respectively. All samples showed similar behavior when heated under nitrogen. A small weight loss below 250 °C could be observed, which corresponds to the evaporation of water. The major mass loss for all samples was observed between 250 °C and 450 °C, which can be correlated to the decomposition and evaporation of most of the PVA. After that the mass is still constantly decreasing which may be explained by remnants of the decomposition products that evaporate.

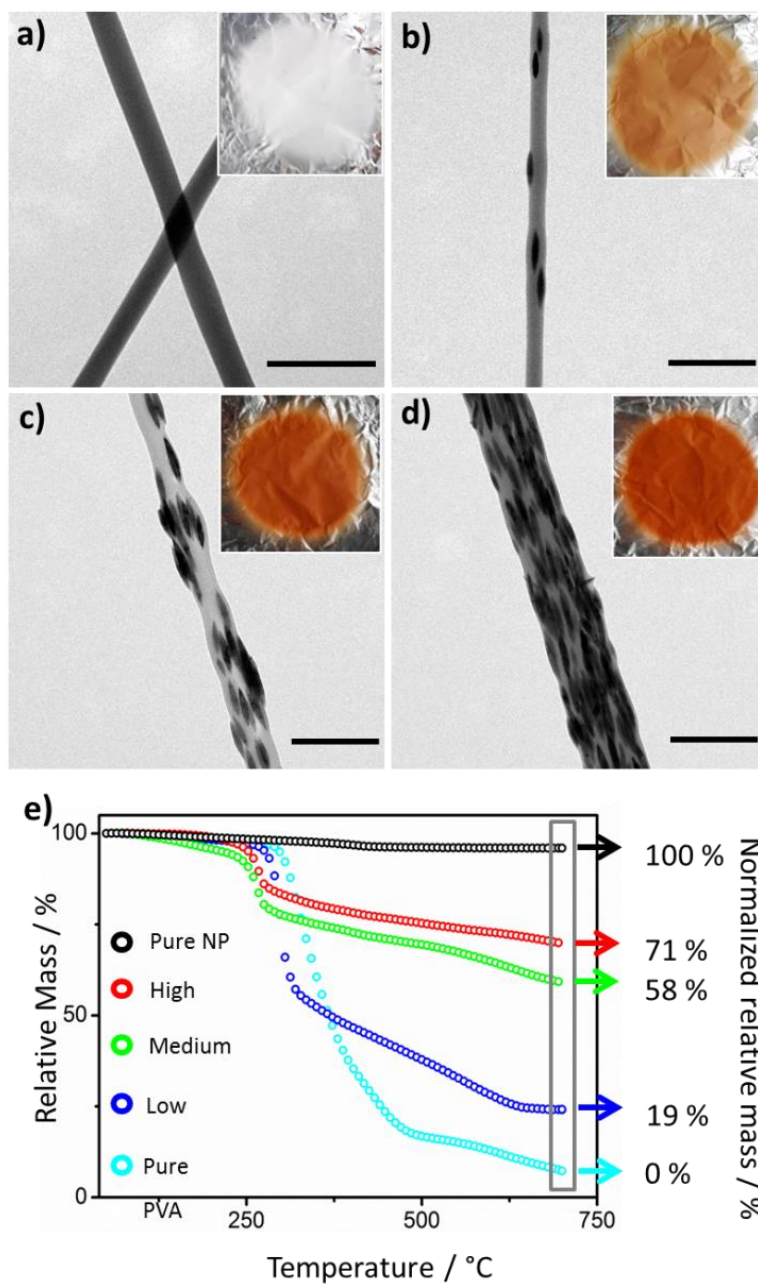


**Figure 3.** Characterization of hematite/PVA nanofibrous mats. TEM images of the PVA nanofibers loaded with 0% (a), 19% (b), 58% (c), 71% (d) of hematite nanoparticles (scale bar = 1  $\mu\text{m}$ ) and the corresponding photographs of the PVA mats (insets). TGA (e) curves of the nanoparticles and the crosslinked PVA mats with different nanoparticle loading.

In order to apply the PVA mats as wound dressings, they were covalently cross-linked after electrospinning to retain the structural integrity of the fibers in aqueous environment. To demonstrate the stability of the cross-linked fibers towards water treatment, scanning electron microscopy (SEM) images of the cross-linked fibers before (**Figure 4a**) and after (**Figure 4b**) water immersion were analyzed. The SEM images showed no change of the fibrous structure after washing, indicating that the PVA scaffold was maintained. The fiber mesh showed a high porosity, which is ideal for wound dressing materials. The permanent entrapment of the hematite particles within the fibers after washing was investigated by FTIR spectroscopy (**Figure 4c**). Therefore, pure hematite nanoparticles, pure PVA fibers and hybrids of both with varying ratios were investigated. The appearance of the characteristic bands for hematite at  $479\text{ cm}^{-1}$  and  $535\text{ cm}^{-1}$  corresponding to the Fe-O vibration<sup>40</sup> in all hematite/PVA fiber samples confirmed the permanent embedment of the particles inside the PVA fibers. The PVA component of the fibers is represented by bands at  $1095\text{ cm}^{-1}$  (C-O-C vibrations of aldehyde crosslinked PVA) as well as at  $1437\text{ cm}^{-1}$  (C-H bending vibration)<sup>41</sup>. Furthermore, the wettability of the cross-linked PVA mats was tested by adding a water droplet on the membrane surfaces. Due to the good wettability of the PVA membrane, the water droplet could spread completely on the PVA mat within 20 s (**Figure 4d** and Figure S2).

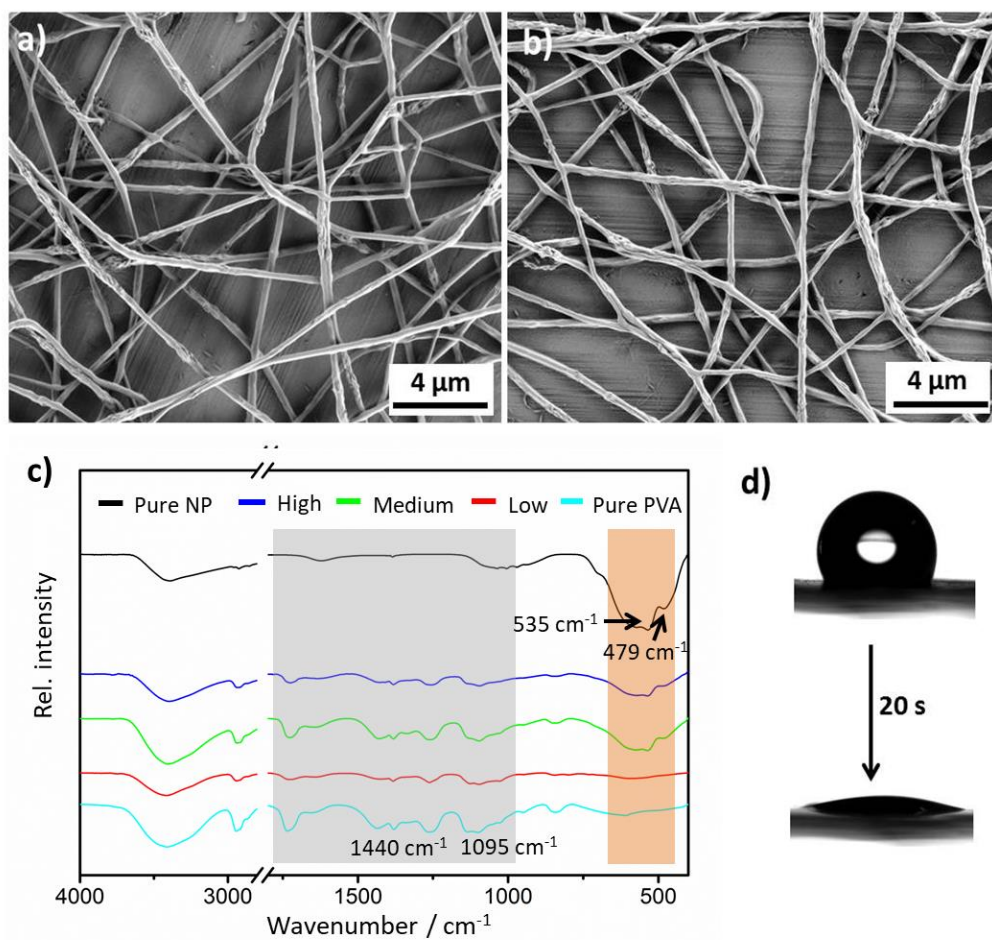
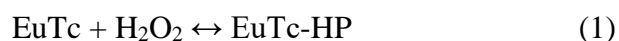


**Figure 4.** Characterization of cross-linked hematite/PVA nanofibrous mats. SEM images of the PVA mat containing 71% of hematite nanoparticles before (a) and after (b) water immersion. FTIR spectra of cross-linked PVA mats containing different amounts of hematite nanoparticles (c). Dynamic wettability of the PVA mat containing 71% of hematite nanoparticles (d).

The enzyme-like activity of hematite PVA fiber meshes was investigated with a europium tetracycline (EuTc) based fluorescence catalase assay.<sup>39</sup> While EuTc alone is not fluorescent, H<sub>2</sub>O<sub>2</sub> binding to the metal center leads to a strong increase of the fluorescence intensity (**Figure 5a**). The fluorescent europium tetracycline hydrogen peroxide complex (EuTc-HP) complex is formed by incubating EuTc and H<sub>2</sub>O<sub>2</sub> for several minutes. A decomposition of H<sub>2</sub>O<sub>2</sub> rapidly shifts the equilibrium between the complexes EuTc-HP and EuTc (equation 1). Thus, it is possible to directly monitor the reduction of the H<sub>2</sub>O<sub>2</sub> level based on the change of the fluorescence intensity.<sup>39</sup>



To investigate a catalase-like activity of the hematite fiber meshes, they were placed in a 96 well plate and treated with an EuTc-HP solution in 3-(*N*-morpholino) propanesulfonic acid (MOPS) buffer. The change of the fluorescence intensity at 620 nm (with  $\lambda_{\text{ex}} = 405$  nm) was monitored over a period of 10 min. Control measurements were conducted using the hematite NPs and the native catalase enzyme. Comparison of the fluorescence spectra of EuTc and EuTc-HP demonstrate the effect of H<sub>2</sub>O<sub>2</sub> binding to the EuTc complex (**Figure 5a**). In the presence of native catalase the present H<sub>2</sub>O<sub>2</sub> was decomposed, which resulted in the expected decrease of fluorescence intensity (**Figure 5b**). A similar behavior could be observed for hematite NPs. Variation of the particle concentration led to a decrease of the fluorescence intensity (**Figure 5c**). Based on the determined catalase-like activity of the hematite NPs the catalytic activity of hematite PVA fiber meshes was investigated. While pure PVA fibers without NPs exhibited no significant effect, the iron oxide loaded fibers showed lower H<sub>2</sub>O<sub>2</sub> levels with increasing hematite loading, demonstrating the use of the nanozyme-in-fiber meshes as catalase mimics for the degradation of H<sub>2</sub>O<sub>2</sub> (**Figure 5d**).

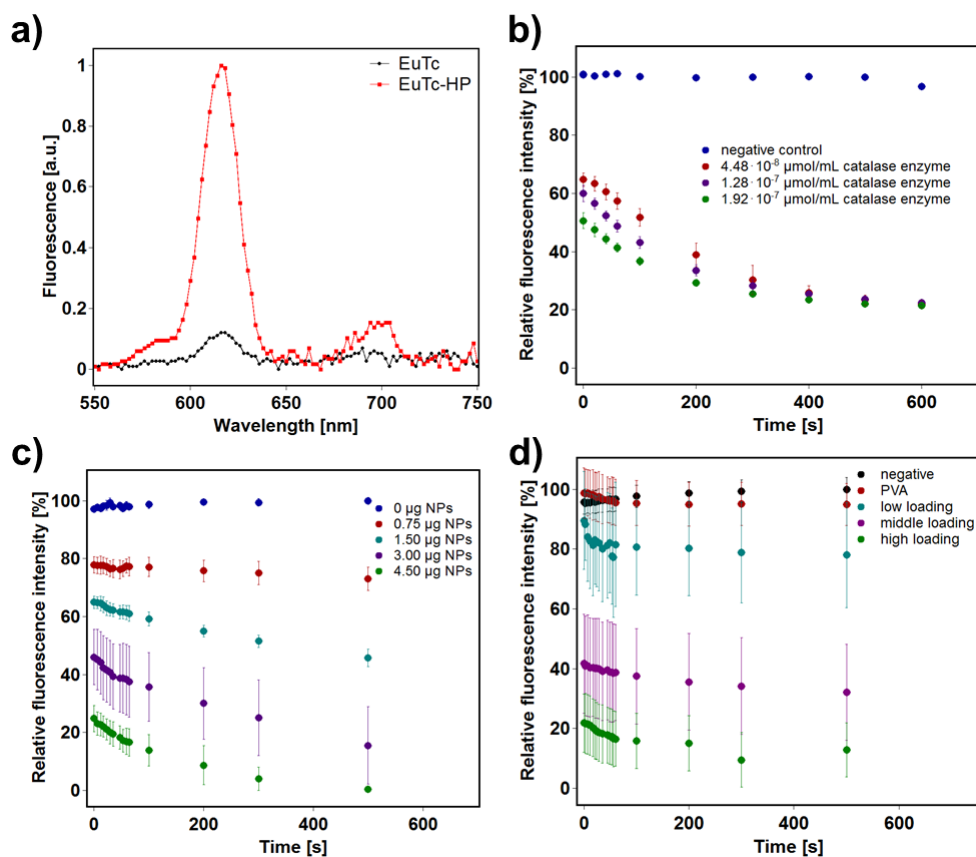


**Figure 5.** Decomposition of  $\text{H}_2\text{O}_2$  catalyzed by native catalase (b), hematite NPs (c) and hematite loaded PVA fiber meshes (d), observed with the fluorescence signal at 605 nm of EuTc-HP. Fluorescence spectra of EuTc and EuTc-HP recorded with  $\lambda_{\text{ex}} = 405$  nm (a). While EuTc shows no fluorescence, the binding of  $\text{H}_2\text{O}_2$  to the metal center increases the fluorescence at  $\lambda_{\text{em}} = 620$  nm. Native catalase (b), hematite nanozyme particles (c) and hematite loaded PVA fiber meshes (d) reduce the  $\text{H}_2\text{O}_2$  level, which leads to the decomposition of EuTc-HP and a subsequent decrease of the fluorescence signal at  $\lambda_{\text{em}} = 620$  nm.

To illustrate the concentration dependency of the catalytic activity, the resulting fluorescence intensity after 5 min was plotted against the concentration of the native enzyme (SI, Figure S4). The iron oxide NPs and the loaded fiber meshes showed a similar concentration dependency of their catalytic activity (**Figure 6a-b**). In all cases, an increasing amount of catalyst leads to a higher decomposition of  $\text{H}_2\text{O}_2$ . With the highest hematite loading of the hematite PVA fiber meshes, a reduction of the fluorescence intensity down to 9.5% - related to 100% control - was achieved. To investigate the reaction mechanism of  $\text{H}_2\text{O}_2$  degradation catalyzed by hematite PVA

fiber meshes, the formation of elemental oxygen, as one of the key reaction products in a catalase-like reaction, was investigated with an oxygen sensitive electrode (**Figure 6c**). While control measurements conducted with pure PVA fibers and without any catalyst show no significant change of the oxygen concentration, the presence of hematite PVA fibers lead to an increase of elemental oxygen, demonstrating the catalase-like reaction process. With increasing hematite loading, higher formation rates of oxygen were observed, which is in agreement with the determined catalytic activities. Further, the influence of the nanozyme membranes on the fibroblast cell growth was investigated. Therefore, the cells were incubated in a medium containing 50  $\mu\text{M}$  of  $\text{H}_2\text{O}_2$  and together with and without the nanozyme membrane. When no nanozyme membrane was applied, all cells died after overnight culturing, indicating that such a concentration of  $\text{H}_2\text{O}_2$  causes apoptosis of fibroblast cells. However, more than 90% of the cells survived when the PVA fibers with hematite nanoparticles were cultured together with  $\text{H}_2\text{O}_2$  in cell media. Thus, the hematite PVA fibers were able to regulate the  $\text{H}_2\text{O}_2$  concentration to a less non-toxic level for fibroblast cells (**Figure 6d**).

### 3. Results and Discussion

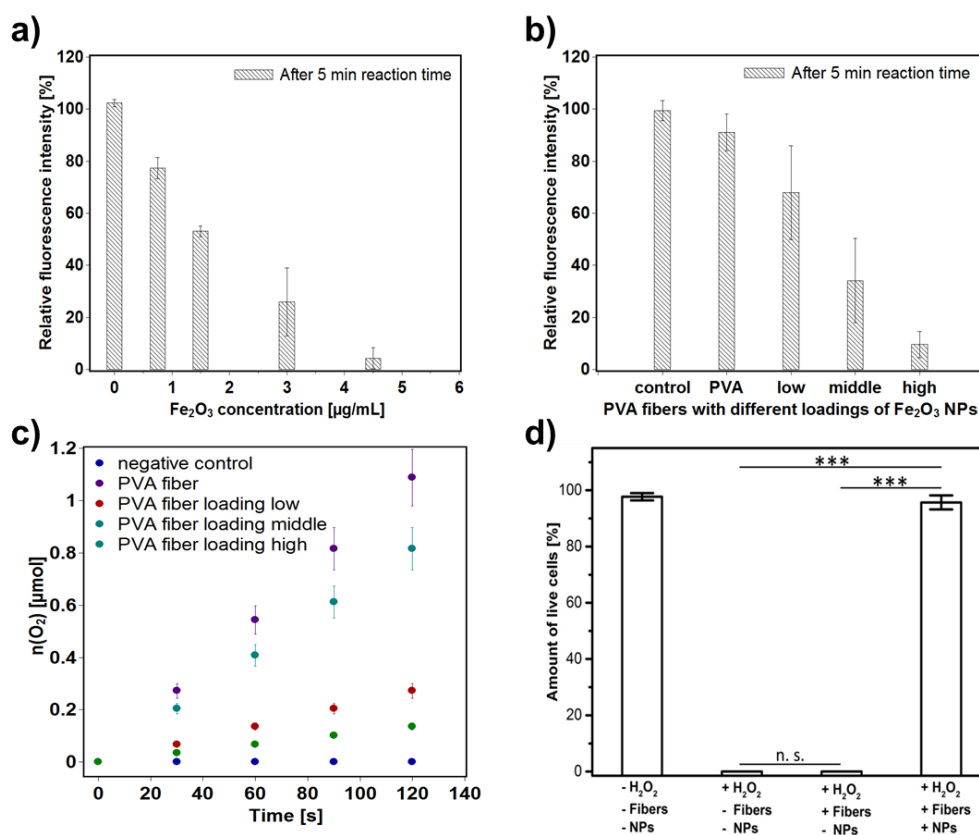


**Figure 6.** Analysis of the catalytic activity and the resulting products. To demonstrate the concentration dependency of the hematite PVA fibers, the relative fluorescence intensity - normalized to 100% control - after a reaction time of 5 min, reflecting the  $\text{H}_2\text{O}_2$  level in the sample solution, is shown for a) hematite NPs and b) for the hematite containing PVA fibers. In both experiments an increasing concentration of catalyst leads to a decrease of  $\text{H}_2\text{O}_2$  levels, demonstrating the catalytic efficiencies. c) To establish the reaction mechanism of the hematite PVA fiber meshes, the formation of elemental oxygen, which is one of the key reaction products in a catalase-like reaction, was monitored using an oxygen sensitive electrode. Increasing hematite loadings show higher formation rates of oxygen. d) Hematite PVA fibers protect cells against cell death triggered by extensive  $\text{H}_2\text{O}_2$  levels. Control measurements conducted without hematite PVA fibers, or pure PVA fibers exhibit no cell protection. n.s. is not significant different. \* $p < 0.05$ , \*\* $p < 0.01$ , \*\*\* $p < 0.001$ .



### 3.2.5 Conclusion

In summary, we demonstrated the fabrication and use of an electrospun nanofibrous membrane with a high porosity, wettability and the catalytic capability to simultaneously decrease the  $\text{H}_2\text{O}_2$  and increase the  $\text{O}_2$  level. Therefore, hematite nanozymes were integrated in various concentrations into PVA membranes *via* electrospinning. To retain the fiber scaffold in the presence of water, the membrane was cross-linked to form a stable fibrous gel. After cross-linking, the membrane showed high water permeability and hence, provided a good accessibility of hydrophilic compounds to the embedded hematite nanozyme particles. The encapsulated hematite showed a high catalase-like activity and quickly converted  $\text{H}_2\text{O}_2$  into  $\text{O}_2$ . When incubating fibroblasts at a  $\text{H}_2\text{O}_2$  concentration of 50  $\mu\text{M}$ , the catalytically active membrane efficiently reduced the  $\text{H}_2\text{O}_2$  concentration and enabled undiminished cell proliferation. Thanks to this catalase-like activity, the hybrid nanofibrilous gel could be used for improving the wound healing process.

#### 3.2.6 References

- (1) Griffin, D. R.; Weaver, W. M.; Scumpia, P. O.; Di Carlo, D.; Segura, T. Accelerated Wound Healing by Injectable Microporous Gel Scaffolds Assembled from Annealed Building Blocks. *Nat. Mater.* **2015**, *14* (7), 737–744.
- (2) Fan, Z.; Liu, B.; Wang, J.; Zhang, S.; Lin, Q.; Gong, P.; Ma, L.; Yang, S. A Novel Wound Dressing Based on Ag/graphene Polymer Hydrogel: Effectively Kill Bacteria and Accelerate Wound Healing. *Adv. Funct. Mater.* **2014**, *24* (25), 3933–3943.
- (3) Loo, A. E. K.; Wong, Y. T.; Ho, R.; Wasser, M.; Du, T.; Ng, W. T.; Halliwell, B. Effects of Hydrogen Peroxide on Wound Healing in Mice in Relation to Oxidative Damage. *PLoS One* **2012**, *7* (11), 49215–49228.
- (4) Sen, C. Wound Healing Essentials: Let There Be Oxygen. *Wound Repair Regen.* **2009**, *17* (1), 1–18.
- (5) Kanta, J. The Role of Hydrogen Peroxide and Other Reactive Oxygen Species in Wound Healing. *Acta Medica (Hradec Kralove)* **2011**, *54*, 97–101.
- (6) Wei, H.; Wang, E. Nanomaterials with Enzyme-like Characteristics (Nanozymes): Next-Generation Artificial Enzymes. *Chem. Soc. Rev.* **2013**, *42* (14), 6060–6093.
- (7) Grunwald, P. *Biocatalysis and Nanotechnology*; Pan Stanford Publishing Pte. Ltd, 2017.
- (8) Gao, L.; Zhuang, J.; Nie, L.; Zhang, J.; Zhang, Y.; Gu, N.; Wang, T.; Feng, J.; Yang, D.; Perrett, S.; Yan, X. Intrinsic Peroxidase-like Activity of Ferromagnetic Nanoparticles. *Nat. Nanotechnol.* **2007**, *2* (9), 577–583.
- (9) Fan, K.; Cao, C.; Pan, Y.; Lu, D.; Yang, D.; Feng, J.; Song, L.; Liang, M.; Yan, X. Magnetoferritin Nanoparticles for Targeting and Visualizing Tumour Tissues. *Nat. Nanotechnol.* **2012**, *7* (7), 459–464.

- (10) Que Jr, L.; Tolman, W. B. Biologically Inspired Oxidation Catalysis. *Nature* **2008**, *455* (7211), 333–340.
- (11) Comba, P.; Gahan, L. R.; Hanson, G. R.; Westphal, M. Phosphatase Reactivity of a dicopper(II) Complex of a Patellamide Derivative--Possible Biological Functions of Cyclic Pseudopeptides. *Chem. Commun.* **2012**, *48* (75), 9364–9366.
- (12) Wiester, M. J.; Ulmann, P. A.; Mirkin, C. A. Enzyme Mimics Based upon Supramolecular Coordination Chemistry. *Angew. Chem. Int. Ed.* **2011**, *50* (1), 114–137.
- (13) André, R.; Natálio, F.; Humanes, M.; Leppin, J.; Heinze, K.; Wever, R.; Schröder, H. C.; Müller, W. E. G.; Tremel, W. V2O5 Nanowires with an Intrinsic Peroxidase-like Activity. *Adv. Funct. Mater.* **2011**, *21* (3), 501–509.
- (14) Korsvik, C.; Patil, S.; Seal, S.; Self, W. T. Superoxide Dismutase Mimetic Properties Exhibited by Vacancy Engineered Ceria Nanoparticles. *Chem. Commun.* **2007**, No. 10, 1056–1058.
- (15) Wang, X.; Hu, Y.; Wei, H. Nanozymes in Bionanotechnology: From Sensing to Therapeutics and beyond. *Inorg. Chem. Front.* **2016**, *3* (1), 41–60.
- (16) Kim, C. K.; Kim, T.; Choi, I. Y.; Soh, M.; Kim, D.; Kim, Y. J.; Jang, H.; Yang, H. S.; Kim, J. Y.; Park, H. K.; Park, S. P.; Park, S.; Yu, T.; Yoon, B. W.; Lee, S. H.; Hyeon, T. Ceria Nanoparticles That Can Protect against Ischemic Stroke. *Angew. Chem. Int. Ed.* **2012**, *51* (44), 11039–11043.
- (17) Korschelt, K.; Ragg, R.; Metzger, C. S.; Klueker, M.; Oster, M.; Barton, B.; Panthöfer, M.; Strand, D.; Kolb, U.; Mondeshki, M.; Strand, S.; Brieger, J.; Nawaz Tahir, M.; Tremel, W. Glycine-Functionalized copper(II) Hydroxide Nanoparticles with High Intrinsic Superoxide Dismutase Activity. *Nanoscale* **2017**, *9* (11), 3952–3960.

- (18) Ragg, R.; Tahir, M. N.; Tremel, W. Solids Go Bio: Inorganic Nanoparticles as Enzyme Mimics. *Eur. J. Inorg. Chem.* **2016**, *2016* (13–14), 1906–1915.
- (19) Chaudhari, K. N.; Chaudhari, N. K.; Yu, J.-S. Peroxidase Mimic Activity of Hematite Iron Oxides ( $\alpha$ -Fe<sub>2</sub>O<sub>3</sub>) with Different Nanostructures. *Catal. Sci. Technol.* **2012**, *2* (1), 119–124.
- (20) Dutta, A. K.; Maji, S. K.; Srivastava, D. N.; Mondal, A.; Biswas, P.; Paul, P.; Adhikary, B. Peroxidase-like Activity and Amperometric Sensing of Hydrogen Peroxide by Fe<sub>2</sub>O<sub>3</sub> and Prussian Blue-Modified Fe<sub>2</sub>O<sub>3</sub> Nanoparticles. *J. Mol. Catal. A Chem.* **2012**, *360*, 71–77.
- (21) Chen, J.; Xu, L.; Li, W.; Gou, X.  $\alpha$ -Fe<sub>2</sub>O<sub>3</sub> Nanotubes in Gas Sensor and Lithium-Ion Battery Applications. *Adv. Mater.* **2005**, *17* (5), 582–586.
- (22) Ozaki, M.; Kratochvil, S.; Matijević, E. Formation of Monodispersed Spindle-Type Hematite Particles. *J. Colloid Interface Sci.* **1984**, *102* (1), 146–151.
- (23) Woo, K.; Lee, H. J.; Ahn, J. P.; Park, Y. S. Sol-Gel Mediated Synthesis of Fe<sub>2</sub>O<sub>3</sub> Nanorods. *Adv. Mater.* **2003**, *15* (20), 1761–1764.
- (24) Wang, X.; Chen, X.; Gao, L.; Zheng, H.; Ji, M.; Tang, C.; Shen, T.; Zhang, Z. Synthesis of  $\beta$ -FeOOH and  $\alpha$ -Fe<sub>2</sub>O<sub>3</sub> Nanorods and Electrochemical Properties of  $\beta$ -FeOOH. *J. Mater. Chem.* **2004**, *14* (5), 905–907.
- (25) Bannwarth, M. B.; Kazer, S. W.; Ulrich, S.; Glasser, G.; Crespy, D.; Landfester, K. Well-Defined Nanofibers with Tunable Morphology from Spherical Colloidal Building Blocks. *Angew. Chemie Int. Ed.* **2013**, *52* (38), 10107–10111.
- (26) Bannwarth, M. B.; Utech, S.; Ebert, S.; Weitz, D. A.; Crespy, D.; Landfester, K. Colloidal Polymers with Controlled Sequence and Branching Constructed from Magnetic Field Assembled Nanoparticles. *ACS Nano* **2015**, *9* (3), 2720–2728.

- (27) Bannwarth, M.; Crespy, D. Combining the Best of Two Worlds: Nanoparticles and Nanofibers. *Chem. - An Asian J.* **2014**, *9* (8), 2030–2035.
- (28) Bannwarth, M. B.; Camerlo, A.; Ulrich, S.; Jakob, G.; Fortunato, G.; Rossi, R. M.; Boesel, L. F. Ellipsoid-Shaped Superparamagnetic Nanoclusters through Emulsion Electrospinning. *Chem. Commun.* **2015**, *51* (18), 3758–3761.
- (29) Ulrich, S.; Hirsch, C.; Diener, L.; Wick, P.; Rossi, R. M.; Bannwarth, M. B.; Boesel, L. F. Preparation of Ellipsoid-Shaped Supraparticles with Modular Compositions and Investigation of Shape-Dependent Cell-Uptake. *RSC Adv.* **2016**, *6* (92), 89028–89039.
- (30) Greiner, A.; Wendorff, J. H. Electrospinning: A Fascinating Method for the Preparation of Ultrathin Fibers. *Angew. Chem. Int. Ed.* **2007**, *46* (30), 5670–5703.
- (31) Abrigo, M.; McArthur, S. L.; Kingshott, P. Electrospun Nanofibers as Dressings for Chronic Wound Care: Advances, Challenges, and Future Prospects. *Macromol. Biosci.* **2014**, *14* (6), 772–792.
- (32) Jiang, S.; Ma, B. C.; Reinholz, J.; Li, Q.; Wang, J.; Zhang, K. A. I.; Landfester, K.; Crespy, D. Efficient Nanofibrous Membranes for Antibacterial Wound Dressing and UV Protection. *ACS Appl. Mater. Interfaces* **2016**, *8* (44), 29915–29922.
- (33) Mahalingam, S.; Edirisinghe, M. Forming of Polymer Nanofibers by a Pressurised Gyration Process. *Macromol. Rapid Commun.* **2013**, *34* (14), 1134–1139.
- (34) Sofokleous, P.; Stride, E.; Bonfield, W.; Edirisinghe, M. Design, Construction and Performance of a Portable Handheld Electrohydrodynamic Multi-Needle Spray Gun for Biomedical Applications. *Mater. Sci. Eng. C* **2013**, *33* (1), 213–223.

- (35) Dong, R.-H.; Jia, Y.-X.; Qin, C.-C.; Zhan, L.; Yan, X.; Cui, L.; Zhou, Y.; Jiang, X.; Long, Y.-Z. In Situ Deposition of a Personalized Nanofibrous Dressing via a Handy Electrospinning Device for Skin Wound Care. *Nanoscale* **2016**, *8* (6), 3482–3488.
- (36) Mi, F. L.; Shyu, S. S.; Wu, Y. B.; Lee, S. T.; Shyong, J. Y.; Huang, R. N. Fabrication and Characterization of a Sponge-like Asymmetric Chitosan Membrane as a Wound Dressing. *Biomaterials* **2001**, *22* (2), 165–173.
- (37) Koo, W. T.; Choi, S. J.; Kim, S. J.; Jang, J. S.; Tuller, H. L.; Kim, I. D. Heterogeneous Sensitization of Metal-Organic Framework Driven Metal@Metal Oxide Complex Catalysts on an Oxide Nanofiber Scaffold Toward Superior Gas Sensors. *J. Am. Chem. Soc.* **2016**, *138* (40), 13431–13437.
- (38) Finnegan, J. R.; Gwyther, J.; Manners, I. Enabling Heterogeneous Gold Catalysis with Patchy Micelles. *Angew. Chemie Int. Ed.* **2017**, *56* (11), 2842–2844.
- (39) Wu, M.; Lin, Z.; Wolfbeis, O. S. Determination of the Activity of Catalase Using a europium(III)-Tetracycline-Derived Fluorescent Substrate. *Anal. Biochem.* **2003**, *320* (1), 129–135.
- (40) Zhang, X.; Liu, H.; Wei, Y. Catalytic Synthesis and Characterization of Spindle-Type  $\alpha$ -Fe<sub>2</sub>O<sub>3</sub> Particles. *J. Mater. Res.* **2011**, *20* (3), 628–635.
- (41) Mansur, H. S.; Sadahira, C. M.; Souza, A. N.; Mansur, A. A. P. FTIR Spectroscopy Characterization of Poly (Vinyl Alcohol) Hydrogel with Different Hydrolysis Degree and Chemically Crosslinked with Glutaraldehyde. *Mater. Sci. Eng. C* **2008**, *28* (4), 539–548.

### 3.2.7 Supporting Information

#### Figures

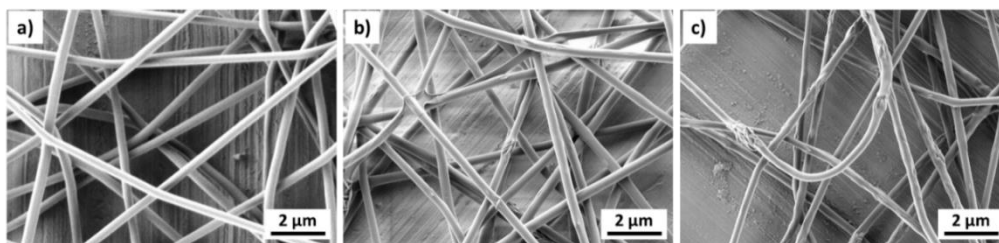


**Figure S1.** SEM images of crosslinked PVA mats containing 0% (a), 19% (b) and 58% (c) of hematite nanoparticles.

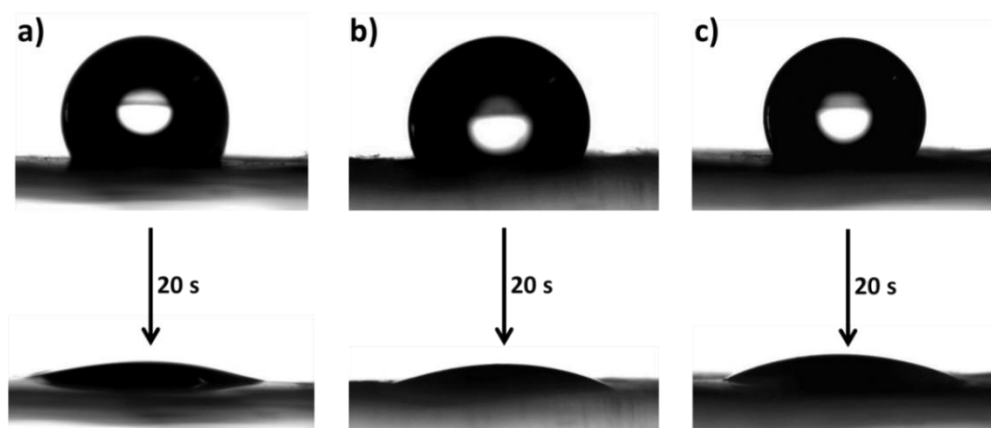


**Figure S2.** Dynamic wettability of the crosslinked PVA mat containing 0% (a), 19% (b), and 58% (c) of hematite nanoparticles.

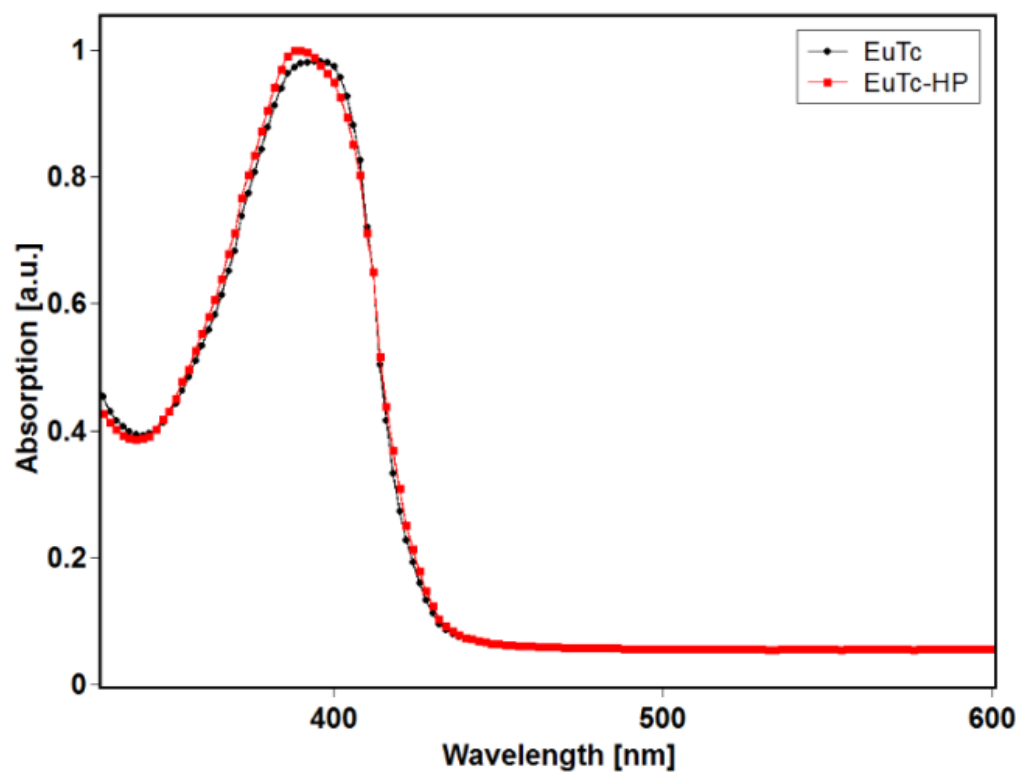
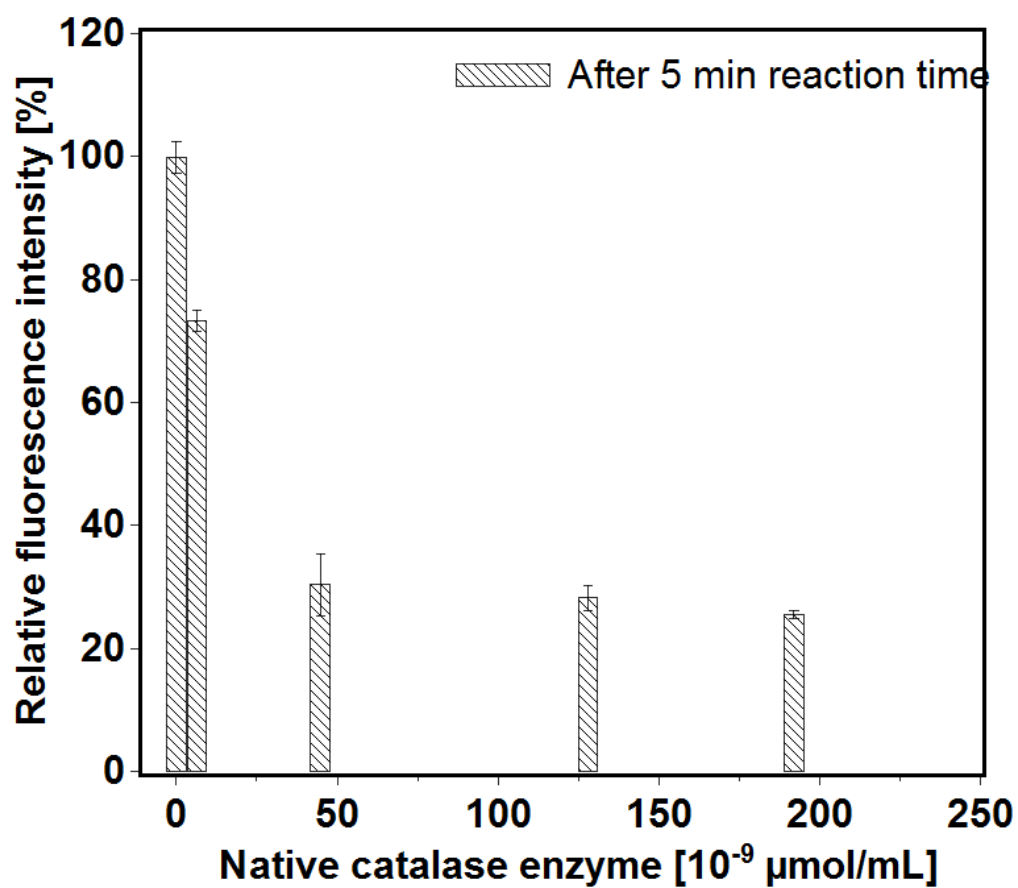
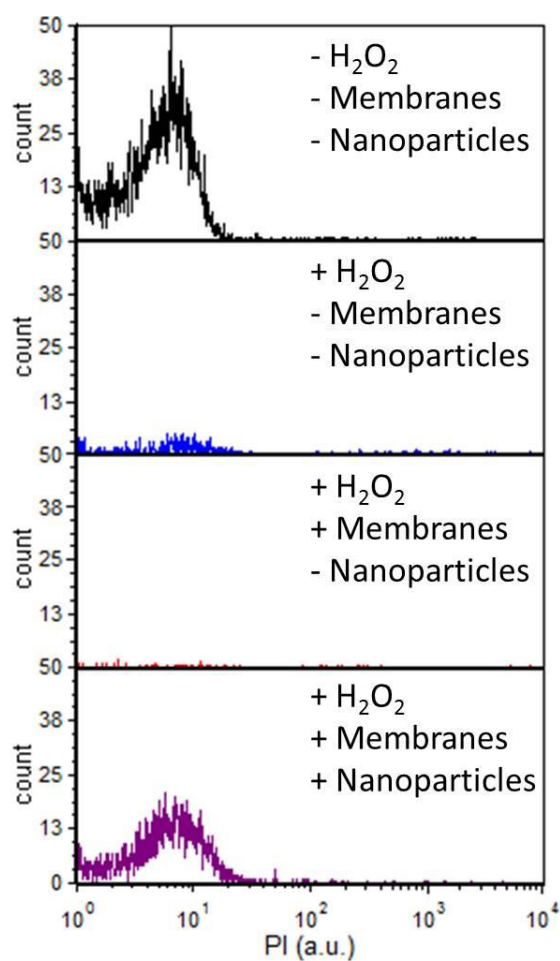


Figure S3. Absorption spectra of EuTc and EuTc-HP.





**Figure S4.** Relative fluorescence intensity (reflecting the H<sub>2</sub>O<sub>2</sub> level) after 5 minutes reaction with native catalase enzyme.



**Figure S5.** Fluorescent intensities of living cells after incubation with different adding materials ( $H_2O_2$ , electrospun membranes without nanoparticles, and membranes with high loading of nanoparticles). The negative control sample is the cells incubated without  $H_2O_2$ , membranes or nanoparticles.

#### Catalase assay<sup>1</sup>

To investigate the catalase activity of natural catalase enzyme and hematite containing PVA fiber meshes, the following solutions were used.

- A) MOPS buffer solution (10 mmol·L<sup>-1</sup>): The appropriate amount of MOPS sodium salt was dissolved in 800 mL of MilliQ water and the pH was set to 6.9. The volumetric flask was filled up to 1 L with MilliQ water and the solution was homogenized.
- B) EuCl<sub>3</sub> solution (6.3 mmol·L<sup>-1</sup> of Eu<sup>3+</sup>): 115.3 mg of EuCl<sub>3</sub>·6 H<sub>2</sub>O were dissolved in 50 mL of A)
- C) Tetracycline hydrochloride solution (2.1 mmol·L<sup>-1</sup>): 50.5 mg of tetracycline hydrochloride were dissolved in 50 mL of A)
- D) EuTc solution: 5 mL of solution B) and 5 mL C) were mixed and filled up to 50 mL with A).

The fibers were placed in a 96 well plate, and the assay was conducted following the procedure described below. In addition, control measurements were done with native catalase. In this case, A solution of native catalase (0.1 mg·mL<sup>-1</sup>) was used.

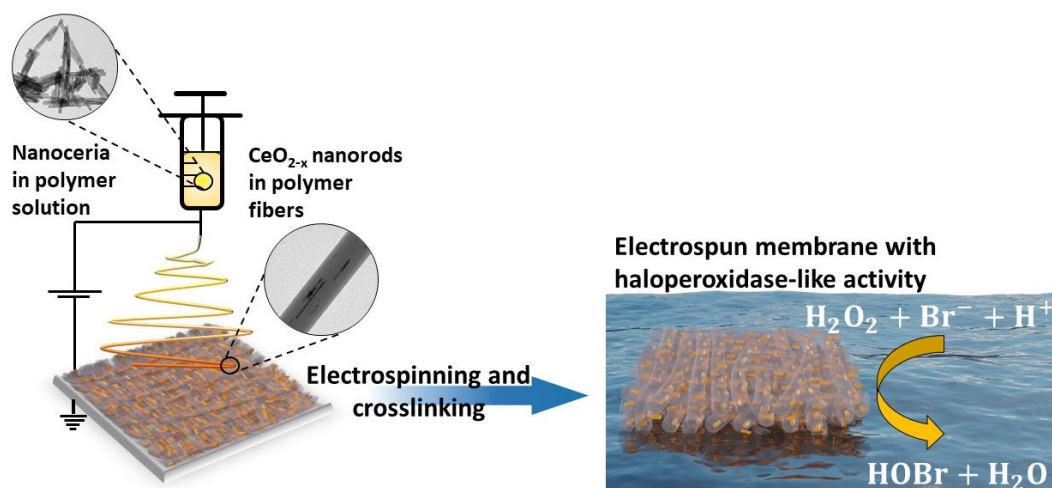
#### References

- (1) Wu, M.; Lin, Z.; Wolfbeis, O. S. Determination of the Activity of Catalase Using a europium(III)-Tetracycline-Derived Fluorescent Substrate. *Anal. Biochem.* **2003**, *320* (1), 129–135.

### 3.3 Nanozymes in Fibrous Membranes with Haloperoxidase-Like Activity

The following chapter describes the preparation of cerium oxide nanorod containing fibrous membranes with a catalytic activity similar to native haloperoxidases. It is possible to facilitate the reaction of  $\text{Br}^-$  and  $\text{H}_2\text{O}_2$  to  $\text{HOBr}$ .  $\text{HOBr}$  can block the cell to cell communication of bacteria. Hence, artificial compounds with an activity similar to native haloperoxidases can inhibit the bacterial adhesion on different surfaces and prevent the biofouling process. We explored in polyvinyl alcohol embedded nanozymes to overcome the disadvantages of “free” particles in solution.

The cover picture was designed during the project in cooperation with all authors.



Detailed authorship contributions are attached in the Appendix (chapter 5.3.4). A great thank goes to Simone Mendler for her support with the bacterial tests, Gunnar Glasser for help with SEM imaging and Stefan Schuhmacher for artwork support.

### 3.3.1 Abstract

The bromination of organic compounds in nature is *inter alia* induced by hypohalous acids like HOCl or HOBr. Hypohalous acids in native environments are formed by the oxidation of halides with hydrogen peroxide. In nature the reaction is catalyzed by the vanadium haloperoxidase enzymes. Hypohalous acids can inhibit the quorum sensing of microorganisms, which is a key step in the biofilm formation and thus in the biofouling mechanism. The presence of native haloperoxidases or material with similar activity on vulnerable surfaces can thus inhibit the biofouling and increase their life time. To mimick the catalytic activity of native haloperoxidase, CeO<sub>2-x</sub> nanorods were prepared. Free or dispersed nanorods are difficult to fix on surfaces, especially when they are movable, because of leaching effects. To overcome this problem the CeO<sub>2-x</sub> nanorods were embedded in polymer matrix *via* electrospinning. The nanorods cocooned in the polymer fiber mesh can still produce hypohalous acids, in presence of halides and hydrogen peroxide, due to their water swellability. In addition to the catalytic activity an increase of mechanical stability can be achieved with the presence of CeO<sub>2-x</sub> nanorods.

### 3.3.2 Introduction

Electrospinning is a scalable and versatile technique to obtain nanofibrous materials with variable porous structures and controllable fiber diameters.<sup>1-2</sup> The nanofibrous materials can be further functionalized and mechanically enhanced by integrating nano-objects, e.g. nanoparticles and nanocapsules, during or after the electrospinning process.<sup>3-4</sup> Additionally, the electrospun nanofibers can orderly arrange into hierarchical structures by controlling their alignment.<sup>5-6</sup> These attributes make electrospun nanofibers attractive for applications such as tissue engineering,<sup>7</sup> wearable electronics,<sup>8</sup> and water purification.<sup>9</sup>

However, material processed by electrospinning, as many other materials, can suffer from biofouling. This is especially critical when the materials are used in an environment containing microorganisms. Biofouling is the nonspecific surface

adhesion of microorganisms.<sup>10</sup> This can be detrimental to the performance of the materials, such as reducing the efficiency of membranes,<sup>11</sup> causing corrosion on metallic surfaces<sup>12</sup> and bacterial infections on implanted medical devices.<sup>13</sup> Cleaning the nanofibrous surfaces to remove the adhered layer is difficult and sometimes is even impossible. Thus, it is essential to develop surfaces that are not susceptible to biofouling.

In last decade, many strategies have been developed to reduce or avoid bacterial adhesion.<sup>14</sup> A number of antimicrobial or antibiotic compounds have been integrated into electrospun mats to release toxic agents into aqueous environments to kill the surrounding bacteria.<sup>15-16</sup> This strategy is highly efficient, but will contribute in the development of antibiotic-resistant bacteria strains.<sup>17</sup> As an alternative, recently, silver nanoparticles have been widely used as antibacterial compounds. These nanoparticles can form on the nanofiber surface by post-reaction after electrospinning,<sup>18-19</sup> or be embedded into the electrospun fibers. A problem common to the use of silver nanoparticles or antibiotics is the decrease of the antifouling activity due to the release of the active compound over time, leading to materials with a limited life span.

Besides the biocidal strategy, one of the most common methods to combat biofouling is to develop the surfaces to which bacteria and cells cannot adhere. For example, surfaces coated with poly(ethylene oxide) or with polymers with zwitterionic groups are known to suppress nonspecific protein adsorption and bacterial adhesion.<sup>20-21</sup>

Another alternative to create anti-fouling surface is to draw inspiration from nature. For example, seaweeds have developed a unique chemical strategy against biofouling. Seaweeds secrete a group of enzymes, vanadium haloperoxidases, that catalyze the oxidation of halides ( $\text{Cl}^-$ , and  $\text{Br}^-$ ) with hydrogen peroxide ( $\text{H}_2\text{O}_2$ ) to form hypohalous acids ( $\text{HOCl}$  and  $\text{HOBr}$ ).<sup>22-23</sup> The presence of hypohalous acids is known to disrupt the quorum sensing of microorganisms, a process that cells and bacteria uses to regulate biofilm formation, the first step in the permanent biofouling of a surface. Thus, the release of hypohalous acids prevents the biofouling of seaweed.<sup>24</sup>

Recently, biomimetic strategies have been developed to replicate the role of natural enzymes, and a variety of nanozymes – inorganic nanoparticle-based artificial enzymes – have been used to address the issues of high production cost and long-term instability in harsh environments.<sup>25-26</sup> Several nanozymes have shown promises to prevent biofouling in marine environments. For example, vanadium pentoxide nanowires were able to catalyze the oxidation of  $\text{Br}^-$  to  $\text{HOBr}$  in presence of  $\text{H}_2\text{O}_2$ .<sup>27</sup> Similarly, cerium oxide nanorods displaying haloperoxidase-like activity have been used for anti-biofouling coatings.<sup>28</sup>

Furthermore, the catalytic activity and stability of nanozymes can be retained by immobilizing them into polymer materials. Compared with the nanozyme dispersions, polymer-embedded nanozymes are more convenient for handling, continuous processing, and avoiding product contamination. The main supporting materials for nanozymes include microgels,<sup>29</sup> porous silicas,<sup>30</sup> metal-organic frameworks,<sup>31</sup> and nanofibrous materials.<sup>32-33</sup> Among these different supporting materials, polymer fibrous membranes have attracted sustained research interest, because the fibrous morphology provides a high specific surface area, which is ideal for catalytic reactions. For example, the immobilized gold nanoparticles within polymer nanofibrous mats were able to catalyze the reaction of transforming 4-nitrophenol to 4-aminophenol reaction for many times.<sup>34</sup> Electrospun  $\text{Fe}_3\text{O}_4$  nanofibers showed a better peroxidase-like catalytic activity than commercial  $\text{Fe}_3\text{O}_4$  nanoparticles.<sup>35</sup> Recently, electrospun PVA mats with hemetites nanoparticles showed the catalase-like activity and these hybrid membranes can be used as a wound dressing material to regulate the  $\text{H}_2\text{O}_2$  concentration in wound sites.<sup>32</sup>

Here, we electrospun  $\text{CeO}_{2-x}$  nanorods with polyvinyl alcohol (PVA) to fabricate nanofibrous mats. After crosslinking, the water-swellaable PVA mats embedding  $\text{CeO}_{2-x}$  nanorods mimicked the haloperoxidase activity in aqueous media. The mechanically robust hybrid membranes were able to catalyze the oxidation of  $\text{Br}^-$  and  $\text{H}_2\text{O}_2$  to  $\text{HOBr}$ , which is similar to natural hapoperoxidase. Thanks to their haloperoxidase-like activity, PVA/ $\text{CeO}_{2-x}$  nanofibrous mats are promising for developing new filtration

membranes and coating materials that resist biofouling in marine environment (see **Figure 1**).

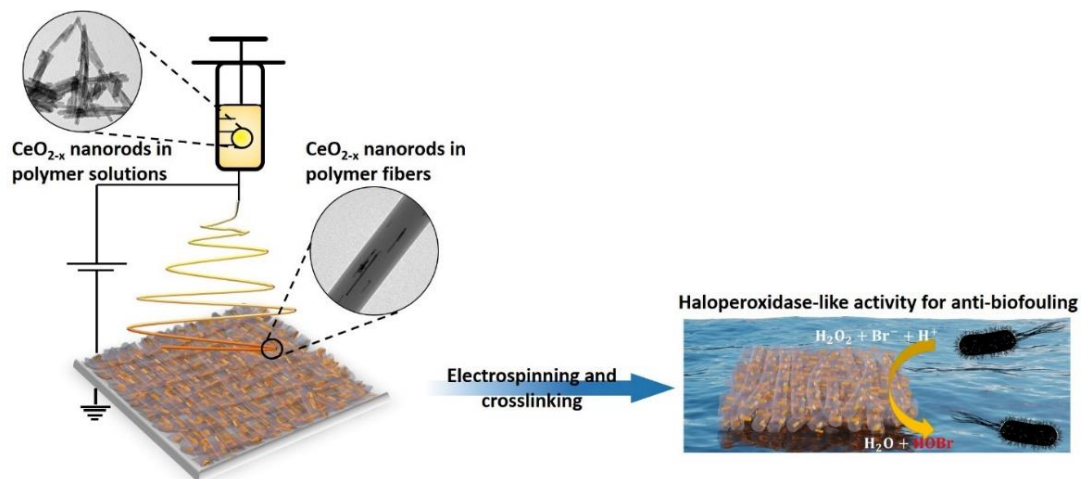


**Figure 1.** Fabrication of ceria nanorods (CeO<sub>2-x</sub>) nanofibrous mats by electrospinning. The hybrid mat can catalyze Br<sup>-</sup> with H<sub>2</sub>O<sub>2</sub> to HOBr, which could be used for preventing surfaces from bacterial adhesion.



### 3.3.3 Experimental

#### Materials

Fomblin<sup>®</sup> Y, cerium(III) nitrate hexahydrate, sodium hydroxide, phenol red and hydrochloric acid (HCl, 37wt.%, AR grade) were purchased from Sigma-Aldrich (Germany), ammonium bromide was from ABCR GmbH (Germany), hydrogen peroxide solution (30%) from Roth (Germany), polyvinyl alcohol (PVA,  $M_w = 125000$  g·mol<sup>-1</sup>) from Polysciences Inc and glutaraldehyde (GA, 50% aqueous solution) from Merck KGaA (Germany). All synthesis, experiments and catalytic tests were conducted using MilliQ water (pH = 6.90, 18.2 MΩ).

#### Synthesis of CeO<sub>2-x</sub> nanorods.

Cerium(III) nitrate hexahydrate (2 mmol) was dissolved in 5 mL of water under an argon atmosphere. Then, 20 mL of a 6 M NaOH solution were added and the reaction mixture was stirred for 30 minutes. The mixture was transferred to the Teflon<sup>®</sup> inlay of a stainless steel autoclave. The autoclave was placed in an electric oven and heated to 373 K for 24 hours. After the natural cooling to room temperature, the precipitate was isolated by centrifugation (9000 rpm, 10 minutes) and washed several times with water and ethanol. The product was dried for 24 hours in an electric oven at 313 K.<sup>36</sup>

#### Electrospinning and cross-linking of PVA/CeO<sub>2-x</sub> nanorods composites

Dispersions with varying concentrations of nanorods were prepared by combining CeO<sub>2-x</sub> nanorods suspensions with a PVA solution to yield suspension containing 10wt.% of PVA and CeO<sub>2-x</sub> nanorods for electrospinning. An ultrasonic tip was used to disperse the nanorods in the PVA solution (d (tip) = 6 mm; 50% amplitude; 5 s pulse, 5 s pause; 3 min). Afterward, the mixtures were mechanically stirred overnight at 900 rpm to get a homogenous dispersion. 1 mL syringe was filled with the nanorod and PVA mixture. Then the electrospinning process was conducted at room temperature with a relative humidity of 20-25% onto an aluminum foil carrier that set at a distance of 20 cm from the nozzle (diameter: 0.8 mm). The feeding rate was

0.3 mL h<sup>-1</sup> and the applied voltages were +18 kV and 0 kV. Fibers without CeO<sub>2-x</sub> nanorods were prepared under same conditions. To crosslink the fibers, they were treated with 1 mL of a 50wt.% glutaraldehyde (GA) solution and 20 μL of a 37 wt.% HCl solution. The crosslinking reaction was conducted in a vacuum oven at room temperature and 1 mbar for 24 h. Finally, unreacted GA and HCl were removed by drying the samples for 24 h at room temperature. Samples for TEM analysis were prepared by placing a TEM grid (copper, 300 mesh) on the aluminum foil to collect the fiber sample for 30 seconds.

#### Characterizations

##### *Powder X-ray diffraction (XRD)*

The solid-state analysis of the pure CeO<sub>2-x</sub> nanorods was conducted on a STOE Stadi P (Germany) diffractometer using the Ag K<sub>α1</sub> radiation. The sample was prepared on a perfluoropolyether film with Fomblin<sup>®</sup> Y. The data were analyzed with the EVA software package.

##### *Swelling ratio of hybrid PVA mats*

The water absorption ratio of the hybrid PVA mats was defined as the swelling ratio in this study. To determine the swelling ratio, the mats were dried at 50 °C under vacuum overnight. Then the dried mats were soaked in demineralized water in a mixer (HLC MKR 23, Ditabis, Germany) at room temperature for 24 hours. The weights of the swollen samples were measured after removing the excessive water on the mats. The swelling ratios of the PVA mats were calculated by the **equation (1)**:

$$\text{Swelling ratio} = \frac{W_S - W_D}{W_D} \times 100\% \quad (1)$$

where  $W_S$  and  $W_D$  are the weights of the swollen and dried samples, respectively. All samples were triplicate in the experiments.

#### *Contact angle measurement*

The static contact angle of water on PVA fiber meshes was analyzed using a goniometer coupled to an IDS uEye camera. For the measurement, 5  $\mu\text{L}$  droplets of water were deposited on the mats surfaces and the contact angle measured after 1 min.

#### *Morphologies of the $\text{CeO}_{2-x}$ nanorods and of the hybrid mats*

The  $\text{CeO}_{2-x}$  nanorods were imaged by transmission electron microscopy using a Tecnai G2 Spirit TEM (FEI, Hillsboro, USA) using  $\text{LaB}_6$  crystal as the cathode, a twin objective and a CCD camera (US 1000, Gatan Pleasanton, USA). The sample was prepared by dispersing the nanorods in ethanol and dropping one drop of the dispersion on a carbon coated copper grid from Science Services. The morphology of the PVA mats were analyzed with JEM1400 transmission electron microscope (JEOL, Japan) and a SU8000 scanning electron microscope (Hitachi, Japan).

#### *Thermogravimetry (TGA).*

The content of nanorods in the PVA mats was determined by thermogravimetric analysis (TGA). The measurements were conducted using a Mettler-Toledo TGA/SDTA-851 thermo-balance (50 to 700  $^{\circ}\text{C}$ , heating rate of 5  $\text{K}\cdot\text{min}^{-1}$ , nitrogen atmosphere, sample weight was about 10 mg). To measure the leakage of nanoparticles from the PVA fibers, thermogravimetric analysis was conducted on samples having been immersed into water for 2 weeks and dried overnight.

#### *Young's modulus of crosslinked fibers determined by atomic force microscopy (AFM)*

The Young's modulus of single fibers was determined by measuring their resistance against bending by applying point loads onto freely suspended fibers. For this purpose, fibers were electrospun onto microstructured silicon wafers (HS-500MG height calibration standard, Budget Sensors, Sofia, Bulgaria), that contained regular arrays of square holes with 5  $\mu\text{m}$  length and 0.5  $\mu\text{m}$  depth. A Nanowizard IV AFM (JPK Instruments, Berlin, Germany) was used to image the sample in tapping mode to find places where a single fiber was spanning one of the square holes. Once such a freely suspended fiber was located, it was imaged in QI mode, where a force distance curve with defined maximum load of 100 nN was recorded for each of the  $256 \times 256$  pixels of the image. For a circular fiber clamped at both ends, the stiffness  $k_F(x)$  at position  $x$  is related to its Young's modulus  $E$  by

$$k_F(x) = \frac{3L^3EI}{(L - [x - x_0])^3(x - x_0)^3} \quad (2)$$

where  $L$  is the length of the suspended fiber segment and  $I = \pi R^4/4$  is the moment of inertia of a fiber with radius  $R$ . From the QI images, we could extract the individual fiber radius  $R$  as well as the values of  $k_F(x)$  for each image pixel along the freely suspended part with length  $L$ . By fitting this experimental curve with **equation (2)**, we obtained the Young's modulus of individual fibers. The offset  $x_0$  is a fitting parameter to account of the small uncertainty in determining the position of end points of the suspended segment. The use of a clamped boundary condition is justified as the fibers showed strong adhesion to the silicon substrate. The same AFM cantilever was used for all experiments to exclude any relative error between experiments due to variation in spring constants. The spring constant of this cantilever was determined by both Sader method<sup>37</sup> and thermal noise method<sup>38</sup> integrated into JPK AFM software giving a value of  $49.9 \pm 3.6$  N/m.

#### *Haloperoxidase-like activity of PVA/CeO<sub>2-x</sub> nanorods composites*

The catalytic activity of the materials was analyzed using a previously reported method.<sup>28, 39-40</sup> Briefly, the kinetic studies were conducted with pure cerium oxide nanoparticles, PVA fibers without cerium oxide nanorods, and PVA fibers with low (6wt.%), medium (14wt.%) and high (22wt.%) loading of cerium oxide nanorods. The PVA fibers were fixed on the bottom of the cuvette with a magnetic stir bar, preventing the fiber mats to float in the path of the UV beam, which would directly influence and distort the UV-Vis signal.

For each measurement, the cuvette contained  $4.4 \times 10^{-3}$  mol·L<sup>-1</sup> of ammonium bromide,  $2.8 \times 10^{-5}$  mol·L<sup>-1</sup> of phenol red,  $4.2 \times 10^{-4}$  mol·L<sup>-1</sup> of hydrogen peroxide and the 18 cm<sup>2</sup> of mats. All solutions were prepared in water and the cuvette contained a final volume of 2.5 mL. In all cases, the hydrogen peroxide solution (30%) was added directly before the measurements. Absorption scans were recorded in intervals of one minute for a total duration of 5 h.

### 3.3.4 Results and Discussion

To obtain the nanoparticles that are functional mimics of natural haloperoxidases, CeO<sub>2-x</sub> nanorods were prepared by hydrothermal synthesis. After the reaction, the products showed rod-like morphology and powder XRD revealed the nanorods to be made of pure CeO<sub>2-x</sub> (**Figure 2a**). The resulting nanoparticles were not functionalized with any surfactants, allowing the direct accessibility for substrate molecules to the catalytic sites of particle surfaces.

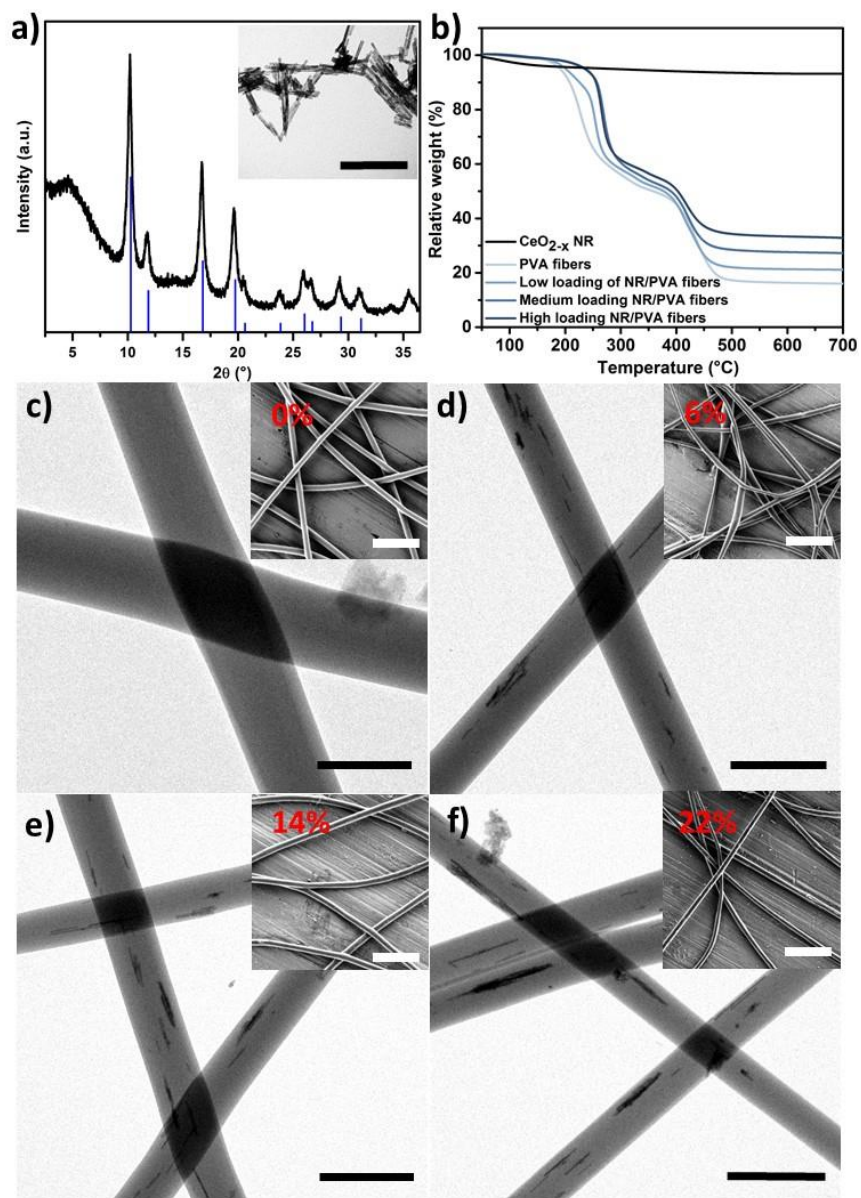


**Figure 2.** (a) XRD spectra of synthesized CeO<sub>2-x</sub> nanorods (NR). Inset is the TEM images of NR (scale bar = 200 nm). (b) TGA curves of the hybrid PVA/CeO<sub>2-x</sub> mats with different NR loading. (The curves from top to bottom are presented the pure CeO<sub>2-x</sub> NR, pure PVA, PVA with 6%, 14% and 22% of CeO<sub>2-x</sub> NR.) TEM images of PVA fibers with (c) 0%, (d) 6%, (e) 14%, and (f) 22% of CeO<sub>2-x</sub> NR (c-f: scale bar = 500 nm, insets: scale bar = 2 μm).

To integrate the nanorods in polymer materials, the suspension of CeO<sub>2-x</sub> nanorods were mixed in a PVA solution. Using ultrasonication ensured the complete dispersion of CeO<sub>2-x</sub> nanorods in the PVA solution. PVA is a water-soluble polymer, to allow the fibers to be used in aqueous systems, the electrospun fibers were covalently crosslinked with glutaraldehyde. The swelling ratio of PVA mats and PVA/CeO<sub>2-x</sub> mats were 192% ± 4% (see Table S1, SI). The high swelling ratio allows the absorption of water and water-soluble substrates penetrate into the PVA fibers to contact with the embedded CeO<sub>2-x</sub> nanorods. Additionally, the mats retained their physical integrity and no leakage of the nanorods was observed even after two weeks of immersion in water (**Figure S1, SI**). It indicates that the PVA/CeO<sub>2-x</sub> nanofibrous mats are promising hybrid materials for long-term use in aqueous environments. The loading of CeO<sub>2-x</sub> nanorods in PVA mats were checked by TGA (**Figure 2b**). The results show that pure CeO<sub>2-x</sub> nanorods are stable in the temperature range studied. However, in the same temperature range, the pure PVA fibers underwent decomposition between 250 °C and 450 °C with the typical two-steps decomposition mechanism of PVA.<sup>41</sup> Above 500 °C the decomposition stopped, and this indicated the formation of stable carbonaceous residues representing ca. 20% of the original PVA weight. All the samples containing PVA and the cerium oxide nanoparticles showed similar behaviors when heated under nitrogen, although the presence of the inorganic nanoparticle slightly improved the thermal stability of the hybrid material. The main difference observed in the decomposition curve is the solid fraction of material remaining after the complete decomposition of PVA. The composition of the solid residue was used to calculate the original loading of cerium oxide nanorods in the hybrid PVA mats with low, medium, and high amount of CeO<sub>2-x</sub> nanorods (respectively 6%, 14%, and 22%). From the TEM images (**Figure 2c-f**) of the electrospun fibers, it showed that the cerium oxide nanorods were homogeneously distributed in the fibers and did not show the presence of any cerium oxide nanorod aggregates suggesting the formation of a homogenous suspension using ultrasonication. Additionally, the nanorods were oriented along the fibers axis direction.



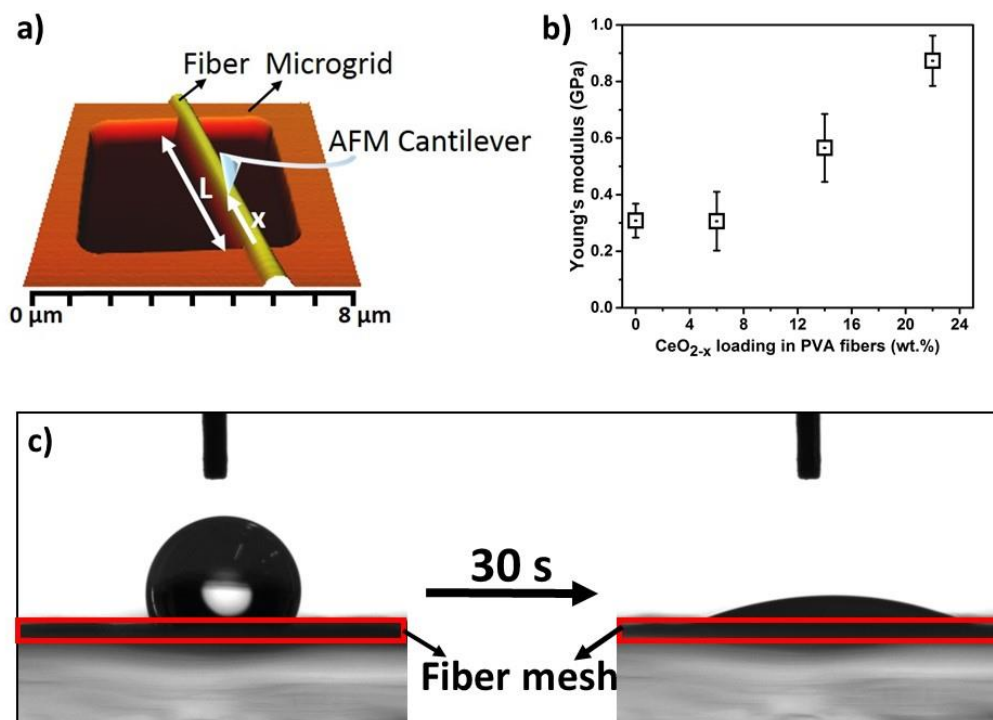


**Figure 3.** (a) Schematics of the AFM bending experiment. A point load is applied by the AFM tip onto the fiber that was spanning on a microgrid. (b) Young's modulus of the PVA mats measured by the AFM bending experiment. (c) Dynamic wettability of the mats containing 6% of CeO<sub>2-x</sub> nanorods.

The long-term stability of the PVA/CeO<sub>2-x</sub> hybrid mats can be influenced not only by the leakage of the nanorods but also by the mechanical properties of the fibers themselves. Therefore, the Young's modulus of PVA fibers with different loading of nanorods was measured by atomic force microscopy (AFM). AFM has become a key method to obtain quantitative mechanical information about nanomaterials and nanofibers using force spectroscopy.<sup>42-43</sup> To measure the mechanical properties of the hybrid PVA/CeO<sub>2-x</sub> fibers, we applied vertical point loads along freely suspended fiber segments by AFM to locally probe their bending stiffness. (**Figure 3a**). From a fit of the stiffness profiles with **equation (2)** (**Figure S2, SI**), the Young's modulus of the fibers was obtained.<sup>42</sup>

For PVA fibers without nanorods, a Young's modulus of  $0.31 \pm 0.06$  GPa was found. The addition of  $\text{CeO}_{2-x}$  nanorods improved the mechanical properties of the fibers by increasing the Young's modulus to  $0.31 \pm 0.10$  GPa,  $0.57 \pm 0.12$  GPa and  $0.87 \pm 0.09$  GPa in the presence of 6%, 14%, and 22% of nanorods respectively (**Figure 3b**, mean values  $\pm$  standard deviations,  $n \geq 5$ ). These results demonstrate that the addition of  $\text{CeO}_{2-x}$  nanorods to the PVA fibers leads to the formation of a composite material with improved mechanical properties.

The wettability of the PVA mats was tested by adding a droplet of water (5  $\mu\text{L}$ ) on the surface. After 30 seconds, the contact angle of water droplet on the PVA mats was  $17.5^\circ \pm 1.1^\circ$ , showing a good wettability and hydrophilicity of PVA mats (**Figure 3c**). The hydrophilic character of the PVA mats allow the fibers to swell in presence of water, improving further the access of the molecular substrates to the embedded nanorods in the PVA fibers.

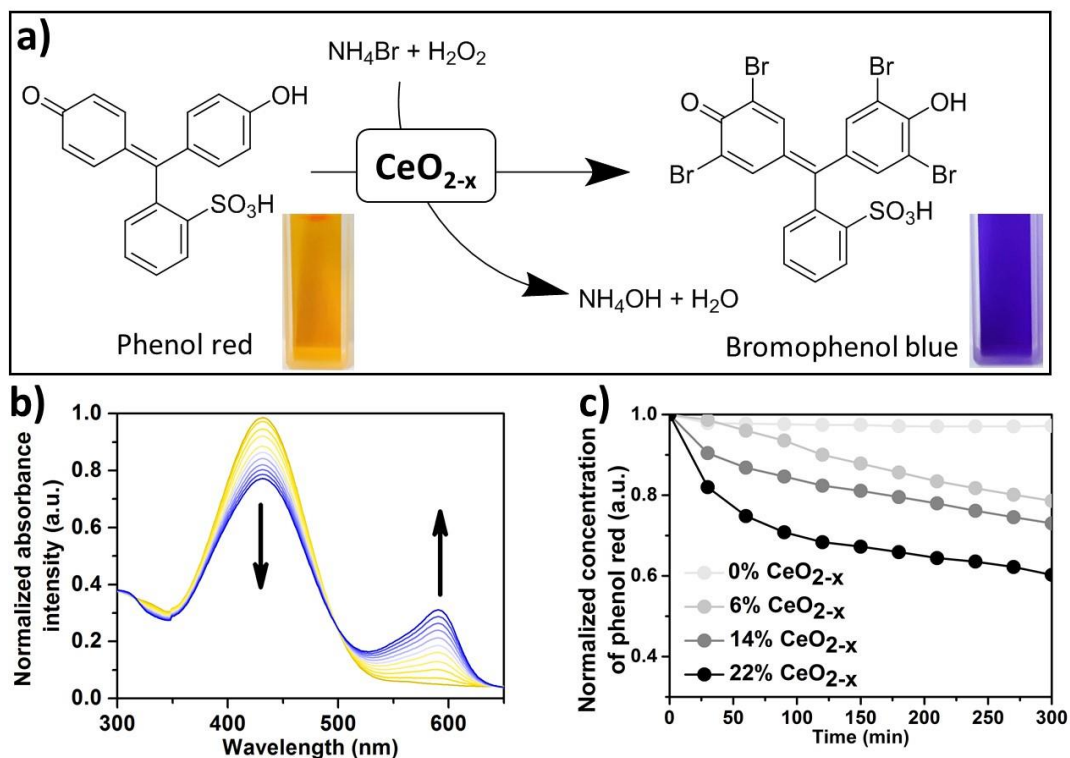


**Figure 4.** Determination of the haloperoxidase-like activity of electrospun and PVA mats with different loadings of  $\text{CeO}_{2-x}$  NRs in presence of  $\text{H}_2\text{O}_2$  and  $\text{NH}_4\text{Br}$ . (a) schematic illustration of the oxidation of phenol red to bromophenol blue catalyzed by  $\text{CeO}_{2-x}$  nanorods. Insets are the photos of phenol red before and after reaction. (b) Time-dependent UV/vis spectra of PVA mats loaded with 6%  $\text{CeO}_{2-x}$ , showing the oxidative bromination of phenol red catalyzed by  $\text{CeO}_{2-x}$  NRs ( $2.8 \times 10^{-5}$  mol/L of phenol red,  $4.4 \times 10^{-3}$  mol/L of  $\text{NH}_4\text{Br}$ ,  $4.2 \times 10^{-4}$  mol/L of  $\text{H}_2\text{O}_2$ , 300 min, 23 - 25 °C). (c) Changes of phenol red with time on different PVA mats (0%, 6%, 14%, and 22% of  $\text{CeO}_{2-x}$  loading).

The haloperoxidase-like activity of  $\text{CeO}_{2-x}$  nanorods/PVA mats were demonstrated by using the phenol red bromination assay. The phenol red ( $\lambda_{\text{max}} = 432$  nm) can be brominated with ammonium bromide ( $\text{NH}_4\text{Br}$ ) and hydrogen peroxide ( $\text{H}_2\text{O}_2$ ) to bromophenol blue ( $\lambda_{\text{max}} = 590$  nm) (**Figure 4a**). This reaction can be catalyzed by the presence of haloperoxidase<sup>23</sup> or haloperoxidase-like nanoparticles.<sup>28</sup> The stepwise bromination of phenol red to bromophenol red and finally to bromophenol blue can be monitored spectrophotometrically.<sup>44</sup> The haloperoxidase-like reaction lead to a decrease of the absorption maximum at 432 and simultaneously to an increase in the absorption at 590 nm (Figure 4b). Control measurements were conducted in presence of the PVA mats without  $\text{CeO}_{2-x}$  nanorods. These control experiment did not show any

change in the absorption spectra and the concentration of phenol red remain constant throughout the experiment, indicating that the mat itself was not able to catalyze the phenol red bromination (**Figure S3, SI**). In contrast, PVA mats containing CeO<sub>2-x</sub> nanorods exhibited haloperoxidase-like activity and facilitate the bromination reaction. The reduction in the concentration of phenol red ( $\lambda_{\text{max}} = 432 \text{ nm}$ ) and the simultaneous increase in the concentration of bromophenol blue ( $\lambda_{\text{max}} = 590 \text{ nm}$ ) increased with increased loading of CeO<sub>2-x</sub> nanorods (**Figure 4c**). The results show that the reaction rate increased with increasing concentration of CeO<sub>2-x</sub> nanorods in the PVA fibers. This indicated that the haloperoxidase-like activity of PVA mats had a clear dependency to the nanorods loading.

#### 3.3.5 Conclusions

In summary, we demonstrated the fabrication of electrospun PVA fiber meshes, in which CeO<sub>2-x</sub> nanorods could be embedded during the spinning process. PVA fibers with different loadings of CeO<sub>2-x</sub> were produced and their catalytic activity in a haloperoxidase-like reaction was investigated. The nanorod containing fibers were still able to brominate organic compounds, like phenol red, in a haloperoxidase-like reaction. The still available catalytic properties of the nanorods are the basis for an antibacterial effect. Native haloperoxidases or artificial materials with similar activity can prevent the biofilm formation and thus the biofouling on vulnerable surfaces. In contrast to “free” nanorods in solution, which are difficult to fix on a special position, the nanorod containing PVA fiber meshes can easily be fixed. Investigations of the mechanical properties of the polymer fibers showed an increased stability in presence of the nanorods. Thanks to the mechanical and catalytic characteristics of nanorod containing PVA fiber meshes, the material could be used to prevent bacterial adhesion also on flexible surfaces like tubes, which are placed under water, where a stiff paint break and the nanorods would leach.

#### 3.3.6 References

1. Xue, J.; Xie, J.; Liu, W.; Xia, Y., Electrospun nanofibers: new concepts, materials, and applications. *Accounts of chemical research* **2017**, *50* (8), 1976-1987.
2. Yang, G.; Li, X.; He, Y.; Ma, J.; Ni, G.; Zhou, S., From nano to micro to macro: Electrospun hierarchically structured polymeric fibers for biomedical applications. *Progress in Polymer Science* **2017**.
3. Zhang, C.-L.; Yu, S.-H., Nanoparticles meet electrospinning: recent advances and future prospects. *Chemical Society Reviews* **2014**, *43* (13), 4423-4448.
4. Jiang, S.; Lv, L.-P.; Landfester, K.; Crespy, D., Nanocontainers in and onto Nanofibers. *Accounts of chemical research* **2016**, *49* (5), 816-823.
5. Xie, J.; Liu, W.; MacEwan, M. R.; Bridgman, P. C.; Xia, Y., Neurite outgrowth on electrospun nanofibers with uniaxial alignment: the effects of fiber density, surface coating, and supporting substrate. *ACS nano* **2014**, *8* (2), 1878-1885.
6. Katta, P.; Alessandro, M.; Ramsier, R.; Chase, G., Continuous electrospinning of aligned polymer nanofibers onto a wire drum collector. *Nano letters* **2004**, *4* (11), 2215-2218.
7. Jiang, T.; Carbone, E. J.; Lo, K. W.-H.; Laurencin, C. T., Electrospinning of polymer nanofibers for tissue regeneration. *Progress in polymer Science* **2015**, *46*, 1-24.
8. Zeng, W.; Shu, L.; Li, Q.; Chen, S.; Wang, F.; Tao, X. M., Fiber-based wearable electronics: a review of materials, fabrication, devices, and applications. *Advanced Materials* **2014**, *26* (31), 5310-5336.
9. Ray, S. S.; Chen, S.-S.; Li, C.-W.; Nguyen, N. C.; Nguyen, H. T., A comprehensive review: electrospinning technique for fabrication and surface

- modification of membranes for water treatment application. *RSC Advances* **2016**, *6* (88), 85495-85514.
10. Garrett, T. R.; Bhakoo, M.; Zhang, Z., Bacterial adhesion and biofilms on surfaces. *Progress in Natural Science* **2008**, *18* (9), 1049-1056.
  11. Kochkodan, V.; Hilal, N., A comprehensive review on surface modified polymer membranes for biofouling mitigation. *Desalination* **2015**, *356*, 187-207.
  12. Tesler, A. B.; Kim, P.; Kolle, S.; Howell, C.; Ahanotu, O.; Aizenberg, J., Extremely durable biofouling-resistant metallic surfaces based on electrodeposited nanoporous tungstite films on steel. *Nature communications* **2015**, *6*, 8649.
  13. Costerton, J. W.; Stewart, P. S.; Greenberg, E. P., Bacterial biofilms: a common cause of persistent infections. *Science* **1999**, *284* (5418), 1318-1322.
  14. Banerjee, I.; Pangule, R. C.; Kane, R. S., Antifouling coatings: recent developments in the design of surfaces that prevent fouling by proteins, bacteria, and marine organisms. *Advanced Materials* **2011**, *23* (6), 690-718.
  15. Zhang, Z.; Tang, J.; Wang, H.; Xia, Q.; Xu, S.; Han, C. C., Controlled antibiotics release system through simple blended electrospun fibers for sustained antibacterial effects. *ACS applied materials & interfaces* **2015**, *7* (48), 26400-26404.
  16. Chen, J.; Liu, Z.; Chen, M.; Zhang, H.; Li, X., Electrospun gelatin fibers with a multiple release of antibiotics accelerate dermal regeneration in infected deep burns. *Macromolecular bioscience* **2016**, *16* (9), 1368-1380.
  17. Romero, D.; Kolter, R., Will biofilm disassembly agents make it to market? *Trends in microbiology* **2011**, *19* (7), 304-306.

18. De Faria, A. F.; Perreault, F. o.; Shaulsky, E.; Arias Chavez, L. H.; Elimelech, M., Antimicrobial electrospun biopolymer nanofiber mats functionalized with graphene oxide–silver nanocomposites. *ACS applied materials & interfaces* **2015**, *7* (23), 12751-12759.
19. GhavamiNejad, A.; Rajan Unnithan, A.; Ramachandra Kurup Sasikala, A.; Samarikhalaj, M.; Thomas, R. G.; Jeong, Y. Y.; Nasser, S.; Murugesan, P.; Wu, D.; Hee Park, C., Mussel-inspired electrospun nanofibers functionalized with size-controlled silver nanoparticles for wound dressing application. *ACS applied materials & interfaces* **2015**, *7* (22), 12176-12183.
20. Ozcan, S.; Kaner, P.; Thomas, D.; Cebe, P.; Asatekin, A., Hydrophobic Antifouling Electrospun Mats from Zwitterionic Amphiphilic Copolymers. *ACS applied materials & interfaces* **2018**, *10* (21), 18300-18309.
21. Yang, W.; Sundaram, H. S.; Ella, J.-R.; He, N.; Jiang, S., Low-fouling electrospun PLLA films modified with zwitterionic poly (sulfobetaine methacrylate)-catechol conjugates. *Acta biomaterialia* **2016**, *40*, 92-99.
22. Sandy, M.; Carter-Franklin, J. N.; Martin, J. D.; Butler, A., Vanadium bromoperoxidase from *Delisea pulchra*: enzyme-catalyzed formation of bromofuranone and attendant disruption of quorum sensing. *Chemical Communications* **2011**, *47* (44), 12086-12088.
23. Kristensen, J. B.; Meyer, R. L.; Laursen, B. S.; Shipovskov, S.; Besenbacher, F.; Poulsen, C. H., Antifouling enzymes and the biochemistry of marine settlement. *Biotechnology advances* **2008**, *26* (5), 471-481.
24. Dobretsov, S.; Teplitski, M.; Paul, V., Mini-review: quorum sensing in the marine environment and its relationship to biofouling. *Biofouling* **2009**, *25* (5), 413-427.

25. Wei, H.; Wang, E., Nanomaterials with enzyme-like characteristics (nanozymes): next-generation artificial enzymes. *Chemical Society Reviews* **2013**, *42* (14), 6060-6093.
26. Korschelt, K.; Tahir, M. N.; Tremel, W., A Step into the Future: Applications of Nanoparticle Enzyme Mimics. *Chemistry–A European Journal* **2018**.
27. Natalio, F.; André, R.; Hartog, A. F.; Stoll, B.; Jochum, K. P.; Wever, R.; Tremel, W., Vanadium pentoxide nanoparticles mimic vanadium haloperoxidases and thwart biofilm formation. *Nature nanotechnology* **2012**, *7* (8), 530.
28. Herget, K.; Hubach, P.; Pusch, S.; Deglmann, P.; Götz, H.; Gorelik, T. E.; Gural'skiy, I. y. A.; Pfitzner, F.; Link, T.; Schenk, S., Haloperoxidase mimicry by CeO<sub>2</sub>-x nanorods combats biofouling. *Advanced Materials* **2017**, *29* (4).
29. Zhang, Z.; Liu, Y.; Zhang, X.; Liu, J., A Cell-Mimicking Structure Converting Analog Volume Changes to Digital Colorimetric Output with Molecular Selectivity. *Nano letters* **2017**, *17* (12), 7926-7931.
30. Kim, M. Y.; Kim, J., Chitosan microgels embedded with catalase nanozyme-loaded mesocellular silica foam for glucose-responsive drug delivery. *ACS Biomaterials Science & Engineering* **2017**, *3* (4), 572-578.
31. Liang, H.; Lin, F.; Zhang, Z.; Liu, B.; Jiang, S.; Yuan, Q.; Liu, J., Multicopper Laccase Mimicking Nanozymes with Nucleotides as Ligands. *ACS applied materials & interfaces* **2017**, *9* (2), 1352-1360.
32. Hu, M.; Korschelt, K.; Daniel, P.; Landfester, K.; Tremel, W.; Bannwarth, M. B., Fibrous Nanozyme Dressings with Catalase-Like Activity for H<sub>2</sub>O<sub>2</sub> Reduction To Promote Wound Healing. *ACS applied materials & interfaces* **2017**, *9* (43), 38024-38031.



33. Breitwieser, M.; Klose, C.; Hartmann, A.; Büchler, A.; Klingele, M.; Vierrath, S.; Zengerle, R.; Thiele, S., Cerium Oxide Decorated Polymer Nanofibers as Effective Membrane Reinforcement for Durable, High-Performance Fuel Cells. *Advanced Energy Materials* **2017**, *7* (6).
34. Fang, X.; Ma, H.; Xiao, S.; Shen, M.; Guo, R.; Cao, X.; Shi, X., Facile immobilization of gold nanoparticles into electrospun polyethyleneimine/polyvinyl alcohol nanofibers for catalytic applications. *Journal of Materials Chemistry* **2011**, *21* (12), 4493-4501.
35. Chen, S.; Chi, M.; Zhu, Y.; Gao, M.; Wang, C.; Lu, X., A Facile synthesis of superparamagnetic Fe<sub>3</sub>O<sub>4</sub> nanofibers with superior peroxidase-like catalytic activity for sensitive colorimetric detection of l-cysteine. *Applied Surface Science* **2018**, *440*, 237-244.
36. Mai, H.-X.; Sun, L.-D.; Zhang, Y.-W.; Si, R.; Feng, W.; Zhang, H.-P.; Liu, H.-C.; Yan, C.-H., Shape-selective synthesis and oxygen storage behavior of ceria nanopolyhedra, nanorods, and nanocubes. *The Journal of Physical Chemistry B* **2005**, *109* (51), 24380-24385.
37. Sader, J. E.; Larson, I.; Mulvaney, P.; White, L. R., Method for the calibration of atomic force microscope cantilevers. *Review of Scientific Instruments* **1995**, *66* (7), 3789-3798.
38. Hutter, J. L.; Bechhoefer, J., Calibration of atomic-force microscope tips. *Review of Scientific Instruments* **1993**, *64* (7), 1868-1873.
39. Colpas, G. J.; Hamstra, B. J.; Kampf, J. W.; Pecoraro, V. L., Functional models for vanadium haloperoxidase: reactivity and mechanism of halide oxidation. *Journal of the American Chemical Society* **1996**, *118* (14), 3469-3478.

40. Chen, C.; Sun, Q.; Ren, D.-X.; Zhang, R.; Bai, F.-Y.; Xing, Y.-H.; Shi, Z., Bromoperoxidase mimic as catalysts for oxidative bromination—synthesis, structures and properties of the diversified oxidation state of vanadium (iii, iv and v) complexes with pincer N-heterocycle ligands. *CrystEngComm* **2013**, *15* (27), 5561-5573.
41. Yang, C.-C.; Lee, Y.-J.; Yang, J. M., Direct methanol fuel cell (DMFC) based on PVA/MMT composite polymer membranes. *Journal of Power Sources* **2009**, *188* (1), 30-37.
42. Corrales, T. P.; Friedemann, K.; Fuchs, R.; Roy, C. m.; Crespy, D.; Kappl, M., Breaking Nano-Spaghetti: Bending and Fracture Tests of Nanofibers. *Langmuir* **2016**, *32* (5), 1389-1395.
43. Stachewicz, U.; Bailey, R. J.; Wang, W.; Barber, A. H., Size dependent mechanical properties of electrospun polymer fibers from a composite structure. *Polymer* **2012**, *53* (22), 5132-5137.
44. Terrón, M. C.; Verhagen, F. J.; Franssen, M. C.; Field, J. A., Chemical bromination of phenol red by hydrogen peroxide is possible in the absence of haloperoxidases. *Chemosphere* **1998**, *36* (6), 1445-1452.

## 3.3.7 Supporting Information

## Figures

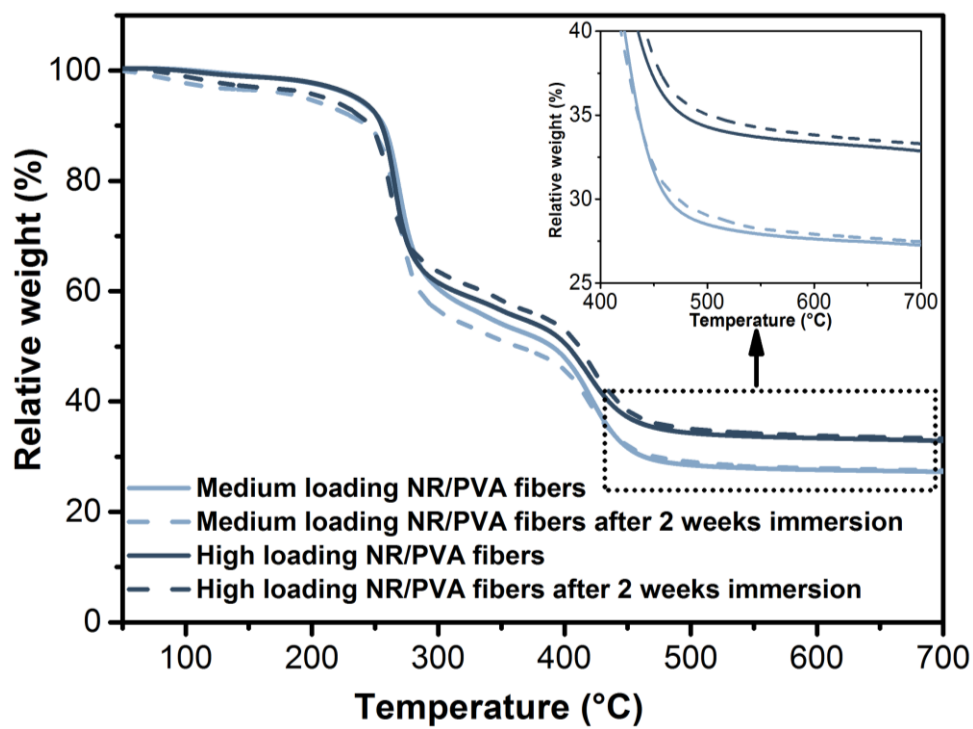


**Figure S1.** TGA curves of the CeO<sub>2-x</sub> NR/PVA membranes with different NR loadings (11% and 17%) before and after immersion in water for 2 weeks.

### 3. Results and Discussion

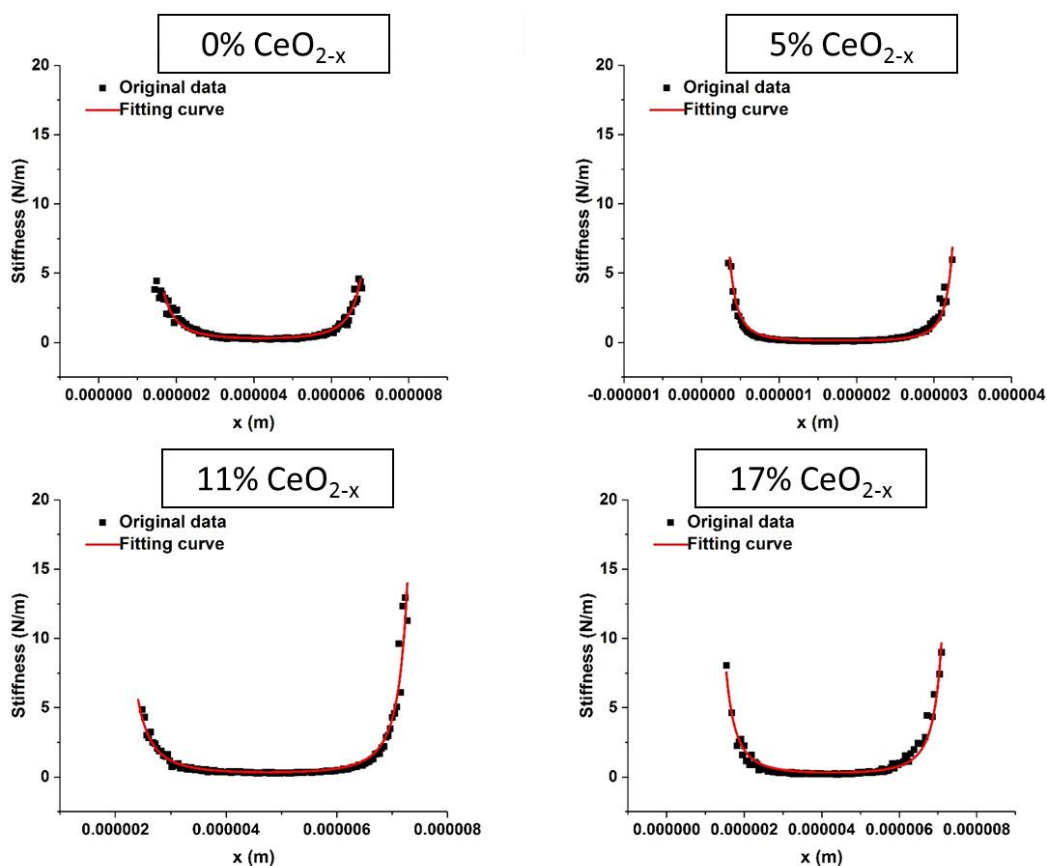


**Figure S2.** Stiffness profiles of single CeO<sub>2-x</sub> NR/PVA fibers with different NR loadings (0%, 5%, 11%, and 17%). The black points are the stiffness data extracted from the QI AFM images and red lines are fits using beam bending theory for a cylindrical fiber clamped at both ends (double clamped beam model, DCBM, equation (2) in main text).

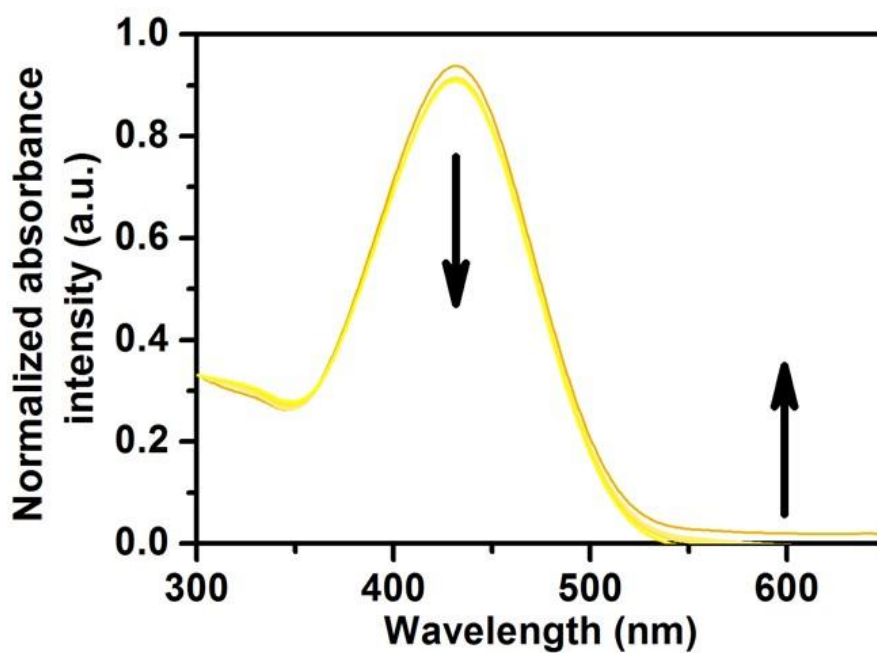


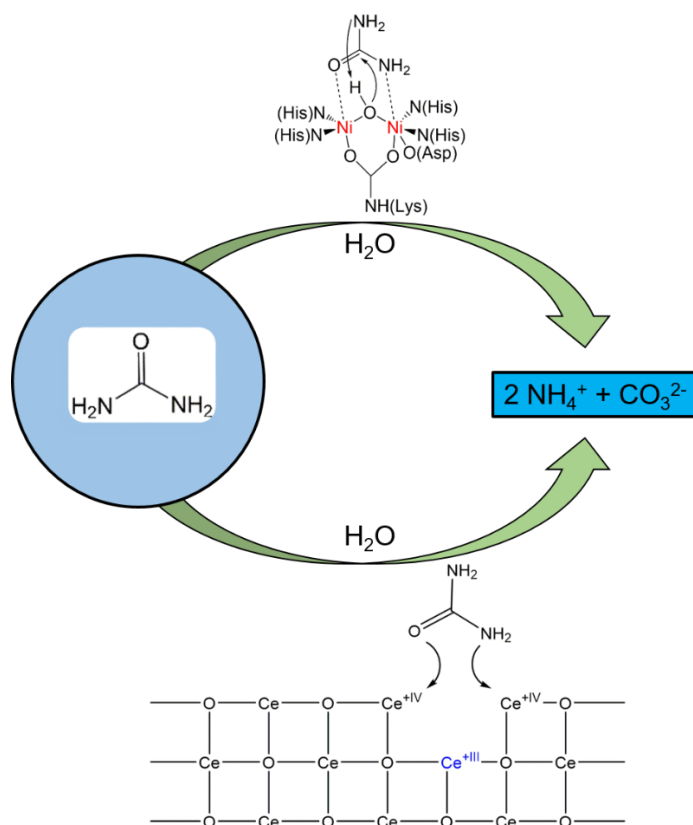
**Figure S3.** Time-dependent UV/vis spectra of PVA membranes without CeO<sub>2-x</sub> nanorods loading. ( $2.8 \times 10^{-5}$  mol/L of phenol red,  $4.4 \times 10^{-3}$  mol/L of NH<sub>4</sub>Br,  $4.2 \times 10^{-4}$  mol/L of H<sub>2</sub>O<sub>2</sub>, 300 min, 23 – 25 °C).

## Tables

**Table S1.** Swelling ratios of PVA mats with different loading of CeO<sub>2-x</sub> nanorods

CeO <sub>2-x</sub> loading in PVA mats	0%	6%	14%	22%
Swelling ratio	188%	196%	188%	195%

### 3.4. CeO<sub>2-x</sub> Nanorods with Intrinsic Urease-Like Activity



In the current section a practical and time-efficient assay for measuring the catalytic activities of urease enzymes and their potential mimics is reported. We found that nanocerium (CeO<sub>2-x</sub> nanorods), facilitates the urea hydrolysis, comparable to the native urease enzyme.

The manuscript was accepted as manuscript for publishing in *Nanoscale* (*Nanoscale*. 2018, Accepted Manuscript, DOI: 10.1039/C8NR03556C). Conducted work was a cooperation with different colleagues. Thus, a detailed authorship contribution is attached in the appendix (chapter 5.3.4).

Thank you very much Sven Kurch for help with BET and TEM measurements, Regine Jung-Pothmann with XRD analysis, Michael Steiert for ICP-MS, Karl-Kopp with the XPS experiments and Stefanie Klassen for AFM measurements.

### 3.4.1 Abstract

The large-scale production and ecotoxicity of urea make its removal from wastewater a health and environmental challenge. Whereas the industrial removal of urea relies on hydrolysis at elevated temperatures and high pressure, nature solves the urea disposal problem with the enzyme urease under ambient conditions. We show that CeO<sub>2-x</sub> nanorods (NRs) act as the first and efficient green urease mimic that catalyzes the hydrolysis of urea under ambient conditions with an activity ( $k_{cat} = 9.58 \times 10^1 \text{ s}^{-1}$ ) about one order of magnitude lower than that of the native jack bean urease. The surface properties of CeO<sub>2-x</sub> NRs were probed by varying the Ce<sup>4+</sup>/Ce<sup>3+</sup> ratio through La doping. Although La substitution increased the number of surface defects, the reduced number of Ce<sup>4+</sup> sites with higher Lewis acidity led to a slight decrease of their catalytic activity. CeO<sub>2-x</sub> NRs are stable against pH changes and even to the presence of transition metal ions like Cu<sup>2+</sup>, one of the strongest urease inhibitors. The low costs and environmental compatibility make CeO<sub>2-x</sub> NRs a green urease substitute that may be applied in polymer membranes for water processing or filters for the waste water reclamation. The biomimicry approach allows the application of CeO<sub>2-x</sub> NRs as functional enzyme mimics where the use of native or recombinant enzyme is hampered because of its costs or operational stability.

### 3.4.2 Introduction

Urea is one of the world's most produced chemicals. 90% of the worldwide production of 200 million tons *per* year is used in the fertilizer industry. The remaining 20% is used as raw material for the synthesis of chemicals.<sup>1</sup> Diesel engines require urea in selective catalytic reduction (urea-SCR) systems, where ammonia, converted from aqueous urea solutions (AdBlue<sup>®</sup>), is used as reductant for nitrogen oxides (NO<sub>x</sub>).<sup>2,3</sup> Urea enters the environment through wastewater from production plants. Fertilizer run-off from fields and agro-breeding farms into rivers and lakes can trigger ocean algae blooms that are toxic to aquatic life.<sup>3-6</sup>

The large-scale production and ecotoxicity of urea makes its premature release<sup>7-8</sup> and removal from wastewater a major environmental problem.<sup>9</sup> As a polar non-ionic compound urea is highly water soluble and shows little affinity to common sorbents. Its industrial removal relies on chemical hydrolysis, which requires complex technical equipment, elevated temperatures and high pressures. Catalytic and electrochemical decomposition or oxidation with strong oxidants are other alternatives, but have high operational costs.<sup>3,9</sup>

Nature solves the urea elimination problem through bio-catalysis with ureases. This group of enzymes catalyzes the hydrolysis of urea to ammonia and carbamate, which degrades in a second step to ammonia and carbonic acid.<sup>10,11</sup> Native urease from jack-beans is a nickel-dependent metalloenzyme with a catalytic rate approximately 10<sup>14</sup> times the rate of the non-catalyzed reaction.<sup>12</sup> The only structural enzyme model was reported by Krebs and coworkers.<sup>13</sup>

Natural ureases are encountered in bacteria, fungi and algae.<sup>14</sup> Recombinant ureases are used in nitrogen containing fertilizers,<sup>1</sup> in food chemistry for the degradation of ethyl carbamate in wine and sherry production,<sup>15</sup> in anticancer therapy<sup>16</sup> and antifungal applications.<sup>17</sup> Shortcomings in large scale utilization are enzyme stability, shelf life and production costs. Immobilization on solid supports allows the separation of urease from reaction media, a strategy used in biotechnology for batch or continuous



processes. Immobilized enzymes show enhanced resistance to changes in reaction conditions (pH, flow conditions, temperature stability).<sup>18</sup>

These drawbacks related to using natural enzymes can be circumvented using enzyme mimics, but only a single metal complex with low activity has been reported.<sup>13</sup> Enzyme mimics based on nanomaterials are - different from natural enzymes and metal complexes – cost-efficient, stable over a wide pH and temperature range, and their activities match - or even excel - those of their natural blueprints.<sup>19-21</sup> However, from the different enzyme classes (oxidoreductases, transferases, hydrolases, lyases, isomerases, ligases) virtually only oxidoreductases,<sup>20-21</sup> but no hydrolytic enzymes have been explored.

From a “green” perspective, urea hydrolysis at ambient temperature is an attractive goal. The versatile activity of ceria as solid catalyst in organic chemistry<sup>22</sup> and the enzyme-like activity of CeO<sub>2-x</sub> nanoparticles as peroxidase,<sup>23</sup> catalase,<sup>24</sup> superoxide dismutase,<sup>25,26</sup> oxidase,<sup>27</sup> haloperoxidase<sup>28</sup> or phosphatase<sup>29</sup> mimics inspired us to explore the urease activity of CeO<sub>2-x</sub> NRs.

The redox activity of CeO<sub>2-x</sub> NRs is based on intrinsic lattice defects. Due to the associated lattice strain these defects accumulate at the particle surfaces, where they reversibly bind oxygen and switch between the Ce<sup>3+</sup> and Ce<sup>4+</sup> states.<sup>30</sup> Lewis acid–base properties of ceria are similarly important for activating organic molecules. Here Ce<sup>4+</sup> cations can function as *acidic* (base adsorption) or *basic* sites (CO<sub>2</sub> adsorption) *via* hydroxyl groups and surface lattice oxide anions.<sup>31</sup> The acid-base properties of ceria have been demonstrated by condensation reactions that are catalyzed by Brønsted or Lewis acids<sup>32</sup> or the SCR reaction of NO, O<sub>2</sub>, and NH<sub>3</sub>.<sup>2,3</sup>

We demonstrate a green route to the hydrolysis of urea under ambient conditions with  $\text{CeO}_{2-x}$  NRs that exhibit a high intrinsic urease-like activity, which is comparable to that of the native enzyme. For the analysis a timesaving method for determining urease activities was devised. The  $\text{Ce}^{3+}/\text{Ce}^{4+}$  surface ratio, which is essential for the urease activity of  $\text{CeO}_{2-x}$  NRs, was tailored by La substitution. The hydrolytic activity was unaffected by typical enzyme inhibitors (heavy metals).  $\text{CeO}_{2-x}$  NRs act as acidic hydrolase, and they are the first reported functional urease mimic (Fig. 1). The low costs, high shelf-life and environmental compatibility of ceria allow a broad application as green enzyme substitute.

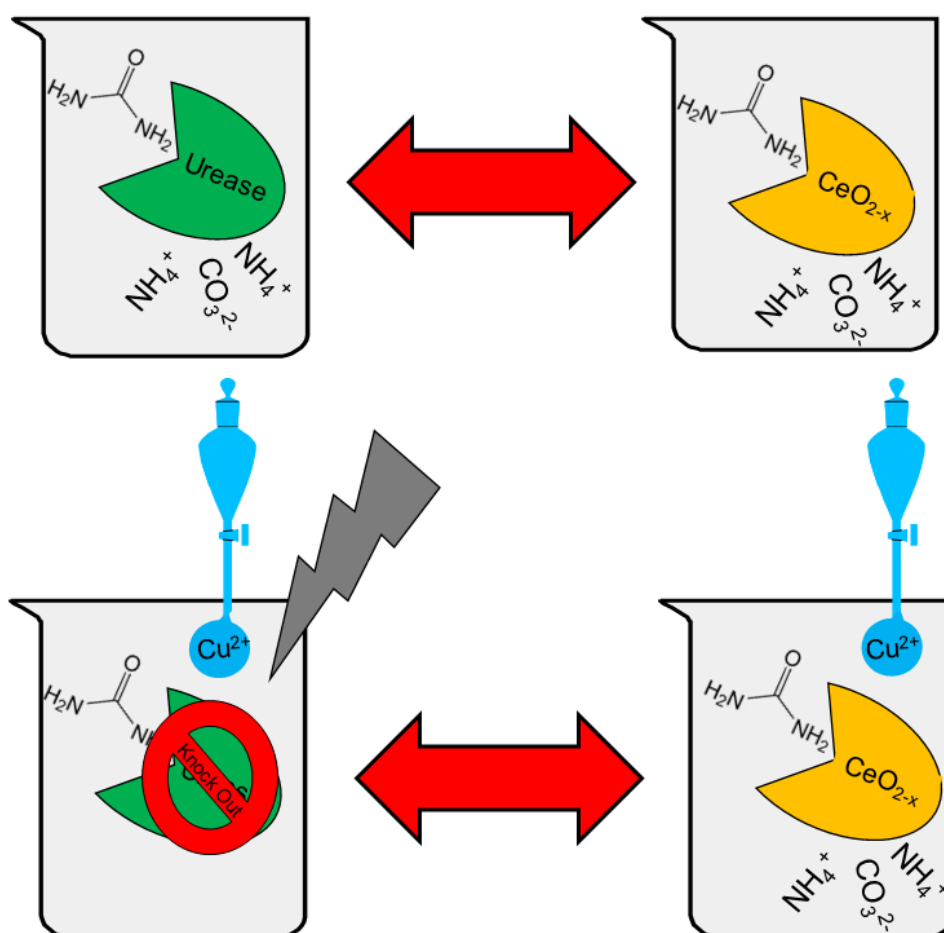


**Fig. 1. Schematic representation of  $\text{CeO}_{2-x}$  NRs and their urease-like activity.**  $\text{CeO}_{2-x}$  NRs mimic the reactions of native urease with an activity comparable to that of native jack bean urease. While  $\text{Cu}^{2+}$ , one of the strongest inhibitors, blocks the activity of native ureases completely, the  $\text{CeO}_{2-x}$  enzyme mimic remained completely unaffected.

### 3.4.3 Experimental

**Chemicals.** The following chemicals were used without further purification: Cerium(III) nitrate hexahydrate 99% from Fluka, sodium hydroxide, phenol red (PR) and sulfuric acid from Sigma-Aldrich, lanthanum(III) nitrate hexahydrate 99.9%, vanadium(IV) oxide sulfate hydrate from ABCR, bulk cerium(IV) oxide from Alfa Aesar, Urease from *Canavalia Ensiformis* (Jack bean and phosphate buffer from Sigma, urea and copper(II) chloride dihydrate from Acros and elemental standard solutions (stock concentration  $1\text{ g L}^{-1}$ ) from Merck Certipur, nickel(II) acetate tetrahydrate 98%, bis(acetylacetonato) dioxomolybdenum (VI), glycine, Fomblin Y from Aldrich, potassium bromate, sodium hydroxide from Sigma-Aldrich and  $\text{TiO}_2$  from Degussa.

**Synthesis of  $\text{CeO}_{2-x}$  nanorods.** 2 mmol of cerium(III) nitrate hexahydrate were dissolved under argon atmosphere in 5 mL of water. After the addition of 20 mL of a 6 M sodium hydroxide solution, the reaction mixture was stirred for 30 min. In the next step, the reaction mixture was transferred into a Teflon<sup>®</sup> inlay which was placed in a 50 mL stainless steel autoclave. The autoclave was placed in an electric oven which was heated to 373 K for 24 h. After cooling to room temperature, the precipitates were isolated *via* ultracentrifugation (9000 rpm, 10 min) and the  $\text{CeO}_{2-x}$  nanorods (NRs) were washed several times with water and ethanol. The product was dried at 333 K for 24 h.<sup>33</sup>

**Synthesis of lanthanum-substituted cerium dioxide nanorods.** Cerium(III) nitrate hexahydrate and lanthanum(III) nitrate hexahydrate were dissolved in the appropriate amounts in 7.5 mL of water under argon atmosphere. After adding 10 mL of a 12 M sodium hydroxide solution the reaction mixture was stirred for 30 min. The solution was transferred into a Teflon<sup>®</sup> inlay that was placed in a 50 mL stainless steel autoclave. The autoclave was placed in an electric oven for 24 h at 373 K. After cooling to room temperature, the precipitate was isolated *via* ultracentrifugation (9000 rpm, 10 min). The product was washed with water and ethanol several times. The NRs were finally dried at 333 K for 24 h.<sup>34</sup>

**Synthesis of MoO<sub>3-x</sub> nanobelts.** MoO<sub>3-x</sub> nanobelts were synthesized as reported elsewhere.<sup>35</sup> 5.5 mmol of molybdenum acetylacetonate were dissolved in 200 mL of water at 313 K. The solution was transferred into a 250 mL Teflon<sup>®</sup>-lined vessel. The vessel was sealed in a stainless steel autoclave, and the reaction was carried out in an electric oven for 20 h at 453 K. The autoclave was cooled naturally to room temperature, and the precipitate was isolated *via* ultracentrifugation (9000 rpm, 10 min.). The product was washed with water several times and dried for 24 h in a desiccator.

**Synthesis of V<sub>2</sub>O<sub>5</sub> nanowires.** V<sub>2</sub>O<sub>5</sub> nanowires were prepared with a method reported before<sup>36</sup> with slightly modifications. 8.0 mmol of vanadium(IV) oxide sulfate hydrate (VOSO<sub>4</sub>·nH<sub>2</sub>O) and 5.0 mmol of potassium bromate (KBrO<sub>3</sub>) were dissolved in 25 mL of water. The green reaction mixture turned red within three minutes (see Supporting Information). The dispersion was stirred for 30 minutes at room temperature. Subsequently, 2 mL of nitric acid were added over a period of one hour until the solvent was dissolved. The red brown solution was transferred into a 50 mL Teflon<sup>®</sup>-lined vessel, which was set into a stainless steel autoclave. The autoclave was placed in an electric oven and heated to 453 K for 24 h. Afterwards it was naturally cooled to room temperature and the yellow precipitate was collected *via* ultracentrifugation (9000 rpm, 10 min.). The product was washed with water and ethanol for several times and dried for 24 h in a desiccator.

**Synthesis of Ni(Gly)<sub>2</sub> dihydrate.** The Ni(Gly)<sub>2</sub> complex was synthesized with a method reported by O'Brien.<sup>37</sup> We changed the metal site from Cu to Ni. Ni(Gly)<sub>2</sub> was synthesized by dissolving 0.2 mol of glycine (Gly) and 0.2 mol of sodium hydrogen carbonate in 250 mL of water at 343 K. In a separate flask 0.1 mol of nickel(II) acetate were dissolved in 250 mL of water at 343 K. The amino acid solution was transferred to the nickel(II) salt solution. After adding 250 mL ethanol the mixture was cooled to 273 K and the precipitates were isolated by vacuum filtration. The product was washed with ethanol and dried for 24 h *in vacuo*. The isolated and purified product was analyzed by IR spectroscopy and elemental analysis. Yield: 19.46 g (80%) purple crystals. Elemental analysis calculated for NiC<sub>4</sub>H<sub>12</sub>N<sub>2</sub>O<sub>6</sub> (242,84 g/mol): 19.78 % C, 4.98 % H, 11.54 % N. Found: 19.73 % C, 4.95 % H, 11.42 % N. IR ( $\tilde{\nu}$ ): 3325, 3270, 3168, 2980, 2936, 1573, 1434, 1405, 1348, 1301, 1181, 1091, 1048, 948, 914, 781, 736, 673 cm<sup>-1</sup>.

**Synthesis of Gly-Ni(OH)<sub>2</sub> nanoparticles.** The synthesis of the glycine functionalized Ni(OH)<sub>2</sub> NPs was conducted on a synthesis route which was reported earlier for Gly-Cu(OH)<sub>2</sub> NPs.<sup>38</sup> Gly-Ni(OH)<sub>2</sub> nanoparticles were synthesized from Ni(Gly)<sub>2</sub>. 4 mmol of the precursor were dissolved in 130 mL of water under constant stirring. After 15 min 6 mL of a 1.2 M sodium hydroxide solution were added with a 12 mL syringe, and the reaction mixture was stirred for 120 minutes. The resulting precipitate was isolated *via* ultracentrifugation, and the product was washed several time with water and ethanol. The NPs were dried *in vacuo* for 24 h. IR ( $\tilde{\nu}$ ): 3639, 1584, 1394 und 1336 cm<sup>-1</sup>.

**Kinetic analysis of urease activity.** The urease activity of the tested materials was measured with an Infinite 200 Pro Plate reader from TECAN and 96 well plates (clear) from Greiner bio-one. To determine urease activities, the following stock solutions were prepared in 0.066 M phosphate buffer solution (pH = 7.4). Phenol red solution: 29.4 mg L<sup>-1</sup>; urea solution: 2.94 M; urease solution: 0.1 mg/mL; nanorod solution: 1 mg mL<sup>-1</sup>. All measurements were conducted at 298 K.

Kinetic analysis of urease-like activity was performed with a 96 well plate reader and a total volume of 300  $\mu$ L for each well. Each concentration was measured three times. Blank measurements were conducted for all test series. Calibration was carried out for all tests by measuring the absorption of phenol red at 560 nm for different concentrations of ammonium carbonate (stock solution, 0.1 M).<sup>39</sup>

Kinetic analysis of the catalysts was conducted by monitoring the absorption change at 560 nm over a period of 4 min for the nanorods and 3 min for native urease (based on the activities). The slope was transformed into molar concentrations of generated ammonium carbonate with the calibration plot. Enzyme/NR concentrations were varied systematically. Each well contained 100  $\mu$ L of phenol red solution and 50  $\mu$ L of urea solution. The volume of enzyme/NR solution was filled up with PBS buffer to 300  $\mu$ L. The amount of urea was varied systematically using optimized catalyst concentrations.

**Scanning Kinetics.** The scanning kinetics was measured with a Cary Varian 5G UV-Vis-NIR spectrometer using a 2 mL glass cuvette. The solution was prepared with 933  $\mu$ L PR solution, 467  $\mu$ L urea solution, 467  $\mu$ L PBS buffer and 933  $\mu$ L of the appropriate catalyst solution. Scans were recorded in 1 min intervals over a period of 10 min for urease and 30 min for the NRs, respectively.

**Leaching tests.** The dissolution behaviors of  $\text{CeO}_{2-x}$  and La-doped cerium oxide nanorods were investigated in MilliQ water and in 2.94 M urea solution. Before the tests, the equipment (tubes, pipette tips, agitators) was leached in sub boiled nitric acid (1.3%) for one week. The membranes were previously leached in MilliQ water. The tubes were filled with MilliQ water or urea solution, and 1 mL of the particle stock solution ( $2 \text{ mg mL}^{-1}$ ) were added to the membrane pipes. The pipes were fixed at the top of the tubes in such a way that the NP containing part of the membrane were immersed in the solvent. The solution was stirred throughout the experiment. After ten days the membrane was removed, 50  $\mu\text{L}$  rhodium standard solution (employed as internal standard for drift correction during ICP-MS measurements; final rhodium concentration in samples:  $5 \text{ } \mu\text{g L}^{-1}$ ) and 1 mL of nitric acid were added. The tube was finally filled up with MilliQ water or urea solution to a total volume of 50 mL. Calibration (0.1, 0.5, 1, 5, 10, 15, 20, 30  $\mu\text{g L}^{-1}$ , either in MilliQ water, or urea solution (for matrix matching) each containing 1.3%  $\text{HNO}_3$  (v/v)) was conducted with Ce and La standard solutions. Rh was added as internal standard for drift correction (final rhodium concentration:  $5 \text{ } \mu\text{g L}^{-1}$ ). For blank samples either MilliQ water or urea solution (containing  $5 \text{ } \mu\text{g L}^{-1}$  Rh as well as 1.3%  $\text{HNO}_3$  (v/v)) were taken. ICP-MS measurements were conducted with an Element 2 from Thermo Scientific (Bremen, Germany). The following isotopes were monitored:  $^{140}\text{Ce}$ ,  $^{139}\text{La}$ ,  $^{103}\text{Rh}$ .

**Inhibition of urease-like activity.** The inhibiting effect of  $\text{Cu}^{2+}$  ions on the catalytic activity of native jack bean urease,  $\text{CeO}_{2-x}$ ,  $\text{Ce}_{0.9}\text{La}_{0.1}\text{O}_{1.95-x}$  and  $\text{Ce}_{0.6}\text{La}_{0.4}\text{O}_{1.80-x}$  was analyzed with a 96 well-plate reader. Every well contained 50  $\mu\text{L}$  of urea solution, 100  $\mu\text{L}$  of PR, 20  $\mu\text{L}$  of a  $\text{CuCl}_2$  solution ( $0.1 \text{ mg mL}^{-1}$ ). The solution was filled up with buffer to a total volume of 300  $\mu\text{L}$ . The absorbance change at 560 nm, representing the urea degradation (analogous to the kinetic analysis) was monitored over a period of 3 minutes.

**Analysis of the La content in La-substituted samples.** The amount of La in the La-doped NRs was analyzed using inductively coupled plasma-mass spectrometry (ICP-MS). The NPs were dissolved using 1 M nitric acid. For ICP-MS measurements an Agilent 7900 was used.

**Transmission electron microscopy (TEM).** TEM analysis of cerium dioxide, lanthanum doped cerium oxide, vanadium pentoxide, titanium oxide and molybdenum oxide nanoparticles were conducted with a transmission electron microscope FEI Tecnai G2 Spirit with an acceleration voltage of 120 kV, using a LaB<sub>6</sub> cathode. TEM images of the Gly-Ni(OH)<sub>2</sub> particles were taken with a Zeiss LEO 906E TEM with an acceleration voltage of 120 kV (Carl Zeiss, Oberkochen, Germany).

**HR-TEM analysis.** HR-TEM images were recorded with a Tecnai F20 of the company FEI using an acceleration voltage of 200 kV. EDX analysis were carried out using EDAX.

**Brunauer/Emmett/Teller (BET) method.** BET measurements were conducted using the gas adsorption setup Autosorb-6B from Quantachrome with nitrogen as analysis gas. The temperature during the measurements was 77 K. Data evaluations were conducted with the software Quantachrome ASiQWin 3.0.

**Powder X-ray diffractometry.** Powder X-ray diffraction measurements were conducted on a Siemens D5000 diffractometer with a Ge (220) monochromator using Cu K<sub>α</sub>-radiation. The data was analyzed using the EVA software package.

**Rietveld Refinements.** The samples for solid state analysis were prepared on a perfluoropolyether film, using Fomblin<sup>®</sup> Y. Diffraction data were collected with a STOE Stadi P (Darmstadt) diffractometer using Mo K<sub>α1</sub>-radiation. The data analysis were analyzed using the EVA software package. Rietveld refinements (for details see below) were done with the *Topas Academic V6* (Coelho Software, Brisbane 2016).<sup>40</sup>



**Raman spectroscopy.** Raman spectra of  $\text{CeO}_{2-x}$  and  $\text{Ce}_{1-x}\text{La}_x\text{O}_{2-x/2}$  were recorded on a HL5R transmission spectrometer (Kaiser Optical). 532 nm laser excitation from a frequency doubled Nd:YAG Laser (Cobolt), operated at 6 mW laser power, was used. The spectral resolution is  $5\text{ cm}^{-1}$ , but the stability of the band position ( $\text{F}_{2g}$ ) of comparable ceria samples is better than  $0.3\text{ cm}^{-1}$ . The sampling time was 80s, and the spectra shown are the sum of 5 accumulations in total. Spectra are normalized to the intensity of the  $\text{F}_{2g}$  band.

**XPS spectroscopy.** XP spectra were recorded on a SSX 100 ESCA spectrometer (Surface Science Laboratories Inc.) equipped with a monochromatic Al  $\text{K}\alpha$  X-ray source (100 W). The X-ray spot size was 250–1000  $\mu\text{m}$ . The binding energy scale of the system was calibrated using  $\text{Au } 4f_{7/2} = 84.0\text{ eV}$  and  $\text{Cu } 2p_{3/2} = 932.67\text{ eV}$  from foil samples. Charging of the powder samples was accounted for by setting the peak of the C 1s signal to 285.0 eV. A Shirley background was subtracted from all spectra. Peak fitting was performed with Casa XPS using 70/30 Gauss–Lorentz product functions. Atomic ratios were determined from the integral intensities of the signals, which were corrected by empirically derived sensitivity factors

**Atomic force microscopy (AFM).** AFM measurements were conducted with a Cypher atomic force microscope from the company Asylum Research (Oxford Instruments, UK). The microscope was equipped with a cantilever TAP300GD-G from Budget Sensors. The samples were prepared by adding 15  $\mu\text{L}$  of a 1.2–1.3  $\text{mg mL}^{-1}$  suspension of the nanoparticles dropwise on mica. The sample was spin-coated with 30 rps. The microscope was used in the AC mode, recorded images were analyzed with the software Gwyddion. Data were levelled by deducting the middle plane and with a plane through three points. The color scale was stretched to the actual data interval.

### 3.4.4 Results and discussion

Cerium oxide ( $\text{CeO}_{2-x}$ ) nanorods (NRs) were synthesized at 373 K from an aqueous solution of cerium(III) nitrate and sodium hydroxide.<sup>33</sup> Size, morphology and phase homogeneity of  $\text{CeO}_{2-x}$  was investigated by (high-resolution) transmission electron microscopy (HR-TEM) (Fig. 2a, b). The X-ray diffractograms (Fig. 2 c) were fully indexed based on the intensities of  $\text{CeO}_2$ . Average NR sizes of 120 x 12 x 9 nm were determined from TEM micrographs (Fig. 2a) and AFM scans (Fig. S1, Supporting Information). The NRs consisted of smaller crystallites with sizes of 6.8 nm, as extracted from the Rietveld Refinements (Table S1, Supporting Information). The BET (Brunauer/Emmett/Teller) surface area of the  $\text{CeO}_{2-x}$  NRs was 100.2  $\text{m}^2 \text{g}^{-1}$ .

Energy dispersive X-ray (EDX) spectra (Fig. S2) showed the signals of Ce without any metal ion impurities. HR-TEM images (Fig. 2b) showed  $d$  spacings of  $\approx 0.3$  nm, corresponding to the (111) planes of the  $\text{CeO}_2$  structure. Selected area electron diffraction (SAED) patterns showed distinct rings, which could be indexed to the  $\text{CeO}_2$  structure, confirming polycrystallinity of the samples (inset to Fig. 2b).

The urease-like activities of native jack bean urease and  $\text{CeO}_{2-x}$  NRs were investigated with a spectrophotometric 96-well plate reader. Kinetic analysis of the catalyzed urea hydrolysis in a urease-like reaction is difficult because neither urea nor its decomposition products (ammonia and carbonate) absorb in the UV-Vis region. Therefore, urease assays are not well established.

As urea degradation catalyzed by native urease lead to a pH increase,<sup>41</sup> the pH change was monitored spectrophotometrically with phenol red.<sup>39</sup> The kinetic studies were conducted in highly diluted phosphate buffered solution (PBS 0.066 M) to allow the analysis of high urease and urea concentrations. Monitoring small pH changes in buffered solution has been used in related assays.<sup>39,42</sup> The activity of native urease in water could be measured for very low concentrations because urease becomes inactivated at high pH values. Kinetic absorption measurements (of phenol red) recorded as a function of time demonstrated the effect of urea degradation by native urease. While the intensity of the band at 434 nm decreased with time in the presence

of native urease and the intensity of the band at  $\lambda_{\text{max}} = 560$  nm increased (Fig. 3a), controls in the absence of the native enzyme or  $\text{CeO}_{2-x}$  NRs showed no significant spectral change (Fig. S3). The change of absorption allowed monitoring the progress of the reaction after calibration with 0.1 M  $(\text{NH}_4)_2\text{CO}_3$  solution (Fig. S4). The linear calibration fit links the absorption change of phenol red (at  $\lambda_{\text{max}} = 560$  nm) and the generated (or added) of ammonium carbonate.<sup>39</sup> The catalytic activities of native urease and the  $\text{CeO}_{2-x}$  urease mimic were analyzed by varying the concentrations. Other metal oxides with high-valent acidic metal center were studied for comparison:  $\text{MoO}_{3-x}$  nanobelts (characterization: Fig. S5-S6),<sup>35</sup>  $\text{V}_2\text{O}_5$  nanowires (characterization: Fig. S7-S8),<sup>36</sup> commercial  $\text{TiO}_2$  nanoparticles and glycine functionalized  $\text{Ni}(\text{OH})_2$  (Gly- $\text{Ni}(\text{OH})_2$ ) NPs (characterization: Fig. S9-S13)<sup>38</sup> as analogue of Ni complexes as structural urease mimics<sup>13</sup> were studied concerning their ability to catalyze urea hydrolysis. None of these compounds showed a significant urease-like activity.

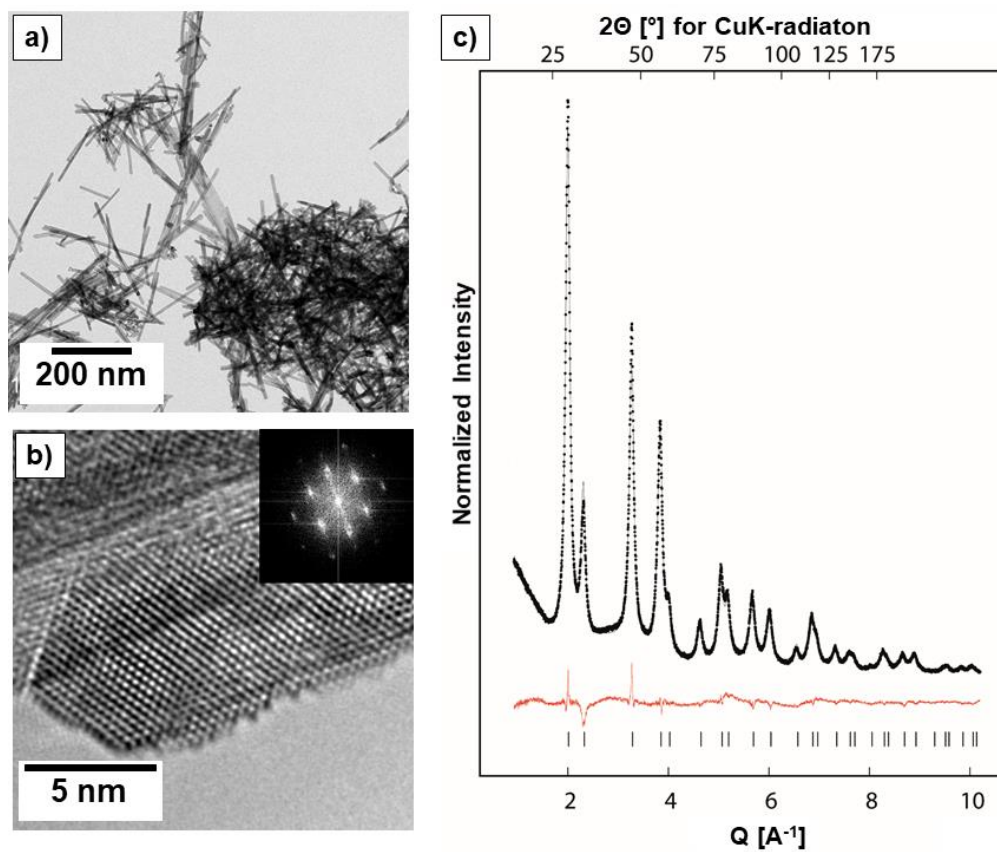


**Fig. 2. Structural characterization of as-synthesized  $\text{CeO}_{2-x}$  NRs.** TEM (a) and HR-TEM images (b) of  $\text{CeO}_{2-x}$  NRs. P-XRD diffractogram (c) with Rietveld refinement (black line) on the diffraction data (red dots) and difference between the measured and calculated profile (red line) for cubic  $\text{CeO}_{2-x}$ .

The hydrolysis of urea could be related to the molar concentration of  $(\text{NH}_4)_2\text{CO}_3$ . Higher amounts of native urease showed a faster urea degradation (Fig. S14). By varying the urea concentration with a fixed amount of enzyme a Michaelis-Menten behavior was derived for native urease (Fig. 3c). With a modified Hill plot the maximum reaction rate  $v_{max} = 2.3 \times 10^{-2} \text{ mM}\cdot\text{s}^{-1}$  and a catalytic turnover number  $k_{cat} = 2.74 \times 10^3 \text{ s}^{-1}$  (298 K) were determined. The results are in harmony with reported values for the native jack bean urease enzyme.<sup>43</sup>

Investigations of  $\text{CeO}_{2-x}$  NRs as urease mimic showed that increasing NR concentrations led to an enhanced urea degradation (Fig. S15). Reactions for  $\text{CeO}_{2-x}$  monitored with fixed catalyst concentrations showed a Michaelis-Menten-like behavior, which is similar to the natural enzyme (Fig. 3d). The plotted data were fitted with a modified Hill-equation to derive turnover numbers based on the model of native enzymes.<sup>44</sup> Catalytic turnover numbers  $k_{cat}$  were calculated for molar NR concentrations, which is a common and widely used approach in enzyme mimetics.<sup>19,38,45,46</sup> The  $k_{cat}$  value is defined as a normalization of  $v_{max}$  to the enzyme concentration  $[\text{E}]$ .<sup>47</sup> The as-calculated turnover number  $k_{cat} = 9.58 \times 10^1 \text{ s}^{-1}$  for  $\text{CeO}_{2-x}$  is about one order of magnitude smaller than that of native urease. In addition to the turnover number (normalized to molar NR concentrations) we determined the catalytic activity normalized to the BET surface area, resulting in a turnover number of  $1.60 \times 10^{-4} \text{ mmol s}^{-1} \text{ m}^{-2}$ .<sup>28</sup> Bulk  $\text{CeO}_{2-x}$  showed no activity because of its lower surface area compared to  $\text{CeO}_{2-x}$  nanoparticles.

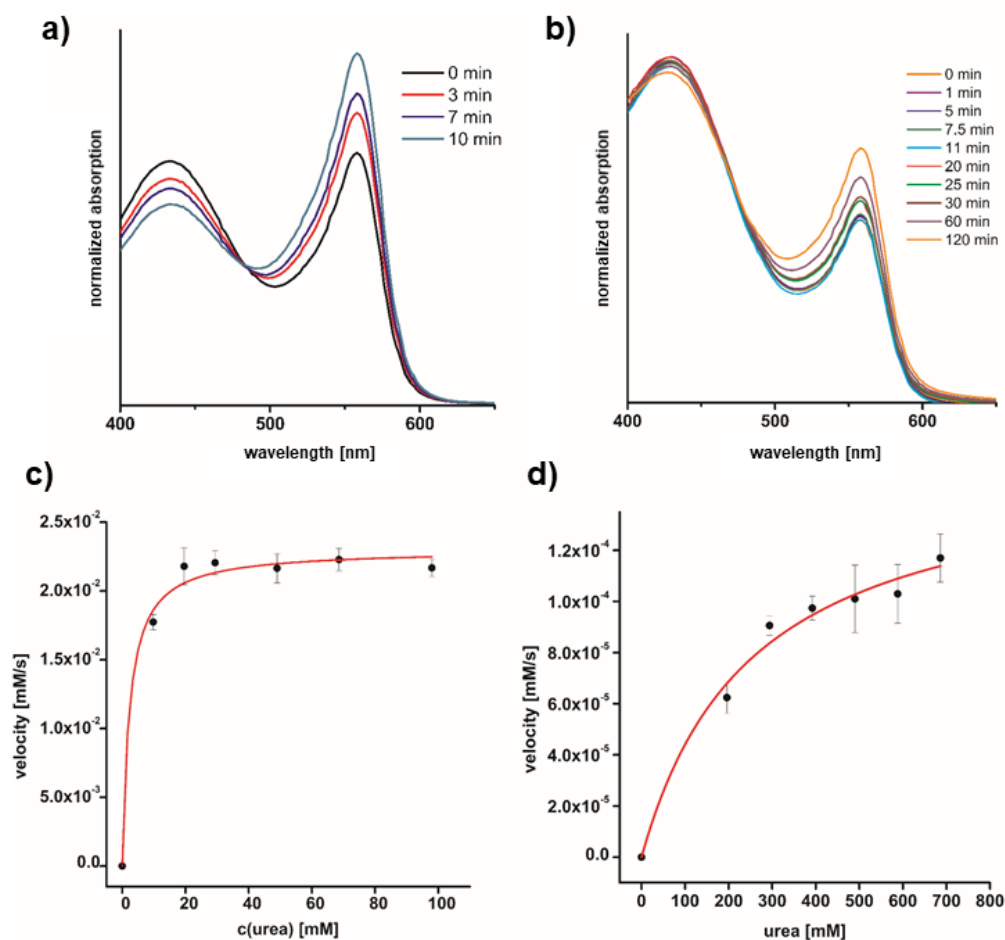


**Fig. 3. Urease activity of native jack bean urease and CeO<sub>2-x</sub> NRs.** Scanning kinetics conducted with native urease (a) and CeO<sub>2-x</sub> NRs (b) show a decrease of the band at  $\lambda = 434$  nm and the simultaneous increase of the intensity of the absorption band at  $\lambda = 560$  nm, confirming the degradation of urea and the pH increase because of a urease-like activity. Both spectra are normalized. Variation of the urea concentrations lead to a typical Michaelis-Menten behavior for native urease (c) and for CeO<sub>2-x</sub> NRs (d). The recorded data were fitted with a modified Hill equation and maximum reaction rates  $v_{max}$  and catalytic turnover numbers  $k_{cat}$  were calculated for a  $8.39 \times 10^{-6}$  mM urease concentration ( $v_{max} = 2.3 \times 10^{-2}$  mM s<sup>-1</sup>;  $k_{cat} = 2.74 \times 10^3$  s<sup>-1</sup> at 298 K) (d), CeO<sub>2-x</sub> ( $C_{NR} = 1.67 \times 10^{-6}$  mM;  $v_{max} = 1.60 \times 10^{-4}$  mM·s<sup>-1</sup>;  $k_{cat} = 9.58 \times 10^1$  s<sup>-1</sup>) (e). The larger error bars of the NR measurements (d) compared to (c) are caused by scattering due to settling of the not soluble catalyst. Turnover numbers of the nanorods are for molar particle concentrations. Kinetic data and errors are averages of three individual measurements.

**Effect of surface defects on the urease-like activity of nanoceria.** The catalytic activity of  $\text{CeO}_{2-x}$  nanoparticles in redox processes is determined by the  $\text{Ce}^{4+}/\text{Ce}^{3+}$  ratio at the nanoparticle surface.<sup>24,25,48</sup> The  $\text{Ce}^{4+}/\text{Ce}^{3+}$  mixed valency of cerium is associated with the presence of oxide surface defects. Substitution of  $\text{Ce}^{4+}$  by  $\text{La}^{3+}$  ions allowed “tuning” the number of defects in a quasi-stoichiometric manner.<sup>34</sup> The  $\text{Ce}^{4+}/\text{Ce}^{3+}$  ratio strongly affects the activity of  $\text{CeO}_{2-x}$ . To study the effect of different  $\text{Ce}^{4+}/\text{Ce}^{3+}$  surface ratio, lanthanum doped cerium oxide NRs with Ce/La ratios of 0.9/0.1 and 0.6/0.4 were synthesized. After addition of sodium hydroxide, the reaction mixture was transferred to a stainless steel autoclave and heated to 373 K for 24 h.<sup>34</sup> The La-doped cerium dioxide samples were characterized in the same manner as the corresponding  $\text{CeO}_{2-x}$  NRs. The composition of as-synthesized  $\text{Ce}_{1-x}\text{La}_x\text{O}_{2-x/2}$  NRs was analyzed using inductively coupled plasma (ICP) mass spectrometry. The synthesis performed with a Ce:La ratio of 0.8:0.2 led to a final composition of 0.86:0.14, and a starting ratio of 0.6:0.4 led to a final composition ratio of 0.62:0.38 (average values from three individual measurements). For the sake of simplicity we use the formulae  $\text{Ce}_{0.9}\text{La}_{0.1}\text{O}_{1.95-x}$  and  $\text{Ce}_{0.6}\text{La}_{0.4}\text{O}_{1.80-x}$ . In the sequel, the characterization of  $\text{Ce}_{0.9}\text{La}_{0.1}\text{O}_{1.95-x}$  is demonstrated in detail and compared with that of “undoped”  $\text{CeO}_{2-x}$  NRs. The analytical data for  $\text{Ce}_{0.6}\text{La}_{0.4}\text{O}_{1.80-x}$  are in harmony with the second composition and listed in the supporting information (Fig. S16 – S21).

EDX spectra of  $\text{Ce}_{0.9}\text{La}_{0.1}\text{O}_{1.95-x}$  and  $\text{Ce}_{0.6}\text{La}_{0.4}\text{O}_{1.80-x}$  NRs show the signals of Ce and La without metal impurities (Fig. S18, S22), indicating the presence of La (and Ce) in the sample. Average NR dimensions (acquired for  $\text{Ce}_{0.9}\text{La}_{0.1}\text{O}_{1.95-x}$ ) were 115 x 20 x 9 nm and 118 x 12 x 9 nm for  $\text{Ce}_{0.6}\text{La}_{0.4}\text{O}_{1.80-x}$ , based on TEM (average for  $\approx 100$  particles, Fig. 4a, Fig. S16) and AFM (Fig. S23). The BET surface areas for  $\text{Ce}_{0.9}\text{La}_{0.1}\text{O}_{1.95-x}$  NRs were 120.8  $\text{m}^2/\text{g}$  and for  $\text{Ce}_{0.6}\text{La}_{0.4}\text{O}_{1.80-x}$  NRs 136.2  $\text{m}^2/\text{g}$ . Rietveld refinements for  $\text{Ce}_{0.9}\text{La}_{0.1}\text{O}_{1.95-x}$  demonstrated that the NRs consisted of smaller crystallites with individual sizes of  $\approx 6.9$  nm. Both  $\text{Ce}_{1-x}\text{La}_x\text{O}_{2-x/2}$  NR samples were analyzed by HR-TEM with  $d$  spacings of  $\approx 0.3$  nm.  $d$  spacings for the La-doped samples had essentially identical values as for the binary  $\text{CeO}_{2-x}$  NRs. HR-TEM analysis revealed the presence of defects/vacancies preferentially at the particle

surfaces (Fig. 4b and Fig. S17, red marks). This is consistent with the ionic radii of  $\text{La}^{3+}$  and  $\text{Ce}^{3+}$  (1.16 and 1.14 Å) which are incompatible with the 8 coordination of  $\text{Ce}^{4+}$  (0.97 Å) in the  $\text{CeO}_2$  structure.<sup>49</sup> Charge compensation requires the presence of oxide defects at the particle surface. Thus, the NRs have a higher surface energy than the bulk material because of the incomplete coordination of the metal atoms and the increased surface area. SAED patterns show discrete rings, which can be indexed to the  $\text{CeO}_2$  structure, similar to  $\text{CeO}_{2-x}$  (insets to Fig. 5b). The defects in  $\text{CeO}_{2-x}$ ,  $\text{Ce}_{0.9}\text{La}_{0.1}\text{O}_{1.95-x}$  and  $\text{Ce}_{0.6}\text{La}_{0.4}\text{O}_{1.80-x}$  NRs were probed by Raman spectroscopy (Fig. 5d and Fig. S20). Raman bands at  $\approx 540$  and  $\approx 600$   $\text{cm}^{-1}$  are associated with oxygen defects indicating a higher defect density for the  $\text{Ce}_{1-x}\text{La}_x\text{O}_{2-x/2}$  NRs.<sup>50</sup> This is corroborated by the observed red-shift of the  $\text{F}_{2g}$  position for  $\text{Ce}_{1-x}\text{La}_x\text{O}_{2-x/2}$  NRs (inset of Fig. 4d). The 3d x-ray photoelectron spectra (XPS) of  $\text{CeO}_{2-x}$  and  $\text{Ce}_{0.9}\text{La}_{0.1}\text{O}_{1.95-x}$  NRs (Fig. 2e) show the presence of Ce in the +3 and +4 oxidation states and a larger amount of  $\text{Ce}^{3+}$  at the surface for  $\text{Ce}_{0.9}\text{La}_{0.1}\text{O}_{1.95-x}$  (by comparison with reference compounds).<sup>51</sup> Quantitative XPS analysis revealed a La/Ce surface ratio of 0.16 for  $\text{Ce}_{0.9}\text{La}_{0.1}\text{O}_{1.95-x}$  and O/Ce and O/(Ce+La) surface ratios of 1.72 for  $\text{CeO}_{2-x}$  and 1.57 for  $\text{Ce}_{0.9}\text{La}_{0.1}\text{O}_{1.95-x}$ , respectively (Tab. S2) We further determined the  $\text{Ce}^{3+}/(\text{Ce}^{3+}+\text{Ce}^{4+})$  ratio for the  $\text{Ce}_{1-x}\text{La}_x\text{O}_{2-x/2}$  NRs. While a ratio of 20.3 was found for the  $\text{Ce}_{0.9}\text{La}_{0.1}\text{O}_{1.95-x}$  NRs, the  $\text{Ce}^{3+}$  portion increased for  $\text{Ce}_{0.6}\text{La}_{0.4}\text{O}_{1.80-x}$  to a ratio of 26.9. This clearly shows that an increasing La content leads to higher  $\text{Ce}^{3+}$  portion at the NR surface.



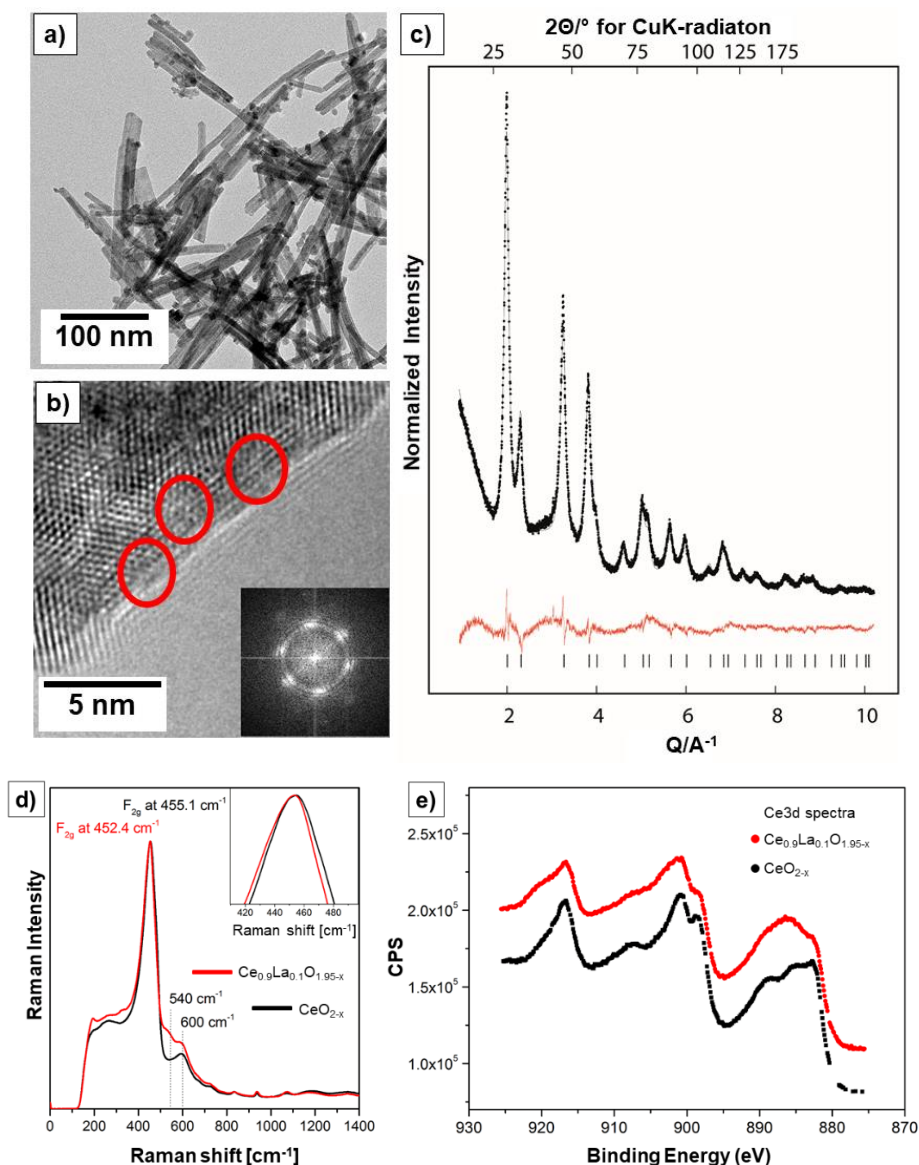


**Fig. 4. Characterization of  $\text{Ce}_{0.9}\text{La}_{0.1}\text{O}_{1.95-x}$ .** Representative TEM (a) and HR-TEM (b) images of  $\text{Ce}_{0.9}\text{La}_{0.1}\text{O}_{1.95-x}$  show the formation of NRs with d spacings of approx. 0.3 nm and the presence of surface defects (red districts). P-XRD diffratogram (c) with Rietveld refinement (black line) on the diffraction data (red dots) and difference between the measured and theoretical profile (red line) for cubic  $\text{CeO}_{2-x}$ . The Raman spectra confirm an oxygen defect structure for both NP samples, which can be monitored based on the bands at 540 and 600  $\text{cm}^{-1}$ , with a higher defect density for the  $\text{Ce}_{0.9}\text{La}_{0.1}\text{O}_{1.95-x}$  (d). The inset in d) shows the red shift of the  $\text{Ce}_{0.9}\text{La}_{0.1}\text{O}_{1.95-x}$  spectra, which further confirms the higher amounts of defects. The sharp peak observable at 194  $\text{cm}^{-1}$  could further prove the lanthanum doping.<sup>52</sup> 3d X-ray photoelectron spectra (e) show a higher amount of  $\text{Ce}^{3+}$  at the NP surface of  $\text{Ce}_{0.9}\text{La}_{0.1}\text{O}_{1.95-x}$ . A quantitative analysis gives a La/Ce ratio of 0.15, suggesting a higher concentration of defects at the NP surface.

The urease-like activity of  $\text{Ce}_{1-x}\text{La}_x\text{O}_{2-x/2}$  and  $\text{CeO}_{2-x}$  NRs was investigated to understand surface property effects. In general, reactions in the presence of  $\text{Ce}_{1-x}\text{La}_x\text{O}_{2-x/2}$  had lower  $v_{max}$  and  $k_{cat}$  values *per* NP such as *per*  $\text{m}^2$  BET surface area. (Fig. 3c, f). The La-substituted ceria NRs showed a linear dependence on the catalyst concentration and the urea degradation was comparable to native urease and  $\text{CeO}_{2-x}$  NRs (Fig. S24 and S25). The kinetic parameters obtained from steady state kinetics of the hydrolysis (for constant concentration of  $\text{Ce}_{0.9}\text{La}_{0.1}\text{O}_{1.95-x}$  and  $\text{Ce}_{0.6}\text{La}_{0.4}\text{O}_{1.80-x}$  NRs) yielded  $v_{max} = 9.5 \times 10^{-5} \text{ mM s}^{-1}$  for  $\text{Ce}_{0.9}\text{La}_{0.1}\text{O}_{1.95-x}$  and a turnover number of  $k_{cat} = 6.79 \times 10^1 \text{ s}^{-1}$ . The values are slightly lower than those recorded for non-substituted  $\text{CeO}_{2-x}$  NRs, but higher than those for  $\text{Ce}_{0.6}\text{La}_{0.4}\text{O}_{1.80-x}$  NRs ( $v_{max} = 9.0 \times 10^{-5} \text{ mM s}^{-1}$  and  $k_{cat} = 4.41 \times 10^1 \text{ s}^{-1}$ ). Comparison of the turnover numbers normalized to the BET surface area supported the results derived for molar NR concentrations. A urea degradation of  $5.90 \times 10^{-6} \text{ mmol s}^{-1} \text{ m}^{-2}$  was determined for  $\text{Ce}_{0.9}\text{La}_{0.1}\text{O}_{1.95-x}$  NRs, while the turnover for  $\text{Ce}_{0.6}\text{La}_{0.4}\text{O}_{1.80-x}$  NRs was  $5.66 \times 10^{-6} \text{ mmol s}^{-1} \text{ m}^{-2}$ . To fully interpret the catalytic activities of La-doped  $\text{CeO}_{2-x}$  NRs two opposing trends must be considered. (i) La doping increases the number of surface defects and the amount of  $\text{Ce}^{3+}$  at the NR surface as probed by Raman and XPS. This leads to a higher activity *per* Ce atom.<sup>48</sup> (ii) La-substitution reduces the total amount of  $\text{Ce}^{4+}$  sites at the NR surface. While the surface contained 33.1 % of  $\text{Ce}^{4+}$  in  $\text{CeO}_{2-x}$  NRs, the value decreased to 30.7 % for  $\text{Ce}_{0.9}\text{La}_{0.1}\text{O}_{1.95-x}$  and 17.4 % for  $\text{Ce}_{0.6}\text{La}_{0.4}\text{O}_{1.80-x}$  NRs (Tab. S2). We found that the rate enhancing effect by surface defects could not compensate for the loss of activity by reducing the number of  $\text{Ce}^{4+}$  sites. In essence, increasing the  $\text{Ce}^{3+}/\text{Ce}^{4+}$  ratio by La-doping did not increase the final activity *per* NP or  $\text{m}^2$  surface area.

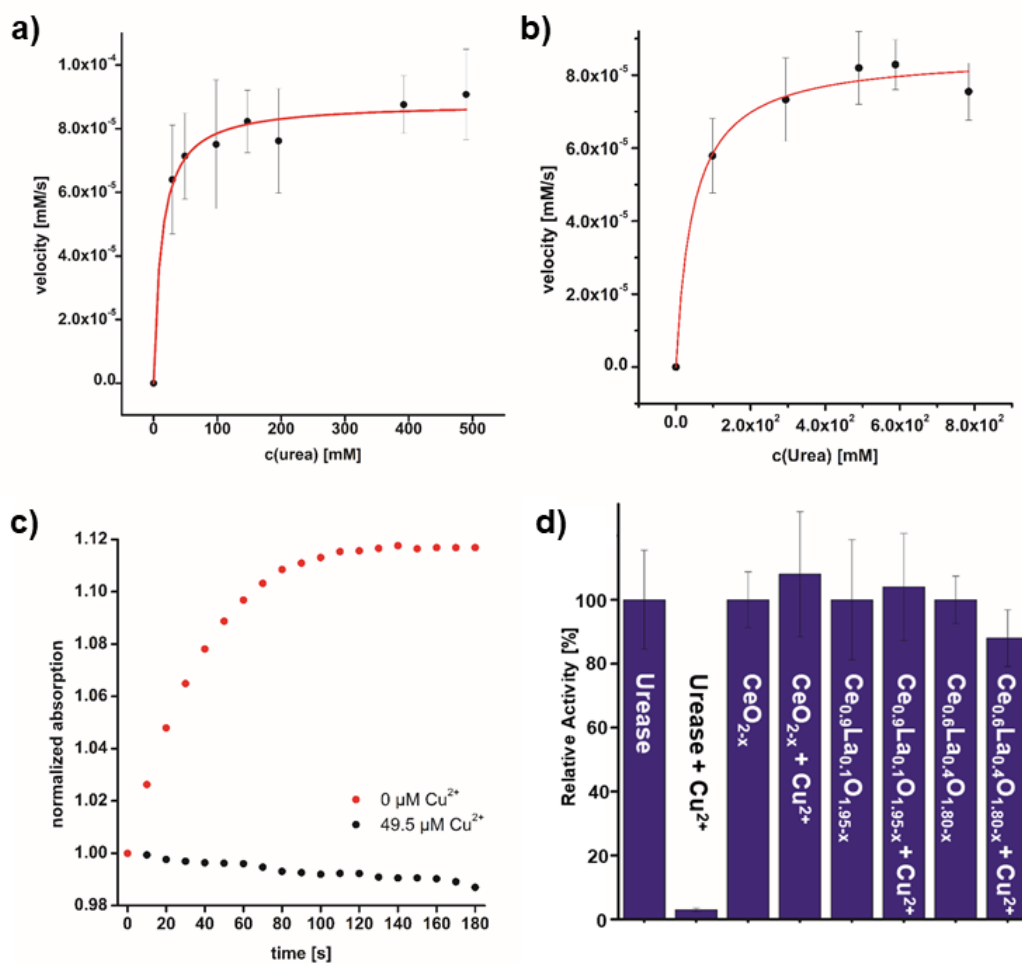


**Fig. 5. Urease activity of lanthanum doped  $\text{CeO}_{2-x}$  NRs.** Measurements conducted with constant catalyst concentrations showed Michaelis Menten-like behavior. The catalytic activities were investigated by monitoring the absorption change at  $\lambda_{\text{max}} = 560$  nm. Catalytic turnover numbers for  $\text{Ce}_{0.9}\text{La}_{0.1}\text{O}_{1.95-x}$  ( $c_{\text{NR}} = 1.40 \times 10^{-6}$  mM;  $v_{\text{max}} = 9.5 \times 10^{-5}$  mM $\text{s}^{-1}$ ;  $k_{\text{cat}} = 6.79 \times 10^1$  s $^{-1}$ ) (a) and  $\text{Ce}_{0.6}\text{La}_{0.4}\text{O}_{1.80-x}$  ( $c_{\text{NR}} = 2.04 \times 10^{-6}$  mM;  $v_{\text{max}} = 9.0 \times 10^{-5}$  mM $\text{s}^{-1}$ ;  $k_{\text{cat}} = 4.41 \times 10^1$  s $^{-1}$ ) (b) were calculated from a modified Hill equation. Kinetic data are for molar NP concentrations. Errors are average values from three individual measurements. Investigations of the effect of metal ions on the catalytic activity of native urease and their nanoparticle mimics show a strong inhibition of native jack bean urease by addition of  $\text{Cu}^{2+}$  ( $49.5 \mu\text{M}$ ) (c). The results are in harmony with the reported inhibition effect of  $\text{Cu}^{2+}$ . In contrast, reactions conducted with  $\text{CeO}_{2-x}$  nanorods,  $\text{Ce}_{0.9}\text{La}_{0.1}\text{O}_{1.95-x}$  and  $\text{Ce}_{0.6}\text{La}_{0.4}\text{O}_{1.80-x}$  were not affected by the heavy metal (d).

Native urease is one of the most active and the most rate enhancing natural enzymes. Urea hydrolysis does not occur in the absence of ureases because  $\text{NH}_3$  elimination ( $k_{cat} = 6.3 \times 10^{-9} \text{ s}^{-1}$ ) is preferred. The corresponding turnover number ( $k_{cat} = 2.5 \times 10^{-27} \text{ s}^{-1}$ ) was calculated by simulations.<sup>1,2,53</sup> While native jack bean urease led to a rate enhancement of  $1.10 \times 10^{30}$  compared to the non-catalyzed reaction, the enhancement with  $\text{CeO}_{2-x}$  NRs compared to the non-catalyzed reaction was still  $3.83 \times 10^{28}$ .

**Long-term stability of  $\text{CeO}_{2-x}$  and  $\text{Ce}_{1-x}\text{La}_x\text{O}_{2-x/2}$  NRs.** For any practical application the stability of  $\text{CeO}_{2-x}$  and  $\text{Ce}_{1-x}\text{La}_x\text{O}_{2-x/2}$  NRs is a stringent requirement. The stability was assessed by immersing  $\text{CeO}_{2-x}$  and  $\text{Ce}_{1-x}\text{La}_x\text{O}_{2-x/2}$  NRs in water and urea solutions. A stock solution of the NRs was added to a leaching membrane, which was placed in a tube, containing 45 mL of MilliQ water, or 2.94 M urea solution. After ten days of stirring the Ce and La leaching was analyzed by ICP-MS. Neither  $\text{CeO}_{2-x}$  nor  $\text{Ce}_{1-x}\text{La}_x\text{O}_{2-x/2}$  NRs showed any signs of degradation or metal leaching. Based on a calibration curve, the Ce contents of  $\text{CeO}_{2-x}$  after 10 days were  $0.4\text{-}2 \mu\text{g L}^{-1}$  and  $5.93\text{-}12.3 \mu\text{g L}^{-1}$  in water and urea solution, respectively. Analytical details for  $\text{CeO}_{2-x}$  and  $\text{Ce}_{1-x}\text{La}_x\text{O}_{2-x/2}$  NRs are compiled in Table S3-S6 (Supporting Information).

The stability and catalytic activity of native or recombinant enzymes depends sensitively on factors like temperature, pH value, salt concentration or metal ions. While native urease is unstable under acidic and strong basic pH values as well as at elevated temperatures,<sup>54,55</sup> for  $\text{CeO}_{2-x}$  nanoparticles a wide variety of applications with different temperature and pH values are reported.<sup>56,57</sup> Particularly with regard to moderate conditions at which enzyme is practically used and the reports on enzyme liability, our studies were focused on the presence of metal ions, like  $\text{Cu}^{2+}$ . The hydrolytic activity of native urease is affected strongly by the presence of metal ions.  $\text{Cu}^{2+}$  is known as one of the strongest metal inhibitors of the native ureases.<sup>58</sup> Although the threshold concentration for  $\text{Cu}^{2+}$  in tap water is set to  $2 \text{ mg L}^{-1}$  by the World Health organization, true  $\text{Cu}^{2+}$  concentrations in waste water can be significantly higher.<sup>59</sup> The effect of  $\text{Cu}^{2+}$  on the activity of the nanoparticle enzyme mimics was investigated by monitoring the change of absorption at 560 nm in the presence and the absence of  $\text{Cu}^{2+}$ . A  $\text{Cu}^{2+}$  concentration of  $49.5 \mu\text{M}$  blocked the activity of native urease

completely, whereas the efficiencies of  $\text{CeO}_{2-x}$ ,  $\text{Ce}_{0.9}\text{La}_{0.1}\text{O}_{1.95-x}$  and  $\text{Ce}_{0.6}\text{La}_{0.4}\text{O}_{1.80-x}$  were not affected significantly by in the presence of  $\text{Cu}^{2+}$  (Fig. 5).

#### 3.4.5 Conclusions

We have shown that  $\text{CeO}_{2-x}$  NRs mimic the enzyme activity of native jack bean urease, one of the most active natural enzymes, which catalyze the hydrolytic decomposition of urea to ammonia. Other metal oxides with high-valent metals like  $\text{TiO}_2$ ,  $\text{V}_2\text{O}_5$ ,  $\text{MoO}_{3-x}$  or NPs of metal complexes Gly-Ni(OH)<sub>2</sub> (containing Ni as the metalcenter of native urease) did not catalyze urea degradation.  $\text{CeO}_{2-x}$  NRs are the first functional urease mimic and a rare example of an enzyme mimic with strong hydrolytic activity. The surface properties of  $\text{CeO}_{2-x}$  NRs were investigated by tuning the  $\text{Ce}^{4+}/\text{Ce}^{3+}$  ratio through La substitution. Although the number of surface defects was increased by La substitution, the lower number of  $\text{Ce}^{4+}$  sites at the NR surface led to a decrease of the catalytic efficiency. While native jack bean urease is strongly inhibited by  $\text{Cu}^{2+}$  ions, the activity of the  $\text{CeO}_{2-x}$  enzyme mimic remained unaffected, indicating a high operational stability. The stability of  $\text{CeO}_2$  NRs was demonstrated by leaching experiments, carried out under operating conditions in water and in urea solutions. These tests confirmed the long-term stability with a solubility close to the detection limit.

Ceria is a side product in lanthanide production. Its low costs, high shelf-life, operational stability and environmental compatibility allow broad application as green catalyst.  $\text{CeO}_2$  NRs could be embedded in polymer membranes for water processing or filters for the reclamation of waste water or aquaculture systems. Our biomimicry approach allows using  $\text{CeO}_{2-x}$  NRs as functional enzyme mimics where a practical use of native or recombinant enzyme is hampered.

#### 3.4.6 References

- 1 B. Krajewska, *J. Mol. Cat. B. Enzym.* 2009, **59**, 22-40.
- 2 C. Tang, H. Zhang, L. Dong, *Catal. Sci. Technol.* 2016, **6**, 1248–1264
- 3 E. Urbańczyk, M. Sowa, W. Simka, *J. Appl. Electrochem.* 2016, **46**, 1011-1029.
- 4 R. M. McCabe, B. M. Hickey, R. M. Kudela, K. A. Lefebvre, N. G. Adams, B. D. Bill, F. M. D. Gulland, R. E. Thomson, W. P. Cochlan, V. L. Trainer, *Geophys. Res. Lett.* 2016, **43**, 366–376.
- 5 K. A. Lefebvre, S. L. Dovel, M. W. Silver, *Mar. Biol.* 2001, **138**, 693–700.
- 6 S. Bargu, M. W. Silver, M. D. Ohman, C. R. Benitez-Nelson, D. L. Garrison, *Nature Geosci.* 2012, **5**, 2-3.
- 7 W. Simka, J. Piotrowski, A. Robak, G. Nawrat, *J. Appl. Electrochem.* 2009, **39**, 1137-1143.
- 8 Y. Qin, J. M. S. Cabral, *Biocatalysis and Biotransformation* 2002, **20**, 1-14.
- 9 D. J. Conley, H. W. Paerl, R. W. Howarth, D. F. Boesch, S. P. Seitzinger, K. E. Havens, C. Lancelot, G. E. Likens, *Science* 2009, **323**, 1014-1015.
- 10 P. A. Karplus, M. A. Pearson, R. P. Hausinger, *Acc. Chem. Res.* 1997, **30**, 330-337.
- 11 B. Zambelli, F. Musiani, S. Benini, S. Ciurli, *Acc. Chem. Res.* 2011, **44**, 520–530.
- 12 E. Jabri, M. B. Carr, R. P. Hausinger, P. A. Karplus, *Science* 1995, **268**, 998-1004.
- 13 D. Volkmer, B. Hommerich, K. Griesar, W. Haase, B. Krebs, *Inorg. Chem.* 1996, **35**, 3792-3803.
- 14 C. Follmer, *Phytochemistry* 2008, **69**, 18–28.
- 15 S. Kodama, F. Yotsuzuka, *J. Food Sci.* 1996, **61**, 304-307.

- 16 H. Chao, *Drug Dev. Deliv.* 2011, **11**, 68-72.
- 17 A. B. Becker-Ritt, A. H. S. Martinelli, S. Mitidieri, V. Feder, G. E. Wassermann, L. Santi, M.H. Vainstein, J. T. A. Oliveira, L. M. Fiuza, G. Pasquali, C. R. Carlini, *Toxicol.* 2007, **50**, 971–983.
- 18 E. Magner, *Chem. Soc. Rev.* 2013, **42**, 6213–6222.
- 19 L. Gao, J. Zhuang, L. Nie, J. Zhang, Y. Zhang, N. Gu, T. Wang, J. Feng, D. Yang, S. Parrett, X. Yan, *Nature Nanotechnol.* 2007, **2**, 577–583.
- 20 H. Wei, E. Wang, *Chem. Soc. Rev.* 2013, **42**, 6060–6093.
- 21 R. Ragg, M. N. Tahir, W. Tremel, *Eur. J. Inorg. Chem.* 2016, 1906–1915.
- 22 L. Vivier, D. Duprez, *ChemSusChem* 2010, **3**, 654–678.
- 23 Z. Tian, J. Li, Z. Zhang, W. Gao, X. Zhou, Y. Qu, *Biomaterials* 2015, **59**, 116–124
- 24 T. Pirmohamed, J. M. Dowding, S. Singh, B. Wasserman, E. Heckert, A. S. Karakoti, J. E. S. King, S. Seal, W. T. Self, *Chem. Commun.* 2010, **46**, 2736–2738.
- 25 C. Korsvik, S. Patil, S. Seal, W. T. Self, *Chem. Commun.* 2007, 1056–1058.
- 26 C. K. Kim, T. Kim, I.-Y. Choi, M. Soh, D. Kim, Y.-J. Kim, H. Jang, H.-S. Yang, J. Y. Kim, H.-K. Park, S. P. Park, S. Park, T. Yu, B. W. Yoon, S.-H. Lee, T. Hyeon, *Angew. Chem. Int. Ed.* 2012, **51**, 11039–11043.
- 27 M. A. Asati, D. S. Santra, M. C. Kaittanis, D. S. Nath, P. J. M. Perez, *Angew. Chem. Int. Ed.* 2010, **48**, 2308–2312.
- 28 K. Herget, P. Hubach, S. Pusch, P. Deglmann, H. Götz, T. E. Gorelik, I. A. Gural'skyi, T. Link, S. Schenk, M. Panthöfer, V. Ksenofontov, U. Kolb, T. Opatz, R. André, W. Tremel, *Adv. Mater.* 2017, **29**, 1603823.
- 29 A. A. Vernekar, T. Das, G. Mugesh, *Angew. Chem. Int. Ed.* 2015, **55**, 1412–1416.

- 30 T. Montini, M. Melchionna, M. Monai, P. Fornasiero, *Chem. Rev.* 2016, **116**, 5987–6041.
- 31 Z. Wu, A. K. P. Mann, M. Li, S. H. Overbury, *J. Phys. Chem. C* 2015, **119**, 7340–7350.
- 32 Y. Wang, F. Wang, Q. Song, Q. Xin, S. Xu, J. Xu, *J. Am. Chem. Soc.* 2013, **135**, 1506–1515.
- 33 H.-X. Mai, L.-D. Sun, Y.-W. Zhang, R. Si, W. Feng, H.-P. Zhang, H.-C. Yan, *J. Phys. Chem. B* 2005, **109**, 24380-24385.
- 34 M. G. Cutrufello, I. Ferino, R. Monaci, E. Rombi, G. Colon, J. A. Navio, *Phys. Chem. Chem. Phys.* 2001, **3**, 2928-2934.
- 35 H. Bai, W. Yi, J. Li, G. Xi, Y. Li, H. Yang, J. Liu, *J. Mater. Chem. A* 2015, **4**, 1566-1571.
- 36 F. Zhou, X. Zhao, C. Yuan, L. Li, *Cryst. Growth Design.* 2008, **8**, 723-727.
- 37 P. O'Brien, *J. Chem. Educ.* 1982, **59**, 1052–1053.
- 38 K. Korschelt, R. Ragg, C. S. Metzger, M. Klueker, M. Oster, B. Barton, M. Panthöfer, D. Strand, U. Kolb, M. Mondeshki, S. Strand, J. Brieger, M. N. Tahir, W. Tremel, *Nanoscale* 2017, **9**, 3952-3960.
- 39 Z. Štefanac, M. Tomašković, z. Raković-Tresić, *Anal. Lett.* 1969, **2**, 197-210.
- 40 R. W. Cheary, A. Coelho, *J. Appl. Crystallogr.* 1992, **25**, 109-121.
- 41 B. Krajewska, *J. Mol. Cat. B* 2009, **59**, 9-21.
- 42 L. Mazzei, M. Cianci, F. Musiani, S. Ciurli, *Dalton Trans.* 2016, **45**, 5455-5459.
- 43 N. E. Dixon, P. W. Riddles, C. Gazzola, R. L. Blakeley, B. Zerner, *Can. J. Biochem.* 1980, **58**, 1335-1344.



- 44 K. A. Johnson, R. S. Goody, *Biochem.* 2011, **50**, 8264-8269.
- 45 R. Ragg, A. M. Schilman, K. Korschelt, C. Wieseotte, M. Klueker, M. Viel, L. Völker, S. Preiß, J. Herzberger, H. Frey, K. Heinze, P. Blümner, M. N. Tahir, F. Natalio, W. Tremel, *J. Mater. Chem. B* 2016, **4**, 7423-7428.
- 46 K. Korschelt, M. N. Tahir, W. Tremel *Chem. Eur. J* 2018, DOI: 10.1002/chem.201800384.
- 47 M. Harada, K. Fukasawa, B. Y. Hiraoka, M. Mogi, A. Barth, K. Neubert, *Biochim. Biophys. Acta* 1985, **830**, 341-344.
- 48 V. Baldim, F. Bedioui, N. Mignet, I. Margail, J.-F. Berret, *Nanoscale* 2018, DOI: 10.1039/C8NR00325D.
- 49 R. D. Shannon, *Acta Crystallogr.* 1976, **A32**, 751-767.
- 50 C. Schilling, A. Hofmann, C. Hess, M. V. Ganduglia-Pirovano, *J. Phys. Chem. C* 2017, **121**, 20834-20849.
- 51 F. Zhang, P. Wang, J. Koberstein, S. Khalid, S.-W. Chan, *J. Surf. Sci.* 2004, **563**, 74-82.
- 52 A. Nakajima, A. Yoshihara, M. Ishigame, *J. Phys. Rev. B* 1994, **50**, 13297-13307.
- 53 G. Estiu, K. M. Merz, Jr., *J. Am. Chem. Soc.* 2004, **126**, 6932-6944.
- 54 F. Azari, S. Hosseinkhani, M. Nemat-Gorgani *Appl. Biochem Biotechnol.* 2001, **94**, 265-277.
- 55 M. I. Zantua, J. M. Bremer, *Soil Biol. Biochem.* 1977, **9**, 135-140.
- 56 C. Xu, X. Qu *NPG Asia Materials* 2014, **6**, e90.
- 57 V. Sajith, C. B. Sobhan, G. P. Peterson *Advances in Mechanical Engineering* 2010, **2**, 581407.

58 W. Zaborska, B. Krajewska, Z. Olech, *J. Enzyme Inhib. Med. Chem.* 2004, **19**, 65-69.

59 E. Erdal, *J. Hazard Mat.* 2008, **159**, 235–258.

## 3.4.7 Supporting Information

## Figures

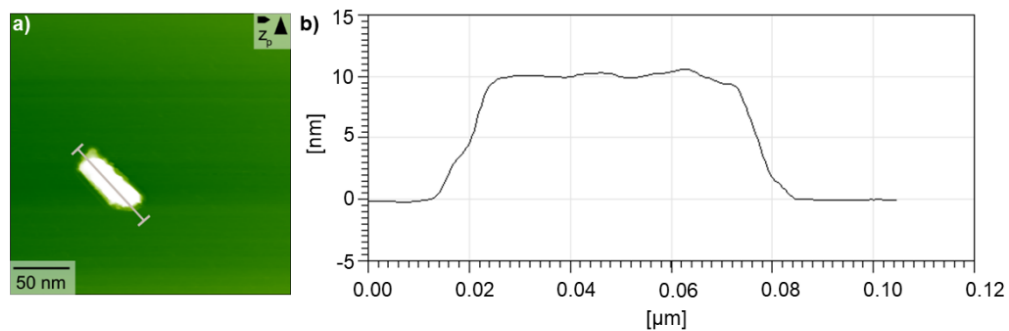


Fig. S1. AFM image of  $\text{CeO}_2$  NRs show a height of approx. 9-11 nm.

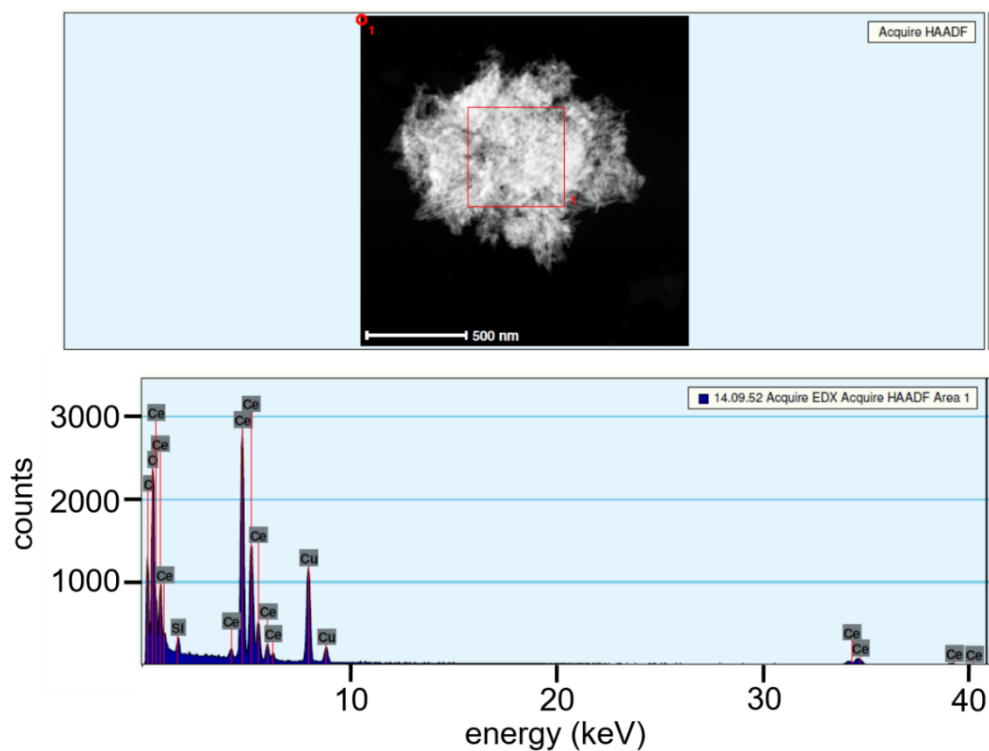
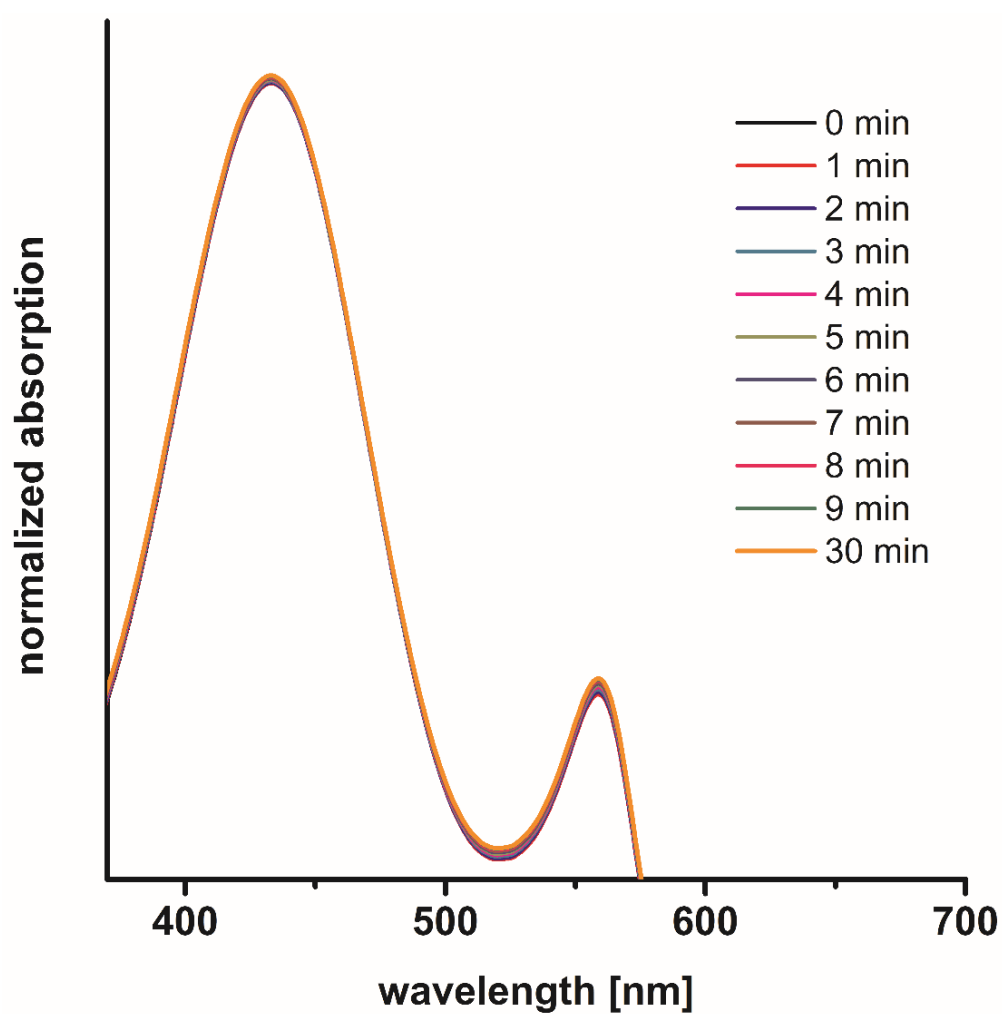
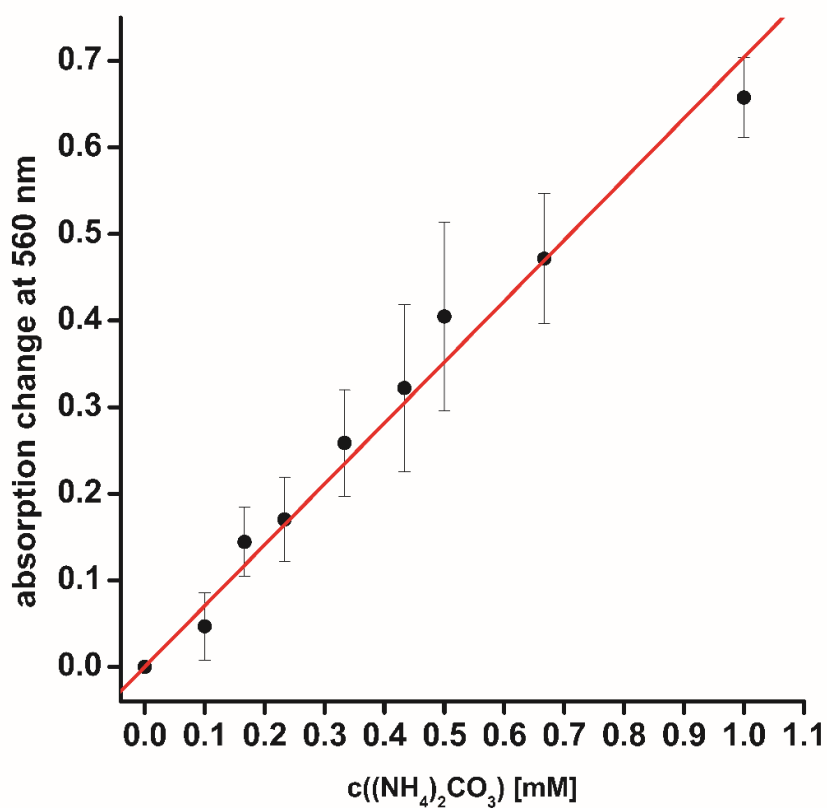


Fig. S2. EDX measurements of  $\text{CeO}_{2-x}$  NRs.



**Fig. S3.** A kinetic absorption scan of a phosphate buffered solution containing phenol red and urea without catalyst show no significant change of absorption neither at 434 nm nor at 560 nm.



**Fig. S4. Calibration conducted with 0.1 M ammonium carbonate ((NH<sub>4</sub>)<sub>2</sub>CO<sub>3</sub>) solution** enables the combination of formed or added amount of ammonium carbonate and the resulting absorption change at 560 nm under given reaction conditions. Calibrations were done prior to each measurement.

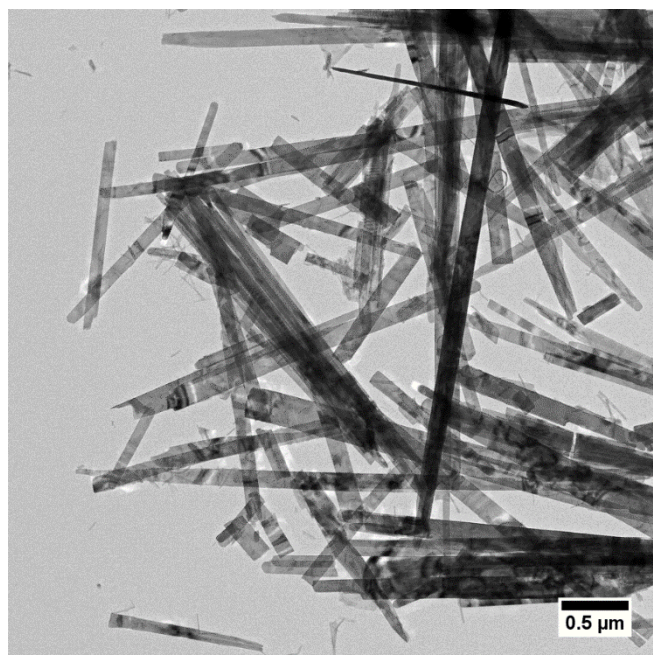


Fig. S5: Representative TEM image of nanostructured MoO<sub>3-x</sub> belts.

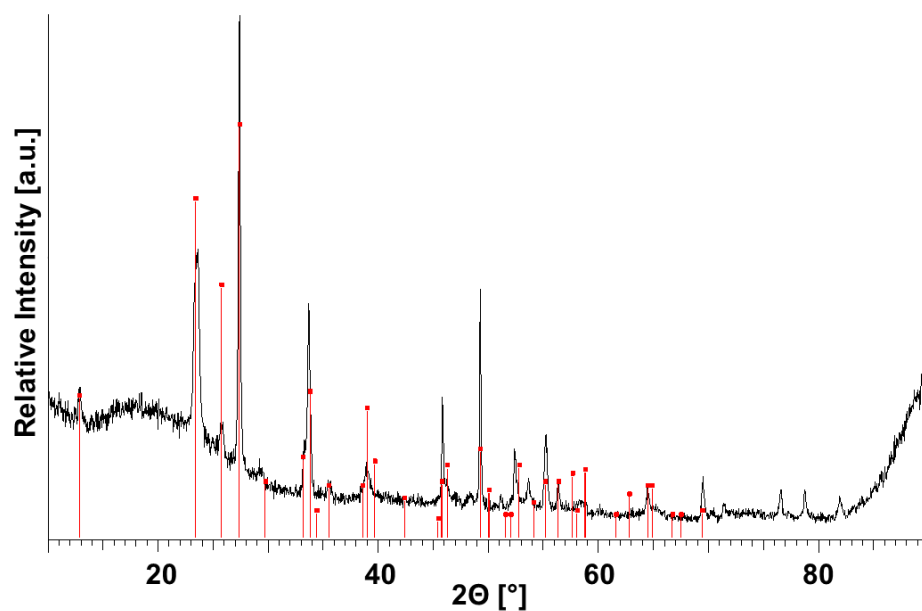


Fig. S6: P-XRD analysis of nanostructured MoO<sub>3-x</sub> belts. The measured pattern fits to the reflex positions of MoO<sub>3</sub> (red).

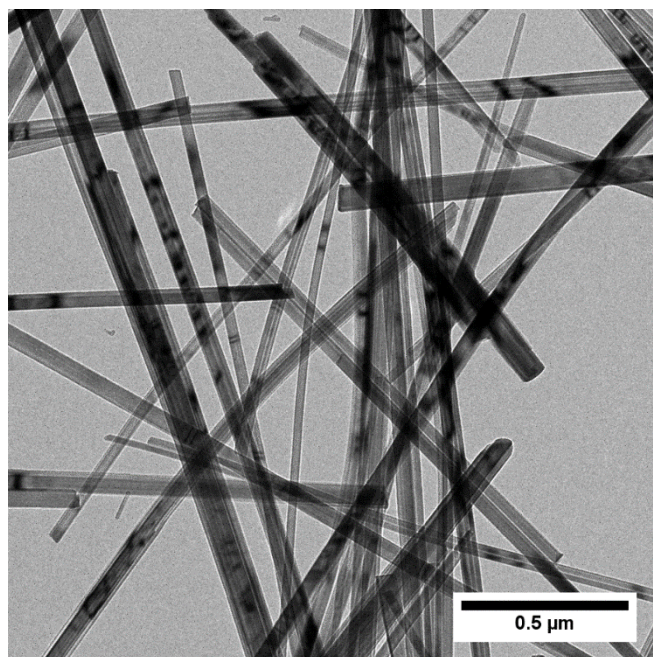


Fig. S7: Representative TEM image of nanostructured  $V_2O_5$  wires.

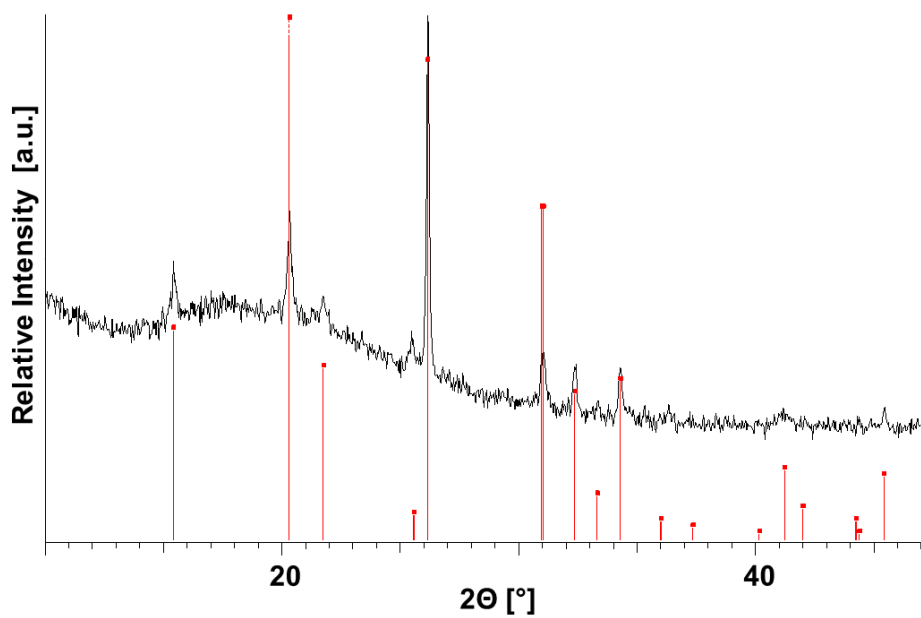


Fig. S8: P-XRD measurement of nanostructured  $V_2O_5$  wires.

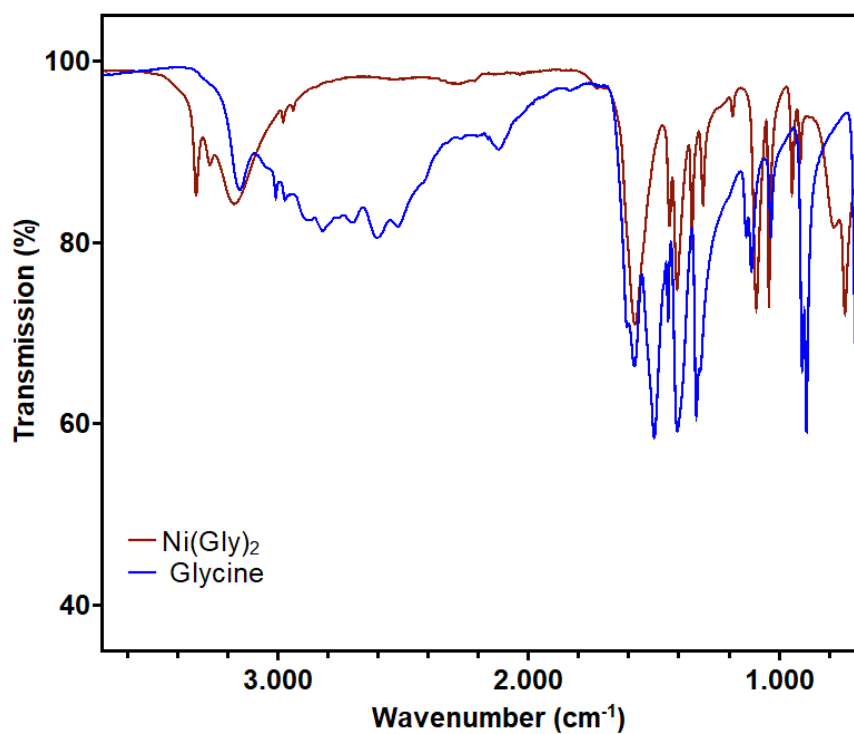


Fig. S9. IR spectra of  $\text{Ni}(\text{Gly})_2$  complex and the amino acid glycine.

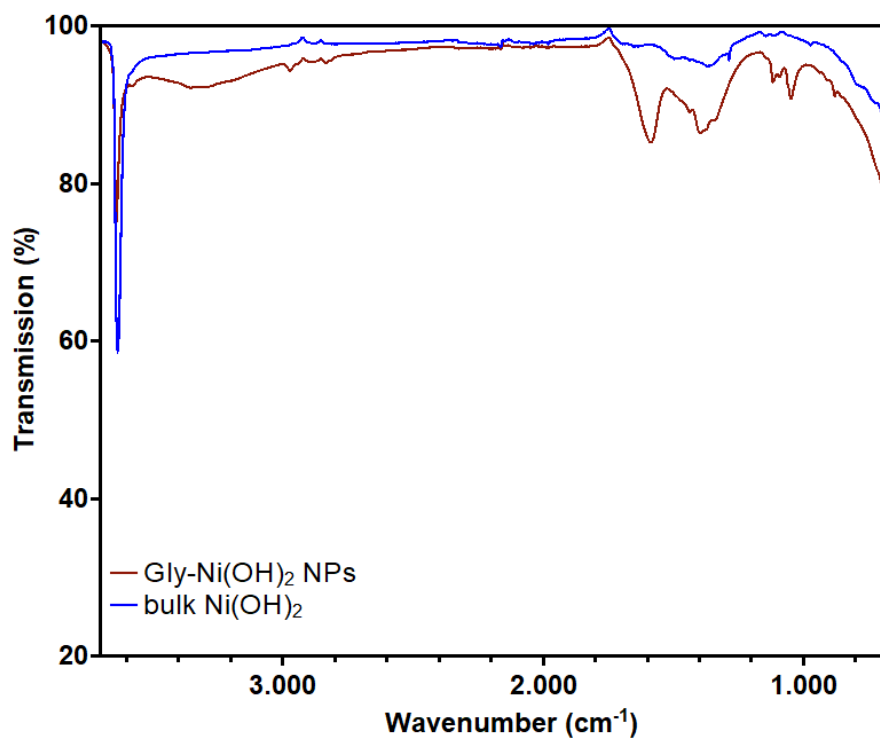
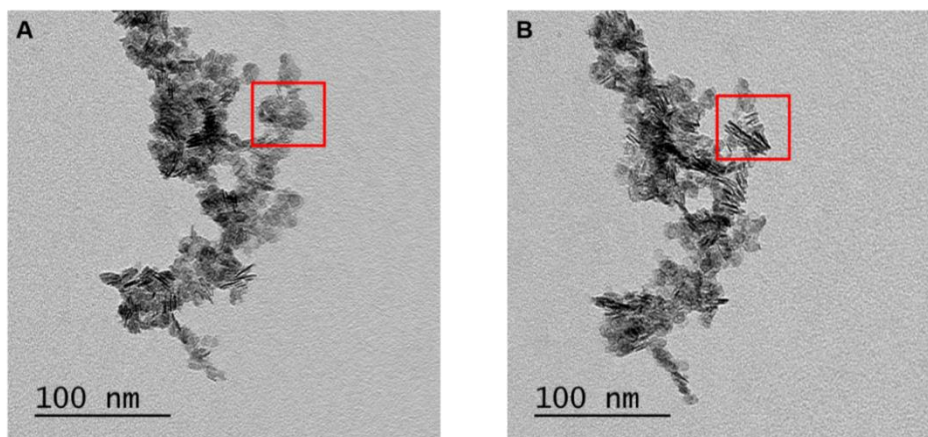
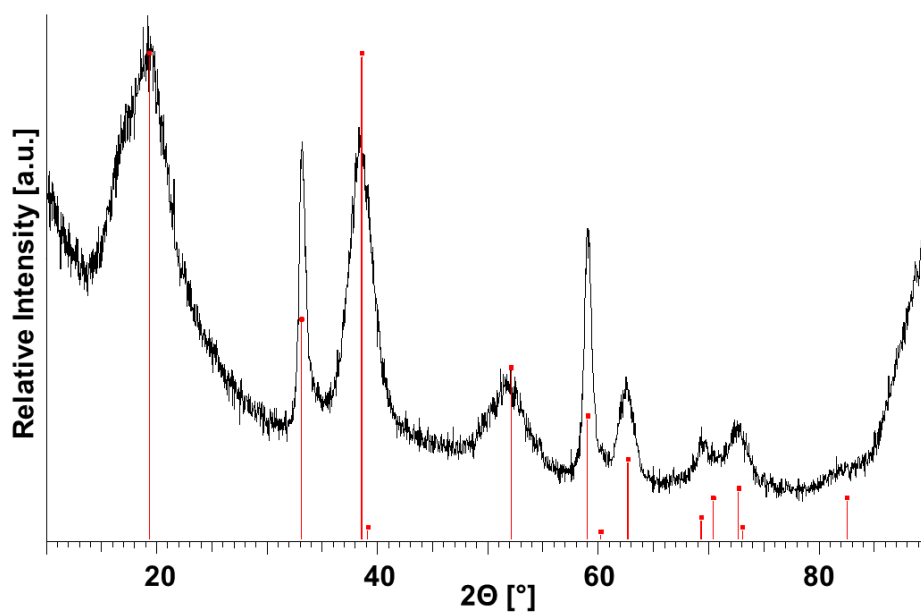


Fig. S10. IR spectra of Gly- $\text{Ni}(\text{OH})_2$  NPs and bulk  $\text{Ni}(\text{OH})_2$ .





**Fig. S11. TEM images of Gly-Ni(OH)<sub>2</sub> NPs.** TEM images show the formation of Ni(OH)<sub>2</sub> nanosheets with a diameter of approx.  $(10.62 \pm 1.29)$  nm. The TEM images were tilted  $-40^\circ$  (A) and  $+40^\circ$  (B) to demonstrate the sheet structure.



**Fig. S12. P-XRD measurement of Gly-Ni(OH)<sub>2</sub> NPs.** Measured pattern (black) and reflex positions of theoprasite (red). The sheet structure, observable in the TEM images of Gly-Ni(OH)<sub>2</sub> NPs, is further demonstrated by the occurrence of broad bands, due to the flat plane, and sharp bands, which appears because of the low thickness of as-synthesized NPs.

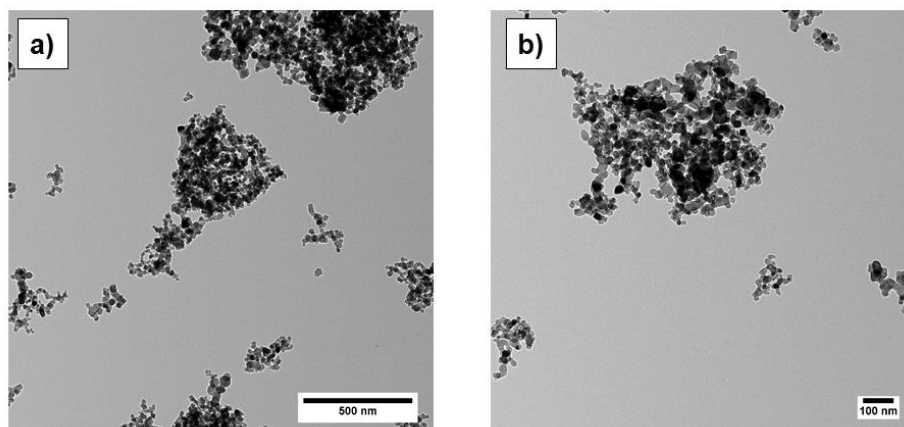


Fig. S13. TEM image of  $\text{TiO}_2$ .

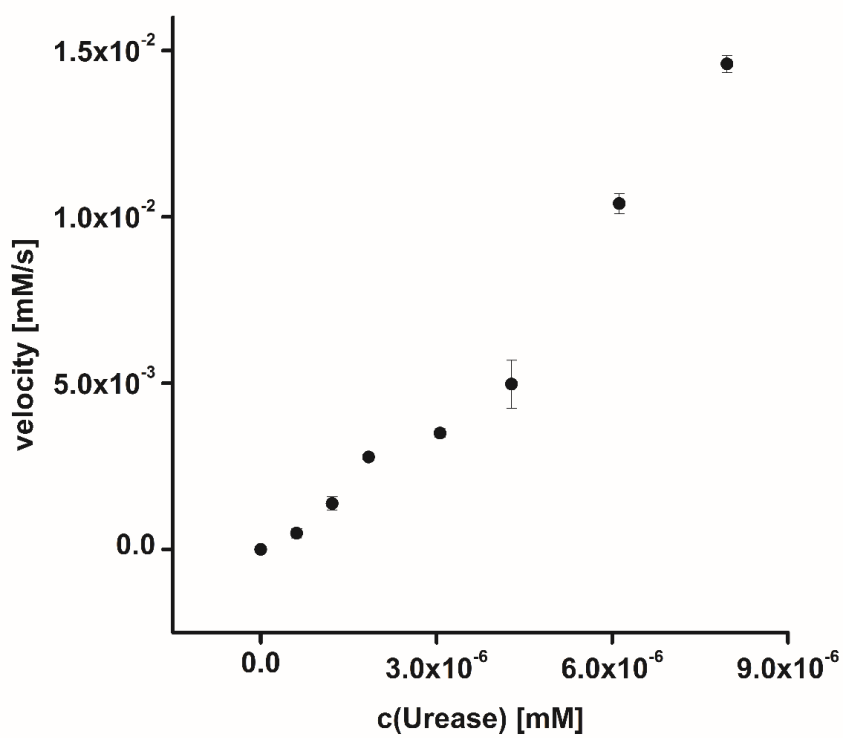
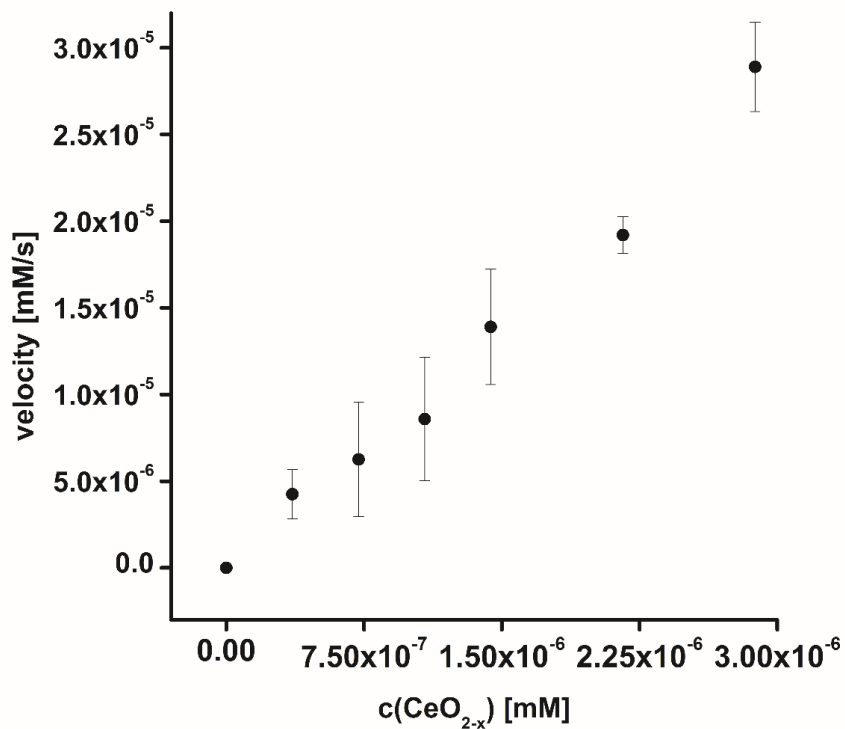


Fig. S14. Variation of the concentration of native urease show that increasing enzyme concentrations lead to higher urea degradation. Error bars are calculated from three replications.



**Fig. S15. Variation of CeO<sub>2-x</sub> NR concentration** shows the dependency of catalyst concentration to substrate degradation. Increasing amount of catalyst lead to an increase of urea decomposition. Error bars are calculated from three replications.

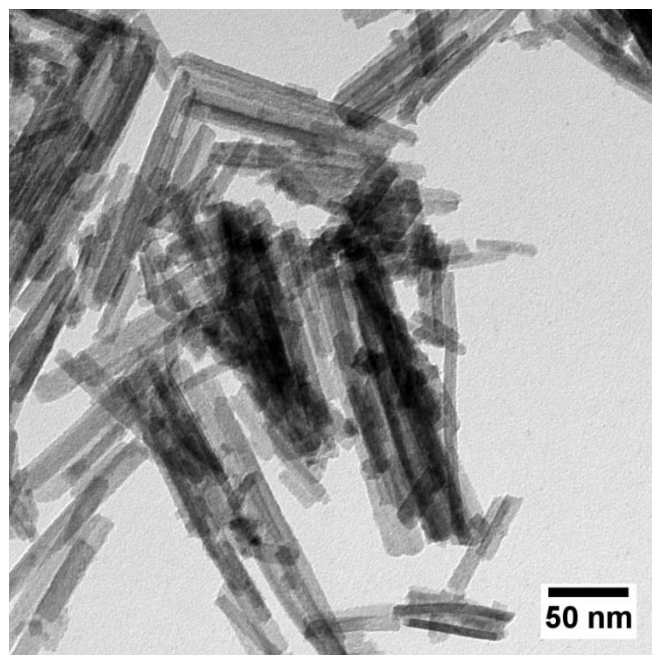


Fig. S16. TEM image of Ce<sub>0.6</sub>La<sub>0.4</sub>O<sub>1.80-x</sub> NRs.

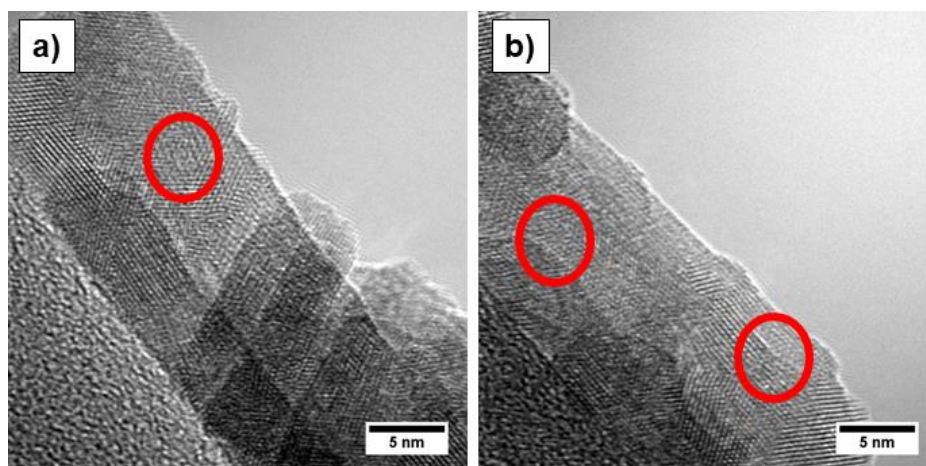
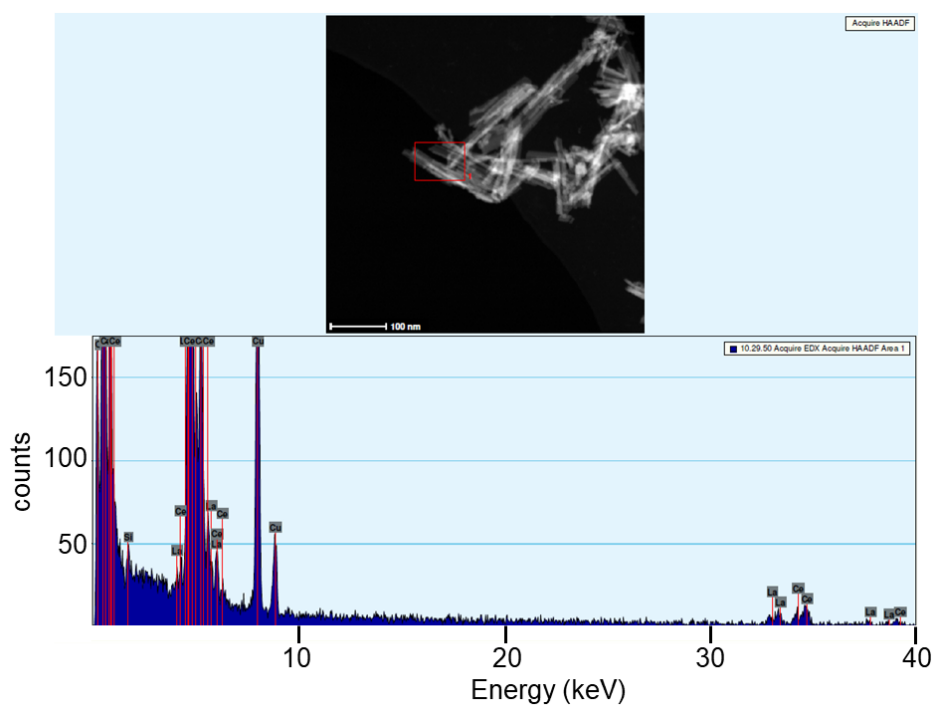
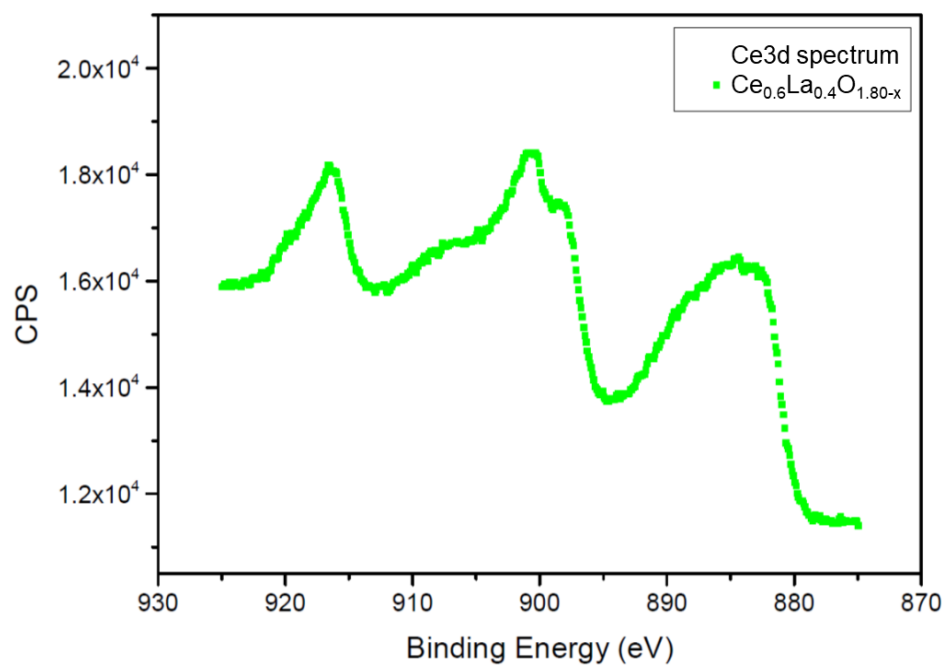


Fig. S17. HR-TEM images of Ce<sub>0.6</sub>La<sub>0.4</sub>O<sub>1.80-x</sub> NRs. The images show the presence of surface defects, similar to the NR sample with a composition of Ce<sub>0.9</sub>La<sub>0.1</sub>O<sub>1.95-x</sub>. The d spacings of 0.3 nm corresponding to the (111) plane of CeO<sub>2</sub>.



**Fig. S18. EDX spectrum of  $\text{Ce}_{0.6}\text{La}_{0.4}\text{O}_{1.80-x}$  NRs.** The spectrum shows the presence of La and Ce in the sample, but no further metal impurities.



**Fig. S19. XPS spectrum of Ce<sub>0.6</sub>La<sub>0.4</sub>O<sub>1.80-x</sub> NRs.** The spectrum shows a higher amount of Ce<sup>3+</sup> compared to the not-doped CeO<sub>2-x</sub> and to the Ce<sub>0.9</sub>La<sub>0.1</sub>O<sub>1.95-x</sub> CeO<sub>2-x</sub> nanorods. A Ce<sup>3+</sup>/(Ce<sup>3+</sup>+Ce<sup>4+</sup>) ratio of 26.9 was calculated.

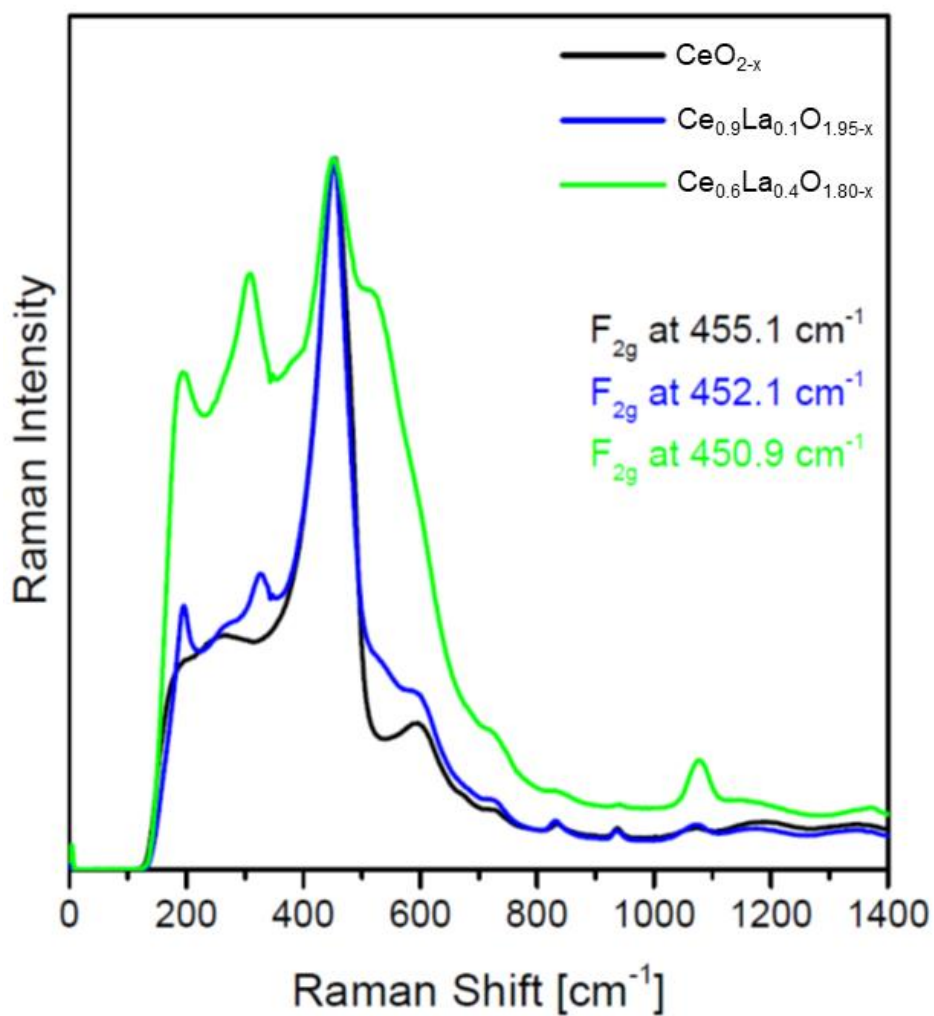
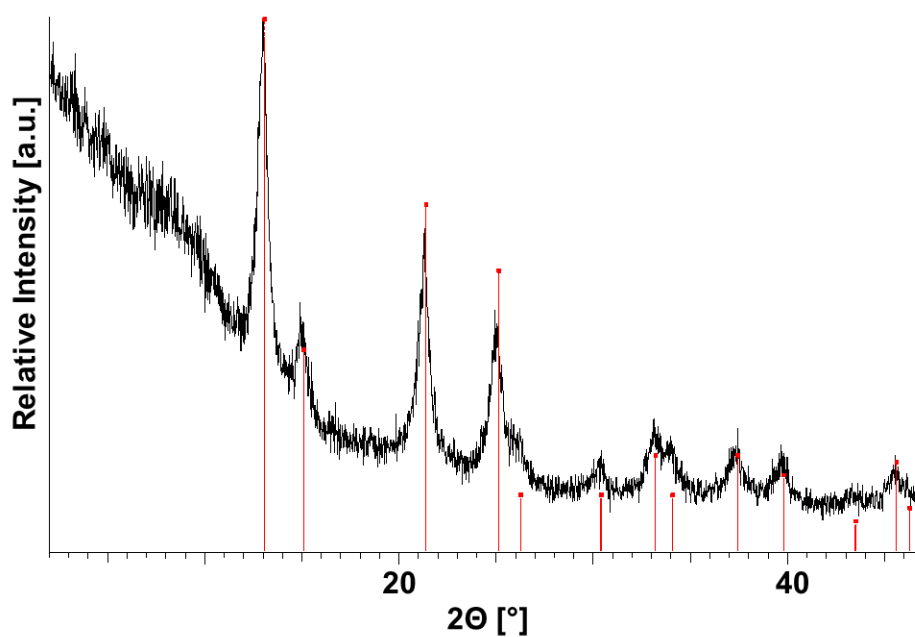
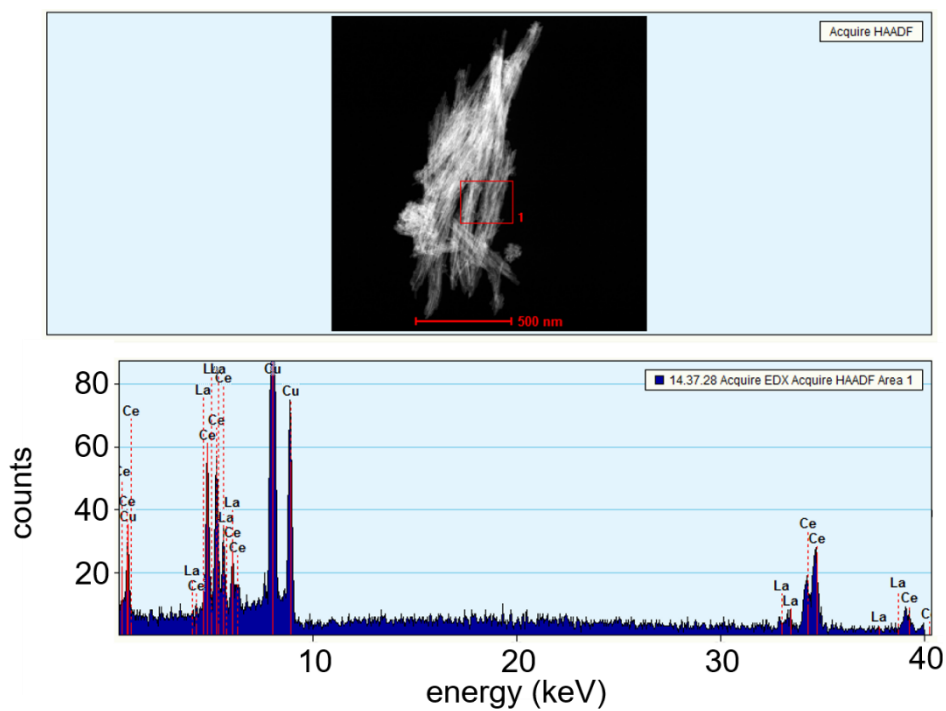


Fig. S20. Raman spectra of  $\text{CeO}_{2-x}$ ,  $\text{Ce}_{0.9}\text{La}_{0.1}\text{O}_{1.95-x}$  and  $\text{Ce}_{0.6}\text{La}_{0.4}\text{O}_{1.80-x}$  NRs.



**Fig. S21. P-XRD measurement of  $\text{Ce}_{0.6}\text{La}_{0.4}\text{O}_{1.80-x}$  NRs.** The reflex positions of the measured pattern (black) shows a shift to higher angles, compared to the control pattern of ceryanite (red). The results are in harmony with the diffractogram measured for  $\text{Ce}_{0.9}\text{La}_{0.1}\text{O}_{1.95-x}$ , where a detailed rietveld refinement was exemplarily done.





**Fig. S22. EDX measurement of  $\text{Ce}_{0.9}\text{La}_{0.1}\text{O}_{1.95-x}$  NRs.** The analysis revealed the presence of La in the sample. The results are in harmony with XPS and ICP-MS analysis.

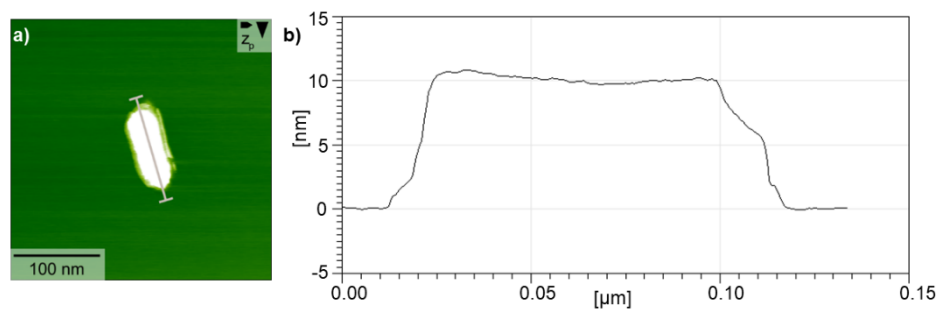


**Fig. S23: AFM image of  $\text{Ce}_{0.9}\text{La}_{0.1}\text{O}_{1.95-x}$  NRs** show a height of approx. 9-11 nm.

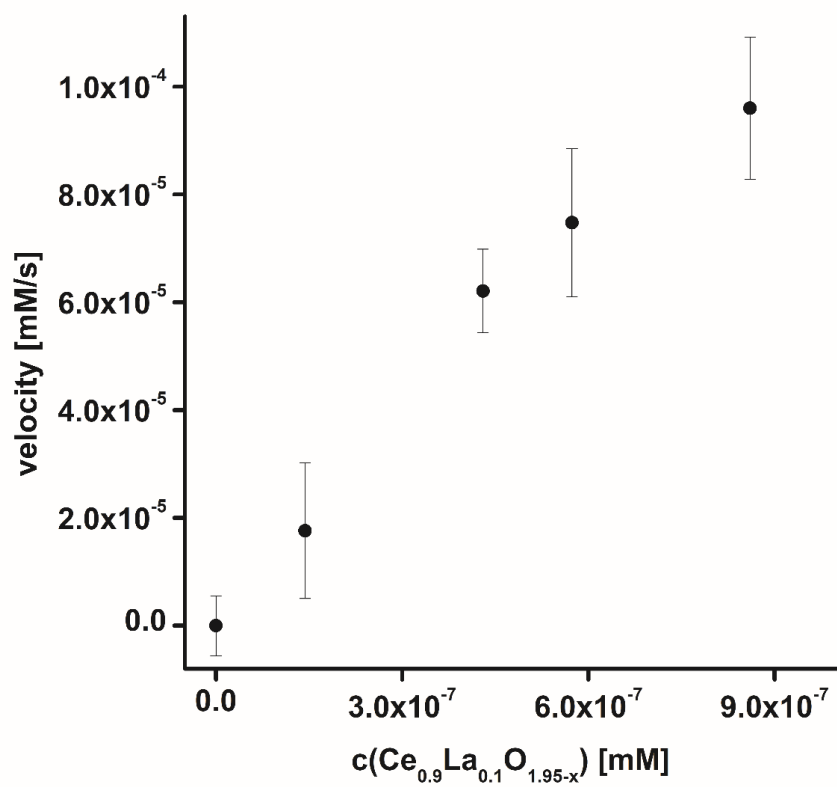


**Fig. S24.** Variation of the  $\text{Ce}_{0.9}\text{La}_{0.1}\text{O}_{1.95-x}$  NR concentration shows an increase of urea degradation with increasing catalyst concentration.

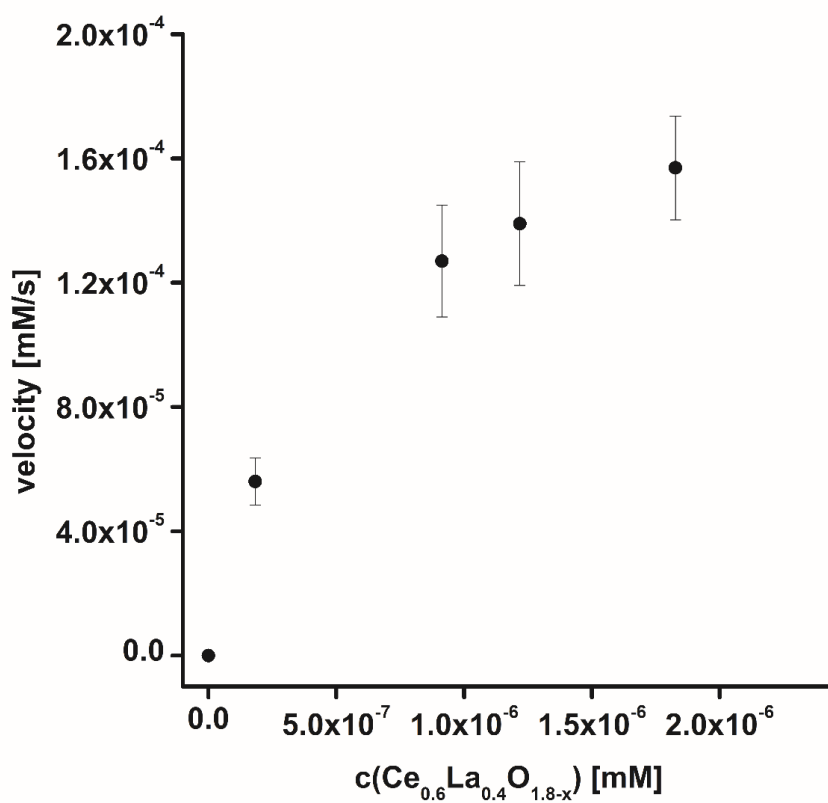


**Fig. S25.** Variation of the  $\text{Ce}_{0.6}\text{La}_{0.4}\text{O}_{1.8-x}$  NR concentration shows an increase of urea degradation with increasing catalyst concentration.

## Tables

Tab. S1. Data received from Rietveld refinements.

	$\text{CeO}_{2-x}$	$\text{Ce}_{0.9}\text{La}_{0.1}\text{O}_{1.95-x}$
Device	STOE Stadi P, Mo $K\alpha_1$ , Mythen 1K, transmission geometry	
Sample Prep	Powder between two vinylacetate foils (15 $\mu\text{m}$ )	
Measurement conditions	1.5 < 2 $\Theta$ /° < 70.83, resolution $\Delta\Theta = 0.015^\circ$ step scan, step size 1°, step time $\Delta t = 180$ s	
Background	Adapted	
$r_{\text{wp}}$	4.95	5.82
Gof	2.09	1.86
Space group	$Fm-3m$	
Lattice Parameter / Å	$a = 5.4071(6)$	$a = 5.9685(2)$
Crystallite size / nm	6.8(3)	5.9(8)

### 3. Results and Discussion

**Tab. S2.** Surface composition from XPS analysis.

	C	O	Ce	La	O/(Ce + La)
	at%	at%	at%	at%	
CeO <sub>2-x</sub>	9.9	57.0	33.1	-	1.72
Ce <sub>0.9</sub> La <sub>0.1</sub> O <sub>1.95-x</sub>	8.5	55.9	30.7	4.9	1.57
Ce <sub>0.6</sub> La <sub>0.4</sub> O <sub>1.80-x</sub>	9.6	55.7	17.4	17.3	1.60

**Tab. S3.** Leaching of Ce of CeO<sub>2-x</sub>NRs in MilliQ water. Data are corrected against standard but not blank corrected, due to the low blank values.

sample	c(Ce) [ $\mu\text{g L}^{-1}$ ]	SD [ $\mu\text{g L}^{-1}$ ]
blank (1)	0.04	0.005
blank (2)	0.03	0.003
blank (3)	0.05	0.004
CeO <sub>2-x</sub> (1)	0.4	0.1
CeO <sub>2-x</sub> (3)	1.6	0.1
CeO <sub>2-x</sub> (2)	0.8	0.1

### 3. Results and Discussion

**Tab. S4.** Leaching of Ce and La of  $\text{Ce}_{0.9}\text{La}_{0.1}\text{O}_{1.95-x}$  NRs in MilliQ water. Data are corrected against standard but not blank corrected, due to the low blank values.

sample	c(Ce) [ $\mu\text{g L}^{-1}$ ]	SD [ $\mu\text{g L}^{-1}$ ]	c(La) [ $\mu\text{g L}^{-1}$ ]	SD [ $\mu\text{g L}^{-1}$ ]
blank (1)	0.2	0.01	0.02	0.003
blank (2)	0.1	0.01	0.01	0.002
blank (3)	0.1	0.01	0.01	0.002
$\text{Ce}_{0.9}\text{La}_{0.1}\text{O}_{1.95-x}$ (1)	4.8	0.2	5.4	0.2
$\text{Ce}_{0.9}\text{La}_{0.1}\text{O}_{1.95-x}$ (2)	3.1	0.2	6.3	0.3
$\text{Ce}_{0.9}\text{La}_{0.1}\text{O}_{1.95-x}$ (3)	5.0	0.2	5.9	0.2

**Tab. S5.** Leaching of Ce of  $\text{CeO}_{2-x}$  NRs in 2.94 M urea solution. Data are corrected against standard but not blank corrected, due to the low blank values.

sample	c(Ce) [ $\mu\text{g L}^{-1}$ ]	SD [ $\mu\text{g L}^{-1}$ ]
blank (1)	0.5	0.02
blank (2)	0.6	0.03
blank (3)	0.4	0.02
$\text{CeO}_{2-x}$ (1)	12.3	0.7
$\text{CeO}_{2-x}$ (2)	8.1	0.3
$\text{CeO}_{2-x}$ (3)	5.9	0.3

### 3. Results and Discussion

**Tab. S6.** Leaching of Ce and La of  $\text{Ce}_{0.9}\text{La}_{0.1}\text{O}_{1.95-x}$  NRs in 2.94 M urea solution. Data are corrected against standard but not blank corrected, due to the low blank values.

sample	c(Ce) [ $\mu\text{g L}^{-1}$ ]	SD [ $\mu\text{g L}^{-1}$ ]	c(La) [ $\mu\text{g L}^{-1}$ ]	SD [ $\mu\text{g L}^{-1}$ ]
blank (1)	0.5	0.02	0.01	0.001
blank (2)	0.6	0.03	0.03	0.003
blank (3)	0.4	0.02	0.01	0.000
$\text{Ce}_{0.9}\text{La}_{0.1}\text{O}_{1.95-x}$ (1)	6.2	0.2	9.4	0.2
$\text{Ce}_{0.9}\text{La}_{0.1}\text{O}_{1.95-x}$ (2)	3.3	0.2	5.2	0.1
$\text{Ce}_{0.9}\text{La}_{0.1}\text{O}_{1.95-x}$ (3)	6.7	0.4	5.5	0.2

#### Calculation of catalytic turnover numbers $k_{\text{cat}}$

Catalytic turnover numbers  $k_{\text{cat}}$  were calculated using the equation  $k_{\text{cat}} = v_{\text{max}}/[E]$  with  $v_{\text{max}}$  as the maximum reaction velocity and  $[E]$  as enzyme or catalyst concentration. The  $v_{\text{max}}$  value was obtained by fitting the recorded data of the substrate variation with a modified Hill equation. In the following we will show the calculation of catalytic activities exemplarily using  $\text{CeO}_{2-x}$  NPs. The comparison of all tested materials is shown in Table S1.

#### Turnover number $k_{\text{cat}}$ calculated for molar NP concentrations

Turnover numbers determined for molar NP concentrations compare a defined object, the enzyme, with the NP, also a defined object. To calculate the molar NP concentrations the size of NPs is needed from TEM measurements (here:  $a = 120$  nm;  $b = 12$  nm and  $c = 9$  nm). With an approximation of a cuboid NP structure a middle particle volume can be determined with:

$$V_{\text{NP}} = a \times b \times c = 1.30 \times 10^4 \text{ nm}^3 = 1.30 \times 10^{-17} \text{ cm}^3.$$

Using the density of  $\text{CeO}_2$  ( $\rho = 7.65 \text{ g cm}^{-3}$ ) it is possible to calculate the weight of one NP:

$$m_{\text{NP}} = \rho \times V_{\text{NP}} = 9.91 \times 10^{-17} \text{ g}.$$

Dividing the used amount of catalyst ( $1.00 \times 10^{-1} \text{ g L}^{-1}$ ) for the measurements through  $m_{\text{NP}}$  gives the amount of NPs per liter.

$$\text{NP/L} = 1.01 \times 10^{15} \text{ L}^{-1}.$$

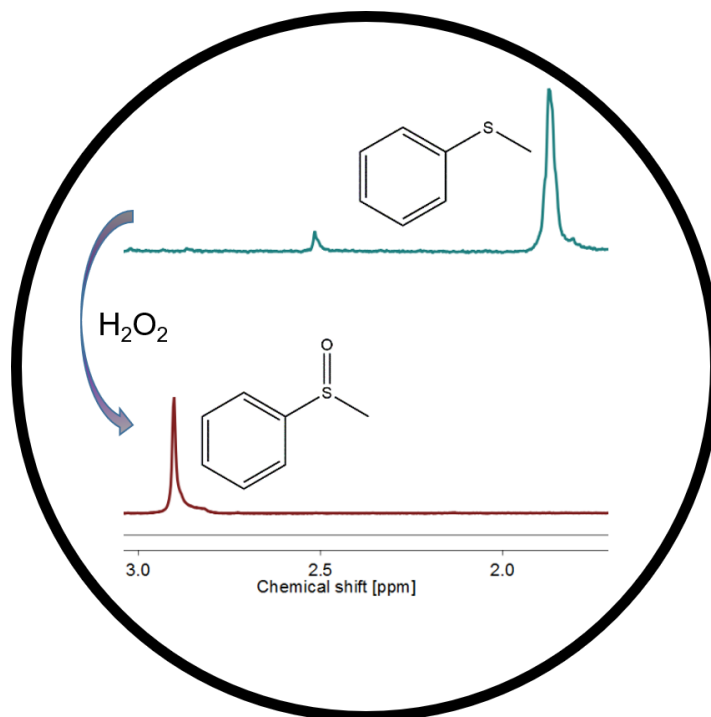
Normalizing the number of NP per liter with the Avogadro number enables the determination of a molar NP concentration.

$$c(\text{NP}) = (\text{NP/L})/N_{\text{A}} = 1.67 \times 10^{-9} \text{ mol L}^{-1} = 1.67 \times 10^{-6} \text{ mM}$$

$$k_{\text{cat}} = v_{\text{max}}/c(\text{NP}) = 9.58 \times 10^1 \text{ s}^{-1}$$



### 3.5 Selective Oxidation of Organic Sulfides with Single Metal Oxide and Mixed Metal Oxide Particles



The current chapter describes the oxidation of various organic sulfides in an aqueous media with hydrogen peroxide as green oxidation agent. The oxidation can be catalyzed with various metal oxide particles like  $V_2O_5$ ,  $MoO_{3-x}$  and  $W_{18}O_{49}$ . An increase of the catalytic activity can be achieved by mixing the metal phases of tungsten and molybdenum. The kinetic studies of all catalysts were conducted with a model system based on methyl phenyl sulfide.

The manuscript is prepared for publication. The following work was a cooperation with different colleagues. Hence, a detailed authorship contribution is attached in the appendix (chapter 5.3.5).

### 3.5.1 Abstract

Classical heterogeneous catalysis is wide spread in uncountable industrial processes. Catalysts enable milder reaction conditions and higher turnover numbers, compared to not catalyzed reactions. In pharmaceutical synthesis, but also in natural processes the selective oxidation of different sulfides is an important reaction step. We demonstrate that single metal oxide particles like  $\text{MoO}_{3-x}$ ,  $\text{V}_2\text{O}_5$  and  $\text{W}_{18}\text{O}_{49}$  can facilitate the oxidation of methyl phenyl sulfide with hydrogen peroxide as green and biocompatible oxidation agent in an aqueous media. A rate enhancement could be achieved by mixing the metal phases in tungsten and molybdenum mixed oxide particles. A broad range of particles with different molybdenum to tungsten (Mo:W) ratios was synthesized and analyzed to find the optimum composition for the catalytic sulfide oxidation. We found that a Mo:W ratio of 1.6:1 showed the best performance in catalyzing the oxidation reaction of methyl phenyl sulfide to methyl phenyl sulfoxide or to methyl phenyl sulfone in presence of one or three equivalents  $\text{H}_2\text{O}_2$ , respectively. In addition to kinetic studies with methyl phenyl sulfide we further report on the oxidation of various sulfides and the effect of an increasing steric hindrance and of different functional groups.

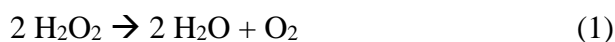
### 3.5.2 Introduction

A myriad of researchers is focused on the omnipresent target of simplifying and accelerating chemical reactions. One of the most efficient and simplest way is the use of catalysts, compounds that are well known to enable milder reaction conditions. An efficient catalysis provides the possibility of converting high amounts of substrate in shorter time.<sup>1</sup> It is thus not surprising that approximately 90% of all chemical production steps in industry are catalyzed.<sup>2</sup> To achieve high catalytic efficiencies in redox processes with metal containing catalysts, there are some central requirements for the active species, like easily changing the oxidation states by providing a sufficient stability, the possibility of a reoxidation into the initial state and the reversible bond formation during the reaction progress, regarding to a surface catalyzed reaction mechanism (e.g. Langmuir-Hinshelwood).<sup>3-5</sup> Metal based nanoparticles (NPs) or

microparticles (MPs) are well known as catalysts in classical heterogeneous catalysis,<sup>6-10</sup> where the specific surface area of the particle is one of the main characteristics.<sup>11</sup> The practical use of small metal based nano- or microparticles with high surface to volume ratios and pronounced densities of active surface sites is of particular interest. This aspect is nowadays important for every material, but it's a key point especially for cost intensive catalysts like e.g. rhodium or platinum. With the use of small nano- or microparticles it is possible to reduce the amount of catalyst by obtaining high efficiencies.<sup>1,12-13</sup> Due to the economic, electronic and coordinative properties, especially transition metals are promising materials.<sup>14</sup> The natural availability of various transition metals, that can be found for example in the active site of native enzymes, which are the probably most optimized catalysts, prove their extraordinary properties as catalytic material. Metals like copper, nickel, iron, molybdenum and manganese are distinguished by high availability in nature and by their functionality in various biological reactions.<sup>15-18</sup>

The oxidation of organic sulfides is a wide spread reaction step in organic synthesis, fine chemistry and pharmaceutical production.<sup>19-21</sup> It is a central issue and target to control the reaction process and to selectively oxidize an organic sulfide (RSR) into the sulfoxide (RSOR) without formation of sulfone as byproduct (RSO<sub>2</sub>R). Preparation steps under mild reaction conditions like room temperature or low amounts of reaction waste are of particular interests from an economic and ecological point of view.<sup>22</sup> In the past decades various oxidation agents like periodates, *tert*-butylnitrite, *meta*-chloroperoxybenzoic acid (*m*-CPBA), and peracetic acid (AcOOH) have been reported.<sup>20,23-25</sup> In recent years, especially the aspect of "green" and harmless reactants, solvents and reaction products came into the fore in scientific research and industrial processes. These methods attracted a lot of attention in general publicity.<sup>22,26-27</sup> Especially reaction agents that are easy and safely to handle came into vogue. While the use of organic compounds is often limited due to safety issues and elaborate product purification from residual acids, the use of hydrogen peroxide (H<sub>2</sub>O<sub>2</sub>) solve these problems.<sup>22,27</sup> Hence, the oxidation of organic compounds with H<sub>2</sub>O<sub>2</sub> is of high interest, in especially as the reaction products elemental oxygen (O<sub>2</sub>)

and water (H<sub>2</sub>O) (eq. 1), are harmless and biocompatible, which simultaneously leads to the reduction of reaction drop.<sup>28-29</sup>



The oxidation of various sulfides, conducted with one equivalent of hydrogen peroxide, lead to the formation of the appropriate sulfoxide, the single oxidized species. The main target of such reactions is to control the product formation without producing double oxidized species like the sulfone.<sup>30</sup>

Various transition metals are known to catalyze redox and oxygen transfer reactions like the oxidation of hexane or various sulfides.<sup>31-32</sup> The maybe most prominent metal species is the molybdenum, which catalyzes different oxygen transfer reactions in nature as active site of the enzymes xanthine oxidase (XO) and sulfite oxidase (SuOx).<sup>33-34</sup> It is not surprising that researchers used the great properties of molybdenum for different oxidation reactions in lab as MoO<sub>3</sub>, or as center of molybdenum complexes.<sup>35-36</sup> In addition to molybdenum similar properties are reported for the transition metals vanadium as vanadium(V) oxytriisopropoxide (VO(*i*-OPr)<sub>3</sub>) and vanadium(V) amine triphenolate complexes,<sup>37-38</sup> scandium as Sc(OTf)<sub>3</sub>,<sup>28</sup> tungsten as WO<sub>3</sub> or as tungstate complex (Na<sub>2</sub>WO<sub>4</sub>),<sup>29,39</sup> zirconium as zirconium tetrachloride (ZrCl<sub>4</sub>)<sup>27</sup> and titanium as titanium chloride (TiCl<sub>3</sub>)<sup>40</sup> or titanium tetraisopropoxide (Ti(O*i*-Pr)<sub>4</sub>).<sup>41</sup> In addition to metal complexes, also natural enzymes, like the native vanadium chloroperoxidase, the vanadium haloperoxidase and different model complexes are well known to catalyze the oxidation of different substrates with H<sub>2</sub>O<sub>2</sub> as oxidation agent.<sup>42-45</sup> In general, most reports on catalytic oxidations of organic sulfides were conducted in organic solvents such as at elevated temperatures, whereas reactions in an aqueous media, solvent free or in two phase systems at room temperature are known, but still rare.<sup>37-45</sup>

In addition to the above mentioned industrial importance, the oxidation of sulfur compounds is also present in biological processes of living organisms. The native sulfite oxidase, an enzyme located in the mitochondria of eukariotes, catalyzes the oxidation of sulfite (SO<sub>3</sub><sup>2-</sup>) into sulfate (SO<sub>4</sub><sup>2-</sup>).<sup>46</sup> Because of the diameters once could

describe a native enzyme as a nanocatalyst with a natural origin. It is thus not surprising that enzymes and nano- or microstructured particles can catalyze similar types of reactions<sup>47</sup> and it was recently reported, that artificial MoO<sub>3</sub> NPs can mimic the native sulfite oxidase enzyme.<sup>48</sup> Similar to the native SuOx a wide variety of metal containing enzymes are able to catalyze oxygen transfer reactions. Observing the mechanisms and the involved active sites of the enzymes, it is conspicuous, that especially molybdenum and vanadium are the most frequently occurring metal species in this natural processes.

Because of the omnipresent target of simplifying and optimizing reaction processes and the central meaning of a selective oxidation of organic sulfides into sulfoxides, we explored the performance of various transition metal oxide catalysts in an aqueous environment using H<sub>2</sub>O<sub>2</sub> as harmless oxidation agent. Inspired by the natural processes and the high frequency of the occurrence of vanadium and molybdenum, we synthesized and analyzed the properties of vanadium pentoxide (V<sub>2</sub>O<sub>5</sub>) and molybdenum oxide (MoO<sub>3-x</sub>) particles in the sulfide oxidation and because of the similarity of molybdenum and tungsten and further reports on WO<sub>3</sub> and Na<sub>2</sub>WO<sub>4</sub>,<sup>29,39</sup> we also investigated the properties of tungsten oxide (W<sub>18</sub>O<sub>49</sub>) particles as catalyst. To explore the influence of a mixed metal surface, we synthesized tungsten and molybdenum mixed oxide particles (Mo<sub>1-y</sub>W<sub>y</sub>O<sub>3-x</sub>), with different Mo:W ratios. All the kinetic studies were conducted with methyl phenyl sulfide (MPS) as representative organic sulfide, due to its low vapour pressure, compared to other organic sulfides. The reaction process was directly monitored with nuclear magnetic resonance (NMR) spectroscopy (Figure 1).

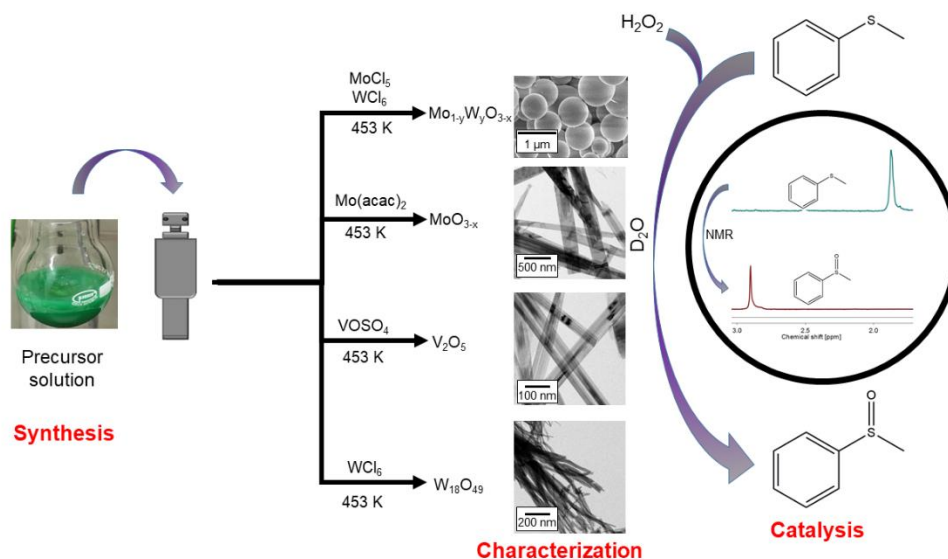


**Figure 1: Schematic representation of the synthesis, the characterization and catalytic procedure of various single metal oxide particles and the tungsten and molybdenum mixed metal oxide microparticles.** All catalysts were synthesized on a solvothermal route, using precursor solutions of appropriate metal salts. Overview TEM and SEM images, respectively, show the formation of  $\text{MoO}_{3-x}$  belts,  $\text{V}_2\text{O}_5$  wires,  $\text{W}_{18}\text{O}_{49}$  wires and  $\text{Mo}_{1-y}\text{W}_y\text{O}_{3-x}$  microspheres. All catalysts are able to facilitate the oxidation of methyl phenyl sulfide (TA) in an aqueous solution using hydrogen peroxide ( $\text{H}_2\text{O}_2$ ) as biocompatible and “green” oxidation agent. The reaction progress was observed with nuclear magnetic resonance (NMR) spectroscopy based on the influence of an oxidation on the chemical shift of the methyl group.

### 3.5.3 Experimental

**Chemicals.** The following chemicals were used without further purification. Vanadium (IV) sulfate oxide hydrate from abcr, Bis(acetylacetonato) dioxomolybdenum(VI), 3-(Trimethylsilyl)propionic-2,2,3,3 d<sub>4</sub> sodium salt, Ethyl(methylthio) acetate, Ethanethiol and (Ethylthio)trimethylsilane from Aldrich, nitric acid 65% from Merck, Potassium bromate, Molybdenum (V) chloride (99.99%), Tungsten (VI) chloride (99.99%) and Methyl phenyl sulfide from Sigma-Aldrich, (Methylthio)acetic acid from Alfa Aesar

**Synthesis of tungsten oxide (W<sub>18</sub>O<sub>49</sub>) wires.** The tungsten oxide wires were synthesized according to a solvothermal method reported earlier.<sup>49</sup> The starting solution was prepared by dissolving 1.27 mmol of tungsten hexachloride (WCl<sub>6</sub>) in 25 mL of ethanol by sonication. Then 5 mL of the precursor solution were injected into a 50 mL Teflon<sup>®</sup>-lined vessel containing another 30 mL of ethanol. After sealing the vessel in a stainless steel autoclave the reaction was started by putting the autoclave in an electric oven for 12 h at 453 K. After the reaction, dark blue particles were collected by centrifugation, rinsed with ethanol two times and dried *in vacuo* for 6 h at 333 K.

**Synthesis of molybdenum oxide (MoO<sub>3-x</sub>) belts.** MoO<sub>3-x</sub> belts were synthesized in similarity to a procedure reported by Bai *et al.*<sup>50</sup> 5.5 mmol of Bis(acetylacetonato) dioxomolybdenum(VI) were dissolved in 200 mL of water and heated to 313 K for complete dissolving. The solution was transferred into a 250 mL Teflon<sup>®</sup>-lined vessel, which was placed in a stainless steel autoclave. The autoclave was set in an electric oven which was heated to 453 K for 20 h. After the autoclave was cooled down to the room temperature, the precipitate was isolated *via* centrifugation (9000 rpm, 10 min.) and the product was washed with water for several times and dried for 24 h in a desiccator.

**Synthesis of vanadium pentoxide ( $V_2O_5$ ) wires.**  $V_2O_5$  wires were prepared using a method reported elsewhere.<sup>51</sup> In comparison to the literature report, we did some small changes in the procedure. In brief, 8.0 mmol  $VOSO_4 \cdot nH_2O$  and 5.0 mmol  $KBrO_3$  were dissolved in 25 mL of water. The green reaction mixture changed the colour within three minutes from green to red (Figure S1). The dispersion was then stirred for 30 min at room temperature. After this time, 2 mL of nitric acid (65 %) were added over a period of one hour, until the precipitate was dissolved. The finally red and clear solution was added into a 50 mL Teflon<sup>®</sup> inlay, which was set into a stainless steel autoclave. The autoclave was placed in an electric oven and heated to 453 K for 24 h. Afterwards, it was naturally cooled to room temperature and the yellow precipitate was collected *via* centrifugation (9000 rpm, 10 min.). The product was washed with water and ethanol for several times and dried for 48 h in a desiccator.

**Synthesis of molybdenum tungsten mixed oxide ( $Mo_{1-y}W_yO_{3-x}$ ) microparticles.** 0.37 mmol of molybdenum (V) chloride and Y mmol (with  $Y = 0.37, 0.24, 0.12, 0.06$ ) tungsten (VI) chloride was dissolved in 100 mL of ethanol to form a clear solution. The as-prepared solutions were transferred to three 50 mL Teflon<sup>®</sup>-lined vessels. After sealing the vessel in a stainless steel autoclave the solvothermal reaction was started by heating the autoclave at 453 K for 12 h in an electric oven. After the reaction, grey particles were collected by centrifugation rinsed with ethanol two times and dried in vacuum for 6 h at 333 K. In a further step, the dried samples were annealed under argon-atmosphere for 24 h at three different temperatures (673 K, 773 K, 873 K).



**Catalytic Sulfoxidation of organic sulfides.** All measurements were conducted in NMR tubes containing 700  $\mu\text{L}$  in total. For the analysis stock solutions of each catalyst (0.014 mmol/mL) and 3-(Trimethylsilyl)propionic-2,2,3,3  $\text{d}_4$  sodium salt (TMSP, 5  $\text{mg}\cdot\text{mL}^{-1}$ ) were prepared in deuterated water ( $\text{D}_2\text{O}$ ). Every sample contained 100  $\mu\text{L}$  catalyst solution, 100  $\mu\text{L}$  TMSP, 0.12 mmol sulfide and 1 or 3 eq hydrogen peroxide, respectively. The reaction solution was filled up with  $\text{D}_2\text{O}$  to achieve a final volume of 700  $\mu\text{L}$ . Hydrogen peroxide ( $\text{H}_2\text{O}_2$ ) was added in one portion to start the reaction. Kinetic studies were conducted in a period of 30 min. The TMSP was used as reference for all spectra and the resonance was set to 0 ppm. A splines baseline correction was used to minimize integration errors. The NMR spectra were evaluated by comparing the integrals of selected resonances.

**X-ray diffraction.** Diffraction data of the single oxide particles were measured with a Siemens D5000 diffractometer with a Ge (220) monochromator using the  $\text{Cu K}\alpha$  radiation. The diffraction data of the tungsten and molybdenum mixed oxide particles were recorded using a Bruker AXS D8 discover diffractometer with a HiStar detector system and graphite monochromatic  $\text{Cu K}\alpha$  radiation. Final data analysis was done with the EVA software package.

**NMR measurements.** NMR-spectra measurements were performed on a Bruker ARX 400 spectrometer with a  $^1\text{H}$  frequency of 399.83 MHz. The samples were prepared like described in the kinetic analysis part. A script was programmed to measure a  $^1\text{H}$ -NMR spectrum every minute. Collected spectra were analyzed with the MestRenova NMR software.

**Raman spectroscopy.** All Raman spectra were measured using a Horiba Yvon Lab RAM HR 800 spectrometer. The spectrometer was provided with Olympus BX41 microscope and a CCD detector system. The width of the entry gap was set to 100  $\mu\text{m}$ . The dimensions of the focal spot were 2 x 2  $\mu\text{m}$ . Further a neodymium-doped yttrium aluminium garnet ( $\text{Nd:Y}_3\text{Al}_5\text{O}_{12}$ , Nd:YAG) laser with an emission wavelength of 532.12 nm and a laser power of 2 mW was used. With the help of a 50x long working distance objective, the laser beam was focused on the previously grinded powder sample. Finally, the spectra were measured with a resolution of 0.5  $\text{cm}^{-1}$  in the range of 150 – 1200  $\text{cm}^{-1}$  in backscattering mode.

**Scanning electron microscopy (SEM).** SEM analysis was conducted for the tungsten and molybdenum mixed oxide microparticles with a FEI Nova NanoSEM 600. The SEM had a low-voltage high-contrast-detector (vCD) and an Everhart-Thornley detector (ETD). The device was engaged with an acceleration voltage in the range of 5 - 10 kV. The previously grinded powder of every sample was placed onto an adhesive carbon tape, which was affixed onto an aluminum stub.

**Transmission electron microscopy (TEM).** TEM images were recorded using a Zeiss LEO 906E TEM with an acceleration voltage of 120 kV (Carl Zeiss, Oberkochen, Germany). The samples were prepared by drop-casting a dispersion of the appropriate particle onto a thin carbon film suspended on a 300 mesh copper TEM grid (3 mm).

**High resolution transmission electron microscopy (HR-TEM).** All HR-TEM images were taken using a Tecnai F20 from FEI, which was operated with an acceleration voltage of 200 kV.

### 3.5.4 Results and discussion

**Synthesis of the single metal oxide and mixed metal oxide particles.** Vanadium, molybdenum and tungsten oxide particles as well as the molybdenum and tungsten mixed metal oxide MPs were synthesized using a solvothermal autoclave synthesis. In brief a solution of the appropriate metal precursor salt was added into a Teflon<sup>®</sup> inlay, which was sealed in a stainless steel autoclave.<sup>49-51</sup> The autoclave was placed in an electric oven to start the reaction process (details see experimental section).

The morphologies of the single metal oxide particles were investigated by transmission electron microscopy (TEM, Figure 1) and high resolution TEM (HR-TEM). The solid state phase was analyzed with powder X-ray diffraction (P-XRD) measurements and Raman spectroscopy. In addition to single metal oxide particles, the molybdenum and tungsten mixed oxide particles with different Mo:W ratios were synthesized and the effect of a mixed metal phase on the catalytic activity in a sulfoxide reaction was investigated. Molybdenum and tungsten mixed oxide particles were characterized with scanning electron microscopy (SEM), Raman spectroscopy and P-XRD measurements.

TEM measurements of the single metal oxide particles show the formation of vanadium pentoxide ( $V_2O_5$ ) and tungsten oxide ( $W_{18}O_{49}$ ) wires as well as the formation of molybdenum oxide ( $MoO_{3-x}$ ) belts (Figure 1). The morphological characterizations of the particles with TEM show a nanostructured surface, diameters in nanometer- and lengths in micrometer ranges (Figure 2 A - C). As-prepared molybdenum and tungsten mixed oxide particles formed spheres with diameters ranging from 0.4 – 2  $\mu m$  (Figure 2 D - G).

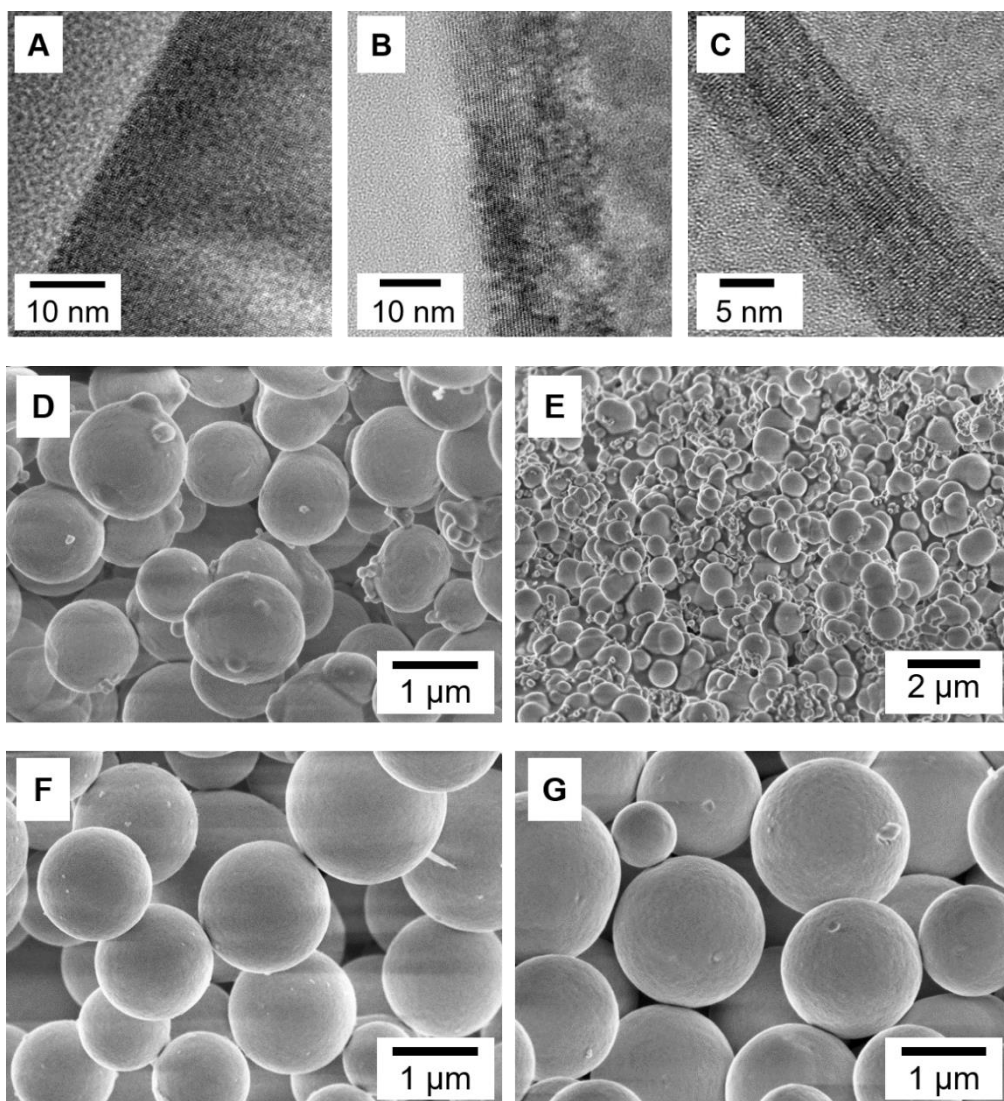


**Figure 2:** HR-TEM images of A)  $\text{MoO}_{3-x}$ , B)  $\text{V}_2\text{O}_5$ , C)  $\text{W}_{18}\text{O}_{49}$  and SEM images of D)  $\text{Mo}_{0.5}\text{W}_{0.5}\text{O}_{2.1}$  E)  $\text{Mo}_{0.62}\text{W}_{0.38}\text{O}_{2.3}$  F)  $\text{Mo}_{0.75}\text{W}_{0.25}\text{O}_{2.4}$  G)  $\text{Mo}_{0.85}\text{W}_{0.15}\text{O}_{2.6}$ . Morphological characterization of single oxide particles show a wire- or belt-like structure with nanostructured surface. The measured diameters are in the nanometer range, whereas their lengths are in the range of several micrometers. In contrast molybdenum and tungsten mixed oxide particles are spheres with diameters ranging from 0.4 – 2  $\mu\text{m}$ . During the measurements of the  $\text{V}_2\text{O}_5$  sample electron beam induced surface damages could be observed. Hence, the surface in TEM image shows an inhomogeneous character.

Investigations of the solid phase with P-XRD measurements show that the single oxide particles were mostly crystalline, whereas preferably broad and weak reflections were recorded for mixed oxide particles, proposing a less ordered and mainly non-crystalline structure (Figure S2 - S5).

To investigate the substitution of molybdenum with tungsten in the  $\text{MoO}_{3-x}$  structure, Raman spectra were recorded for the single metal and the mixed metal oxide particles. The Raman bands recorded for the single metal oxide particles are summarized in the supporting information (Tables S1 – 3), where a detailed assignment to the corresponding modes is given.<sup>52-54</sup> The occurring Raman bands in the  $\text{MoO}_{3-x}$  spectrum are in harmony with literature reports for orthorhombic  $\text{MoO}_3$  (Figure 3 A, Table S1).<sup>52</sup> In the Raman spectrum of  $\text{W}_{18}\text{O}_{49}$ , a band broadening can be observed, due to a great diversity of W-O-W bond lengths, which are further explainable with a high amount of oxygen vacancies in a distorted  $\text{ReO}_3$  structure (Figure 3 C, Table S3).<sup>53</sup> The spectra of the molybdenum and tungsten mixed oxide MPs show four main peaks, that get weaker with increasing Mo:W ratio. The sharpest bands can be observed in the Raman spectrum of Mo:W ratio of 1:1. The band with the highest intensity occurring at  $809\text{ cm}^{-1}$  is related to the terminal  $\nu(\text{M}=\text{O})$  band and the belonging stretching mode. O-M-O stretching vibrations of the linking oxygen atoms lead to a Raman band at  $710\text{ cm}^{-1}$ . The occurrence of further bands at  $260\text{ cm}^{-1}$  and  $329\text{ cm}^{-1}$  are attributed to the O-M-O deformation mode. Generally, it is observable that an increasing Mo:W ratio leads to a Raman band shift to higher wavenumbers.

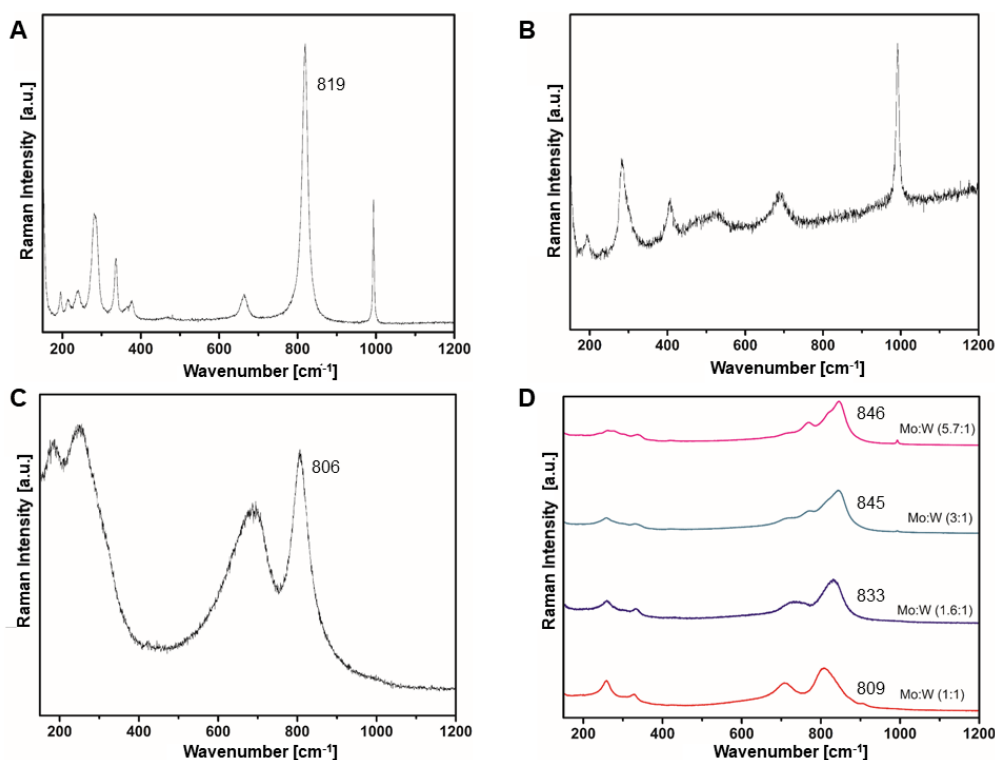


**Figure 3: Raman spectra of (A)  $\text{MoO}_{3-x}$ , (B)  $\text{V}_2\text{O}_5$ , (C)  $\text{W}_{18}\text{O}_{49}$  and (D)  $\text{Mo}_{1-y}\text{W}_y\text{O}_{3-x}$  with different Mo:W ratios.** A detailed assignment of the observed Raman bands is given in the supporting information (Table S1-S3). The numbers given in the spectra are the wavenumbers of the maximum, that can be assigned to the stretching mode of the terminal  $\nu(\text{M}=\text{O})$  band.

**Sulfide oxidation.** As-synthesized particles were investigated on their ability of catalyzing the oxidation of organic sulfides in an aqueous environment with  $\text{H}_2\text{O}_2$  as harmless oxidation agent. To analyse the catalytic activities of the different catalysts, methyl phenyl sulfide (MPS) was used as representative organic sulfide. All reactions were conducted in NMR tubes with a total volume of 700  $\mu\text{L}$  and the reaction was monitored by  $^1\text{H}$ -NMR spectroscopy using deuterated water ( $\text{D}_2\text{O}$ ) as solvent. Kinetic studies were conducted by recording NMR spectra in an one minute range over a period of 30 min. The formation of methyl phenyl sulfoxide (MPSO) was observed based on the methyl resonances of MPS and MPSO. While the NMR signal of the  $\text{CH}_3$  group of MPS can be observed at 1.87 ppm, the signal of the MPSO is shifted to lower fields (2.91 ppm) (Figure S6-S7). The shift can be explained with the -I effect of the oxygen atom, which binds to the sulfide. To enable a better comparability of individual measurements 3-(Trimethylsilyl)-propionic-2,2,3,3  $\text{d}_4$  sodium salt (TMSP) was used

### 3. Results and Discussion

as internal standard and the methyl resonance of TMSF was manually set to 0 ppm. The kinetic analysis of  $\text{MoO}_{3-x}$ ,  $\text{W}_{18}\text{O}_{49}$ , and  $\text{V}_2\text{O}_5$  particles demonstrated a high selectivity of the MPS oxidation with  $\text{H}_2\text{O}_2$  to the MPSO without the formation of a double oxidized sulfone. While  $\text{V}_2\text{O}_5$  only showed a moderate activity,  $\text{W}_{18}\text{O}_{49}$  and especially  $\text{MoO}_{3-x}$  demonstrated great catalytic properties (Figure 4 A - C). The sulfoxide formation over a period of 30 min shows the different catalytic activities and the formation of MPSO within the first 30 min (Figure 4 D). Control measurements using only  $\text{H}_2\text{O}_2$  or the catalyst did not show an oxidation of TA (Figure S8 - S9).

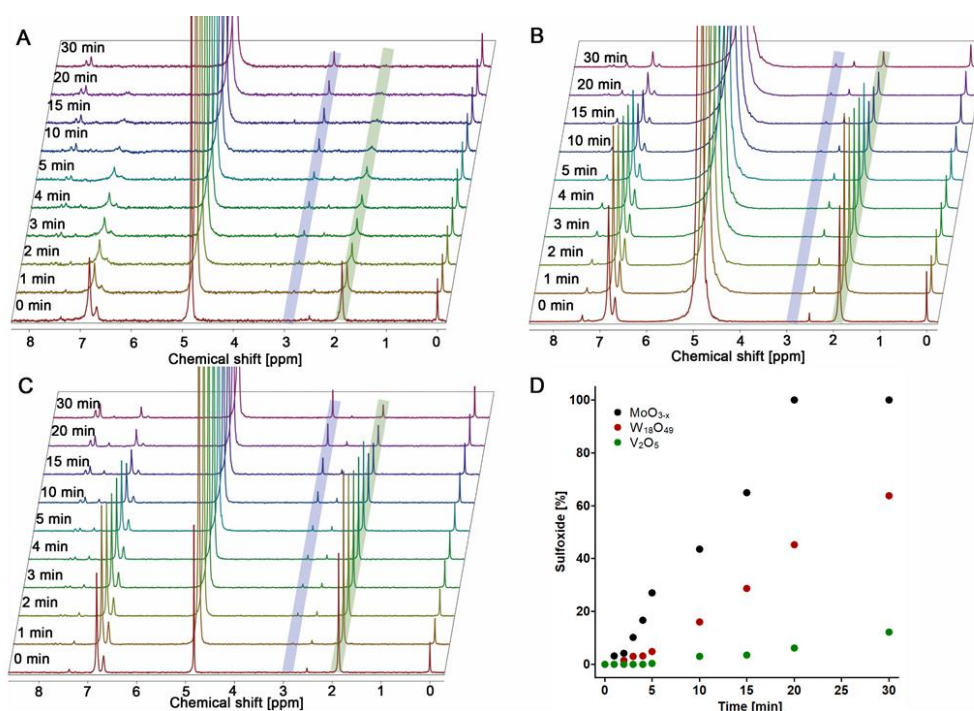


**Figure 4: Catalytic studies of the oxidation of MPS with hydrogen peroxide catalyzed by (A)  $\text{MoO}_{3-x}$ , (B)  $\text{V}_2\text{O}_5$  and (C)  $\text{W}_{18}\text{O}_{49}$ .** All catalysts facilitated the oxidation of the MPS in presence of  $\text{H}_2\text{O}_2$ . (D) Formation of MPSO over time. While  $\text{MoO}_{3-x}$  and  $\text{W}_{18}\text{O}_{49}$  showed the strongest activity with a turnover of 100% and 63.9% after 30 min reaction time,  $\text{V}_2\text{O}_5$  only showed a slight activity. The signals observable at a chemical shift of 2.5 ppm can be explained by a two phase system, where MPS is partially not dissolved in the aqueous phase. A high selectivity is observable for all catalysts because only the single oxidized MPSO was formed.

Motivated by the great performance of  $\text{MoO}_{3-x}$  and  $\text{W}_{18}\text{O}_{49}$  during the kinetic studies, we further investigated the effect of mixing the metal phase by preparing tungsten and molybdenum mixed oxide particles. The particles were prepared with different Mo:W ratios (1:1, 1.6:1, 3:1 and 5.7:1) and their catalytic activities were analyzed with the above described procedure for the single metal oxide particles. It is observable that the  $\text{Mo}_{1-y}\text{W}_y\text{O}_{3-x}$  particles with Mo:W ratios of 1.1, 1.6:1 and 3:1 showed the highest activities. Hence, we show the results of the kinetic studies here in detail (Figure 5 A - C). The main characteristic of a heterogeneous catalyst is the surface area, which represents the active part. Thus, a normalization of the activities to the Brunauer Emmett Teller (BET) surface area is useful and necessary to identify possible influences of the mixed solid phase. The results of the BET measurements show a decrease of the surface area with increasing Mo:W ratio. The calculated and normalized activities demonstrate a pronounced activity of the  $\text{Mo}_{1-y}\text{W}_y\text{O}_{3-x}$  particles in comparison to the single metal oxide particles  $\text{MoO}_{3-x}$  and  $\text{W}_{18}\text{O}_{49}$ . Calculated data show that the highest turnover *per* minute and  $\text{m}^2$  surface area could be achieved with  $\text{Mo}_{0.62}\text{W}_{0.38}\text{O}_{2.3}$  (Mo:W ratio 1.6:1) (Figure 5 D). At this point it is worth to mention that because of the not soluble catalyst (Figure S10) and the limited solubility of MPS in water, the mixing of the sample solution plays a crucial role. It was possible to achieve a 100 % oxidation of TA to MPSO using the  $\text{Mo}_{0.62}\text{W}_{0.38}\text{O}_{2.3}$  particles within 18 min in case the reaction mixture in the NMR tube was shaken for 10 seconds with a vortexer. Without shaking the tube, a total oxidation was achieved after 32 min. Hence, all experiments were strictly conducted with a 10 seconds mixing step.

To investigate a possible double oxidation of MPS to the methyl phenyl sulfone, studies were conducted with the same procedure in presence of three equivalents of  $\text{H}_2\text{O}_2$  over a period of 48 h. The experiments confirmed the positive effect of a mixed metal phase, because after 48 h the  $\text{Mo}_{1-y}\text{W}_y\text{O}_{3-x}$  particles show higher activities than  $\text{MoO}_{3-x}$  and  $\text{W}_{18}\text{O}_{49}$  particles. Control measurements conducted without catalyst but in presence of  $\text{H}_2\text{O}_2$  only showed the formation of approx. 35 % MPSO, but no sulfone. Also the experiments with three equivalents of  $\text{H}_2\text{O}_2$  show that the particles with a Mo:W ratio of 1.6:1 exhibit the highest activity (Figure S 11).



### 3. Results and Discussion

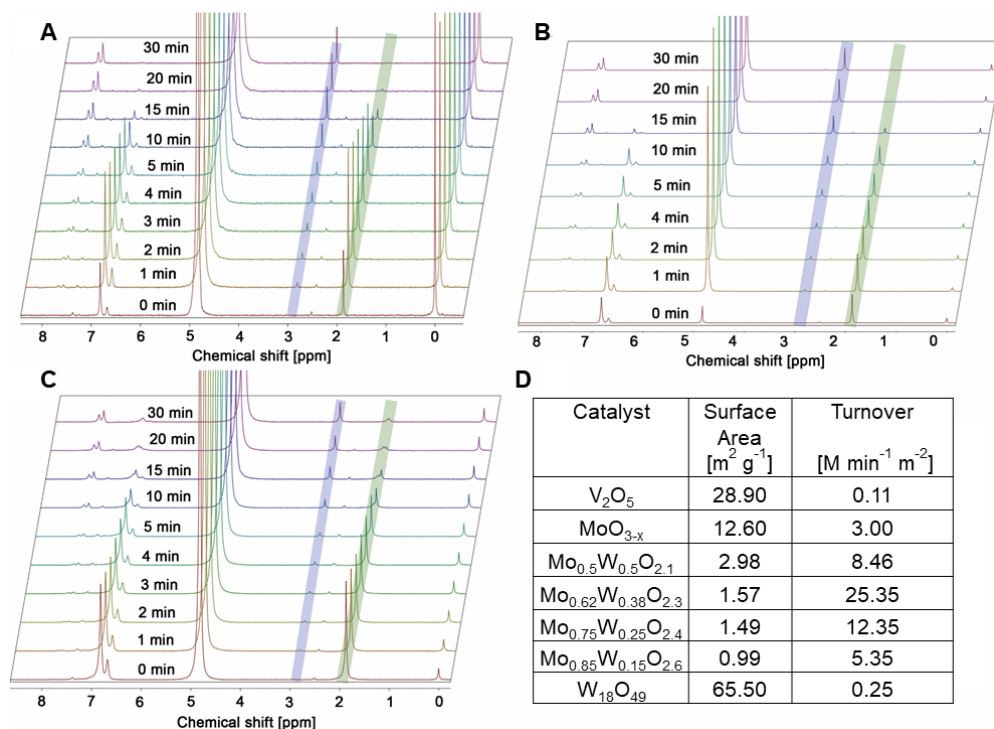


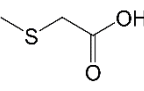
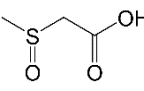
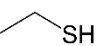
**Figure 5: Kinetic analysis of the oxidation of MPS with H<sub>2</sub>O<sub>2</sub> catalyzed by Mo<sub>1-y</sub>W<sub>y</sub>O<sub>3-x</sub> microspheres.** All catalysts facilitated the observed oxidation reaction significantly by providing a high selectivity to the single oxidation product. NMR spectra of the reaction conducted with a Mo:W ratio of (A) 1:1, (B) 1.6:1 and (C) 3:1 are shown, illustrating the progress of the catalytic reaction. (D) Turnover numbers were calculated normalized to the BET surface area. As-calculated turnover numbers show that the mixed oxide particles exhibit pronounced catalytic activities compared to the single metal oxide particles. An optimum Mo:W ratio of 1.6:1 was determined and used for further studies.

In addition to the kinetic studies of the oxidation of MPS, we investigated the possibility of oxidizing different organic sulfides with a wide variety of functional groups (Table 1). For the studies the most active particles ( $\text{Mo}_{0.62}\text{W}_{0.38}\text{O}_{2.3}$ ) were used. We found, that substrates with low steric hindrance like 2-Hydroxyethyl methyl sulfide were oxidized after a few minutes, whereas an increase of the steric hindrance led to higher reaction times and finally, like for example in case of diphenyl sulfide, to a not possible oxidation (Table 1). In addition to the diphenyl sulfide the oxidation of trimethylsilyl ethyl sulfide was not successful and reactions with ethane thiol formed various by-products. Nevertheless, except the three mentioned examples, all other substrates could be oxidized with high turnovers in short reaction times. In addition, it is observable, that these reactions run under high selectivity without the formation of any byproducts. (Figure S12-S17). The catalyzed reactions run much faster than the control measurements in absence of the catalyst (Figure S18-S21). Except for the dimethyl sulfide a double oxidation with three equivalents of  $\text{H}_2\text{O}_2$  was not possible (Figure S22).

### 3. Results and Discussion

**Table 1: Tested substrates for the sulfide oxidation reaction with one equivalent H<sub>2</sub>O<sub>2</sub> and Mo<sub>0.62</sub>W<sub>0.38</sub>O<sub>2.3</sub> particles in aqueous solution.**

Substrate	Structure	Product	Time [min]	Turnover [%]	Selective
Methyl phenyl sulfide			18	100	Yes
2-Hydroxyethyl methyl sulfide			5	100	Yes
Diphenyl sulfide			720*	XX	X
Dimethyl sulfide			3	100	Yes
Allyl methyl sulfide			7	100	Yes
Ethyl(methylthio) acetate			16	100	Yes
Trimethylsilyl ethyl sulfide			30*	XX	XX

Substrate	Structure	Product	Time [min]	Turnover [%]	Selective
(Methylthio) acetic acid			30	90	Yes
Ethane thiol		XX	30	**	No

\*no reaction observable, \*\*various byproducts like diethyldisulfide and different oxidized species

### 3.5.5 Conclusion

In conclusion we synthesized various single metal oxide particles, like  $\text{MoO}_{3-x}$ ,  $\text{V}_2\text{O}_5$  and  $\text{W}_{18}\text{O}_{49}$ , which catalyze the sulfide oxidation of methyl phenyl sulfide into methyl phenyl sulfoxide with one equivalent  $\text{H}_2\text{O}_2$  as green and biocompatible oxidation agent. The oxidation was possible in an aqueous solution or a two-phase system, respectively, depending on the solubility of the organic sulfide and was further selective to a single oxidation reaction. Mixing the metal phase of molybdenum and tungsten by synthesizing  $\text{Mo}_{1-y}\text{W}_y\text{O}_{3-x}$  microparticles, led to a significant increase of the catalytic turnover. We found an optimum Mo:W ratio of 1.6:1. An oxidation of methyl phenyl sulfide into the methyl phenyl sulfone with three equivalents  $\text{H}_2\text{O}_2$  catalyzed by  $\text{MoO}_{3-x}$ ,  $\text{W}_{18}\text{O}_{49}$  and the  $\text{Mo}_{1-y}\text{W}_y\text{O}_{3-x}$  particles was also possible and confirmed the  $\text{Mo}_{0.62}\text{W}_{0.38}\text{O}_{2.3}$  as the most active compound. In addition to the kinetic studies with methyl phenyl sulfide we used a wide variety of organic sulfides with different functional groups. Overall the oxidation into the sulfoxide was possible under a high selectivity with good product formation rates.

### 3.5.6 References

- 1) R. Schlögl, *Angew. Chem. Int. Ed.* 2015, **54**, 3465-3520.
- 2) F. Shüth, *Chem. unserer Zeit* 2006, **40**, 92-103.
- 3) J. C. Védrine, *Catalysts* 2017, **7**, 341.
- 4) A. M. Gómez-Marín, J. P. Hernández-Ortiz, *J. Phys. Chem. C* 2014, **118**, 2475-2486.
- 5) M. Zhao, C. Chen, *ACS Catal.* 2017, **7**, 7490-7494.
- 6) A. M. Molenbroek, S. Helveg, H. Topsoe, B. S. Clausen, *Top Catal* 2009, **52**, 1303-1311.
- 7) J. Huang, T. Jiang, H. Gao, B. Han, Z. Liu, W. Wu. Y. Chang, G. Zhao, *Angew. Chem.* 2004, **116**, 1421-1423.
- 8) M. Kishida, T. Fujita, K. Umakoshi, J. Ishiyama, H. Nagata, K. Wakabayashi, *J. Chem. Soc. Chem. Commun.* 1995, 763-764
- 9) Z. Zhang, H. Che, J. Gao, Y. Wang, X. She, J. Sun, P. Gunawan, Z. Zhong, F. Su, *Catal. Sci. Technol.* 2012, **2**, 1207-1212.
- 10) Y. Tang, B. Li, N. Zhang, S. Wang, Y. Wen, P. Jin, X. Wang, *CrystEngComm.* 2012, **14**, 3854-3857.
- 11) N. Mizuno, M. Misono, *Chem. Rev.* 1998, **98**, 199-217.
- 12) K. Korschelt, M. N. Tahir, W. Tremel, *Chem. Eur. J.* 2018, DOI: 10.1002/chem.201800384.
- 13) J. Biener, A. Wittstock, T. F. Baumann, J. Weissmüller, M. Bäumer and A. V. Hamza, *Materials* 2009, **2**, 2404-2428.
- 14) Dyker, *Angew. Chem. Int. Ed.* 1999, **38**, 1698-1712.
- 15) B. Krajewska, *J. Mol. Catal. B: Enzymatic* 2009, **59**, 9-21

- 16) G. Schwarz, R. R. Mendel, M. W. Ribbe, *Nature* 2009, 460, 839-847.
- 17) I. A. Abreu, D. E. Cabelli, *Biochim Biophys Acta* 2010, **1804**, 263-274.
- 18) A. Butler, *Coord. Chem. Rev.* 1999, **187**, 17-35.
- 19) S. Caron, R. W. Dugger, S. G. Ruggeri, J. A. Ragan, Da. H. Brown Ripin, *Chem. Rev.* 2006, **106**, 2943-2989
- 20) B. Yu, Z.-F. Diao, A.-H. Liu, X. Han, B. Li, L.-N. He, X.-M. Liu, *Curr. Org. Synth.* 2014, **11**, 156-160.
- 21) B. Zhang, M.-D. Zhou, M. Cokoja, J. Mink, S.-L. Zangb, F. E. Kühn, *RSC Adv.* 2012, **2**, 8416-8420.
- 22) R. D. Chakravarthy, V. Ramkumar, D. K. Chand, *Green Chem.* 2014, **16**, 2190-2196.
- 23) F. Ruff, A. Fábian, Ö. Farkas, Á. Kucsman, *Eur. J. Org. Chem.* 2009, 2102-2111.
- 24) V. T. Mathad, S. Govindan, N. K. Kolla, M. Maddipatla, E. Sajja, V. Sundaram, *Org. Proc. Res. Dev.* 2004, **8**, 266-270.
- 25) R. W. Murray, R. Jeyaraman, M. K. Pillay, *J. Org. Chem.* 1987, **52**, 746-748.
- 26) K. Bahrami M. M. Khodaei, M. S. Arabi, *J. Org. Chem.* 2010, **75**, 6208-6213.
- 27) K. Bahrami, *Tetrahedron Lett.* 2006, **47**, 2009-2012.
- 28) M. Matteucci, G. Bhalay, M. Bradley *Org. Lett.* 2003, **5**, 235-237.
- 29) R. Noyori, M. Aoki, K. Sato, *Chem. Commun.* 2003, 1977-1986.
- 30) M. M. Khodaei, K. Bahrami, M. Khedri, *Can. J. Chem.* 2007, **85**, 7-11
- 31) R. K. Graselli, *Top. Catal.* 2002, **21**, 79-88.
- 32) Z.-R. Tian, W. Tong, J.-Y. Wang, N.-G. Duan, V. V. Krishnan, S. L. Suib, *Science* 2009, **276**, 926-930.

- 33) R. Hille, *Dalton Trans.* 2013, **42**, 3029-3042.
- 34) J. Haber, E. Lalik, *Catal. Today* 1997, **33**, 119-137.
- 35) A. A. Said, M. M. A. El-Wahab, A. M. Alian, *IOP Conf. Ser.: Mater. Sci. Eng.* 2014, **64**, 012058.
- 36) C. J. Carrasco, F. Montilla, A. Galindo, *Catal. Comm.* 2016, **84**, 134-136.
- 37) G. Licini, V. Conte, A. Coletti, M. Mba, C. Zonta, *Coord. Chem. Rev.* 2011, **255**, 2345-2357.
- 38) M. Mba, M. Pontini, S. Lovat, C. Zonta, G. Bernardinelli, P. E. Kündig, G. Licini, *Inorg. Chem.* 2008, **47**, 8616-8618.
- 39) V. V. Thakur, A. Sudalai, *Tetrahedron Asymmetry* 2003, **14**, 407-410.
- 40) K. Kaczorowska, Z. Kolarska, K. Mitka, P. Kowalski, *Tetrahedron* 2005, **61**, 8315-8327.
- 41) O. Bortolin, F. Di Furia, G. Licini, G. Modena, *Synthesis* 1988, **37**, 171-174.
- 42) J. C. Cruz, J. García, M. Ayala, *TIP* 2015, **18**, 5-12.
- 43) T. S. Smith, V. L. Pecoraro, *Inorg. Chem.* 2002, **41**, 6754-6760.
- 44) H. B. ten Brink, H. L. Dekker, H. E. Schoemaker, R. Wever, *J. Inorg. Biochem.* 2000, **80**, 91-98.
- 45) H. B. ten Brink, A. Tuynman, H. L. Dekker, W. Hemrika, Y. Izumi, T. Oshiro, H. E. Schoemaker, R. Wever, *Inorg. Chem.* 1998, **37**, 6780-6784.
- 46) R. M. Garrett, J. L. Johnson, T. N. Graf, A. Feigenbaum, K. V. Rajagopalan, *Proc. Natl. Acad. Sci. USA* 1998, **95**, 6394-6398.
- 47) H. Wei, E. Wang, *Chem. Soc. Rev.* 2013, **42**, 6060-6093.
- 48) R. Ragg, F. Natalio, M. N. Tahir, H. Janssen, A. Kashyap, D. Strand, S. Strand, W. Tremel, *ACS Nano* 2014, **8**, 5182-5189.

- 49) D. Spetter, F. Hoshyargar, J. K. Sahoo, M. N. Tahir, R. Branscheid, B. Barton, M. Panthöfer, U. Kolb, W. Tremel, *Eur. J. Inorg. Chem.* **2017**, 2190-2194.
- 50) H. Bai, W. Yi, J. Li, G. Xi, Y. Li, H. Yang, J. Liu, *J. Mater. Chem A* 2016, **4**, 1566-1571.
- 51) F. Zhou, X. Zhao, C. Yuan, L. Li, *Cryst. Growth Design.* **2008**, **8**, 723-727.
- 52) M. Dieterle, G. Mestl, *Phys. Chem. Phys.* **2002**, **4**, 822-826.
- 53) G. L. Frey, A. Rothschild, J. Sloan, R. Rosentsveig, R. Popovitz-Biro, R. Tenne, *J. Solid State Chem.* **2001**, **162**, 300-314.
- 54) L. Abello, E. Husson, Y. Repelin, G. Lucazeau, *Spectrochim. Act.* **1983**, **39A**, 641-651.



## 3.5.7 Supporting Information

## Tables

Table S1. Characteristic Raman bands recorded for MoO<sub>3-x</sub>.<sup>1</sup>

Wavenumber [cm <sup>-1</sup> ]	Characteristic band
194	B <sub>2g</sub> , $\tau$ O=M=O twist
214	A <sub>g</sub> , rotational rigid MoO <sub>4</sub> chain mode, R <sub>c</sub>
240	B <sub>3g</sub> , $\tau$ O=M=O twist
282	B <sub>2g</sub> , $\nu_{as}$ O=M=O wagging
337	A <sub>g</sub> , B <sub>1g</sub> , $\delta$ O-M-O bend
377	B <sub>1g</sub> , $\delta$ O-M-O scissor
664	B <sub>2g</sub> , B <sub>3g</sub> , $\nu_{as}$ O-M-O stretch
819	A <sub>g</sub> , $\nu_a$ M=O stretch
994	A <sub>g</sub> , $\nu_{as}$ M=O stretch

Table S2. Characteristic Raman bands recorded for  $V_2O_5$ .<sup>2</sup>

Wavenumber [ $\text{cm}^{-1}$ ]	Characteristic band
193	$A_g$ , $\delta$ O=V=O wagging
283	$B_{2g}$ , $\delta$ O-V-O bend
306	$B_{1g}$ , $\delta$ $V_3$ -O bend (triply coordinated oxygen)
408	$A_g$ , $\delta$ V-O-V bend
522	$A_g$ , $\nu_s$ , $V_3$ -O stretch (triply coordinated oxygen)
687	$B_{2g}$ , $\nu_{as}$ , $V_2$ -O stretch (doubly coordinated oxygen)
992	$A_g$ , $\nu_s$ , V=O stretch

**Table S3. Characteristic Raman bands recorded for  $W_{18}O_{49}$ .<sup>3</sup>**

<b>Wavenumber [<math>cm^{-1}</math>]</b>	<b>Characteristic band</b>
187	O-W-O bend
256	O-W-O bend
695	W-O-W stretch
806	W=O stretch

## Figures

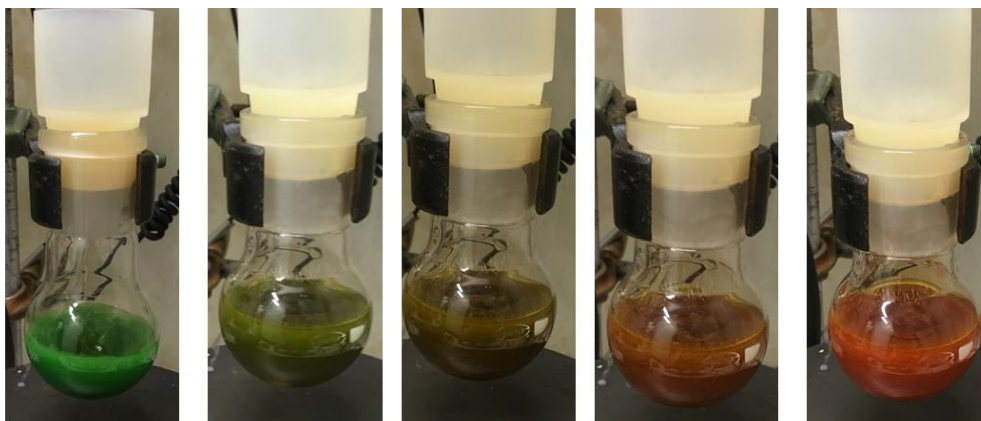


Figure S1. Colour change of the reactin mixture within the first three minutes of the  $V_2O_5$  synthesis.

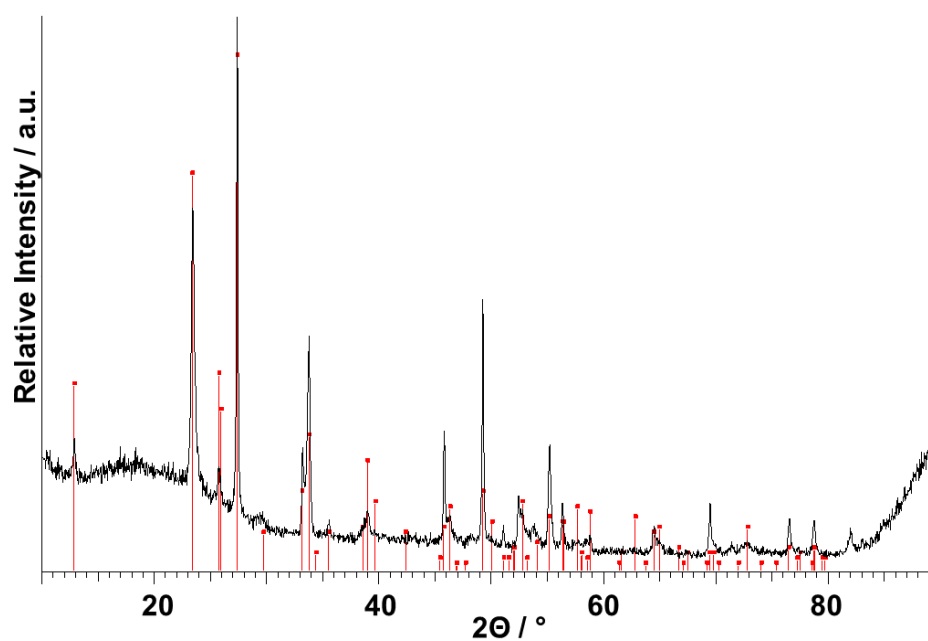
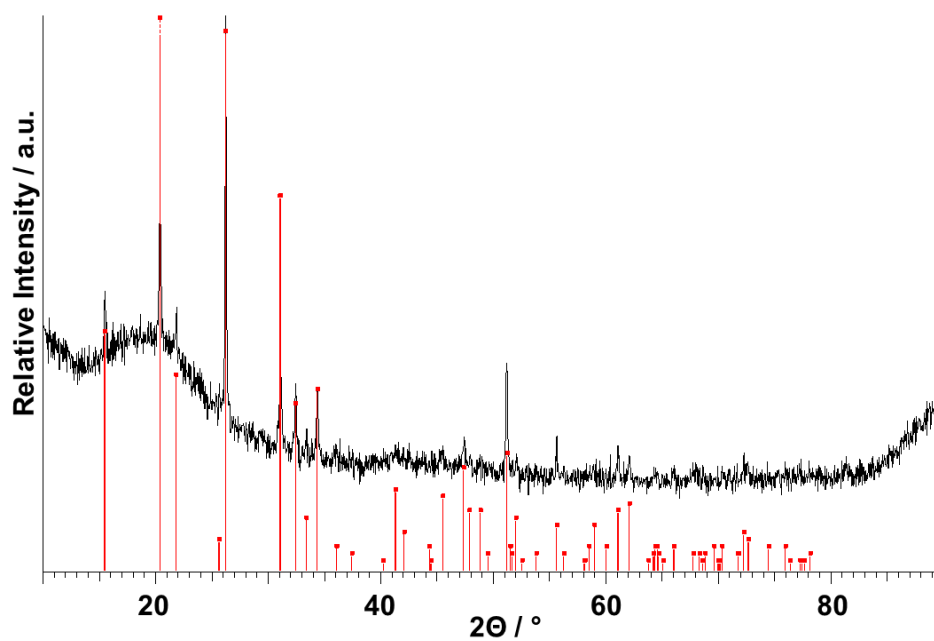
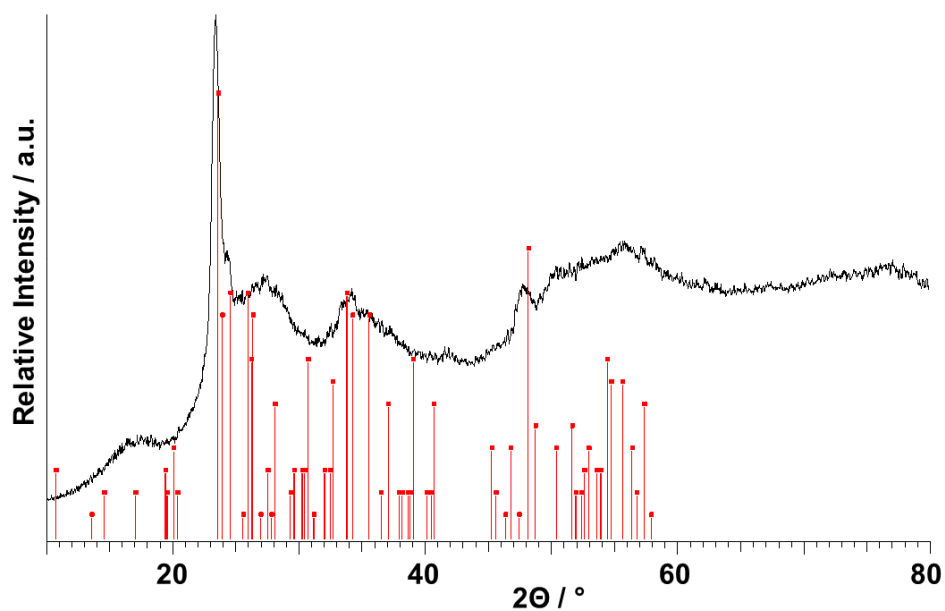


Figure S2. X-ray analysis of molybdenum oxide particles. A comparison of the measured pattern (black) with reflex positions of  $MoO_3$  from literature confirm the formation of  $MoO_{3-x}$  particles.



**Figure S3. X-ray analysis of vanadium pentoxide wires.** The measured pattern (black) fits well to the reflex positions of V<sub>2</sub>O<sub>5</sub> (sherbinaite).



**Figure S4. X-ray analysis of tungsten oxide wires.** The measured pattern (black) fits to the reflex positions of W<sub>18</sub>O<sub>49</sub>.

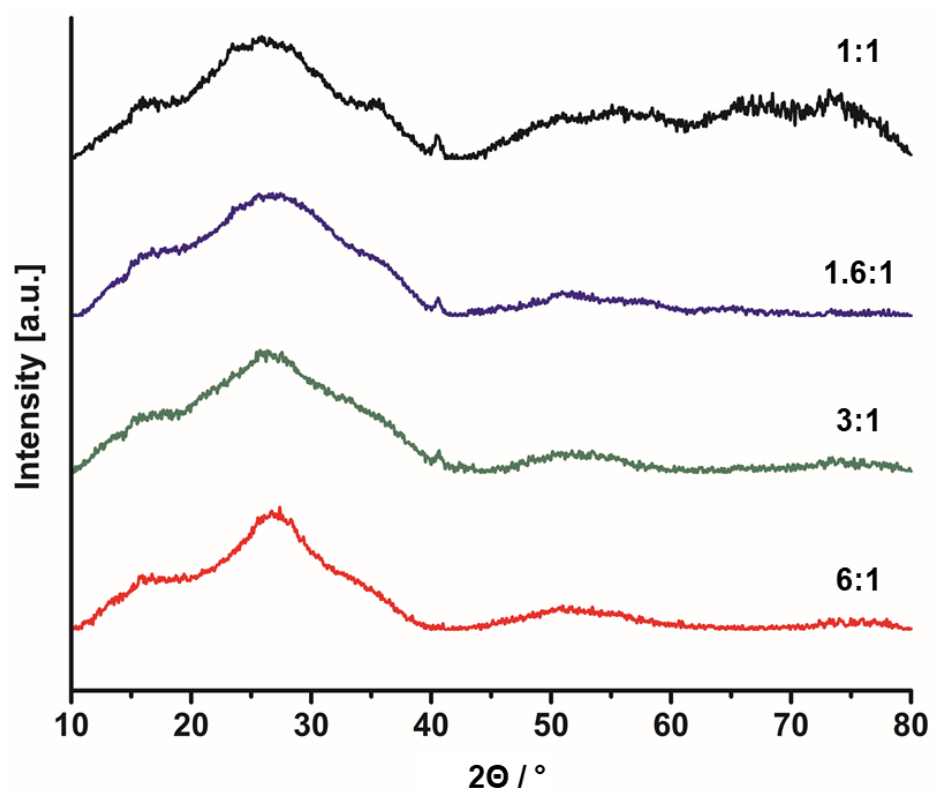
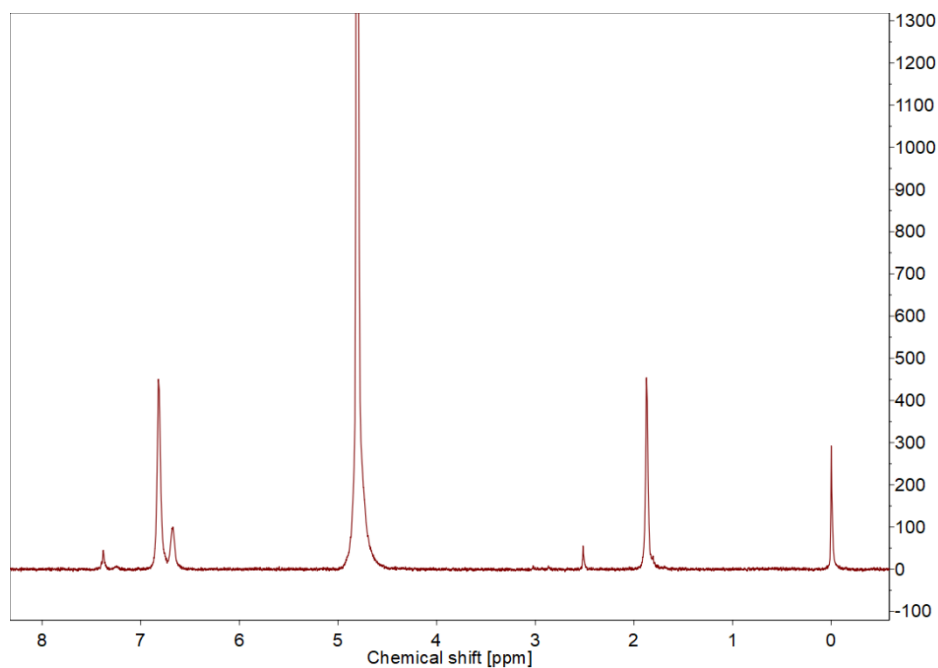
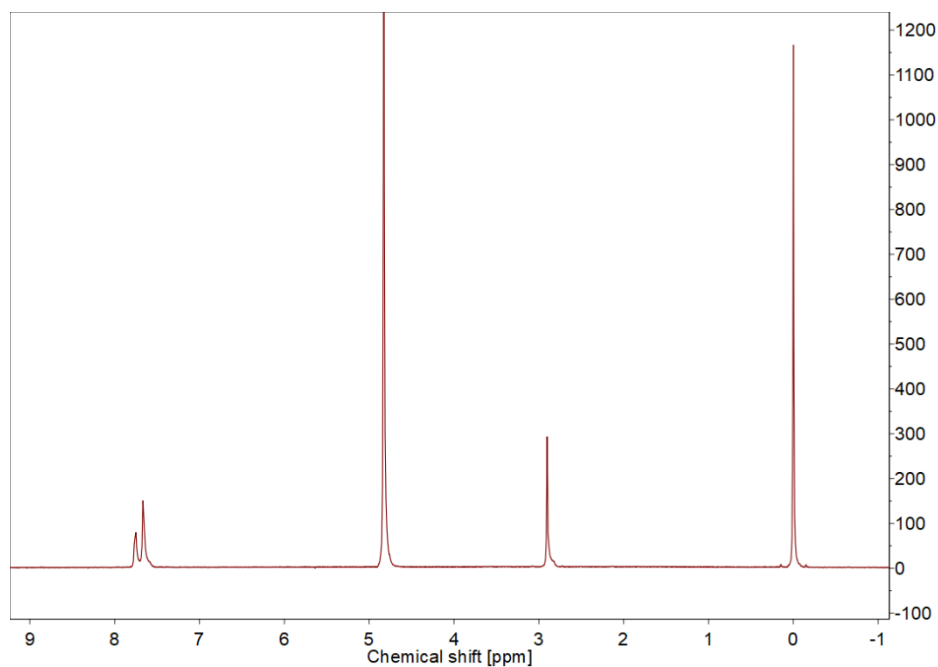


Figure S5. X-ray analysis of molybdenum and tungsten mixed oxide particles with Mo:W ratios 1:1 (black), 1.6:1 (blue), 3:1 (green) and 6:1 (red).



**Figure S6.** NMR spectrum of Methyl phenyl sulfide in  $D_2O$  with 3-(Trimethylsilyl)propionic-2,2,3,3  $d_4$  sodium salt (TMSP) as internal standard. The chemical shift of the methyl resonance of TMSP was manually set to 0 ppm.



**Figure S7.** NMR spectrum of methyl phenyl sulfoxide in  $D_2O$  with 3-(Trimethylsilyl)propionic-2,2,3,3  $d_4$  sodium salt (TMSP) as internal standard. The chemical shift of the methyl resonance of TMSP was manually set to 0 ppm.

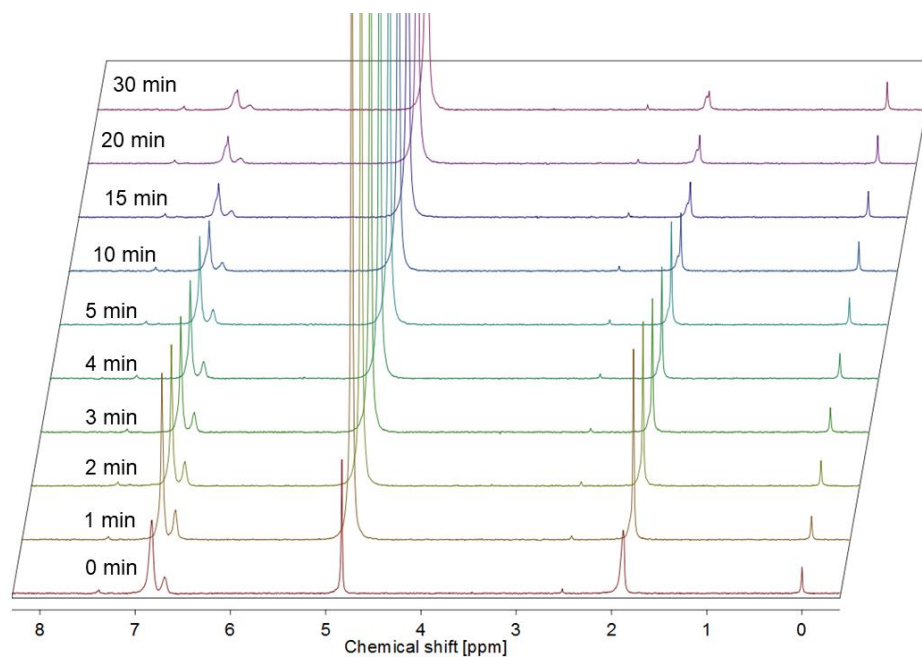


**Figure S8. Control measurements conducted in presence of H<sub>2</sub>O<sub>2</sub> without catalyst showed no oxidation of TA within 30 minutes.** The chemical shift of the methyl resonance of TMS was manually set to 0 ppm.

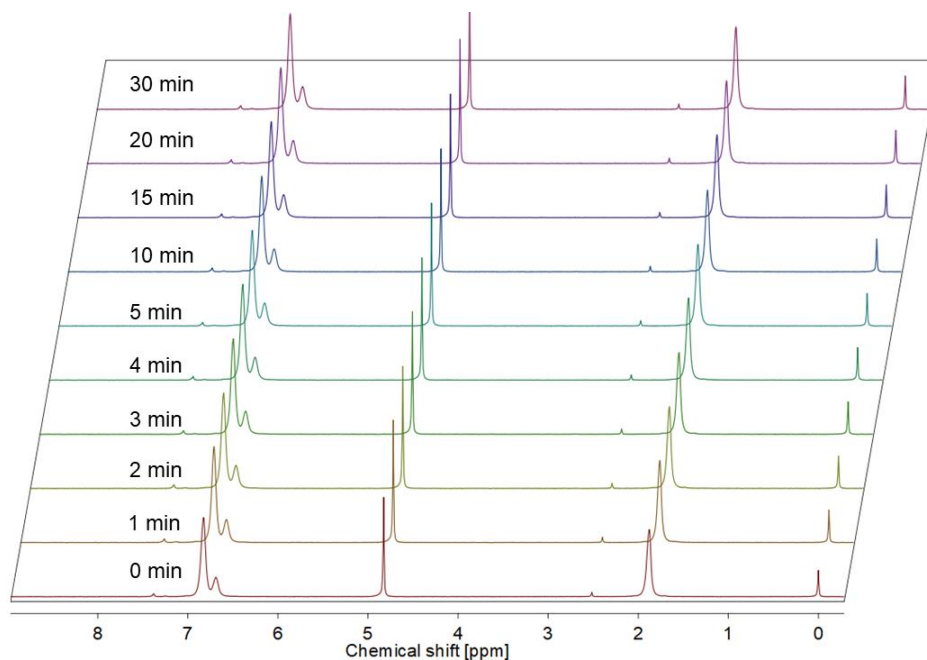


**Figure S9. Control measurements conducted in presence of catalyst without hydrogen peroxide did not show an oxidation of TA within 30 minutes.** The chemical shift of the methyl resonance of TMS was manually set to 0 ppm.





**Figure S10.** A photograph of the NMR tube after 30 minutes of the reaction, show the precipitation of the heterogeneous catalyst.

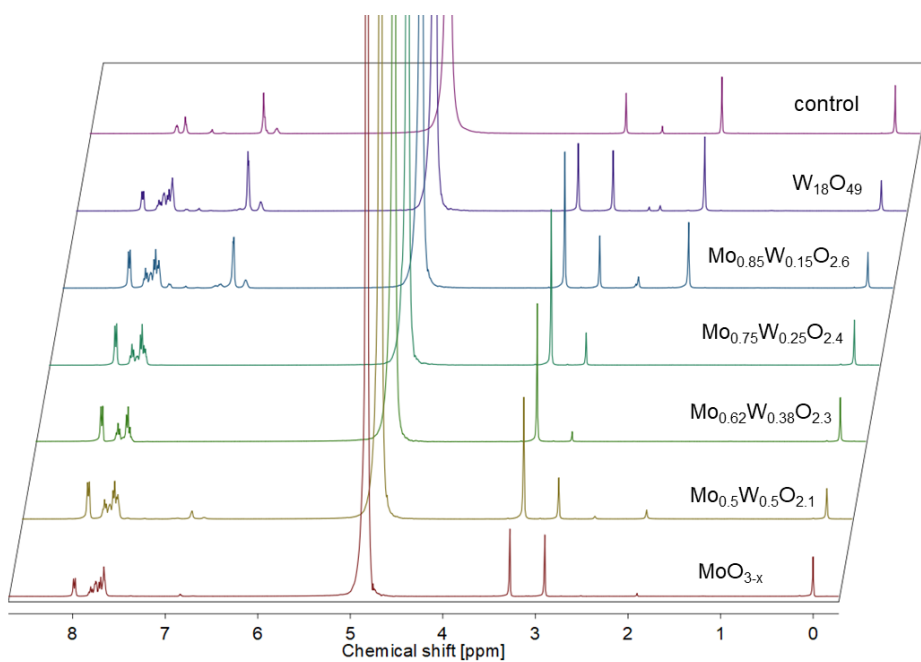


**Figure S11.** Oxidation of methyl phenyl sulfide with three equivalents of  $\text{H}_2\text{O}_2$  after 48 h in presence of the different catalysts. Highest activity was achieved using the mixed metal oxide particles with a Mo:W ratio of 1.6:1.

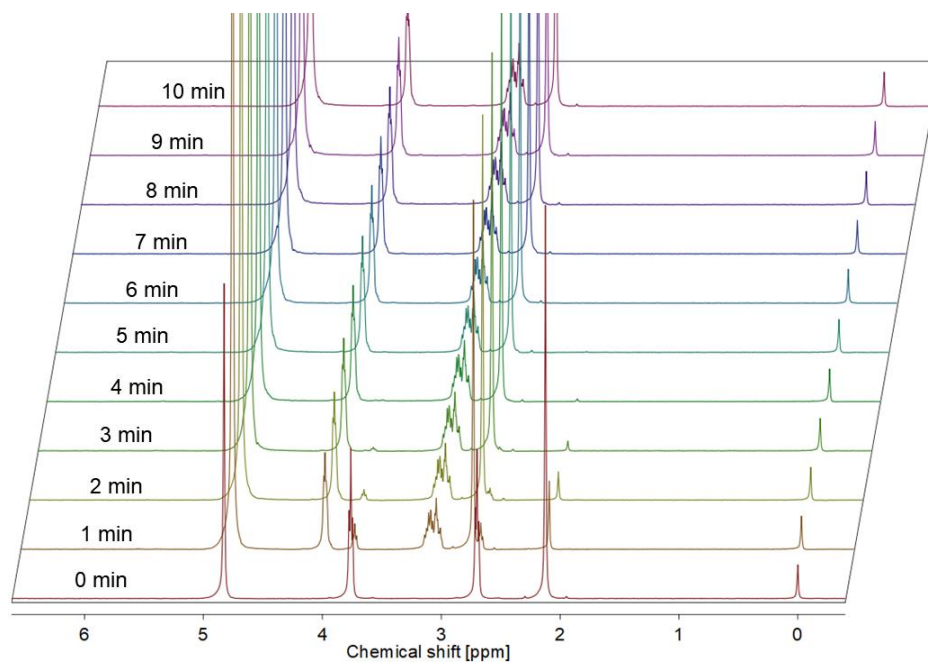


**Figure S12.** Oxidation of 2-Hydroxyethyl methyl sulfide with  $\text{Mo}_{0.62}\text{W}_{0.38}\text{O}_{2.3}$  in presence of one equivalent  $\text{H}_2\text{O}_2$ .

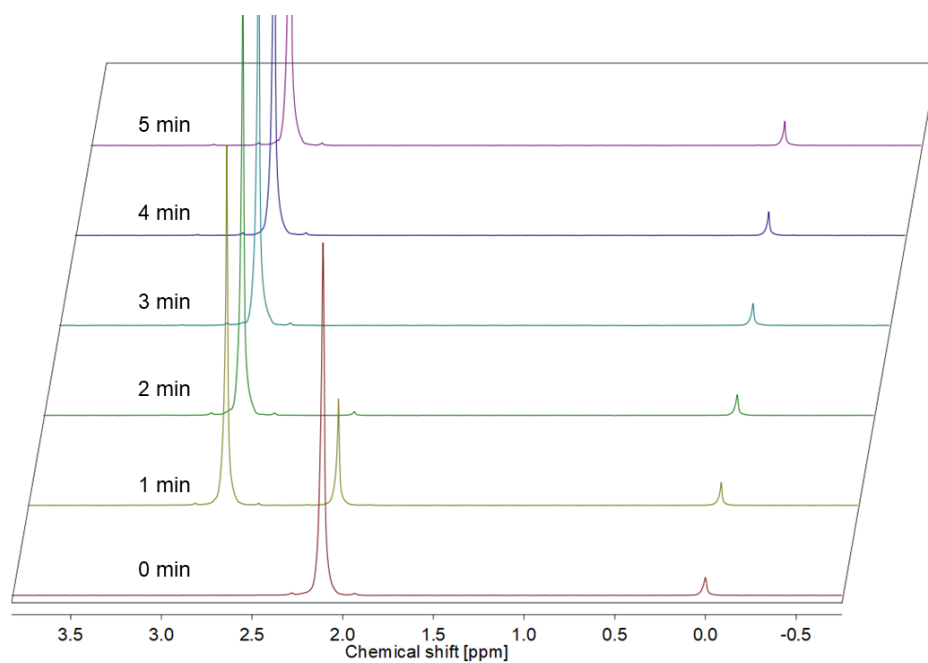


**Figure S13.** Oxidation of dimethyl sulfide with  $\text{Mo}_{0.62}\text{W}_{0.38}\text{O}_{2.3}$  in presence of one equivalent  $\text{H}_2\text{O}_2$ .

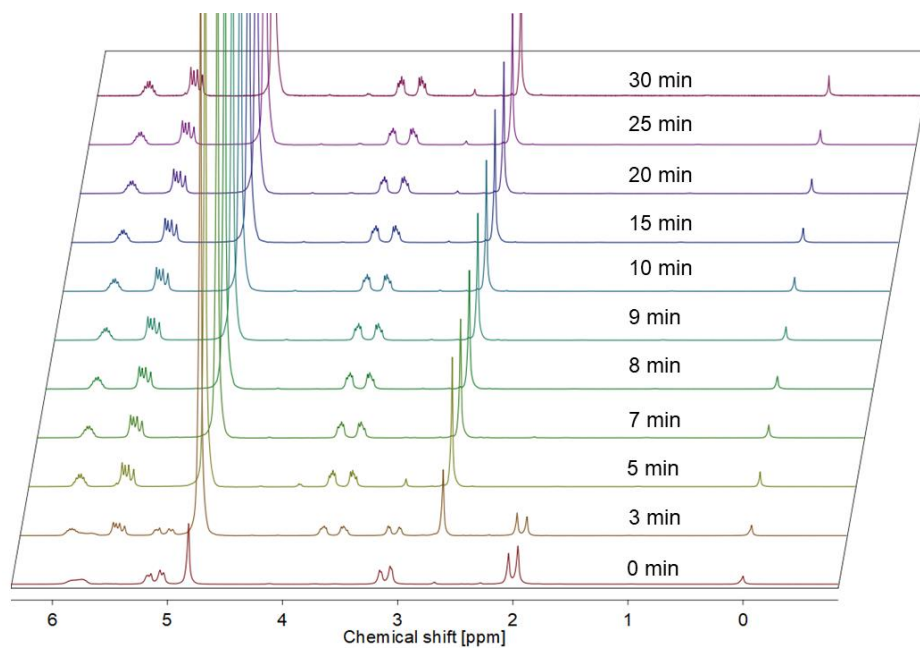


**Figure S14.** Oxidation of allyl methyl sulfide with  $\text{Mo}_{0.62}\text{W}_{0.38}\text{O}_{2.3}$  in presence of one equivalent  $\text{H}_2\text{O}_2$ .

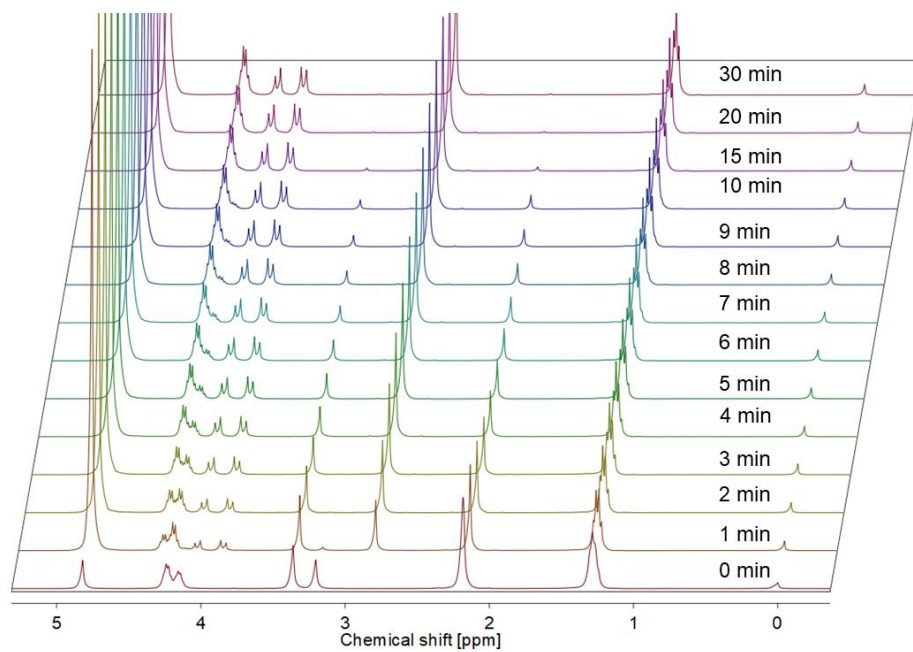


**Figure S15.** Oxidation of ethyl (methylthio) acetate with  $\text{Mo}_{0.62}\text{W}_{0.38}\text{O}_{2.3}$  in presence of one equivalent of  $\text{H}_2\text{O}_2$ .

### 3. Results and Discussion

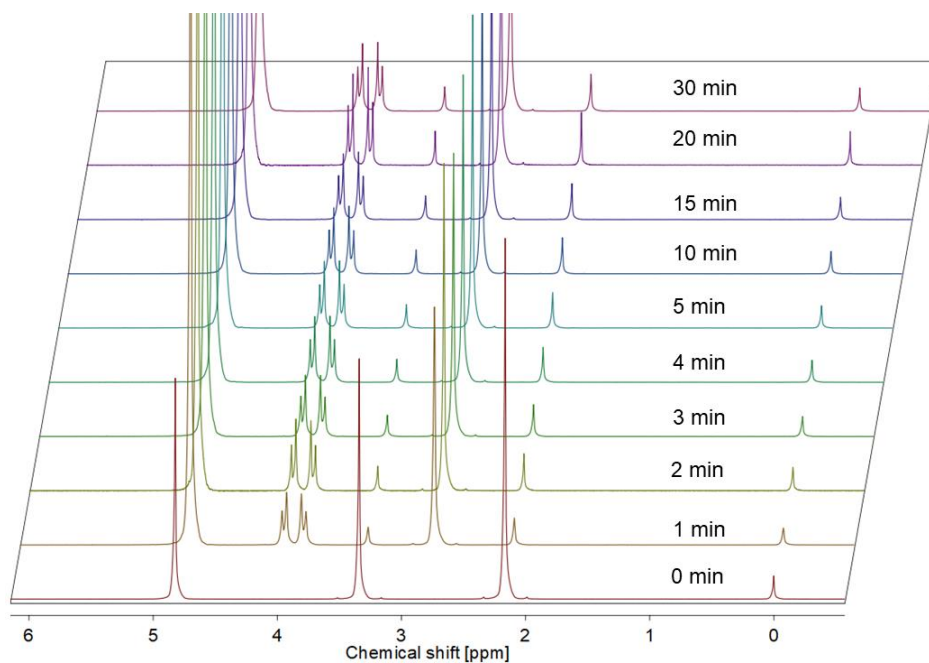


**Figure S16.** Oxidation of (methylthio) acetic acid with  $\text{Mo}_{0.62}\text{W}_{0.38}\text{O}_{2.3}$  in presence of one equivalent  $\text{H}_2\text{O}_2$ .

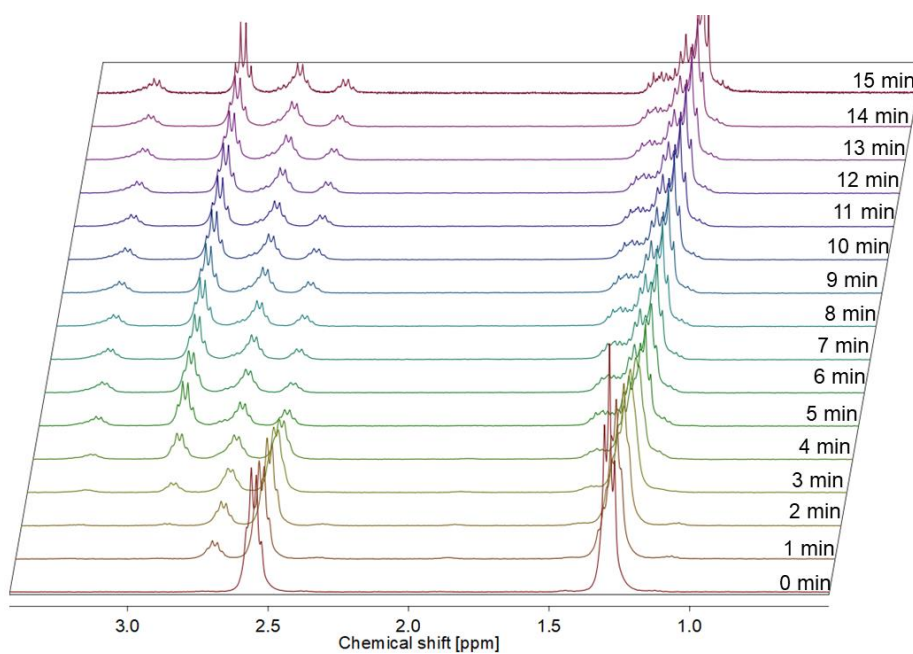


**Figure S17.** Oxidation of ethanethiol with  $\text{Mo}_{0.62}\text{W}_{0.38}\text{O}_{2.3}$  in presence of one equivalent  $\text{H}_2\text{O}_2$ .

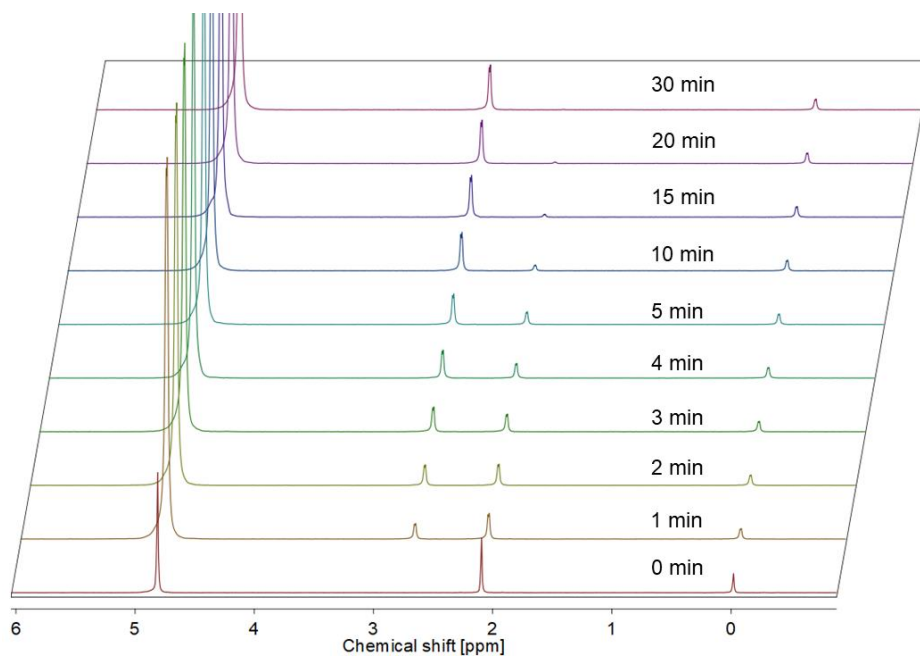


**Figure S18.** Oxidation of dimethyl sulfide without catalyst in presence of one equivalent  $\text{H}_2\text{O}_2$ .

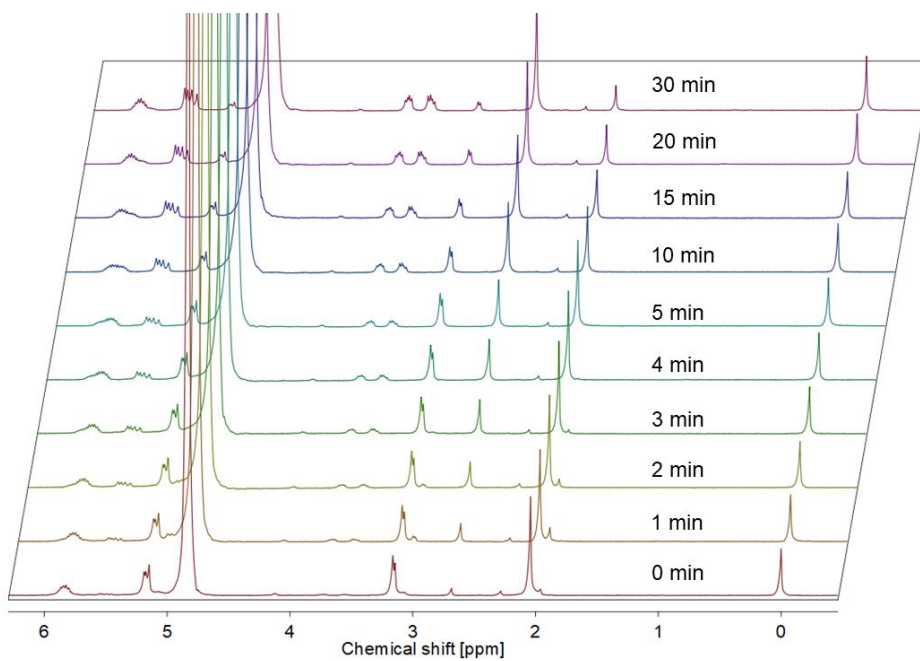


**Figure S19.** Oxidation of allyl methyl sulfide without catalyst in presence of one equivalent  $\text{H}_2\text{O}_2$ .

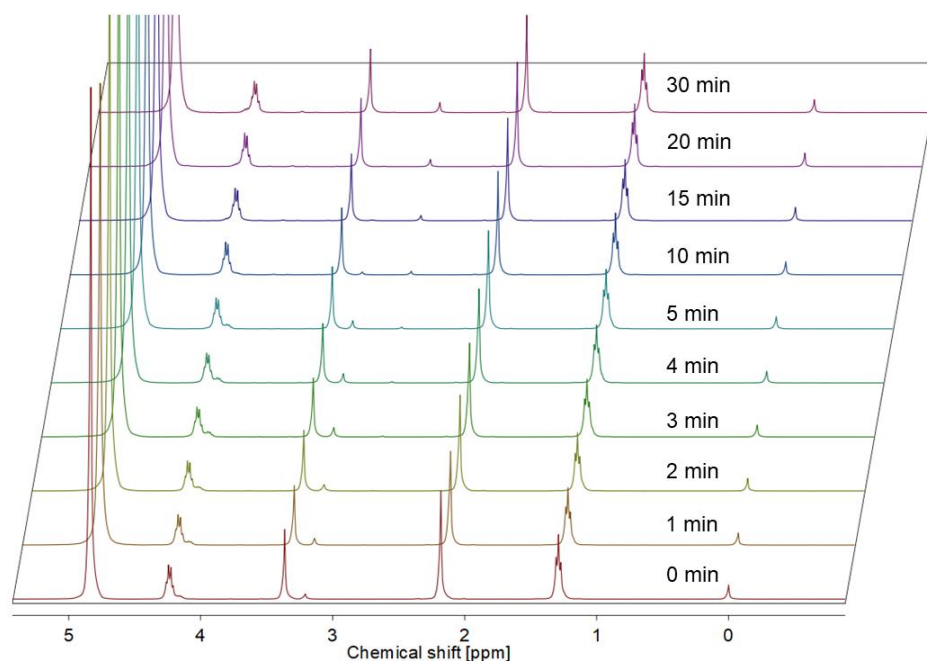


**Figure S20.** Oxidation of (methylthio) acetate without catalyst in presence of one equivalent  $\text{H}_2\text{O}_2$ .

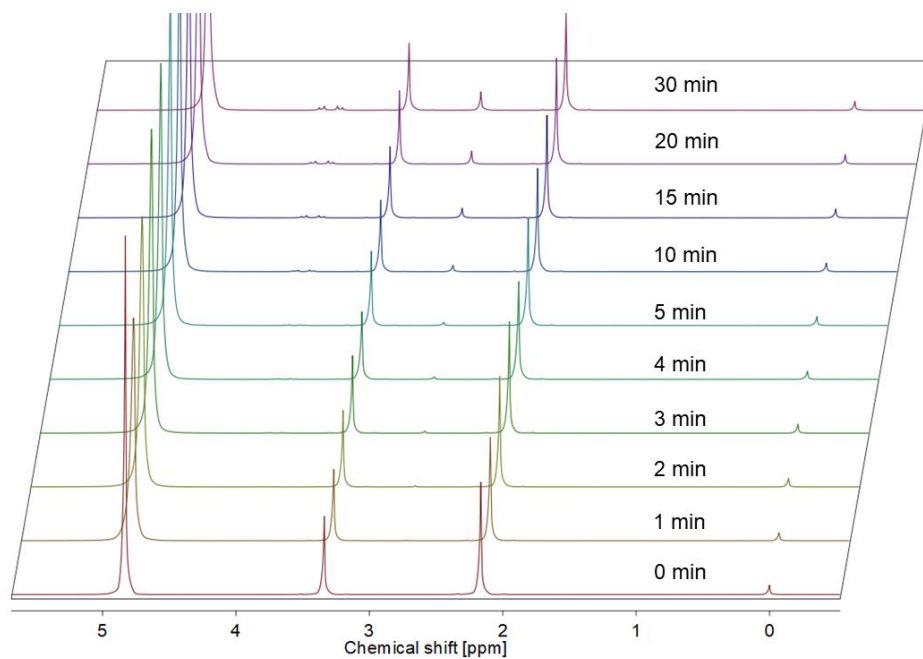


**Figure S21.** Oxidation of (methylthio) acetic acid without catalyst in presence of one equivalent  $\text{H}_2\text{O}_2$ .

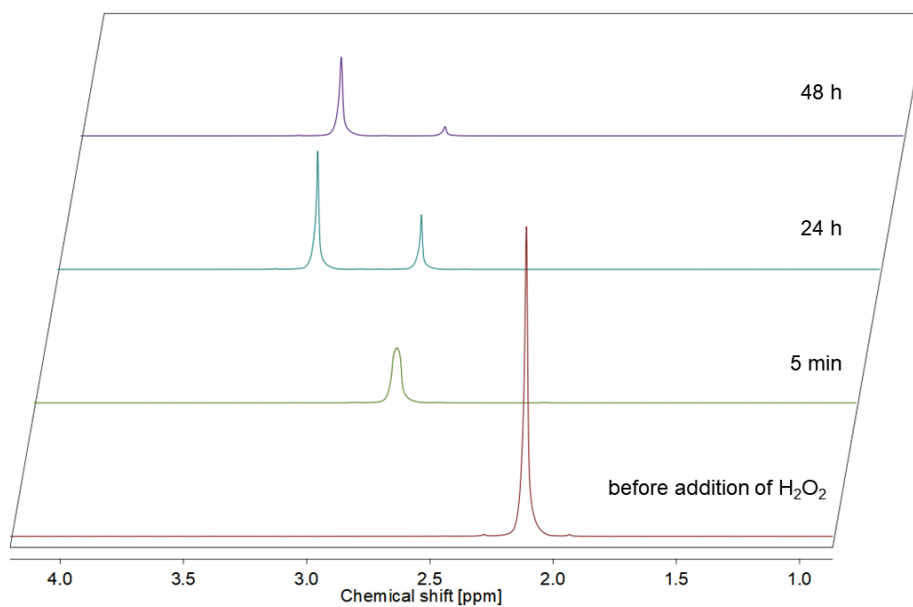


**Figure S22. Oxidation of dimethyl sulfide with Mo<sub>0.62</sub>W<sub>0.38</sub>O<sub>2.3</sub> in presence of three equivalent H<sub>2</sub>O<sub>2</sub>.**

#### Characterization of the organic substrates

All organic compounds were characterized by  $^1\text{H}$  NMR spectroscopy (400 MHz,  $\text{D}_2\text{O}$ ) and electrospray ionization mass spectrometry (ESI-MS).

#### Methyl phenyl sulfide.

$^1\text{H}$ NMR (400 MHz,  $\text{D}_2\text{O}$ )  $\delta$  1.74 (s, 3 H), 6.43 – 6.83 (m, 5 H)

#### Methyl phenyl sulfoxide.

$^1\text{H}$ NMR (400 MHz,  $\text{D}_2\text{O}$ )  $\delta$  2.88 (s, 3 H), 7.58 - 7.75 (m, 5 H)

HR ESI-MS (m/z):  $[\text{M}+\text{H}^+]$  calculated 141.0374; measured 141.0399 ( $\text{M} = 140.20 \text{ g mol}^{-1}$ )

#### Methyl phenyl sulfone.

$^1\text{H}$ NMR (400 MHz,  $\text{D}_2\text{O}$ )  $\delta$  3.25 (s, 3 H), 7.77-7.80 (m, 3 H), 7.95-7.97 (d,  $J = 8.15$  Hz, 2 H)

HR ESI-MS (m/z):  $[\text{M}+\text{H}^+]$  calculated 157.0323; measured 157.0323 ( $\text{M} = 156.20 \text{ g mol}^{-1}$ )

#### 2-Hydroxyethyl methyl sulfide.

$^1\text{H}$ NMR (400 MHz,  $\text{D}_2\text{O}$ )  $\delta$  2.12 (s, 3 H), 2.66 – 2.72 (t,  $J = 6$  Hz, 2 H), 3.72 – 3.80 (t,  $J = 6$  Hz, 2 H)

ESI-MS (m/z): ( $\text{M} = 92.16 \text{ g mol}^{-1}$ )

#### 2-(Methylsulfinyl) ethanol.

$^1\text{H}$ NMR (400 MHz,  $\text{D}_2\text{O}$ )  $\delta$  2.75 (s, 3 H), 3.01 – 3.18 (m, 2 H), 3.96 – 4.04 (t,  $J = 3$  Hz, 2 H)

ESI-MS (m/z):  $[\text{M} + \text{Na}^+]$  calculated 131.01, measured 131.01 ( $\text{M} = 108.16 \text{ g mol}^{-1}$ )



**Diphenyl sulfide.**

$^1\text{H}$ NMR (400 MHz,  $\text{D}_2\text{O}$ )  $\delta$  6.49 – 6.64 (m, 6 H), 6.73 – 6.89 (m, 4 H)

**Dimethyl sulfide.**

$^1\text{H}$ NMR (400 MHz,  $\text{D}_2\text{O}$ )  $\delta$  2.11 (s, 6 H)

**Dimethyl sulfoxide.**

$^1\text{H}$ NMR (400 MHz,  $\text{D}_2\text{O}$ )  $\delta$  2.75 (s, 6 H)

ESI-MS (m/z): to low molar mass ( $M = 78.01 \text{ g mol}^{-1}$ )

**Dimethyl sulfone.**

$^1\text{H}$ NMR (400 MHz,  $\text{D}_2\text{O}$ )  $\delta$  3.16 (s, 6 H)

ESI-MS (m/z): to low molar mass ( $M = 94.00 \text{ g mol}^{-1}$ )

**Allyl methyl sulfide.**

Bad solubility of the substrate lead to a double peak formation. Hence, the signals in the NMR spectrum was integrated completely.

$^1\text{H}$ NMR (400 MHz,  $\text{D}_2\text{O}$ )  $\delta$  1.82 – 2.15 (s\*, 3 H), 2.97 - 3.21 (dd\*, 2 H), 4.99 – 5.26 (dd\*, 2 H), 5.68 – 5.93 (dd, 1 H)

\* two signals observable due to bad solubility in water.

**Allyl methyl sulfoxide.**

$^1\text{H}$ NMR (400 MHz,  $\text{D}_2\text{O}$ )  $\delta$  2.67 (s, 3 H), 3.49 – 3.58 (dd, 1 H), 3.65 – 3.77 (dd, 1 H), 5.34 – 5.63 (dd, 2 H), 5.81– 5.99 (m, 1 H).

ESI-MS (m/z):  $[\text{M} + \text{Na}^+]$  calculated 127.02, measured 127.01 ( $M = 104.17 \text{ g mol}^{-1}$ )

**Ethyl(methylthio) acetate.**

$^1\text{HNMR}$  (400 MHz,  $\text{D}_2\text{O}$ )  $\delta$  1.28 (t,  $J = 3$  Hz, 3 H), 2.18 (s, 3 H), 3.36 (s, 2 H),

**Ethyl (methylsulfoxyl) acetate.**

$^1\text{HNMR}$  (400 MHz,  $\text{D}_2\text{O}$ )  $\delta$

ESI-MS (m/z):  $[\text{M} + \text{H}^+]$  calculated 151.0423, measured 151.0423  
( $M = 150.21 \text{ g mol}^{-1}$ )

**(Methylthio) acetic acid.**

$^1\text{HNMR}$  (400 MHz,  $\text{D}_2\text{O}$ )  $\delta$  2.16 (s, 3 H), 3.34 (s, 2 H)

**(Methylsulfinyl) acetic acid.**

$^1\text{HNMR}$  (400 MHz,  $\text{D}_2\text{O}$ )  $\delta$  2.80 (s, 3 H), 3.96 (s, 2 H), 3.78 – 3.92 (d, 1 H), 3.94 – 4.08 (d, 1H)

ESI-MS (m/z):  $[\text{M} + \text{Na}^+]$  calculated: 144.99, measured: 145.00 ( $M = 122.14 \text{ g mol}^{-1}$ )

**Ethane thiol.**

$^1\text{HNMR}$  (400 MHz,  $\text{D}_2\text{O}$ )  $\delta$  1.19 – 1.36 (t, 3 H), 2.47 – 2.61 (q, 2 H)

**References**

- 1) M. Dieterle, G. Mestl, *Phys. Chem. Phys.* **2002**, *4*, 822-826.
- 2) L. Abello, E. Husson, Y. Repelin, G. Lucazeau, *Spectrochim. Act.* **1983**, *39A*, 641-651.
- 3) G. L. Frey, A. Rothschild, J. Sloan, R. Rosentsveig, R. Popovitz-Biro, R. Tenne, *J. Solid State Chem.* **2001**, *162*, 300-314.

### 4. Conclusion and Outlook

The present doctoral thesis describes the successful exploration of novel nanoparticulate enzyme mimics and the investigation of their catalytic activity in classical heterogeneous catalysis. Each subproject was inspired and motivated by native enzymes, their crucial role in nature, or their practical applications in everyday life. As soon as the native inspiration was found, the practical strategy can be described in four steps. First, the chemical characteristics of the enzyme catalyzed reaction were monitored and interpreted, which simultaneously gave the boundary conditions for the possible enzyme replacement. In a second step, the selected nanoparticles were synthesized, and their solid phase, morphology and surface characteristics were characterized. With an appropriate lab assay, which was in most cases a spectrophotometrical method, the catalytic activity was explored and compared to the native enzyme. Assuming a positive result and a high catalytic activity, the practical application for the nanoparticles with an enzyme-like activity was explored in final experiments.

It was possible to show, that nanoparticles can mimic native enzymes and they can overcome the limitations of using native enzymes in different practical applications. Nevertheless, it is important to elaborate the properties of the nanoparticles on a transparent way, enabling a fair comparison with their natural counterparts, but also with other nanoparticles that show a similar activity. The greatest difference between nanoparticles and native enzymes is the number of catalytic active sites. While an enzyme usually has one active site domiciled in a protein backbone with specific binding pockets, their artificial counterparts exhibit large surface areas with high numbers of active surface atoms. Paying attention to such imbalances, a novel calculation method was developed during this doctoral thesis. Using this method, it is possible to approximate the catalytic activity of a nanoparticle normalized to one surface site, following the example of the native inspiration.

The first project was focused on the exploration of a functional superoxide dismutase mimic. Superoxide radicals are the most frequently occurring reactive oxygen species and elevated levels lead to a broad range of serious diseases. To mimic the native superoxide dismutase enzyme, glycine functionalized copper(II) hydroxide nanoparticles were synthesized, starting with a copper glycine complex as precursor. As-prepared particles were characterized with x-ray diffraction measurements, proving the solid phase as copper(II) hydroxide, infrared and solid state nuclear magnetic resonance spectroscopy, investigating the surface properties and proving the functionalization with glycine. The superoxide dismutase-like activity of the nanoparticles was analyzed with a iodinitro tetrazolium chlorid based spectrophotometric assay. I was able to show, that glycine functionalized copper(II) hydroxide nanoparticles can catalyze the decomposition reaction of superoxide radicals with an activity higher than the native CuZn superoxide dismutase enzyme. The nanoparticle activity was normalized to a single particle as well as to an active surface site. It was further proved that the superoxide radical decomposition, catalyzed by the copper nanoparticles, shows characteristics of a catalytic cycle. This was analyzed by monitoring the oxidation state of the copper ions during the reaction progress. Because of the reaction mechanism of the radical decomposition, copper ions shuttling between the oxidation states +II and +I. Monitoring the paramagnetic shift of a  $^1\text{H}$ -NMR signal proved the reoxidation of the copper(I) species into the initial oxidation state. It is known, that high concentrations of superoxide radicals are present in the smoke of commercial cigarettes. While a practical use of the native enzyme is not possible because of the decomposition, an application of the glycine functionalized copper(II) hydroxide nanoparticles as part of the commercial filter system demonstrated a significant reduction of the radical concentration and the toxic effect of the cigarette smoke extract.

The second subproject of this thesis was focussed on hydrogen peroxide, another representative of the group of reactive oxygen species. Hydrogen peroxide is an omnipresent oxygen compound and is naturally decomposed by native peroxidases. A special representative of this group is the catalase enzyme, which facilitates the transformation of hydrogen peroxide into elemental oxygen and water. Hydrogen peroxide is *inter alia* present in the wound liquid, where elevated levels can decelerate the healing mechanism. The target of this project was to control the hydrogen peroxide level and protect fibroblasts against cell death. We fabricated hematite nanoparticle containing electrospun polyvinyl alcohol based nanofibrous membranes with high porosity and wettability. These characteristics are important to enable the diffusion of hydrogen peroxide into the fiber meshes and allowing the contact to the catalytic active hematite nanoparticles. The previously prepared hematite nanoparticles facilitated the decomposition of hydrogen peroxide as free particle in solution as well as embedded into the fiber mesh, comparable to the native catalase enzyme. Cell experiments further proved that the catalase-like activity of hematite containing polymer fibers efficiently protected fibroblasts against cell death. These characteristics could significantly improve the wound healing process.

To further establish the knowledge of embedding nanoparticles in polymer fiber meshes *via* electrospinning, a third project implemented. Native haloperoxidase enzymes catalyze the oxidation reaction of halides with hydrogen peroxide into hypohalous acids. These acids can affect the cell to cell communication of bacteria and inhibit the formation of a biofilm, an early step of the biofouling process. Recently, reports on different nanoparticles, which can mimic the native haloperoxidase and prevent biofouling, were published. Cerium oxide nanorods were embedded into the PVA fibers. The nanorods were still able to form hypohalous acids in presence of halides and hydrogen peroxide. In addition to their catalytic properties, the mechanical stability of the fiber meshes increased in presence of the nanorods. The catalytic activity and the mechanical stability are the basic requirements for inhibiting the biofilm formation, even on movable surfaces like under water tubes.

The fourth study was focussed on the exploration of the first artificial compound for mimicking the activity of the native urease enzyme. Ureases are a group of enzymes which catalyse the hydrolysis of urea. Most studies in the field of enzyme mimics are focussed on the exploration of oxido reductases, whereas Lewis acid base reactions are rare. It was shown, that cerium oxide nanorods can mimic the catalytic activity of native jack bean urease with an activity comparable to the enzyme. A wide variety of metal oxide particles was additionally synthesized and investigated without success. The kinetic studies were conducted with a time efficient spectrophotometric assay, which could be executed with a 96 well plate reader or an UV-Vis spectrophotometer. The surface of cerium oxide nanorods contains  $\text{Ce}^{3+}$  and  $\text{Ce}^{4+}$  ions, which amounts are directly connected to the number of oxygen vacancies at the particle surface. Hence the ratio of  $\text{Ce}^{4+}/\text{Ce}^{3+}$  strongly affects the catalytic activity. Investigations of the surface characteristics were conducted by tuning the  $\text{Ce}^{4+}/\text{Ce}^{3+}$  ratio with a direct substitution of cerium with lanthanum. Raman measurements and XPS analysis confirmed the lanthanum doping and the increasing number of surface defects with higher amount of lanthanum. The catalytic efficiency of native urease is strongly affected by the presence of different metal ions. One of the strongest inhibitors are  $\text{Cu}^{2+}$  ions which are present in waste waters from different sources. It was found that even low amounts of  $\text{Cu}^{2+}$  can knock down the urease activity of jack bean urease, whereas the nanorod activity was not affected. Leaching experiments in water and urea solution proved the long-term stability of cerium oxide nanorods and lanthanum doped cerium oxide nanorods, where metal concentrations close to the detection limit were found. The reported trials prove the possibility of mimicking the native urease enzyme and substituting them for example in the water reclamation, where cerium oxide nanorods could be used for enabling in a higher process stability even in presence of enzyme inhibitors like metal ions.

The last project, described in this thesis, reported on the catalytic activity of different single metal oxide particles, like  $V_2O_5$ ,  $MoO_{3-x}$  and  $W_{18}O_{49}$ . All nanoparticles were previously synthesized, completely characterized and their properties as catalyst in a sulfide oxidation reaction were tested. The kinetic studies were conducted with methyl phenyl sulfide as representative organic sulfide, which was oxidized into methyl phenyl sulfoxide in presence of one equivalent hydrogen peroxide. The reaction progress was monitored online with  $^1H$  NMR spectroscopy and turnover numbers were calculated. It was found, that the  $MoO_{3-x}$  and  $W_{18}O_{49}$  particles showed the highest activity, whereas  $V_2O_5$  was less active. We further found, that mixing the metal phases of molybdenum and tungsten significantly increased the catalytic activity.  $Mo_{1-y}W_yO_{3-x}$  microparticles were prepared with different Mo:W ratios. It was found that  $Mo_{0.62}W_{0.38}O_{2.3}$  microparticles showed the highest activity of all tested materials and the reaction runs completely selective without formation of byproducts. Using the  $Mo_{0.62}W_{0.38}O_{2.3}$  microparticles a wide variety of organic sulfides was testing and primary high turnovers and high selectivities were achieved.

Nanoparticles with an enzyme-like activity are perfect systems for substituting their natural counterparts. The exploration of practical applications can currently be divided in two groups. First, applications, mostly *in vivo*, which try to mimic the native enzyme inside their natural surroundings, and second, applications, where the enzyme-like catalytic activity was used to combat environmental problems by simultaneously overcoming the limitations of native enzymes. The projects, described in the present thesis, are great examples, belonging to the second group. Because of the fact, that exploring nanomaterials with enzyme-like activities is still a young field of research, a lot of basic research must be done. As an example, the coupling of two different nanoparticles with unequal activities, could enable reaction cascades. In theory the active sites of center one would transfer a substrate A into product B, which could then be used as a substrate by center two for forming product C. Such cascades are interesting, especially in cases, where a toxic substrate A is transferred into a slightly less toxic compound B. In addition, the disadvantages like the biocompatibility of nanoparticles must be investigated and potentially improved. Of course, novel enzymes or reaction types need to be explored and the connected applications must be investigated and reported.



## 5. Appendix

### 5.1 List of Figures

#### 5.1.1 Inorganic Nanoparticles as Enzyme Mimics

Figure 1: Schematic Representation of advantages and disadvantages of native enzymes, compared to nanoparticle enzyme mimics, the so called “nanozymes”. 5

#### 5.1.2 A Step into the Future – Applications of Nanoparticle Enzyme Mimics

Figure 1: Nanoceria combat ischemic stroke diseases. 26

Figure 2: Retrieval of mitochondrial structure by reducing oxidase stress with TPP-ceria NPs. 28

Figure 3: Cerium oxide NPs can promote the wound healing process. 30

Figure 4: *In vivo* tumor imaging with MNPs. 33

Figure 5: Tumor treatment with MNPs and H<sub>2</sub>O<sub>2</sub> forming ROS. 34

Figure 6: MoO<sub>3</sub>-TPP NPs with intrinsic sulfite oxidase activity. 36

Figure 7: Antifouling properties of nanoceria. 39

Figure 8: Reduction of superoxide radicals in cigarette smoke using the intrinsic superoxide dismutase-like activity of Gly-Cu(OH)<sub>2</sub> NPs. 41

---

### 5.1.3 Glycine-Functionalized Copper(II) Hydroxide Nanoparticles with High Intrinsic Superoxide Dismutase Activity

Figure 1: Synthesis, enzymatic activity and application of Gly-Cu(OH) <sub>2</sub> NPs.	66
Figure 2: TEM imaging of Gly-Cu(OH) <sub>2</sub> NPs.	68
Figure 3: Phase characterization and functionalization of Gly-Cu(OH) <sub>2</sub> NPs.	70
Figure 4: Catalytic efficiency of Gly-Cu(OH) <sub>2</sub> NPs and reduction of superoxide concentration in cigarette smoke.	74
Figure S1: TEM image of Cu(OH) <sub>2</sub> .	82
Figure S2 IR spectra of <i>cis</i> -bis(glycinato) copper(II) monohydrate and glycine.	83
Figure S3: Oxygen evolution of Gly-Cu(OH) <sub>2</sub> NPs when exposed to superoxide radicals by xanthine/xanthine oxidase (XO)	84
Figure S4: Schematic representation of a spherical Cu(OH) <sub>2</sub> NP showing the catalytically active Cu atoms at the NP surface and inactive atoms inside the NP volume	84
Figure S5: NMR spectra of the SOD-like reaction catalyzed by Gly-Cu(OH) <sub>2</sub> NPs recorded with the Evan's method.	85
Figure S6: Setup for cigarette smoke experiments.	86
Figure S7: Inhibition of INT reduction by Gly-Cu(OH) <sub>2</sub> NPs and CuZn SOD.	87
Figure S8: Cytotoxicity of cigarette smoke extract (CSE) for A549 cells.	87

---

#### 5.1.4 Fibrous Nanozyme Dressings with Catalase-like Activity for H<sub>2</sub>O<sub>2</sub> Reduction to Promote Wound Healing

- Figure 1: Figure 1. Schematic illustration of the fabrication procedure of hematite nanofibrilous gels *via* electrospinning and their use as catalase mimics to convert hydrogen peroxide into water and oxygen to yield an improved fibroblast growth. 100
- Figure 2: TEM pictures of  $\alpha$ -Fe<sub>2</sub>O<sub>3</sub> spindle-shaped particles. 106
- Figure 3: Characterization of hematite/PVA nanofibrous mats. 108
- Figure 4: Characterization of cross-linked hematite/PVA nanofibrous mats. 110
- Figure 5: Decomposition of H<sub>2</sub>O<sub>2</sub> catalyzed by native catalase (b), hematite NPs (c) and hematite loaded PVA fiber meshes (d), observed with the fluorescence signal at 605 nm of EuTc-HP. 112
- Figure 6: Analysis of the catalytic activity and the resulting products. 114
- Figure S1: SEM images of crosslinked PVA mats containing 0% (a), 19% (b) and 58% (c) of hematite nanoparticles. 121
- Figure S2 Dynamic wettability of the crosslinked PVA mat containing 0% (a), 19% (b), and 58% (c) of hematite nanoparticles. 121
- Figure S3: Absorption spectra of EuTc and EuTc-HP. 122
- Figure S4: Relative fluorescence intensity (reflecting the H<sub>2</sub>O<sub>2</sub> level) after 5 minutes reaction with native catalase enzyme. 123
- Figure S5: Fluorescent intensities of living cells after incubation with different adding materials (H<sub>2</sub>O<sub>2</sub>, electrospun membranes without nanoparticles, and membranes with high loading of nanoparticles). 124

---

**5.1.5 Nanozymes in Fibrous Membranes with Haloperoxidase-Like Activity**

- Figure 1. Fabrication of ceria nanorods ( $\text{CeO}_{2-x}$ ) nanofibrous mats by electrospinning. 130
- Figure 2. (a) XRD spectra of synthesized  $\text{CeO}_{2-x}$  nanorods (NR). Inset is the TEM images of NR (scale bar = 200 nm). (b) TGA curves of the hybrid PVA/ $\text{CeO}_{2-x}$  mats with different NR loading. 137
- Figure 3. Schematics of the AFM bending experiment. 139
- Figure 4. Determination of the haloperoxidase-like activity of electrospun and PVA mats with different loadings of  $\text{CeO}_{2-x}$  NRs in presence of  $\text{H}_2\text{O}_2$  and  $\text{NH}_4\text{Br}$ . 141
- Figure S1. TGA curves of the  $\text{CeO}_{2-x}$  NR/PVA membranes with different NR loadings (11% and 17%) before and after immersion in water for 2 weeks. 149
- Figure S2. Stiffness profiles of single  $\text{CeO}_{2-x}$  NR/PVA fibers with different NR loadings (0%, 5%, 11%, and 17%). 150
- Figure S3. Time-dependent UV/vis spectra of PVA membranes without  $\text{CeO}_{2-x}$  nanorods loading. 151

**5.1.6 CeO<sub>2-x</sub> Nanorods with Intrinsic Urease-Like Activity**

Figure 1: Schematic representation of CeO <sub>2-x</sub> NRs and their urease-like activity.	156
Figure 2: Characterization of as-synthesized CeO <sub>2-x</sub> NRs.	166
Figure 3: Urease activity of native jack bean urease and CeO <sub>2-x</sub> NRs.	168
Figure 4: Characterization of Ce <sub>0.9</sub> La <sub>0.1</sub> O <sub>1.95-x</sub> .	171
Figure 5: Urease activity of Ce <sub>1-x</sub> La <sub>x</sub> O <sub>2-x/2</sub> NRs.	173
Figure S1: AFM images of CeO <sub>2-x</sub> NRs.	181
Figure S2: EDX measurements of CeO <sub>2-x</sub> NRs.	181
Figure S3: A kinetic absorption scan of a phosphate buffered solution containing phenol red and urea without catalyst.	182
Figure S4: Calibration conducted with 0.1 M ammonium carbonate ((NH <sub>4</sub> ) <sub>2</sub> CO <sub>3</sub> ) solution.	183
Figure S5: Representative TEM image of nanostructured MoO <sub>3-x</sub> belts.	184
Figure S6: P-XRD analysis of nanostructured MoO <sub>3-x</sub> belts.	184
Figure S7: Representative TEM image of nanostructured V <sub>2</sub> O <sub>5</sub> wires.	185
Figure S8: P-XRD measurement of nanostructured V <sub>2</sub> O <sub>5</sub> wires.	185
Figure S9: IR spectra of Ni(Gly) <sub>2</sub> complex and the amino acid glycine.	186
Figure S10: IR spectra of Gly-Ni(OH) <sub>2</sub> NPs and bulk Ni(OH) <sub>2</sub> .	186
Figure S11: TEM images of Gly-Ni(OH) <sub>2</sub> NPs.	187

Figure S12: P-XRD measurement of Gly-Ni(OH) <sub>2</sub> NPs.	187
Figure S13: TEM image of TiO <sub>2</sub> .	188
Figure S14: Variation of the concentration of native urease.	188
Figure S15: Variation of CeO <sub>2-x</sub> .	189
Figure S16: TEM image of Ce <sub>0.6</sub> La <sub>0.4</sub> O <sub>1.80-x</sub> NRs.	190
Figure S17: HR-TEM images of Ce <sub>0.6</sub> La <sub>0.4</sub> O <sub>1.80-x</sub> NRs.	190
Figure S18: EDX spectrum of Ce <sub>0.6</sub> La <sub>0.4</sub> O <sub>1.80-x</sub> NRs.	191
Figure S19: XPS spectrum of Ce <sub>0.6</sub> La <sub>0.4</sub> O <sub>1.80-x</sub> NRs.	192
Figure S20: Raman spectra of CeO <sub>2-x</sub> , Ce <sub>0.9</sub> La <sub>0.1</sub> O <sub>1.95-x</sub> and Ce <sub>0.6</sub> La <sub>0.4</sub> O <sub>1.80-x</sub> NRs.	193
Figure S21: P-XRD measurement of Ce <sub>0.6</sub> La <sub>0.4</sub> O <sub>1.80-x</sub> NRs.	194
Figure S22: EDX measurement of Ce <sub>0.9</sub> La <sub>0.1</sub> O <sub>1.95-x</sub> NRs.	195
Figure S23: AFM image of Ce <sub>0.9</sub> La <sub>0.1</sub> O <sub>1.95-x</sub> NRs.	195
Figure S24: Variation of Ce <sub>0.9</sub> La <sub>0.1</sub> O <sub>1.95-x</sub> .	196
Figure S25: Variation of Ce <sub>0.6</sub> La <sub>0.4</sub> O <sub>1.80-x</sub> .	197

### 5.1.7 Selective Oxidation of Organic Sulfides with Single Metal Oxide and Mixed Metal Oxide Particles

- Figure 1. Schematic representation of synthesis, characterization and catalytic efficiency of various transition metal oxide particles and tungsten and molybdenum mixed oxide microparticles. 208
- Figure 2: HR-TEM images of A)  $\text{MoO}_{3-x}$ , B)  $\text{V}_2\text{O}_5$ , C)  $\text{W}_{18}\text{O}_{49}$  and SEM Images of (D)  $\text{Mo}_{0.5}\text{W}_{0.5}\text{O}_{2.1}$  (E)  $\text{Mo}_{0.62}\text{W}_{0.38}\text{O}_{2.3}$  (F)  $\text{Mo}_{0.75}\text{W}_{0.25}\text{O}_{2.4}$  (E)  $\text{Mo}_{0.85}\text{W}_{0.15}\text{O}_{2.6}$ . 214
- Figure 3: Raman spectra of (A)  $\text{MoO}_{3-x}$ , (B)  $\text{V}_2\text{O}_5$ , (C)  $\text{W}_{18}\text{O}_{49}$  and (D)  $\text{Mo}_{1-y}\text{W}_y\text{O}_{3-x}$  with different Mo:W ratios. 216
- Figure 4: Catalytic studies of the oxidation of MPS with hydrogen peroxide catalyzed by (A)  $\text{MoO}_{3-x}$ , (B)  $\text{V}_2\text{O}_5$  and (C)  $\text{W}_{18}\text{O}_{49}$ . 217
- Figure 5: Kinetic analysis of the oxidation of TA with  $\text{H}_2\text{O}_2$  catalyzed by mixed oxide  $\text{Mo}_{1-y}\text{W}_y\text{O}_{3-x}$  microspheres. 219
- Figure S1. Colour Change of the reaction mixture within the first three minutes of the  $\text{V}_2\text{O}_5$  synthesis. 230
- Figure S2: X-ray analysis of molybdenum oxide particles. 230
- Figure S3: X-ray analysis of vanadium pentoxide wires. 231
- Figure S4: X-ray analysis of tungsten oxide wires. 231
- Figure S5. X-ray analysis of molybdenum and tungsten mixed oxide particles with Mo:W ratios 1:1 (black), 1.6:1 (blue), 3:1 (green) and 6:1 (red). 232

- 
- Figure S6: NMR spectrum of Methyl phenyl sulfide in D<sub>2</sub>O with 3-(Trimethylsilyl)propionic-2,2,3,3 d<sub>4</sub> sodium salt (TMSP) as internal standard. 233
- Figure S7: NMR spectrum of methyl phenyl sulfoxide in D<sub>2</sub>O with 3-(Trimethylsilyl)propionic-2,2,3,3 d<sub>4</sub> sodium salt (TMSP) as internal standard. 233
- Figure S8: Control measurements conducted in presence of H<sub>2</sub>O<sub>2</sub> without catalyst showed no oxidation of TA within 30 minutes. 234
- Figure S9: Control measurements conducted in presence of catalyst without hydrogen peroxide did not show an oxidation of TA within 30 minutes. 234
- Figure S10: A photograph of the NMR tube after 30 minutes of the reaction, show the precipitation of the heterogeneous catalyst. 235
- Figure S11. Oxidation of methyl phenyl sulfide with three equivalents of H<sub>2</sub>O<sub>2</sub> after 48 h in presence of the different catalysts. 235
- Figure S12. Oxidation of 2-Hydroxyethyl methyl sulfide with Mo<sub>0.62</sub>W<sub>0.38</sub>O<sub>2.3</sub> in presence of one equivalent H<sub>2</sub>O<sub>2</sub>. 236
- Figure S13. Oxidation of dimethyl sulfide with Mo<sub>0.62</sub>W<sub>0.38</sub>O<sub>2.3</sub> in presence of one equivalent H<sub>2</sub>O<sub>2</sub>. 236
- Figure S14. Oxidation of allyl methyl sulfide with Mo<sub>0.62</sub>W<sub>0.38</sub>O<sub>2.3</sub> in presence of one equivalent H<sub>2</sub>O<sub>2</sub>. 237
- Figure S15. Oxidation of ethyl (methylthio) acetate with Mo<sub>0.62</sub>W<sub>0.38</sub>O<sub>2.3</sub> in presence of one equivalent of H<sub>2</sub>O<sub>2</sub>. 237



Figure S16. Oxidation of (methylthio) acetic acid with $\text{Mo}_{0.62}\text{W}_{0.38}\text{O}_{2.3}$ in presence of one equivalent $\text{H}_2\text{O}_2$ .	238
Figure S17. Oxidation of ethanethiol with $\text{Mo}_{0.62}\text{W}_{0.38}\text{O}_{2.3}$ in presence of one equivalent $\text{H}_2\text{O}_2$ .	238
Figure S18. Oxidation of dimethyl sulfide without catalyst in presence of one equivalent $\text{H}_2\text{O}_2$ .	239
Figure S19. Oxidation of allyl methyl sulfide without catalyst in presence of one equivalent $\text{H}_2\text{O}_2$ .	239
Figure S20. Oxidation of (methylthio) acetate without catalyst in presence of one equivalent $\text{H}_2\text{O}_2$ .	240
Figure S21. Oxidation of (methylthio) acetic acid without catalyst in presence of one equivalent $\text{H}_2\text{O}_2$ .	240
Figure S22. Oxidation of dimethyl sulfide with $\text{Mo}_{0.62}\text{W}_{0.38}\text{O}_{2.3}$ in presence of three equivalent $\text{H}_2\text{O}_2$ .	241

## 5.2 List of Tables

### 5.2.1 Inorganic Nanoparticles as Enzyme Mimics

Table 1. Inorganic Nanoparticles with enzyme like activities and practical Applications.	6
--	---

### 5.2.2 Glycine-Functionalized Copper(II) Hydroxide Nanoparticles with High Intrinsic Superoxide Dismutase Activity

Table S1: Details of the X-ray powder diffraction measurement and the refinement of the x-ray diffraction data.	88
Table S2: Catalytic activities of Gly-Cu(OH) <sub>2</sub> NPs, bulk Cu(OH) <sub>2</sub> and natural CuZn SOD with respect to molar concentration and <i>per</i> active site.	90
Table S3: Change of absorbance at 290 nm due to the formation of uric acid in presence (three different concentrations) and in absence (control) of Gly-Cu(OH) <sub>2</sub> NPs.	90

### 5.2.3 Nanozymes in Fibrous Membranes with Haloperoxidase-Like Activity

Table S1: Swelling ratios of PVA mats with different loading of CeO <sub>2-x</sub> nanorods	151
---	-----

**5.2.4 CeO<sub>2-x</sub> Nanorods with Intrinsic Urease-Like Activity**

Tab. S1. Data received from Rietveld refinements.	198
Tab. S2. Surface composition from XPS analysis.	199
Tab. S3. Leaching of Ce of CeO <sub>2-x</sub> NRs in MilliQ water. Data are corrected against standard but not blank corrected, due to the low blank values.	199
Tab. S4. Leaching of Ce and La of Ce <sub>0.9</sub> La <sub>0.1</sub> O <sub>1.95-x</sub> NRs in MilliQ water. Data are corrected against standard but not blank corrected, due to the low blank values.	200
Tab. S5. Leaching of Ce of CeO <sub>2-x</sub> NRs in 2.94 M urea solution. Data are corrected against standard but not blank corrected, due to the low blank values.	200
Tab. S6. Leaching of Ce and La of Ce <sub>0.9</sub> La <sub>0.1</sub> O <sub>1.95-x</sub> NRs in 2.94 M urea solution. Data are corrected against standard but not blank corrected, due to the low blank values.	201

### 5.2.5 Selective Oxidation of Organic Sulfides with Single Metal Oxide and Mixed Metal Oxide Particles

Table 1: Tested substrates for the sulfide oxidation reaction with one equivalent $\text{H}_2\text{O}_2$ and $\text{Mo}_{0.62}\text{W}_{0.38}\text{O}_{2.3}$ particles in aqueous solution.	221
Table S1: Characteristic Raman bands recorded for $\text{MoO}_{3-x}$ .	227
Table S2: Characteristic Raman bands recorded for $\text{V}_2\text{O}_5$ .	228
Table S3: Characteristic Raman bands recorded for $\text{W}_{18}\text{O}_{49}$ .	229

## 5.3 Author Contributions

In the current section detailed authorship contributions of published and accepted manuscripts are listed.

### 5.3.1 Manuscript: “A Step into the Future – Applications of Nanoparticle Enzyme Mimics”

The manuscript “A Step into the Future – Applications of Nanoparticle Enzyme Mimics” was published as concept article in the scientific journal *Chemistry A European Journal* (*Chem. Eur. J.*, **2018**, DOI: 10.1002/chem.201800384). All authors agreed with publishing the manuscript in a scientific journal.

**K. Korschelt:** Writing manuscript.

M. N. Tahir: Supervision, critical revision of the manuscript for important intellectual content

W. Tremel: Supervision, critical revision of the manuscript for important intellectual content

### **5.3.2 Manuscript: “Glycine-Functionalized Copper(II) Hydroxide Nanoparticles with High Intrinsic Superoxide Dismutase Activity”**

The manuscript “Glycine-Functionalized Copper(II) Hydroxide Nanoparticles with High Intrinsic Superoxide Dismutase Activity” was published in the scientific journal *Nanoscale* (*Nanoscale* **2017**, *9*, 3952–3960). All authors agreed with publishing the manuscript in a scientific journal.

**K. Korschelt:** Conception and design of all studies, acquisition and evaluation of data (synthesis of precursor complex and nanoparticles, infrared spectroscopy, superoxide dismutase activity, Evan’s method, oxygen formation, cigarette smoke experiments, atomic absorption spectroscopy), development of the novel calculation method for activities normalized to one active site, evaluation and interpretation of data, writing manuscript, critical revision of the manuscript for important intellectual content.

R. Ragg: Conception and design of studies (Synthesis of precursor complex and nanoparticles, oxygen formation, superoxide dismutase activity), data interpretation, development of the novel calculation method for activities normalized to one active site, critical revision of the manuscript for important intellectual content.

C. S. Metzger: Design of studies and the belonging acquisition and interpretation of data (cigarette smoke experiments, AlamarBlue<sup>®</sup> assay), critical revision of the manuscript for important intellectual content.

M. Kluenker: Development of the novel calculation method for activities normalized to one active site, interpretation of data, critical revision of the manuscript for important intellectual content.

M. Oster: Conception and design of studies (Synthesis of precursor complex and nanoparticles, oxygen formation, superoxide dismutase activity), data interpretation, critical revision of the manuscript for important intellectual content.

B. Barton: High resolution transmission electron microscopy.

M. Panthöfer: Solid state analysis and rietveld refinements.

D. Strand: Conception and design of studies (cell experiments), interpretation of belonging data.

U. Kolb: High resolution transmission electron microscopy.

M. Mondeshki: Solid state nuclear magnetic resonance spectroscopy, atomic absorption spectroscopy, critical revision of the manuscript for important intellectual content.

S. Strand: Conception and design of studies (cell experiments), interpretation of belonging data, critical revision of the manuscript for important intellectual content.

J. Brieger: Design of cigarette smoke experiments, interpretation of data, critical revision of the manuscript for important intellectual content, supervision.

M. N. Tahir: Conception and design of studies (synthesis, superoxide dismutase), data interpretation, critical revision of the manuscript for important intellectual content.

W. Tremel: Conception and design of studies, data interpretation, writing manuscript, critical revision of the manuscript for important intellectual content, supervision.

### **5.3.3 Manuscript: “Fibrous Nanozyme Dressings with Catalase-like Activity for H<sub>2</sub>O<sub>2</sub> Reduction to Promote Wound Healing”**

The manuscript “Fibrous Nanozyme Dressings with Catalase-like Activity for H<sub>2</sub>O<sub>2</sub> Reduction to Promote Wound Healing” was published in the scientific journal *ACS Applied Materials and Interfaces* (*ACS Appl. Mater. Interfaces*, **2017**, 9 (43), 38024-38031). All authors agreed with publishing the manuscript in a scientific journal.

M. Hu: Conception and design of studies and the acquisition of belonging data (electrospinning and cross-linking, cell experiments, water stability), interpretation of data, writing manuscript, critical revision of the manuscript for important intellectual content.

**K. Korschelt:** Conception and design of studies (cell experiments), conception and design of studies and acquisition of belonging data (catalytic measurements, oxygen formation, interpretation of data, writing manuscript, critical revision of the manuscript for important intellectual content.

P. Daniel: Conception and design of studies and the acquisition of belonging data (nanoparticle synthesis and characterization), interpretation of data, writing manuscript, critical revision of the manuscript for important intellectual content.

K. Landfester: Critical revision of the manuscript for important intellectual content.

W. Tremel: Supervision, critical revision of the manuscript for important intellectual content.

M. B. Bannwarth: Supervision, Conception and design of studies, interpretation of data, critical revision of the manuscript for important intellectual content.



### **5.3.4 Manuscript: “Nanozymes in Fibrous Membranes with Haloperoxidase-Like Activity for combating biofouling”**

The manuscript “Nanozymes in Fibrous Membranes with Haloperoxidase-Like Activity for combating biofouling” was prepared for submission to a journal with a peer review process.

M. Hu: Research idea, Conception and design of studies and the acquisition of belonging data (electrospinning and cross-linking, water contact angle), interpretation of data, writing manuscript, critical revision of the manuscript for important intellectual content.

**K. Korschelt:** Research idea, Conception, design of studies and acquisition of belonging data (nanoparticle synthesis, characterization, catalytic measurements), interpretation of data, writing manuscript, critical revision of the manuscript for important intellectual content.

M. Viel: Conception, design of studies and the acquisition of belonging data (nanoparticle synthesis, characterization, catalytic measurements)), interpretation of data, writing manuscript, critical revision of the manuscript for important intellectual content.

M. Kappl: AFM measurements, Critical revision of the manuscript for important intellectual content.

K. Landfester: Critical revision of the manuscript for important intellectual content.

H. Thérien-Aubin: Supervision, Critical revision of the manuscript for important intellectual content.

W. Tremel: Supervision, critical revision of the manuscript for important intellectual content.

### 5.3.5 Manuscript: “CeO<sub>2-x</sub> Nanorods with Intrinsic Urease-Like Activity”

The manuscript “CeO<sub>2-x</sub> Nanorods with Intrinsic Urease-Like Activity” was accepted for publication in the scientific journal *Nanoscale* (*Nanoscale*, **2018**, Accepted Manuscript, DOI: 10.1039/C8NR03556C). All authors agreed with publishing the manuscript in a scientific journal.

**K. Korschelt:** Research idea, conception and design of all studies, acquisition and evaluation of data (development urease assay, synthesis and characterization of all nanoparticles, catalytic studies of all used nanoparticles, leaching tests except ICP-MS measurements, Inhibition studies), evaluation and interpretation of data, writing manuscript, critical revision of the manuscript for important intellectual content.

R. Schwidetzky: Development of urease assay, synthesis Ni(OH)<sub>2</sub> nanoparticles, acquisition and evaluation of belonging data, interpretation of data.

F. Pfitzner: First experiments and support with the synthesis of lanthanum doped cerium oxide nanoparticles, interpretation of data.

J. Strugatchi: Acquisition and evaluation of data (vanadium pentoxide nanowires, lanthanum doped cerium oxide), kinetic studies of urease-like activity of various particles.

C. Schilling: Raman and XPS measurements.

M. von der Au. ICP-MS analysis for the leaching tests, Conception and design of studies, data interpretation, critical revision of the manuscript for important intellectual content.

K. Kirchhoff: HR-TEM, EDX.

M. Panthöfer: Rietveld Refinements, critical revision of the manuscript for important intellectual content.

I. Lieberwirth: HR-TEM, EDX.

M. N. Tahir: Data interpretation, critical revision of the manuscript for important intellectual content.

C. Hess: Raman and XPS studies.

B. Meermann: ICP-MS analysis for leaching tests, Conception and design of studies, data interpretation, critical revision of the manuscript for important intellectual content.

W. Tremel: Supervision, writing manuscript, critical revision of the manuscript for important intellectual content.

### **5.3.6 Manuscript: “Selective Oxidation of Organic Sulfides with Single Metal Oxide and Mixed Metal Oxide Particles”**

The manuscript “Selective Oxidation of Organic Sulfides with Single Metal Oxide and Mixed Metal Oxide Particles” was prepared for publishing in a scientific journal with a peer review process. All authors agreed with publishing the manuscript in a scientific journal.

D. Spetter: Conception and design of all studies, acquisition and evaluation of data (synthesis and characterization of tungsten oxide and mixed metal oxide particles, kinetic studies), evaluation and interpretation of data, critical revision of the manuscript for important intellectual content.

**K. Korschelt:** Conception and design of all studies, acquisition and evaluation of data (synthesis and characterization of vanadium and molybdenum oxide particles, kinetic studies, oxidation of various sulfides), ESI-MS measurements, evaluation and interpretation of data, writing manuscript, critical revision of the manuscript for important intellectual content.

M.Oster: Preliminary studies during diploma thesis, support in sulfide oxidation experiments and ESI-MS measurements, critical revision of the manuscript for important intellectual content.

K. Kirchhoff: HR-TEM

M.N. Tahir: Conception and design of studies, data interpretation, critical revision of the manuscript for important intellectual content

W. Tremel: Supervision, critical revision of the manuscript for important intellectual content